Simulated Data Studies for the T2K Neutrino Oscillation Analysis Using the Near Detector

Adam James Speers

This thesis is submitted for the degree of
DOCTOR OF PHILOSOPHY
in
PARTICLE PHYSICS

Department of Physics
Lancaster University
Lancaster, United Kingdom
March 2026

Abstract

The Tokai to Kamioka (T2K) experiment relies on advanced reconstruction and analysis software to maximise the usefulness of its detector data. The work presented in this thesis covers a range of improvements to the ND280 analysis and focuses primarily on the validation of the Production 7 (P7) software upgrade, and simulated data studies using the newly-developed GUNDAM fitter. P7 was a major upgrade for the ND280 reconstruction software, with changes including new reconstruction algorithms for several subdetectors. The validation process ensured existing analysis tools continued to work as well as they did prior to P7. The correction algorithm for timing errors in T2K run 8 ("timeslips") was determined to function correctly in P7, and the reconstruction efficiencies of objects in ND280's time projection chambers (TPCs) and electromagnetic calorimeter (ECal) segments was approximately equal to the the previous values. The new 4π solid-angle selection, which had been developed just prior to P7, was validated and implemented into the main T2K analysis for the first time. The efficiency and purity of the main CC0pi sample in the 4π selection, the most important sample in the T2K analysis, is $46.84 \pm 0.13\%$ and $79.89 \pm 0.13\%$, respectively, compared to P6 values of 47.49 ± 0.13 and 78.99 ± 0.13. GUNDAM is a newly-developed fitter which improves the agreement between the Monte Carlo (MC) simulation and the detector data by adjusting parameters in the MC. Simulated data studies use modified MC in place of real detector data, in order to test the efficacy of the fitter in a variety of alternative physical models beyond the nominal model used to generate the MC. A total of 19 studies were tested by fitting the modified MC to the nominal MC. GUNDAM was shown to be fully capable of performing good-quality fits across them all, with the majority of postfit χ^2 values being < 10 even for extreme divergences from the nominal model.

Declaration

The work presented in this thesis was performed by the author, either individually or in collaboration with members of the T2K collaboration, of which the author was a member. All work not performed by the author is referenced appropriately. None of the work presented here has previously been submitted as part of another qualification.

The author assisted in the construction of the SuperFGD detector during his time at the J-PARC site in early 2023, working alongside other T2K collaborators to install some of the many thousands of wavelength-shifting fibres into the detector. The author also assisted in preparing the ND280 detector for its first data-taking in years, which included the reconnection and/or testing of various electrical systems and the detector's liquid cooling system. in November 2024, the author performed data acquisition (DAQ) shifts, ensuring the detector was running correctly during beam time.

This thesis primarily concerns the author's work in two main areas: the validation of Production 7, and fake data studies using the GUNDAM fitter. The validation work involved the rigorous testing of existing T2K software, including the timeslip corrections for run 8, and the TPC-ECal matching algorithm, using both Monte Carlo simulation and real detector data. The validation of the recently-developed 4π solid-angle selection involved significant changes to various selection parameters, and allowed for its implementation into the T2K analysis for the first time. This was achieved with assistances from members of the Selection, Systematics, and Validation working group, amongst others.

The fake data studies using GUNDAM are the first of its kind using the new fitter. The specific fake data studies investigated and their associated parameters were developed by the NIWG group, but the generation of GUNDAM inputs using these parameters, the GUNDAM fit itself, and all subsequent analysis was performed by the author with assistance from the GUNDAM working group. The author has also contributed to the development of GUNDAM itself via input at working group meetings.

Acknowledgements

Firstly, I would like to thank my PhD supervisor, Laura Kormos. Her assistance over the last four years has been invaluable, and she has been there to support me throughout my research, thesis writing, and the occasional physics conference. I would also like to thank my deputy PhD supervisor and former masters supervisor Helen O'Keeffe, who inspired me towards neutrino physics in the first place.

My time as a PhD student at Lancaster would not have been nearly as enjoyable without my friends and colleagues in the particle physics PhD office, who always provided a great excuse to drag myself to the office and maybe even do some work. Our many erudite discussions covered topics such as the definition of tea, the topological classification of foodstuffs, and the conceptual pairings of various corrective lenses to alcoholic drinks. A massive thanks to Hannah Alarakia-Charles, Elliot Sampson, Sasha Jenkins, Rebecca Harris, Beth McCusker, Martina Tancock, Henry Lay, Niam Patel, and everybody else who made the PhD office such a great place to be!

I would also like to thank all the other PhDs, postdocs, and academics at Lancaster, both within and without the Lancaster T2K group, who have shared their expertise and provided tremendous help throughout the years, and without whom I would probably still be struggling to install ROOT. Thank you to Matt Lawe, Tom Dealtry, Tom Jones, Alex Finch, Joe Walsh, Tristan Doyle and Yongheng Xu for all your support.

Outside of Lancaster, I also found myself in Tokai for five months, where I was fortunate enough to joined by other PhD students who helped make the entire LTA a great adventure. Henry Wallace, Menai Lamers James, Katharina Lachner, Nick Latham, Paul Morrison, Ewan Miller, and everybody else at T2K I met in Japan, thank you for making it such an amazing time. Between the trips to Tokyo, Kyoto, Nara, and Nikko, the visits to incredible restaurants and to Joyful Honda, and the innumerable evenings spent at karaoke, it is without hyperbole I would say they were some the best months of my life.

Of course, this PhD would not have even existed without the T2K collaboration itself, and everyone in it. It has been a privilege to work with so many people, and to feel a part of something larger. Special thanks to the GUNDAM group: Ciro, Léna, Margherita, Clark, Adrien, Tristan, Vlada, and everybody else who has supported me through my final GUNDAM analysis. I would also like to thank Dave Hadley, Sophie King, Alexander

Izmaylov and Laura Munteanu for all the help in the early stages of my PhD.

I would also like to thank all the great people I've met at Lancaster over the years, outside of physics: Isabel, Isla, Hannah, Emily, Virginia, Eleanor, Luke, Rose and Jeffrey. Thanks also goes to everybody I've gamed with in the Lancaster University Roleplaying Society, throughout my undergrad and postgrad years.

Finally, I'd like to thank all my family and friends in Liverpool, who have always kept in touch despite me disappearing off to Lancaster for the better part of eight years. Thanks to my friends James, Ben, and Sean for our almost daily Discord chats. Huge thanks goes to Mum, Dad, and Ben, for all your love and support throughout my life. I couldn't have done it without any of you, and I hope I've made you proud.

Contents

List of Figures

List of Tables

Chapter 1

Introduction

The neutrino is a fundamental particle of miniscule mass, zero electric charge, interacts with particles only via the weak force and is particularly difficult to detect even with the most sensitive of particle detectors. It also possesses a range of unusual properties unseen in other particles in the Standard Model: neutrinos can oscillate between their three flavours (electron, muon, and tau) as they propagate; for example, a neutrino initially produced as a muon neutrino may interact as an electron neutrino after it has propagated some distance. They also have a small but non-zero mass, far lower than any other massive particle.

Neutrinos therefore present a great trove of physics beyond the Standard Model, and are the subject of study for multiple experiments. To explore neutrino oscillation, “long-baseline” neutrino experiments utilise two detectors: one very close to a neutrino beam source (the “near” detector), and one positioned far enough away for neutrino oscillation to occur (the “far” detector). By comparing measurements in neutrino beam composition between the near and far detector, the nature of neutrino oscillation can be probed.

The Tokai to Kamioka (T2K) experiment is one such experiment, with the near detector complex (ND280) located 280 m from the neutrino beam source, and the far detector (Super-Kamiokande) 295 km away. The position of the far detector, coupled with the neutrino beam peak energy, was chosen to maximise oscillation probability, which ensures the observation of as much neutrino flavour-changing as possible. Muon neutrinos (or antineutrinos, depending on the beam setting) produced at the beam source produce muons when interacting with nuclei via charged-current interactions; events within the detectors allow the neutrino beam composition to be measured from the particles produced. The

T2K experiment produces world-leading measurements for neutrino oscillation parameters, and the continued success of the experiment is achieved by the ongoing upgrades to its detection and analysis capabilities throughout the lifespan of the project.

This thesis is focused on work relating to two such advancements at T2K: the validation of the Production 7 (P7) software upgrade, which improves the reconstruction of ND280 data; and simulated data studies performed using GUNDAM, a new fitting engine designed to improve the quality of near detector simulations. Production 7 is a major upgrade to the reconstruction software for ND280 that implements new reconstruction algorithms for various subdetectors. The validation ensured that existing analysis tools would continue to function as expected. It also introduced a new selection which allows the analysis of muons propagating in a full 4π solid-angle range; whereas previous selections would only identify forward-going muons. The oscillation analysis relies on Monte Carlo (MC) simulations of the experiment, which are compared with detector data to constrain parameter uncertainties in the detector, beam flux, and physical models, the latter of which includes the neutrino oscillation parameters themselves. This fit is performed using a fitter which adjusts parameters of the simulation to bring the results closer to real data. GUNDAM is a newly-introduced fitter, still under development, which replaced the previous BANFF fitter. Simulated data studies, also known as "fake" data studies, utilise reweighted MC (the "simulated data") in place of real detector data, to analyse how effective GUNDAM is at fitting simulations from alternative physical models.

Chapter 2 presents an overview of the history of the neutrino and the theory of its interactions and oscillations. Chapter 3 describes the T2K experiment, including the accelerator complex, beam source, and both detectors. Chapter 4 provides further detail on the ND280 detector, as it is the focus of the work in this thesis, describing its constituent subdetectors as well as the other detectors within the ND280 detector complex. Chapter 5 explores the Monte Carlo simulation used at ND280 and provides an in-depth description of the parameters used within it. Chapter 6 introduces the selections used in the analysis, and the criteria used to separate detector events into different topologies. It also describes the new 4π solid-angle selection. Chapter 7 presents the validation work performed by the author for Production 7, including the alterations necessary to the 4π selection to prepare it for full implementation, corrections for timeslip errors (errors in event timestamps due to a hardware issue) in T2K Run 8, and a comparison of ECal systematic parameters between P7 and previous values. Chapter 8 describes how the fitting of MC simulation to detector data is performed, and gives an overview of the GUNDAM fitter and how it works. Chapter 9 introduces the set of 19 simulated data sets that GUNDAM was tested against, the results and analysis of which is in chapter 10. Finally, chapter 11 presents the conclusions and discusses future work for GUNDAM, simulated data studies, and beyond.

Chapter 2

Theory

Neutrinos are electrically neutral fundamental particles and have an extremely small mass. As they only interact via the weak interaction and gravity, and with very small cross sections, they will very rarely interact with other matter and will typically pass straight through stars and planets with little obstruction. This makes them very difficult to study as they do much the same with particle detectors, leaving no trace of their passage. Neutrino detectors therefore typically rely on large detection volumes and high neutrino fluxes in order to maximise the probability of observing neutrino interactions. The detectors must also be able to measure the momentum and position of particles to a high degree of accuracy; the neutrino interaction rate can be low within even large detectors, so the ability to reconstruct events accurately is critical.

Neutrinos exhibit unusual properties in contrast with other fundamental particles. For example, they can change flavour as they propagate, known as "oscillation". Additionally, their mass is so small it is suspected that they gain mass via a different mechanism to other particles. This chapter will give an overview of neutrino physics beginning with the history of neutrino discoveries, followed by neutrinos within the Standard Model, neutrino physics beyond the Standard Model, neutrino interactions with other particles, and some of the unanswered questions in neutrino physics.

2.1 A Brief History of Neutrino Physics

The first hints of the existence of the neutrino emerged in 1914, with the discovery by James Chadwick that β decay showed a range of energies in a continuous spectrum [1]. β decay is the emission of an electron from an atomic nucleus and was expected to have a fixed total energy for identical nuclei, as was seen in α and γ decays. Prior to the hypothesis of the neutrino, β decay was believed to occur via the interaction:

$$^{A}_{Z}X \rightarrow ^{A}_{Z+1} Y + e^{-} \tag{2.1}$$

where nuclei X, with A nucleons and Z protons, would decay to nuclei Y by transforming a neutron to a proton and emitting an electron. A continuous energy spectrum would suggest the violation of the well-established conservation of momentum, and remained an unsolved problem for years.

In 1930, Wolfgang Pauli published an open letter [2] presenting a "desperate remedy": an undetected neutral particle of negligible ($\ll m_{\text{electron}}$) mass that is emitted alongside the electron and carries some of the emission energy, resulting in a range of electron energies but conserving momentum across the entire process. This was a controversial idea, as at the time the proton and the electron were the only known subatomic particles.

The theory was further developed by Enrico Fermi, who named the new particle the "neutrino" (Italian for "little neutral one") and created a theoretical framework for β decay, published in 1934 [3]. β decay was now described as:

$$n^{0} \rightarrow p^{+} + e^{-} + \bar{\nu}_{e} \tag{2.2}$$

where a neutron n decays into a proton p, electron e and (electron anti)neutrino $\bar{\nu}_{e}$. (At the time neutrino flavour and parity was unknown to physics, so in 1934 the $\bar{\nu}_{e}$ was simply known as ν.) Critically, this also suggested the neutrino could be detected via inverse β decay, where the neutrino is captured by a proton to produce a neutron and electron:

$$\bar{\nu}_{e} + p^{+} \rightarrow n^{0} + e^{+} \tag{2.3}$$

This process was used by Clyde Cowan and Frederick Reines in their 1953 experiment which confirmed the neutrino's existence, utilising two 100-litre water tanks surrounded by scintillator layers [4].

The muon neutrino was hypothesised in 1941, following observations of a similar "missing energy" in muon decays [5]. It was first observed in 1962 at the Brookhaven National Laboratory [6]. In this experiment, interactions of neutrinos from from a neutrino beam were observed in a spark chamber (an early type of particle detector). If the neutrino was "flavourless", the same number of electron-producing and muon-producing events would be observed; however, only six electron events were identified compared to 29 muon events, thus demonstrating the existence of distinct muon and electron neutrinos.

The hypothesis of the tau neutrino coincided with the discovery of the tau lepton in the 1975 [7], and was first observed in 2000 by the DONUT (Direct Observation of the NU Tau) experiment at Fermilab [8]. A tau neutrino beam was created using a 800 GeV proton beam targeted at a large block of tungsten to produce $\mathrm{D_s}$ mesons which decay to produce tau leptons, which themselves subsequently decay into tau neutrinos. DONUT utilised sheets of nuclear emulsion, which is a type of material that charged particles will permanently etch tracks in to as they pass through it. In conjunction with measurements from DONUT's scintillation detectors and drift chambers, tau neutrino interactions were identified by the ~ 2 mm track created by the resultant tau lepton before it decayed.

2.2 Neutrinos and the Standard Model

The Standard Model (SM) is the currently accepted framework of particle physics, describing the interactions of the strong, weak, and electromagnetic forces and all known elementary particles [9]. Despite being known to be incomplete (e.g. it does not include gravity or, more relevantly here, neutrino oscillation) it remains one of the most successful theories in physics. It consists of twelve spin-1/2 fermions alongside four spin-1 vector bosons and one spin-0 scalar boson, shown in figure 2.1.

The fermions consist of six quarks and six leptons, each subdivided into three generations ordered by increasing particle mass. There are three flavours of quarks with an electric charge of $+2/3\ e$ (elementary charge): up, charm, and top (u, c, t); and three with an electric charge of $-1/3\ e$: down, strange, and bottom (d, s, b). The leptons consist of three flavours of charged leptons with an electric charge of $-1\ e$: the electron, the muon, and the tau (e, μ, τ). Each charged lepton has an associated neutrino (with no electric charge) of the same flavour: the electron neutrino, muon neutrino, and tau neutrino $(\nu_e, \nu_\mu, \nu_\tau)$. Neutrinos cannot change flavour, and lepton flavour is always conserved in the SM. Each fermion has an associated antiparticle with identical properties, but opposite electrical charge.

Fermions in the SM interact via three fundamental forces, which are mediated by the vector bosons: the strong nuclear force, mediated by gluons; the weak nuclear force, mediated by W and Z bosons; and electromagnetism, mediated by photons. The Higgs boson, the only spin-0 particle, is central to the Higgs mechanism, which gives massive particles their mass. It is hypothesised that neutrinos get their mass by another process due to their extremely low mass. This is discussed in section 2.5.

The strong force is described by quantum chromodynamics (QCD) and affects particles with colour charge, which in the SM is only quarks and gluons. The strong force is the strongest of the fundamental forces, with a coupling constant of $\alpha_S = 0.1181$ [10]. It is responsible for binding together quarks in hadrons and the nucleons in atomic nuclei. There are three colour charges: red, blue, and green; as well as three anti-colour charges: anti-red, anti-blue, and anti-green. Bound states must be colour neutral, which is possible via three different (anti-)colour charges (seen in baryons) or a pair of a colour and its anti-colour (seen in mesons).

The electromagnetic force is described by quantum electrodynamics (QED) and affects particles with electric charge, which in the SM are the quarks, W bosons, and the charged leptons. The electromagnetic coupling constant is also known as the fine-structure constant, and is equal to $\alpha = 0.007297 \approx 1/137$ [10].

The weak force is usually described in terms of electroweak theory, where it is unified with electromagnetism. The weak force interacts with all fermions, and is the only force in the SM through which neutrinos can interact. At typical particle interaction distances, it is also the weakest force in the SM beyond very short ranges, and the second-weakest in physics after gravity. The weak coupling constant is on the order $\alpha_W \sim 10^{-6}$; the large mass of the weak bosons suppresses interactions.

Within the SM, neutrinos are described as massless spin-1/2 leptons without any electric or colour charge. Consequently, they can only couple to the $W^{\pm}$ and Z^0 bosons and only interact via the weak interaction. Neutrinos are observed to always have a left-handed helicity, i.e. spin is projected in the opposite direction to particle momentum, and antineutrinos to always have a right-handed helicity, i.e. spin is projected in the same direction as particle momentum. This observation suggests that neutrinos must be massless, as the helicity can flip for massive particles due to the momentum depending on the observer's reference frame. Massless particles always travel at the speed of light so helicity is always in the same direction for every observer, which is observed with neutrinos.

Interactions via the charged $W^{\pm}$ boson are known as charged-current (CC) and interactions via the neutral Z^0 boson are known as neutral-current (NC). Decays of the Z^0 are

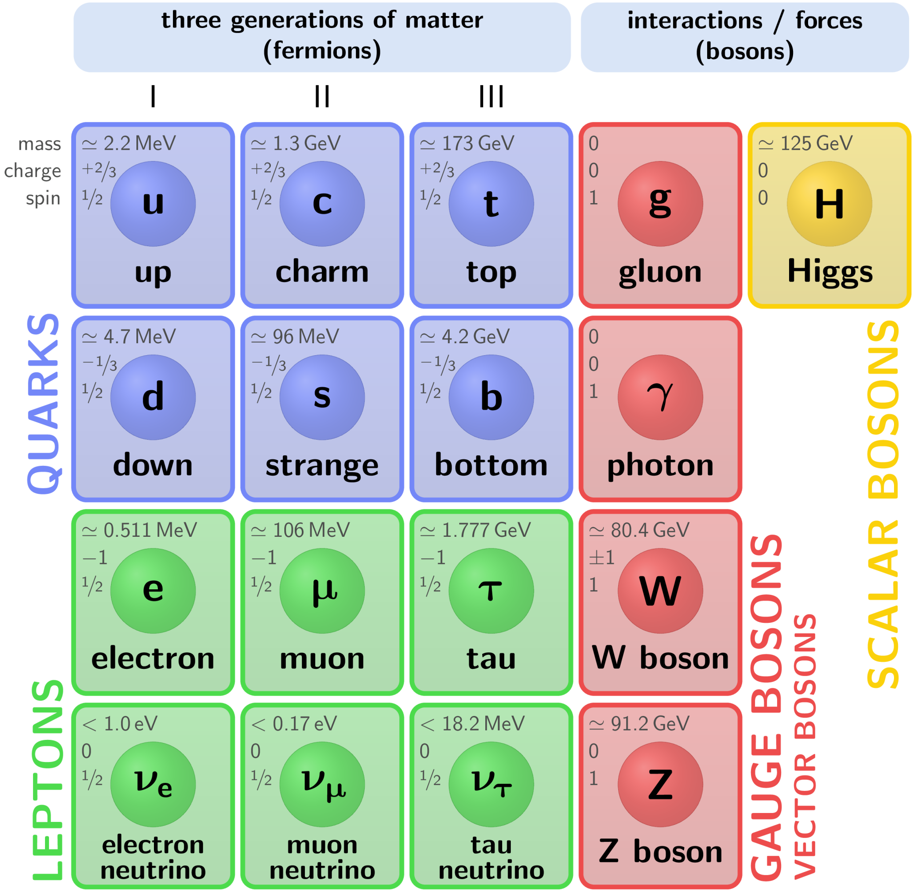

Figure 2.1: Particles of the Standard Model arranged by type, charge and spin. The spin-1/2 fermions are split between quarks and leptons and grouped into three generations. The spin-1 gauge bosons govern the strong, weak, and electromagnetic interactions, while the spin-0 Higgs boson couples massive particles to the Higgs field. Figure adapted from [11].

shown to support the existence of the three neutrino flavours that have been observed. The decay width Γ_Z of the Z^0 resonance can be expressed as the sum of its different decay products:

$$\Gamma_Z = 3\Gamma_{Z\to l^+ + l^-} + \Gamma_{Z\to hadrons} + N_\nu \Gamma_{Z\to\nu\bar{\nu}} \tag{2.4}$$

where $\Gamma_{Z\to l^+ + l^-}$ is the partial decay width of the Z to a charged lepton-antilepton pair, $\Gamma_{Z\to hadrons}$ is the partial decay width of Z to hadrons, and $\Gamma_{Z\to\nu\bar{\nu}}$ is the partial decay width for a neutrino-antineutrio pair. N_ν is the number of neutrino flavours in the SM. Lepton universality means each neutrino flavour is equally likely, so the decay width will be the same for each. The charged lepton and hadron decay widths can be determined experimentally, and the neutrino-antineutrino widths can be calculated directly from the SM. This has produced a result of $N_\nu = 2.984 \pm 0.008$ [10], which suggests that the three observed neutrinos, ν_e , ν_μ and ν_τ , are the the only neutrinos that can exist within the SM. This method assumes that all neutrino flavours will interact via the weak force and that all neutrino masses are $m_\nu < \frac{m_Z}{2}$; “sterile” neutrinos (see section 2.5) may exist that cannot be produced in Z decays.

2.3 Neutrinos Beyond the Standard Model

Experimental results show that neutrinos in reality differ significantly from their SM description. Neutrinos have been shown to change flavours as they propagate, a phenomenon known as neutrino oscillation. This process necessitates the existence of more than one neutrino mass eigenstate, meaning that neutrinos are actually massive particles.

2.3.1 The Solar Neutrino Problem

Experimental evidence for neutrino oscillations first came to attention at the Homestake experiment, which was designed to measure the neutrino flux from the Sun [12]. The experiment was performed by Raymond Davis Jr., and was designed to test the Standard Solar Model that had recently been developed by John Bahcall [13]. The experiment ran from 1970 to 1992.

The experiment consisted of a tank of 3.8×10^5 litres of C_2Cl_4 located 1.5 km underground at the Homestake gold mine, South Dakota, USA. Fusion reactions in the Sun generate electron neutrinos, which would be captured by the chlorine via the reaction:

$$\nu_e +^{37}\text{Cl} \rightarrow e^- +^{37}\text{Ar} \tag{2.5}$$

The argon atoms could then be collected and counted to calculate the neutrino flux. The Standard Solar Model predicted an electron neutrino capture rate of 7.9 ± 2.6 SNU (Solar neutrino units, 1 SNU is equal to a neutrino flux producing 10^{-36} captures per target atom per second), but the experiment showed an observed rate of just 2.9 ± 0.9 SNU [14]. This discrepancy between theory and experiment became known as the “solar neutrino problem”. Other neutrino detection experiments throughout the 20th century, such as GALLEX [15] and the Kamioka Observatory [16], confirmed this deficit in solar neutrinos.

In 2002, the Sudbury Neutrino Observatory (SNO) published results showing a resolution to the problem [17] [18]. SNO was able to measure the total solar neutrino flux via NC interactions, which are sensitive to all neutrino flavours in addition to the ν_e flux. This was achieved using a spherical tank containing 1000 tons of heavy water (D_2O), which could measure two distinct neutrino-deuterium interactions:

$$\begin{aligned} &1) \quad \nu_e + d \rightarrow p + p + e^- \\ &2) \quad \nu_x + d \rightarrow n + p + v_x \end{aligned} \tag{2.6}$$

where ν_x refers to a neutrino of any flavour. The first interaction is a CC process that only occurs with an electron neutrino incident on a deuterium nucleus. The second interaction is an NC process that can occur with any of the three neutrino flavours. Additionally, NC elastic scattering between neutrinos and electrons could also occur within the detector:

$$\nu_x + e^- \rightarrow \nu_x + e^- \tag{2.7}$$

The total neutrino flux measured using the NC interactions matched solar model predictions, but the ν_e component measured via the CC interaction was found to only be a third as much as expected. This demonstrated that ν_e from the Sun were being transformed into other flavours as they propagated, conclusively solving the solar neutrino problem.

The discovery of neutrino oscillations also resolved the similar "atmospheric neutrino anomaly", where the number of ν_μ detected from cosmic ray interactions in the atmosphere was significantly lower than expected. ν_μ oscillating to the nearly-undetectable ν_τ explains the deficit [19].

2.3.2 Neutrino Oscillations

The theory of neutrino oscillations was first developed by Bruno Pontecorvo in 1957. Following the observation of neutral kaons oscillating between particle and antiparticle states, he theorised that a similar process may occur in neutrinos [20]. This was later developed into flavour oscillation between the two known neutrino flavours, ν_e and ν_μ [21][22].

Neutrino oscillation is the process by which neutrinos change flavour as they propagate. Neutrinos possess three flavour eigenstates, $|\nu_e\rangle$, $|\nu_\mu\rangle$, and $|\nu_\tau\rangle$ but also three mass eigenstates, $|\nu_1\rangle$, $|\nu_2\rangle$ and $|\nu_3\rangle$.

Neutrinos interact with the weak interaction as flavour eigenstates, but propagate as free particles as mass eigenstates. Each flavour eigenstate consists of a mixture of mass eigenstates, described by the unitary Pontecorvo–Maki–Nakagawa–Sakata (PMNS) matrix, U_{PMNS}.

The mixing is given as:

$$\begin{pmatrix} \nu_e \\ \nu_\mu \\ \nu_\tau \end{pmatrix} = U_{\text{PMNS}} \begin{pmatrix} \nu_1 \\ \nu_2 \\ \nu_3 \end{pmatrix} \tag{2.8}$$

where ν_e , ν_μ and ν_τ are the three neutrino flavour eigenstates and ν_1 , ν_2 and ν_3 are the three mass eigenstates. U can parameterised by the mixing angles θ_{12}, θ_{13} and θ_{23} as:

$$U_{\text{PMNS}} = \begin{pmatrix} 1 & 0 & 0 \\ 0 & c_{23} & s_{23} \\ 0 & -s_{23} & c_{23} \end{pmatrix} \begin{pmatrix} c_{13} & 0 & s_{13}e^{-i\delta_{\text{CP}}} \\ 0 & 1 & 0 \\ -s_{13}e^{i\delta_{\text{CP}}} & 0 & c_{13} \end{pmatrix} \begin{pmatrix} c_{12} & s_{12} & 0 \\ -s_{12} & c_{12} & 0 \\ 0 & 0 & 1 \end{pmatrix} \tag{2.9}$$

where $c_{ij} = \cos\theta_{ij}$, $s_{ij} = \sin\theta_{ij}$, and δ_{CP} is the CP-violating phase.

Two-Flavour Oscillation

To demonstrate how the PMNS matrix allows for neutrino oscillations, a simpler two flavour case with only electron and muon neutrinos will be considered here [23].

The neutrino flavour eigenstates ν_e and ν_μ mix with the mass eigenstates ν_1 and ν_2 via a single mixing angle, θ:

$$\begin{pmatrix} \nu_e \\ \nu_\mu \end{pmatrix} = \begin{pmatrix} \cos\theta & \sin\theta \\ -\sin\theta & \cos\theta \end{pmatrix} \begin{pmatrix} \nu_1 \\ \nu_2 \end{pmatrix} \tag{2.10}$$

Each flavour state is a linear superposition of the mass states:

$$\begin{aligned} |\nu_e\rangle &= \cos\theta\,|\nu_1\rangle + \sin\theta\,|\nu_2\rangle \\ |\nu_\mu\rangle &= -\sin\theta\,|\nu_1\rangle + \cos\theta\,|\nu_2\rangle \end{aligned} \tag{2.11}$$

The mass states $|\nu_\kappa\rangle$ where $\kappa = 1, 2$ propagate according to the time-dependent Schrödinger equation:

$$i\frac{\partial}{\partial t}|\nu_\kappa(x,t)\rangle = E\,|\nu_\kappa(x,t)\rangle = -\frac{1}{2m_\kappa}\frac{\partial^2}{\partial x^2}|\nu_\kappa(x,t)\rangle \quad \kappa = 1, 2 \tag{2.12}$$

For a neutrino produced at space-time position $(0,0)$ that propagates to (x,t), the solution is the plane wave:

$$|\nu_\kappa(x,t)\rangle = e^{-(iE_\kappa t - p_\kappa x)}\,|\nu_\kappa(0,0)\rangle = e^{-i\phi_\kappa}\,|\nu_\kappa(0,0)\rangle \tag{2.13}$$

where E_κ is the energy of the mass state $|\nu_\kappa\rangle$, $p_\kappa = (E, \mathbf{p})$ is the neutrino 4-momentum, and $x = (t, \mathbf{x})$ is the space-time 4-vector. The phase $\phi = E_\kappa t - p_\kappa x$ is Lorentz invariant. The flavour eigenstates from equation 2.11 now become:

$$\begin{aligned} |\nu_e(x,t)\rangle &= e^{-i\phi_1}\cos\theta\,|\nu_1(0,0)\rangle + e^{-i\phi_2}\sin\theta\,|\nu_2(0,0)\rangle \\ |\nu_\mu(x,t)\rangle &= -e^{-i\phi_1}\sin\theta\,|\nu_1(0,0)\rangle + e^{-i\phi_2}\cos\theta\,|\nu_2(0,0)\rangle \end{aligned} \tag{2.14}$$

In matrix form, this becomes:

$$\begin{pmatrix} |\nu_e(x,t)\rangle \\ |\nu_\mu(x,t)\rangle \end{pmatrix} = \begin{pmatrix} e^{-i\phi_1} & 0 \\ 0 & e^{-i\phi_2} \end{pmatrix} \begin{pmatrix} \cos\theta & \sin\theta \\ -\sin\theta & \cos\theta \end{pmatrix} \begin{pmatrix} |\nu_1(0,0)\rangle \\ |\nu_2(0,0)\rangle \end{pmatrix} \tag{2.15}$$

Similarly, by taking the inverse of the mixing matrix, the mass eigenstates can be expressed in terms of the flavour eigenstates:

$$\begin{pmatrix} |\nu_1\rangle \\ |\nu_2\rangle \end{pmatrix} = \begin{pmatrix} \cos\theta & -\sin\theta \\ \sin\theta & \cos\theta \end{pmatrix} \begin{pmatrix} |\nu_e\rangle \\ |\nu_\mu\rangle \end{pmatrix} \tag{2.16}$$

Combining equations 2.15 and 2.16 and multiplying the matrices together gives an equation for the evolved flavour states at (x,t) in terms of the initial states at $(0,0)$:

$$\begin{pmatrix} |\nu_e(x,t)\rangle \\ |\nu_\mu(x,t)\rangle \end{pmatrix} = \begin{pmatrix} c^2e^{-i\phi_1} + s^2e^{-i\phi_2} & -cse^{-i\phi_1} + sce^{-i\phi_2} \\ -cse^{-i\phi_1} + sce^{-i\phi_2} & s^2e^{-i\phi_1} + c^2e^{-i\phi_2} \end{pmatrix} \begin{pmatrix} |\nu_e(0,0)\rangle \\ |\nu_\mu(0,0)\rangle \end{pmatrix} \tag{2.17}$$

where $c = \cos\theta$ and $s = \sin\theta$, e.g. $cs \equiv \cos\theta\sin\theta$.

The probability P of observing ν_μ at space-time point (x,t) from a neutrino starting as ν_e at (0,0) is

$$P(\nu_e(0,0) \to \nu_\mu(x,t)) = |\,\langle\nu_\mu(x,t)|\nu_e(0,0)\rangle\,|^2 \tag{2.18}$$

Evaluating this amplitude from equation 2.17 gives:

$$\begin{aligned} \langle\nu_\mu(x,t)|\nu_e(0,0)\rangle = (&\cos\theta\sin\theta(e^{i\phi_2} - e^{i\phi_1})\,\langle\nu_e(0,0)| \\ &+(\sin^2\theta e^{i\phi_1} + \cos^2\theta e^{i\phi_2})\,\langle\nu_\mu(0,0)|)\,|\nu_e(0,0)\rangle \end{aligned} \tag{2.19}$$

Because $\langle\nu_\mu| = |\nu_\mu\rangle^*$, the exponents have changed signs. As the flavour eigenstates are orthogonal, $\langle\nu_e|\nu_e\rangle = 1$ and $\langle\nu_\mu|\nu_e\rangle = 0$, so the amplitude becomes:

$$\langle\nu_\mu(x,t)|\nu_e(0,0)\rangle = \cos\theta\sin\theta(e^{i\phi_2} - e^{i\phi_1}) \tag{2.20}$$

Equation 2.18 now becomes:

$$\begin{aligned} P(\nu_e(0,0) \to \nu_\mu(x,t)) &= |\cos\theta\sin\theta(e^{i\phi_2} - e^{i\phi_1})|^2 \\ &= \cos^2\theta\sin^2\theta(e^{i\phi_2} - e^{i\phi_1})(e^{-i\phi_2} - e^{-i\phi_1}) \\ &= 2\cos^2\theta\sin^2\theta(1 - \cos(\phi_2 - \phi_2)) \end{aligned} \tag{2.21}$$

Which can be rearranged using trigonometric identities to produce:

$$P(\nu_e(0,0) \to \nu_\mu(x,t)) = \sin^2(2\theta)\sin^2\left(\frac{\phi_2 - \phi_1}{2}\right) \tag{2.22}$$

The phase difference $\phi_2 - \phi_1$ can also be simplified further. Assuming that neutrinos are travelling at a relativistic speed, we can approximate $t \approxeq x$ in natural units ($c = 1$). Additionally, momentum can be approximated using Taylor expansion as:

$$p = \sqrt{E^2 - m^2} = E\sqrt{1 - \frac{m^2}{E^2}} \approx E - \frac{m^2}{2E} \tag{2.23}$$

As $\phi_i = E_i t - p_i x$, the phase difference now becomes:

$$\begin{aligned} \phi_2 - \phi_1 &= (E_2 - E_1)t - (p_2 - p_1)x \\ &= (E_2 - E_1 - \left(E_2 - \frac{m_2^2}{E_2}\right) + \left(E_1 - \frac{m_1^2}{E_1}\right))x \\ &= \left(\frac{m_1^2}{2E_1} - \frac{m_2^2}{2E_2}\right)x \end{aligned} \tag{2.24}$$

Assuming the energies of the mass states are identical, and replacing x with L as is convention, equations 2.22 and 2.24 can be combined to give the two-flavour oscillation probability as:

$$P(\nu_e(0,0) \to \nu_\mu(x,t)) = \sin^2(2\theta)\sin^2\left(\frac{\Delta m_{12}^2 L}{4E}\right) \tag{2.25}$$

where $\Delta m_{12}^2 = m_1^2 - m_2^2$. The ν_e survival probability is simply

$$P(\nu_e \to \nu_e) = 1 - \sin^2(2\theta)\sin^2\left(\frac{\Delta m_{12}^2 L}{4E}\right) \tag{2.26}$$

The oscillation probability can be calculated for more intuitive units. With L in kilometres, E in GeV, and Δm^2_{12} in eV^2, the probability becomes

$$P(\nu_e \to \nu_\mu) = \sin^2(2\theta)\sin^2\left(\frac{1.27\Delta m^2_{12}L}{E}\right) \tag{2.27}$$

Three-Flavour Oscillation

For the case of three neutrino flavours, the probability of oscillation from ν_α to ν_β is written as:

$$\begin{aligned} P(\nu_\alpha \to \nu_\beta) = \delta_{\alpha\beta} - 4\sum_{i>j} Re(U^*_{\alpha i}U_{\beta i}U_{\alpha j}U^*_{\beta j})\sin^2\left(\Delta m^2_{ij}\frac{L}{4E}\right) \\ +2\sum_{i>j} Im(U^*_{\alpha i}U_{\beta i}U_{\alpha j}U^*_{\beta j})\sin\left(\Delta m^2_{ij}\frac{L}{2E}\right) \end{aligned} \tag{2.28}$$

where ν_α and ν_β are neutrinos of some flavours α and β, U_{xy} are elements of the PMNS matrix and $\delta_{\alpha\beta}$ is the Kronecker delta. Δm^2_{ij} is the difference between the square of the masses of mass states ν_i and ν_j.

2.3.3 Matter Effects

The oscillation probabilities given above are for neutrinos propagating through a vacuum; however, the probabilities change if they propagate through matter, such as the Earth. This is relevant in, for example, the T2K experiment, where the neutrino beam passes through the Earth's crust. All neutrino flavours can interact with surrounding particles via NC interactions, and ν_e can interact via CC interactions with electrons. For ν_e, this correction is known as the Mikheyev-Smirnov-Wolfenstein (MSW) effect [24][25]. This introduces additional terms to the ν_e oscillation probability:

$$\begin{aligned} &\mp 8\frac{aL}{4E}c^2_{12}s^2_{13}s^2_{23}(1-2s^2_{13})\cos\left(\frac{\Delta m^2_{32}}{4E}\right)\sin\left(\frac{\Delta m^2_{13}}{4E}\right) \\ &\pm 8\frac{a}{\Delta m^2_{31}}c^2_{13}s^2_{13}s^2_{23}(1-2s^2_{13})\sin\left(\frac{\Delta m^2_{31}}{4E}\right) \end{aligned} \tag{2.29}$$

where $c_{ij} = \cos\theta_{ij}$, $s_{ij} = \sin\theta_{ij}$, $a = 7.56 \times 10^{-5} \times \rho \times E_\nu$, in which ρ is the matter density in g cm^{-3} and E_ν is the neutrino energy in GeV. The signs of the terms in equation 2.29 changes if it is a neutrino or antineutrino.

2.3.4 Mass Ordering

Three-flavour neutrino oscillation depends on the independent mass differences Δm^2_{21} and Δm^2_{31}. The third mass difference, Δm^2_{32}, can be expressed as $\Delta m^2_{32} = \Delta m^2_{31} - \Delta m^2_{21}$. It has been shown from solar neutrino studies that $\Delta m^2_{21} > 0$ [26], where the heavier mass state has been declared ν_2. These studies utilised the strong matter effects experienced by solar neutrinos passing through the Earth, and compared the measurements to neutrinos directly incident to the detector from space. Yet, the sign for Δm^2_{31} remains unknown. This allows for two different mass orderings (sometimes called "hierarchies") of the neutrino mass eigenstates: "normal ordering" (NO), $\nu_1 < \nu_2 < \nu_3$; and "inverted ordering" (IO), $\nu_3 < \nu_1 < \nu_2$, as shown in figure 2.2.

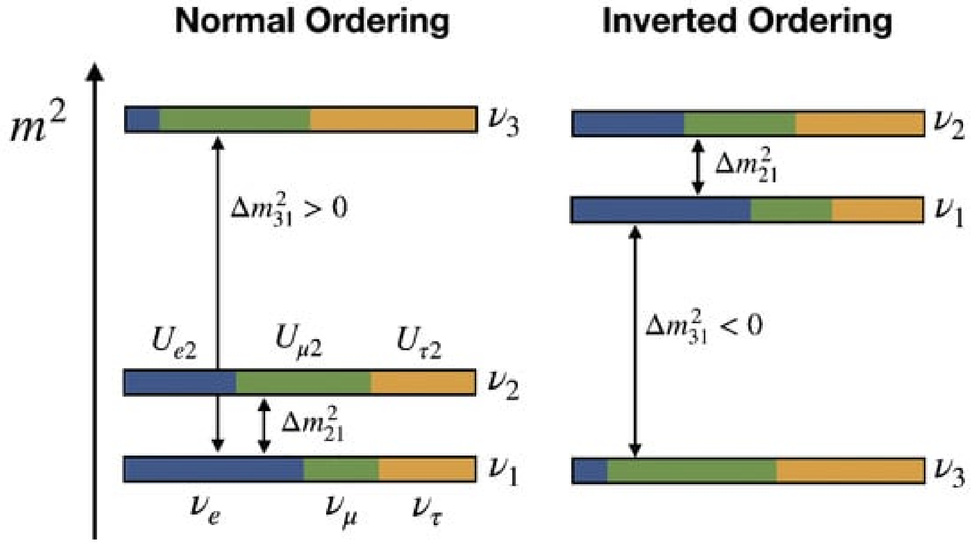

Figure 2.2: Possible orderings for the neutrino mass eigenstates ν_1 , ν_2 and ν_3 . The coloured segments of each mass shows the flavour mixing, with blue for ν_e , green for ν_μ and yellow for ν_τ . Figure adapted from [27]

Currently, experimental evidence points towards normal ordering [28]; however, it is not strong enough statistically to determine at this time. The 2025 T2K-SK joint fit finds a 1.2σ exclusion of the inverted mass ordering [29].

Similarly, as the oscillation parameters only rely on the mass *difference*, determining the absolute masses of the neutrino mass states is also very difficult. The Karlsruhe Tritium Neutrino Experiment (KATRIN) has determined an upper bound of $m_\nu < 0.45$ eV at a 90% confidence level through the measurement of beta decays of tritium [30].

2.3.5 Neutrino Experiments

The values of the neutrino mass differences, mixing angles, and CP-violating phase are a major focus in neutrino physics, and multiple experiments are focused on determining these parameters. No single neutrino experiment is sensitive to all of the oscillation parameters, and it is only through the combined efforts of multiple experiments that we can constrain the uncertainties for the full set of parameters.

These oscillation experiments can be categorised by their neutrino source: accelerator experiments, which generate a neutrino beam via a particle accelerator; reactor experiments, which use the neutrinos produced by nuclear reactors; and astrophysical experiments, which observe neutrinos produced from astrophysical sources such as the sun and supernovae, as well as atmospheric neutrinos produced by cosmic rays.

Accelerator Experiments

Accelerator experiments typically utilise an accelerated beam of protons incident on a target to produce mesons, which then decay to produce neutrinos. This method allows for a high degree of control over neutrino beam energy and flavour, so it can be fine-tuned to meet the needs of the experiment.

The composition of the beam is initially measured by a “near detector”, where the neutrino content is characterised. This detector is placed close (≤ 1 km) to the beam source, to minimise neutrino oscillation occurring in the interim. A “far detector” is positioned a significant distance away where the beam can be measured after significant oscillation has occurred. The far detector is positioned to maximise oscillation occurring after the beam passes through the near detector (i.e. where the probability to observe $\nu_\mu \to \nu_e$ is highest), which is typically hundreds of kilometres away. This distance is called the “baseline”.

The T2K experiment, located in Japan, uses a 295 km baseline to primarily measure $\nu_\mu \to \nu_e$ appearance and ν_μ disappearance. The near detector, ND280, is positioned 280 m from the beam source and uses a combination of plastic scintillator detectors and gas time projection chambers. The far detector, Super-Kamiokande, is a water Cherenkov detector containing 50,000 tons of ultrapure water. The neutrino beam itself has a peak energy of 0.6 GeV. As the main focus of this thesis, the T2K experiment is described in detail in chapter 3. The most recent best-fit results from T2K provide the following parameter constraints: $\delta_{\mathrm{CP}} = -2.18^{+1.22}_{-0.47}$, $\sin^2\theta_{23} = 0.559^{+0.018}_{-0.078}$, and $\Delta m^2_{32} = 2.506^{+0.039}_{-0.052} \times 10^{-3}\,\mathrm{eV}^2$

[31].

The NOνA experiment [32], located in the USA, similarly measures $\nu_\mu \rightarrow \nu_e$ appearance and ν_μ disappearance. It has a 810 km baseline, and both near and far detectors are fully liquid scintillator. The NOνA neutrino beam has a peak energy of 2 GeV. The most recent NOνA results present the following constraints on the oscillation parameters: $\sin^2\theta_{23} = 0.55^{+0.06}_{-0.02}$, and $\Delta m^2_{32} = 2.431^{+0.036}_{-0.034}\,(-2.479^{0.036}_{0.036}) \times 10^{-3}\,\mathrm{eV}^2$ for normal (inverted) ordering [33].

The next generation of accelerator experiments is currently under construction. At T2K, an upgrade to the N280 detector was completed in 2024, (see section 4.7). Additionally, the successor to Super-K, Hyper-Kamiokande (Hyper-K), is expected to begin data taking before the end of the decade [34]. Hyper-K is a water Cherenkov detector and has a fiducial mass eight times that of Super-K so will offer superior detection of accelerator and astrophysical neutrinos. An entirely new long-baseline experiment, The Deep Underground Neutrino Experiment (DUNE), is currently under construction, with the neutrino source and near detector located at Fermilab in Batavia, Illinois, and the far detector at the Sanford Underground Research Facility in Lead, South Dakota [35]. As the experiment will use a 1300 km baseline, the increased matter effects are expected to give it a high sensitivity to neutrino CP-violation and mass ordering.

Reactor Experiments

Nuclear reactors produce large amounts of electron antineutrinos via β decay of fission products, with an energy of $\sim 0 - 10$ MeV [36]. These neutrinos are measured using inverse beta decay interactions ($\bar{\nu_e} + p \rightarrow e^+ + n$) within the detectors, which are observed via the gamma rays emitted when the e^+ annihilates with an e^- ($e^+ + e^- = 2\gamma$).

Many recent reactor experiments have short baselines (< 2 km), and are specialised towards the measurement of $\sin\theta_{13}$ [36], such as Daya Bay [37], Double CHOOZ [38], and RENO [39]. The Daya Bay experiment, located near Hong Kong, consists of eight neutrino detectors clustered in three groups around six nuclear reactors, with the longest baseline being 1.9 km [40] [37]. Each detector consists of a tank of 20 tons of gadolinium-doped liquid scintillator, instrumented by 192 PMTs. Daya Bay results constrain θ_{13} to $\sin\theta_{13} = 0.0851 \pm 0.0024$, which is currently the most accurate measurement for this mixing angle [41]. It has also constrained $\Delta m^2_{32} = 2.466 \pm 0.060(-2.571 \pm 0.060) \times 10^{-3}$ eV^2

for normal (inverted) ordering.

The KamLAND experiment, situated at the same site as Super-K, observes neutrinos from Japan's commercial nuclear reactors (55 reactor cores in total). It has an average baseline of $\sim$ 180 km [42], which is unusually large for a reactor experiment. The detector consists of a spherical stainless steel containment vessel, 18 m in diameter, containing a nylon balloon, 13 m in diameter, filled with 1000 tons of liquid scintillator [43]. The containment vessel is instrumented with 1,879 photomultiplier tubes (PMTs) and filled with non-scintillating oil to support the inner balloon. Shortly after it began taking data in 2002, it was able to demonstrate $\bar{\nu_e}$ disappearance to a high degree of confidence [43]. Using a combination of KamLAND and external solar neutrino measurements, it has presented oscillation parameter constraints of: $\tan^2\theta_{12} = 0.452^{+0.035}_{-0.033}$, $\Delta m^2_{21} = 7.50^{+0.19}_{-0.20} \times 10^{-5}\,\mathrm{eV}^2$, and $\sin^2\theta_{13} = 0.020^{+0.016}_{-0.016}$.

Astrophysical Experiments

Astrophysical experiments observe neutrinos from a wide range of sources, including the Sun, supernovae, and cosmic ray interactions in the atmosphere, amongst others.

The IceCube Neutrino Observatory, located in Antarctica, consists of 86 strings, each with 60 PMT modules, embedded between 1,450 and 2,450 metres deep in Antarctic ice [44]. Covering a total volume of 1 cubic kilometre, it is the largest neutrino detector in the world. It has observed neutrino oscillation in atmospheric neutrinos and presented constraints of $\sin^2\theta_{23} = 0.51 \pm 0.05$ and $\Delta m^2_{32} = 2.41 \pm 0.07 \times 10^{-3}$ eV^2.

Current Oscillation Parameter Measurements

Table 2.1 shows the current global best-fit values of the neutrino oscillation parameters. These measurements are determined by combining results from multiple neutrino oscillation experiments.

2.4 Neutrino Interactions

As discussed in section 2.2, neutrinos only interact via the weak interaction and gravity. As gravity is almost always far too weak to be considered in particle physics experiments (and even more so for neutrino experiments), neutrino detection relies only on weak interactions. Charged-current (CC) interactions are mediated by $W^{\pm}$ bosons and

Parameter	Global Best-Fit Measurement
$\sin^2(\theta_{12})$	0.307 ± 0.012
Δm^2_{21}	$(7.50 \pm 0.19) \times 10^{-5}$ eV^2
$\sin^2(\theta_{13})$	$(2.16 \pm 0.06) \times 10^{-2}$
$\sin^2(\theta_{23})$ (Inverted Order)	0.537 ± 0.020
$\sin^2(\theta_{23})$ (Normal Order)	$0.534^{+0.015}_{-0.019}$
Δm^2_{32} (Inverted Order)	$(-2.527 \pm 0.034) \times 10^{-3}$ eV^2
Δm^2_{32} (Normal Order)	$(2.451 \pm 0.026) \times 10^{-3}$ eV^2
δ_{CP}	$1.21^{+0.19}_{-0.22}\ \pi$ rad

Table 2.1: Global best-fit measurements for the neutrino oscillation parameters [10]. The results for the $\sin^2(\theta_{12})$ and Δm^2_{32} parameters are dependent on whether normal ordering or inverted ordering is used, so results for both orderings are shown. These results are obtained by combining the results of multiple neutrino experiments.

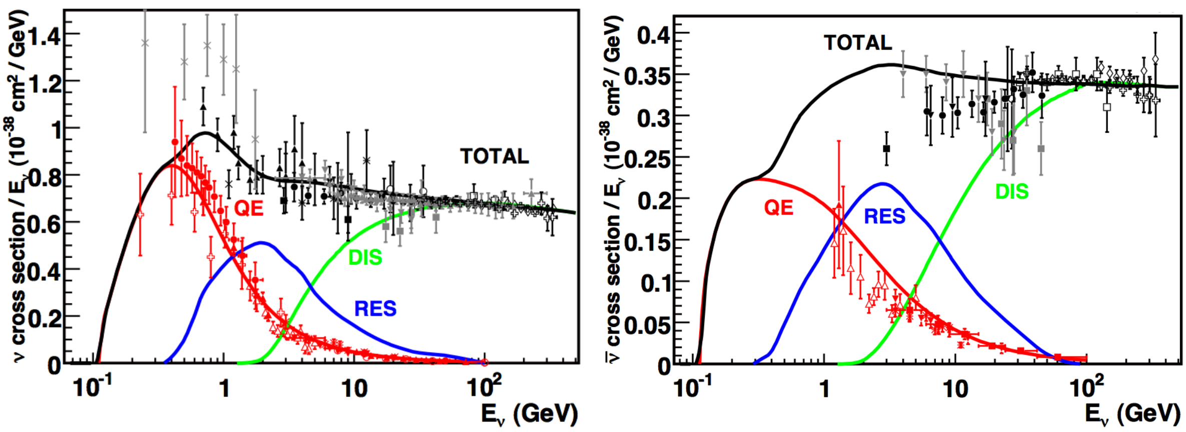

Figure 2.3: Per nucleon CC cross sections for neutrinos (left) and and antineutrinos (right), plotted as a function of neutrino energy. The cross sections for quasi-elastic (red), resonant (blue) and deep inelastic scattering (green) interactions are plotted separately to show their peak interaction energies. [45]

neutral-current (NC) interactions are mediated by Z^0 bosons. CC neutrino interactions result in a charged lepton of the neutrino flavour, so are the primary interaction type measured in neutrino oscillation experiments. NC interactions can still produce charged particles as decay products, but these are often just a background to be filtered out as they do not reveal any information about the neutrino flavour.

At energies below 1 GeV, quasi-elastic interactions between neutrinos and nucleons in an atomic nucleus are dominant, known as CCQE (charged current quasi-elastic) interactions. This is shown in figure 2.3. These produce a charged lepton matching the flavour of the neutrino:

$$\begin{aligned} \nu_l + n &\rightarrow l^- + p \\ \bar{\nu}_l + p &\rightarrow l^+ + n \end{aligned} \tag{2.30}$$

At higher energies, in the 1-5 GeV range, resonant (RES) interactions become dominant. The nucleon is excited to a higher energy resonant state (typically a Δ_{1232} resonance) and will emit a pion as it de-excites. These interactions are also knowns as single pion production (SPP). Examples of these processes include:

$$\begin{aligned} \nu_l + p &\rightarrow l^- + p + \pi^+ \\ \nu_l + n &\rightarrow l^- + p + \pi^0 \\ \nu_l + n &\rightarrow l^- + n + \pi^+ \end{aligned} \tag{2.31}$$

At energies beyond 10 GeV, deep inelastic scattering (DIS) becomes the dominant mode of interaction. The energy is high enough to break the nucleon apart, producing a hadronic shower.

2.5 Further Neutrino Theories

Beyond the measurement of the oscillation parameters, there remain multiple unanswered questions in neutrino physics. One hypothesis is that neutrinos may be Majorana fermions, rather than Dirac fermions. A Dirac fermion has distinct particles and antiparticles, while a Majorana fermion is its own antiparticle. If neutrinos are Majorana fermions, the PMNS matrix gains an additional multiplicative term:

$$\begin{pmatrix} e^{\alpha_1} & 0 & 0 \\ 0 & e^{\alpha_2} & 0 \\ 0 & 0 & 1 \end{pmatrix} \tag{2.32}$$

where α_1 and α_2 are the Majorana phases. All other fundamental fermions in the SM are known to be Dirac fermions as they have a distinct measurable charge that changes sign between particle and antiparticles. As neutrinos are neutral, the possibility they are Majorana particles remains open. This hypothesis is currently being tested in neutrinoless double beta decay experiments such as SNO+ [46], which attempt to observe double beta decay in which the two produced antineutrinos annihilate each other. A Feynman diagram of this interaction is shown in figure 2.4.

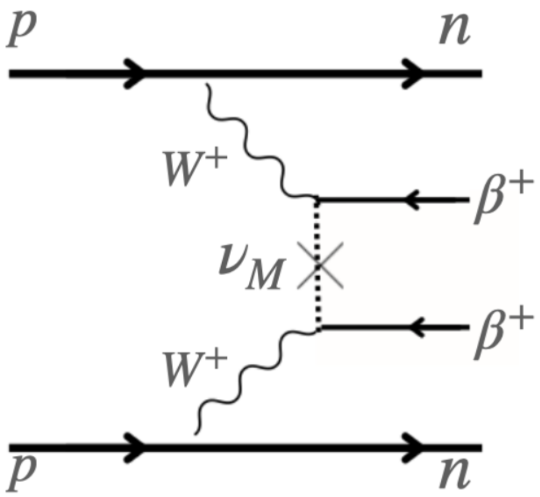

Figure 2.4: Feynman diagram of the hypothesised interaction for neutrinoless double beta decay. Diagram adapted from [47].

Also hypothesised is the potential existence of "sterile neutrinos" [48]. These neutrino states do not interact with the weak force, so are impossible to detect directly. Right-handed neutrinos and left-handed antineutrinos, if they exist, may be sterile neutrinos, explaining why they have never been observed. Neutrinos may gain their mass via the "see-saw" mechanism, where a larger sterile neutrino mass means a smaller mass for observed neutrinos, and this could explain how neutrinos have masses many orders of magnitude lower than other fermions.

The measurement of the CP-violating phase in the PMNS matrix could potentially have ramifications far beyond neutrino physics. The matter-antimatter asymmetry observed in the universe today is a mystery that physics has not been able to resolve. CP violation in the quark sector has been measured but is not large enough to explain matter dominance [49]. A non-zero value for δ_{CP}, the CP-violating phase, has been measured to a confidence of 2σ (90%) [50]; however, a measurement of 5σ is necessary to sufficiently demonstrate CP violation occurring in neutrino oscillations. If future measurements are able to demonstrate a sufficiently large phase value, it could help explain the formation of the universe [51].

Chapter 3

The T2K Experiment

The Tokai to Kamioka (T2K) Experiment is a long-baseline neutrino experiment in Japan designed to measure neutrino oscillation parameters and the neutrino mass differences [52]. A beam of muon (anti)neutrinos is first produced by the accelerator complex located at the J-PARC (Japan Proton Accelerator Research Complex) facility in Ibaraki Prefecture. The initial beam composition is measured by a suite of near detectors (INGRID and ND280) located 280 metres downstream from the neutrino production target, before travelling 295 kilometres through the Earth's crust to the far detector, Super-Kamiokande (figure 3.1). By comparing the characteristics of the neutrino beam between the near and far detectors the neutrino oscillation parameters can be determined. T2K aims to make precision measurements of the $\sin^2\theta_{13}$, $\sin^2\theta_{23}$ and Δm^2_{32} parameters, as well as constrain the CP-violating phase δ_{CP} [53].

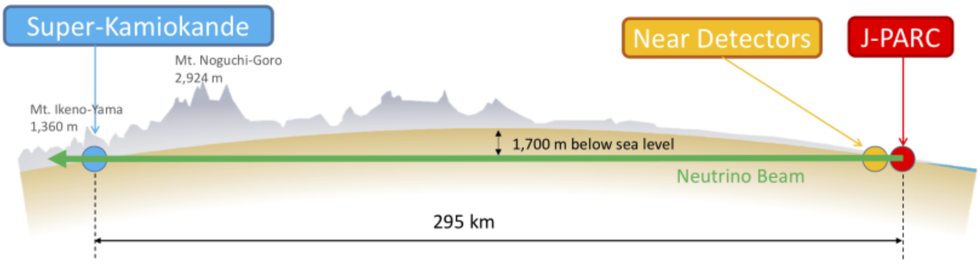

Figure 3.1: Overview of the T2K neutrino beam, showing the position of the near and far (Super-Kamiokande) detectors in relation to the beam source at J-PARC. Figure adapted from [52].

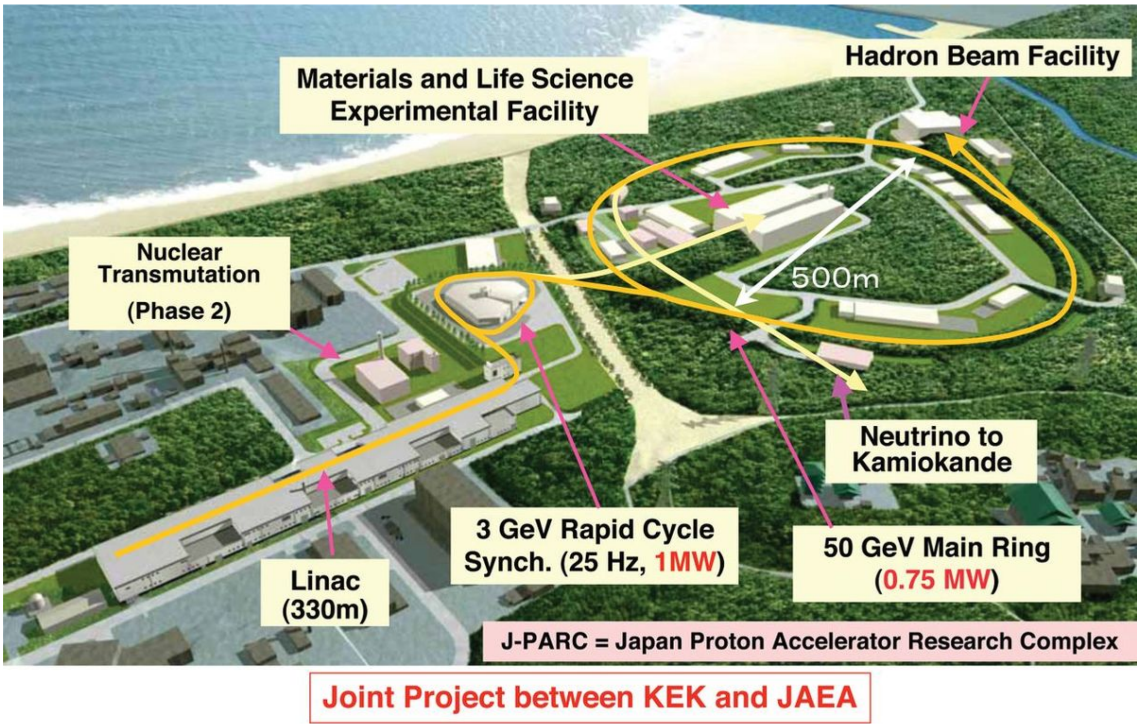

Figure 3.2: Overview of the J-PARC accelerator complex, with the proton acceleration path highlighted in yellow. Figure adapted from [55]

3.1 Beam and Accelerator Complex at J-PARC

J-PARC (Japan Proton Accelerator Research Complex) is a particle accelerator complex located in Tokai, Ibaraki Prefecture, on the west coast of Japan. The neutrino beam is generated here, and it is the site for the INGRID and ND280 detectors. The complex consists of three accelerators: a linear accelerator (LINAC), a rapid-cycling synchrotron (RCS) and the main ring (MR) synchrotron (figure 3.2).

To produce the neutrino beam, H^- ions are first accelerated to 400 MeV in the LINAC. The ions are then stripped of their electrons to form protons and then injected into the RCS. The RCS accelerates them up to 3 GeV, with two bunches per cycle. The protons are then injected into the MR and accelerated further to 30 GeV, where they are grouped into eight bunches. They can then be extracted via slow extraction for the hadron beamline or fast extraction for the neutrino beamline. For fast extraction, the eight bunches are extracted in a single cycle by a set of five kicker magnets. Each bunch contains $\sim 4.1 \times 10^{13}$ protons, for a total of $\sim 3.3 \times 10^{14}$ protons per pulse (full cycle of the MR) [54]. Each extraction is known as a "spill" and lasts $\sim 5\ \mu$s.

After fast extraction, the proton beam is directed towards a rod-shaped graphite target

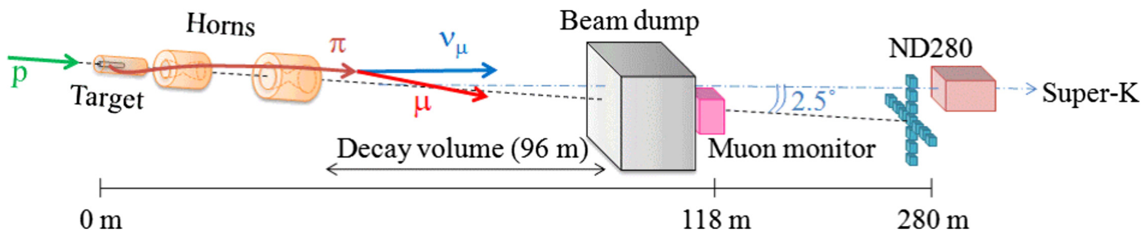

Figure 3.3: Diagram of the T2K neutrino beamline. The three magnetic horns, muon monitor and INGRID (blue cross) are positioned along the neutrino axis, while the ND280 detector and Super-K are 2.5° off-axis. Figure adapted from [56].

91.4 cm long and 2.6 cm in diameter. Protons colliding with the target interact with the carbon atoms and produce a shower of secondary hadrons, primarily pions and kaons. The number of protons that collide with the target are referred to as “Protons on Target” (POT) which is the primary value used in describing the beam flux as it can be more easily measured as opposed to the neutrino beam itself. Three magnetic horns are used to collect the charged mesons and refocus them into a narrow beam. The horns are also used to select between positively- and negatively-charged particles, depending on the horn polarity. In “Forward Horn Current” (FHC), the horns select positively-charged particles and therefore produce a beam of muon neutrinos via the following dominant channels:

$$\pi^+ \rightarrow \mu^+ + \nu_\mu$$

$$K^+ \rightarrow \mu^+ + \nu_\mu$$

$$K^+ \rightarrow \pi^0 + \mu^+ + \nu_\mu$$

Pion decays to positrons are possible, but very unlikely due to helicity suppression. The mesons decay along a 96 m decay volume after which the beam dump, a 75-ton graphite block, absorbs the remaining charged particles (mainly muons and hadrons) as they could decay to produce electron neutrinos, which would contaminate the muon neutrino beam.

The horns can also be set to “Reverse Horn Current” (RHC) which instead selects negatively-charged particles and produces a beam of muon antineutrinos. The proton beam naturally favours positively-charged products, thus the FHC beam is purer and has a greater neutrino flux compared to RHC.

The muon monitor (MUMON) is positioned behind the beam dump, which tracks high-energy ($>$ 5 GeV) muons that pass through the beam dump [56]. This is used to monitor the beam stability and direction as the muons will follow the same track as the neutrinos

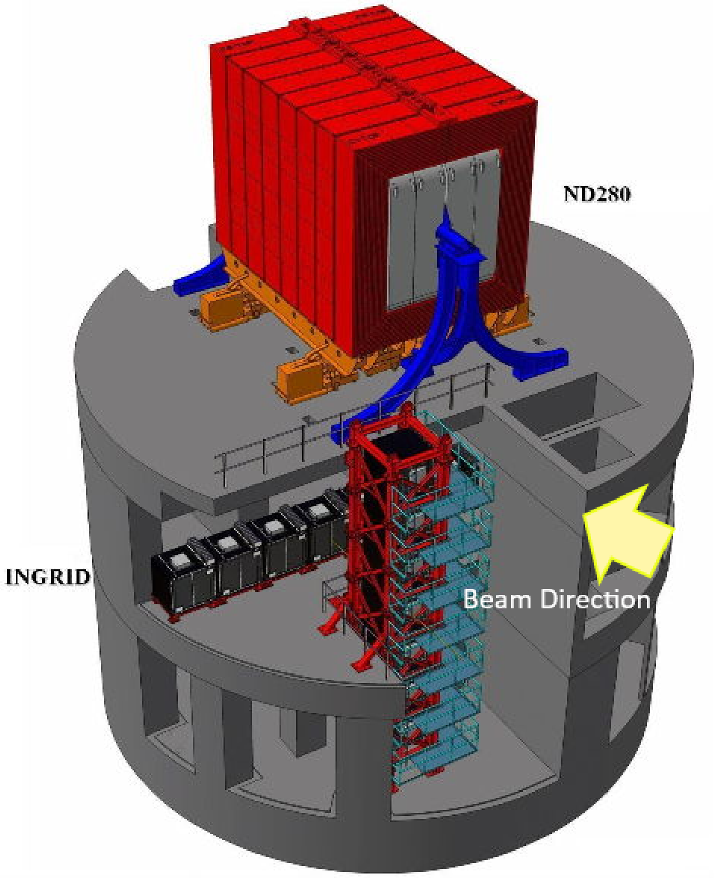

Figure 3.4: Overview of the T2K near detector complex, showing the position of the ND280 detector and INGRID. Neutrino beam direction is along the yellow arrow. These detectors are responsible for measuring the characteristics of the neutrino beam prior to neutrino oscillation. WAGASCI and Baby MIND are located on the lowest floor, to the right of INGRID's vertical stack when facing along beam direction. Figure adapted from [57].

in the beam. The beam will then pass through a thick layer of sand to the near detector complex 280 m downstream, containing the INGRID, ND280, WAGASCI and Baby MIND detectors. Figure 3.4 shows the positon of INGRID and ND280 within the near detector complex; WAGASCI and Baby MIND are positioned on the lower floor, beneath ND280. The full layout of the neutrino beamline, including target, magnetic horns, and beam dump, is shown in figure 3.3.

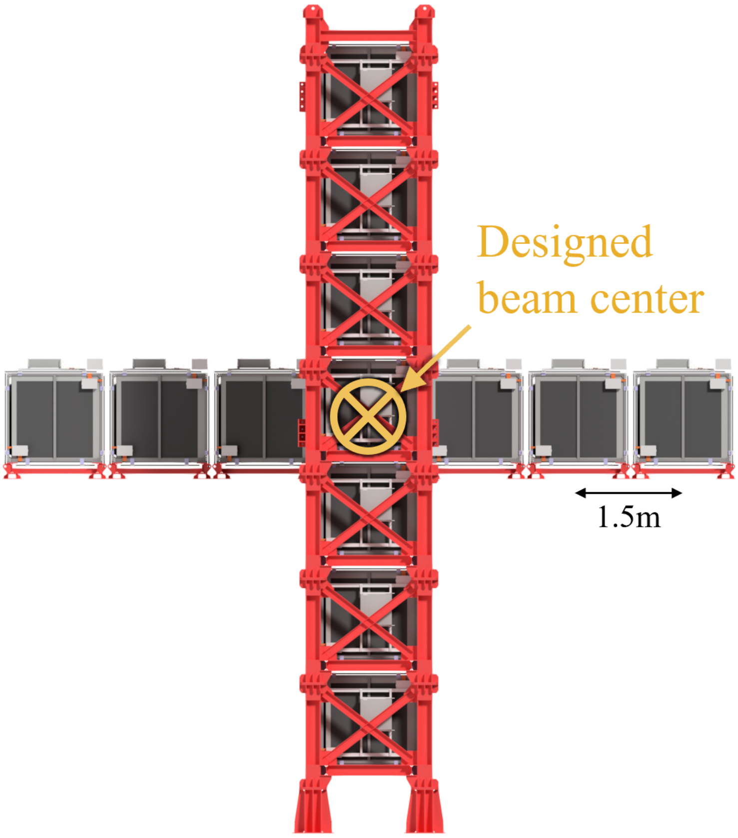

Figure 3.5: The INGRID detector, showing the arrangement of the 14 modules. The two lines of detector modules overlap at the centre of the cross, which corresponds to the centre of the neutrino beam [59].

3.2 INGRID

The Interactive Neutrino GRID (INGRID) is an on-axis iron-scintillator detector used to measure the beam direction and intensity. It consists of 14 detector modules arranged in a cross shape, with the neutrino beam aimed through its centre (figure 3.5). INGRID can measure the beam direction to a precision of at least 0.4 mrad, which is well within the ±1 mrad accuracy required [58].

Each INGRID module is made from 11 plastic scintillator planes and 9 iron target plates, shown in figure 3.6. Each scintillator plane is made from two layers of 24 scintillator bars, in alternating orientation. The iron plates measure 124 × 124 × 6.5 cm, for a mass of 7.1 tonnes of iron per module. No iron plate is between the final two scintillator planes. The four faces parallel to be beam direction (top, bottom, sides) are covered in veto planes containing 22 scintillator bars arranged perpendicular to the beam direction.

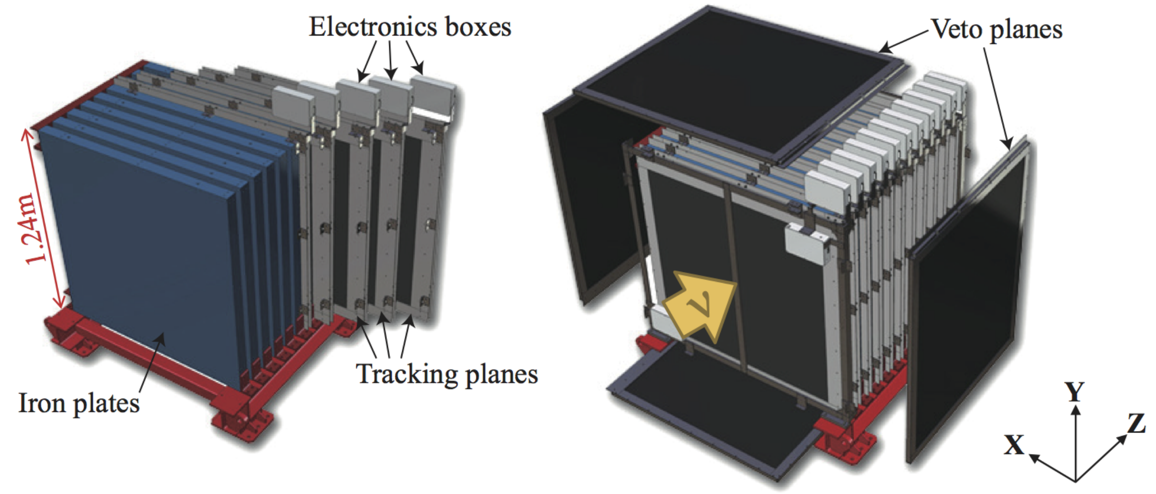

Figure 3.6: Schematic of one of the 14 INGRID modules showing the position of the scintillator planes and iron plates, as well as the veto planes. Neutrino beam direction is along the yellow arrow . Figure adapted from [59].

3.3 ND280

The Near Detector at 280 metres (ND280) is positioned 280 metres away from the beam target and 2.5° off-axis from the neutrino beam. Its primary purpose is to measure the beam composition close to the source to take pre-oscillation measurements. The off-axis angle means the beam has a peak neutrino energy of $\sim$ 0.6 GeV, which maximises the effect of neutrino oscillation at the far detector and thus reduces the overall uncertainty in oscillation parameter measurements. Figure 3.7 shows the energy spectrum, as well as how it is affected by different off-axis angles.

The detector consists of a number of sub-detectors: 13 electromagnetic calorimeter (ECal) modules, the pi-zero detector (PØD), three time projection chambers (TPCs), two fine-grain detectors (FGDs) and the side muon range detector (SMRD). ND280 and its sub-detectors are discussed in detail in chapter 4.

3.4 WAGASCI and Baby MIND

The main target mass within the ND280 near detector is its FGDs, which are made from plastic scintillator. The far detector, Super-Kamiokande (see section 3.5), is a water-cherenkov detector, with water as the only target mass. Thus, there remains a non-cancelling systematic uncertainty between the near and far detectors due to the different neutrino-nucleus interactions between carbon (plastic) and oxygen (water). To reduce this

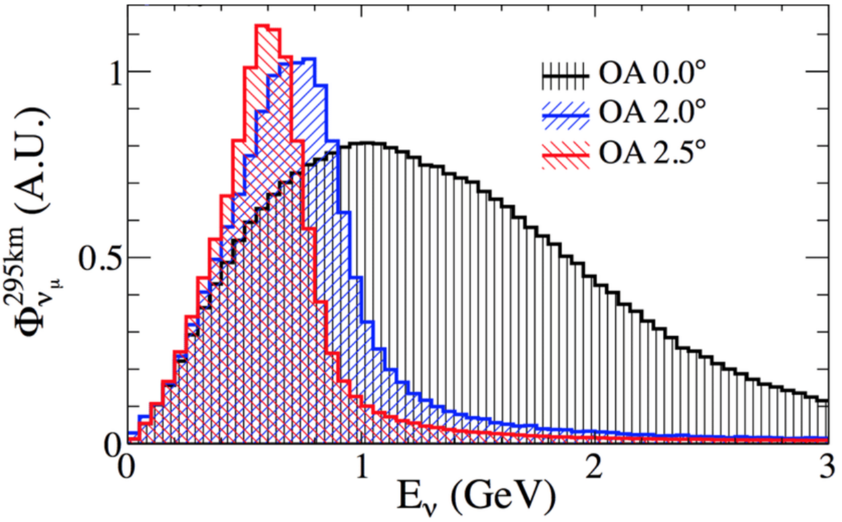

Figure 3.7: T2K beam energy spectrum at 295 km from beam source, showing how off-axis angles of 0° (black), 2° (blue), and 2.5° (red) affect the peak energy and the width of the peak. The ND280 and Super-K detectors are positioned 2.5° off-axis to give a beam energy of 0.6 GeV with a narrow peak. The spectrum at the near detector is similar. Figure adapted from [60].

uncertainty, the WAter-Grid- And-SCIntilator-Dectector (WAGASCI) [61] has been built.

The WAGASCI detector, shown in figure 3.8, is positioned 1.5° off-axis from the neutrino beam, so has a slightly higher neutrino energy. It consists of two water modules and one plastic scintillator module, called the "proton module". Inside each module is a 3D grid structure of plastic scintillator with the cells filled with the target material. The plastic scintillator bars used to construct the grid are very thin (3 mm) to maximise target area whilst taking accurate measurements of particle interactions. Placed a short distance away from the left and right sides of the detector are the wall muon range detectors (wall MRDs). These detectors consist of alternating iron and plastic scintillator layers and are used to identify muons and measure muon momenta to help reconstruct neutrino interactions in the main modules.

The Baby Magnetised Iron Neutrino Detector (Baby MIND) [62] is located directly downstream from WAGASCI. It is used to perform charge identification and momentum measurements on muons leaving WAGASCI. Baby MIND consists of 33 magnetised iron plates (30 mm thick) and 18 plastic scintillator planes. The magnetised plates produce a magnetic field of 1.5 T allowing for precise moun measurements in the energy region 0.3-5.0 GeV, which is otherwise degraded by multiple scatterings.

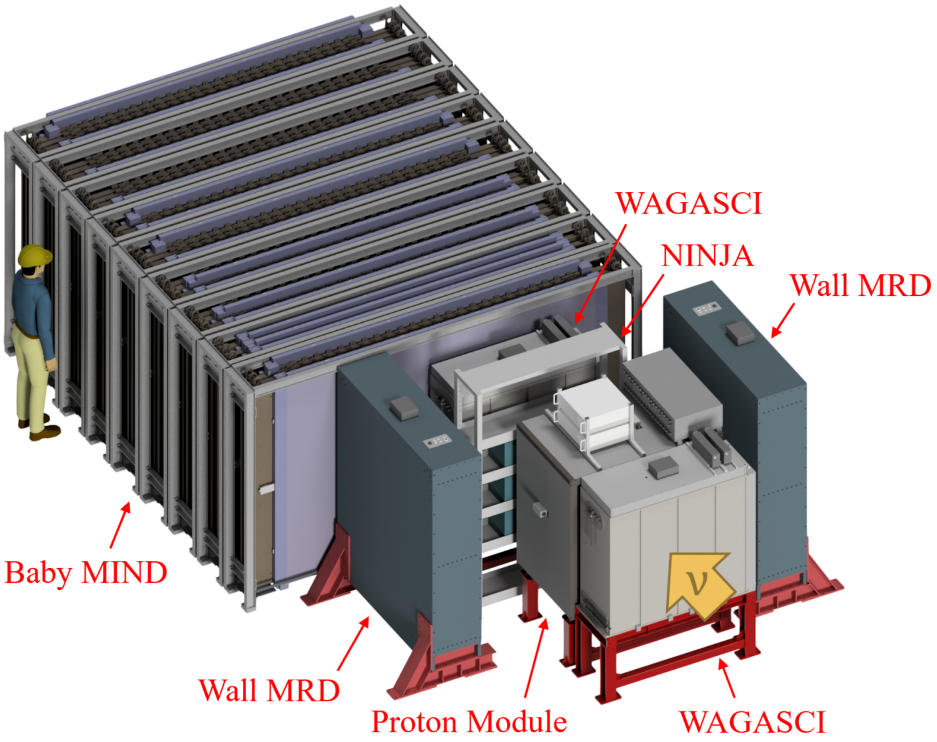

Figure 3.8: Positions of the WAGASCI and Baby MIND detectors, as well as the two wall muon range detectors (MRDs). The NINJA detector is not part of T2K, it is instead a separate experiment investigating neutrino-nucleus interactions using an emulsion detector [63]. Figure adapted from [64].

3.5 Super-Kamiokande

Super-Kamiokande [65] (Super-K) is a water-Cherenkov neutrino detector situated 1 km below Mt. Ikenoyama near Hida, Gifu Prefecture near the west coast of Japan. It is positioned 295 km away from the J-PARC site and is 2.5° off-axis from the neutrino beam, the same as ND280. SK functions as the "far detector" for the T2K experiment and measures the composition of the neutrino beam to identify changes in neutrino flavour. The 1 km overburden of rock reduces interactions of cosmic ray particles within the detector. By comparing beam measurements between ND280 and SK, the neutrino oscillation parameters can be calculated. SK, as its own experiment, is also involved in solar and atmospheric neutrino measurements and is part of the supernova early warning system (SNEWS) [66].

Super-Kamiokande consists of a cylindrical steel tank 41.4 m tall and 39.3 m in diameter, and filled with 50,000 tons of ultrapure water. The tank is divided into the "inner" and "outer" detectors (ID and OD, respectively), which are optically separated by a steel cylinder covered in black plastic sheeting (figure 3.9). The ID is the fiducial volume for the detector, whilst the OD is used to veto muons and other particles entering the detector The ID measures 36.2 m tall and 33.8 m in diameter and is lined with 11,129 inward-facing Hamamatsu R3600 photomultiplier tubes (PMTs). Each PMT measures 50 cm in diameter for a total coverage of 40% across the walls of the ID. The OD has 1,885 outward-facing PMTs, each 20 cm in diameter and mounted to wavelength-shifting planes. Although OD PMT covereage is only 7%, it can still veto muons entering the detector at almost 100% efficiency [52].

As a water Cherenkov detector, SK functions by detecting the Cherenkov radiation emitted by particles as they pass through the water. Cherenkov radiation is emitted when a charged particle travels through a medium at a higher speed than the speed of light in that medium, which is around $0.75c$ in water. Charged-current quasi-elastic (CCQE) interactions between neutrinos from the T2K beam and oxygen nuclei in the water produce an (anti-)electron or (anti-)muon depending on the flavour of the neutrino, and the resultant lepton will have enough energy to emit Cherenkov radiation. Cherenkov radiation is emitted in a cone shape following the trajectory of the particle, which is detected by the PMTs.

The properties of the Cherenkov cones allow for particle identification. Minimally ionising particles like muons do not change their momentum much as they propagate, so generate well-defined cones of light that are detected as a clear ring of PMT hits. Highly ionising

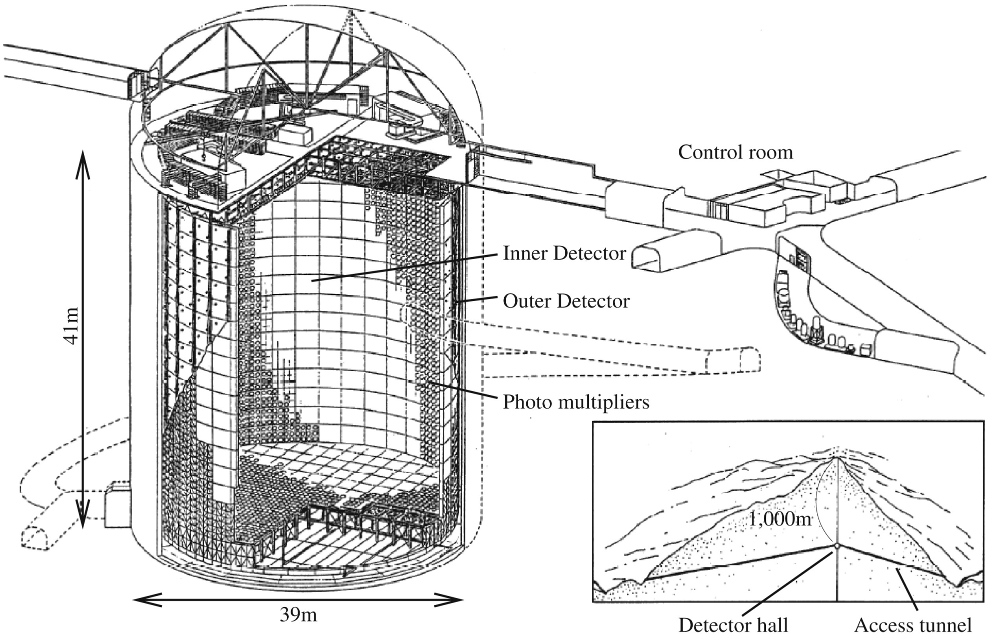

Figure 3.9: Overview of the Super-Kamiokande neutrino detector including the inner and outer detectors, and photomultiplier tubes. The location of the detector within Mt. Ikenoyama is also shown. Figure adapted from [52].

particles like electrons, on the other hand, scatter more easily and produce a fuzzy ring pattern. A comparison of the ring shapes is shown in figure 3.10. By measuring the occurrences of these interactions, $\nu_\mu \to \nu_e$ appearance and ν_μ disappearance in the beam can be found by comparing with data from ND280, which is then used to calculate the neutrino oscillation parameters. ν_τ will occur within the beam but these would almost never produce a τ lepton as the energy threshold required is ~ 3.5 GeV, beyond the off-axis neutrino beam's peak of 0.6 GeV. Additionally, a τ lepton would decay almost instantly to other leptons or mesons, so it cannot be observed easily [67].

In 2020 the water in SK was doped with gadolinium sulfate $Gd_2(SO_4)_3$ to improve neutron capture [69]. Neutrons are emitted from nuclei in interactions with anti-neutrinos in inverse beta decay reactions:

$$\bar{\nu}_{e(\mu)} + p \to e^+(\mu^+) + n$$

Neutron capture occurs when the neutron produced is absorbed by another nuclei and emits gamma rays, which is the main method to differentiate between neutrino and anti-neutrino interactions in SK. Historically, this was done by observing neutron capture on hydrogen atoms, but gadolinium has a much higher neutron capture cross section and will capture 90% of all such neutrons, improving from $< 20\%$ capture rate with just hydrogen.

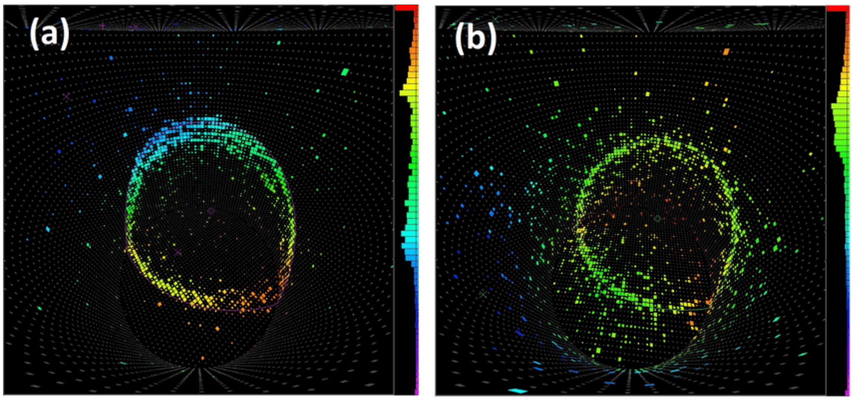

Figure 3.10: Rings of Cherenkov radiation detected in Super-Kamiokande. (a) shows sharp rings emitted by a muon, while (b) shows the fuzzy rings seen from electrons. Figure adapted from [68].

Compared to hydrogen, gadolinium neutron capture produces a more energetic gamma ray (8 MeV vs 2.2 MeV) in a shorter time ($\sim 20\mu$s vs $\sim 180\mu$s) which will help distinguish ν and $\bar{\nu}$ interactions.

Chapter 4

The ND280 Detector

The ND280 detector is one of the main detectors that make up T2K's near detector complex. Its primary purpose is to measure the composition, flux and energy spectrum of the neutrino beam prior to oscillation. It is positioned 2.5° off-axis from the centre of the neutrino beam, where the neutrino energy is optimal for oscillation to be observed at Super-K (see figure 3.7). The detector consists of multiple sub-detectors (figure 4.1): the pi-zero detector (PØD), the time projection chambers (TPCs), the fine-grained detectors (FDGs), the electromagnetic calorimeters (ECals) and the side muon range detector (SMRD). The sub-detectors are enclosed within a magnet yoke (except the SMRD, which is embedded within the yoke). The PØD, TPCs, FGDs and downstream ECal module are held within a metal frame known as the "basket", which measures 6.5 m ×2.6 m ×2.5 m. The full dimensions of the detector with the magnet closed measure 7.6 m ×5.6 m ×6.1 m. The nature of the sub-detectors are discussed in detail below, beginning with components common to multiple sub-detectors. Also discussed is the recent upgrade to ND280, replacing the PØD with a suite of new sub-detectors (section 4.7).

4.1 Common Components

Several of the sub-detectors share similar components, particularly plastic scintillator and wavelength-shifting fibre, and the associated photosensors. Additionally, the magnet surrounding the detectors provides a constant magnetic field throughout all of the sub-detectors.

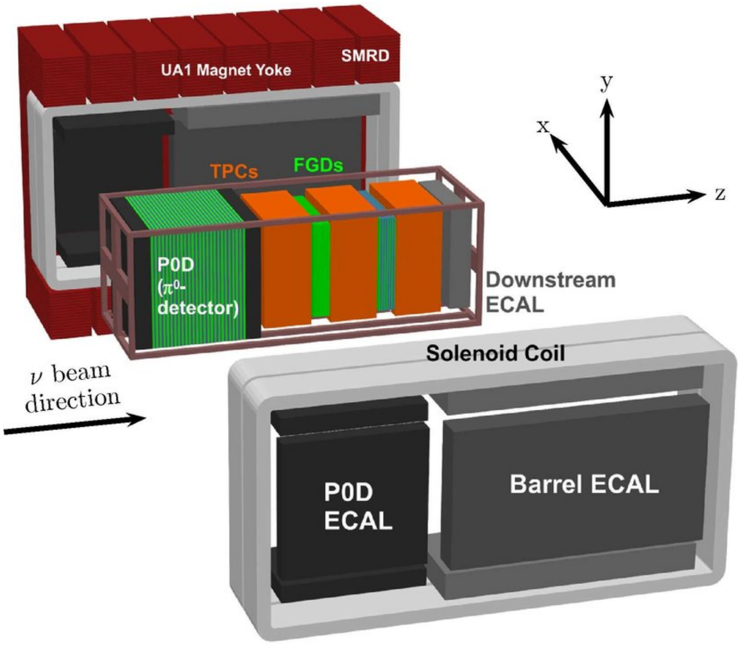

Figure 4.1: Exploded view of the ND280 detector, showing the constituent sub-detectors. The PØD, TPCs, FGDs and the downstream ECal are within the metal-framed “basket”. The magnet solenoid coils surround the ECals and inner detectors around the top, back, bottom and front sides. The magnet yoke segments on the right side of the detector are not shown. During data taking, the yoke fully encloses the inner detectors. Diagram adapted from [52].

4.1.1 Plastic Scintillator

Plastic scintillator bars are present within the PØD, the FGDs and the ECal, while the SMRD uses larger scintillator slabs. The bars and slabs are constructed of extruded polystyrene. Charged particles passing through the polystyrene deposit energy into the atoms, which then emit light as they de-excite. As polystyrene emits scintillation light in the ultraviolet range, it is doped with 1% PPO and 0.03% POPOP to shift the UV light into blue light. A thin layer of co-extruded polystyrene mixed with 25% TiO_2 coats the scintillator to reflect light back into the bar which minimises light loss and prevents light bleeding between different bars.

4.1.2 Wavelength-shifting fibre

Wavelength-shifting (WLS) fibres (Kuraray double-clad Y11, 1 mm diameter) are present in all of the plastic scintillator bars, typically running straight through a central hole down the middle of the bar’s cross-section. They collect light emitted by the scintillator and feed it to the photodetectors. As the name suggests, the WLS fibres shift the peak wavelength of absorbed light: the absorption spectrum of the fibres is centred at 430 nm (blue) and emission is centred at 476 nm (green). This reduces self-absorption effects within the fibre and improves photon detection efficiency for the photodetectors [70].

4.1.3 Multi-Pixel Photon Counters

Multi-Pixel Photon Counters (MPPCs) [71], manufactured by Hamamatsu Photonics, are the photodetectors used in all scintillator detectors in ND280. Each counter module measures 5 mm × 6 mm and contains 667 avalanche photodiodes (APDs). Each APD measures $50 \times 50\ \mu\text{m}^2$, and the sensitive area of each MPPC counter measures 1.3 mm $\times$ 1.3 mm^2. MPPCs are not affected by strong magnetic fields so are safe for use within the 0.2 T field generated by the magnet, and their small size is ideal for the limited space in the detector.

4.1.4 ND280 Magnet

The magnet yoke encloses all of ND280's sub-detectors (except for the SMRD), containing the aluminium solenoid coils which, when powered, provide a 0.2 T magnetic field through the entire detector. Charged particles will curve as they pass through the magnetic field, which is used in particle identification and momentum calculations from reconstructed particle tracks. The magnet has been refurbished following its previous use in CERN's UA1 and NOMAD experiments, and consists of water-cooled aluminium solenoid coils surrounded by the flux return yoke. The arrangement of the coils and yoke is shown in figure 4.1.

There are four solenoid coils, each made from aluminium bars with 5.45 cm × 5.45 cm square cross-sections and bored with a central 23 mm hole for the water cooling. When energised, the magnet draws 2.9 kA at 155 V. The yoke consists of 16 C-shaped segments made of low-carbon steel plates, which are fitted on rails so the magnet can be opened and the inner detectors accessed. The magnet has a total weight of 850 tons. As the magnet yoke was effectively the first part of the detector to be constructed, it presents strict size constraints on the rest of the detector.

4.2 Pi-Zero Detector

The PØD [72] was the most upstream of the inner sub-detectors (those within the basket), and was designed to measure the cross-sections of neutrino interactions that generate π^0s. π^0s produced through NC interactions and are the dominant background to $\nu_\mu \to \nu_e$ signal at Super-K, as they most commonly decay to two photons which can produce electrons that mimic the final state of a ν_e CC interaction [10]. π^0 CC interactions produce a charged lepton, so can be more easily identified and rejected. By constraining the π_0 background, the uncertainty in the ν_e appearance rate at the far detector is reduced.

The detector was comprised of a water target region, separated into "upstream" and "central" water targets, between two ECal sections (figure 4.2). A "target region" is where the majority of reconstructed neutrino events occur, and the PØD was designed to detect neutrino interactions with water. The water target region consists of layers of scintillator, brass sheets and water bags. There are a total of 26 scintillator layers, containing 134 horizontal (2.2 m long) and 126 vertical (2.34 m long) triangular scintillator bars. Each bar was threaded with a wavelength-shifting fibre; one end was mirrored while the other was connected to an MPPC for electronic readout. The water bags (2.8 cm thick) could be filled and emptied, and data was taken in both configurations. The purpose of the water was to allow for a measurement of π^0-producing neutrino interactions with water that could be compared with the rate at Super-K, specifically the neutral current process $\nu_\mu + N \to \nu_\mu + N + \pi^0 + X$. The 25 water target layers each had two bags, for a total of 50 in the PØD. When filled, the PØD contains 2.9 tonnes of water.

The ECal sections used alternating layers of horizontal and vertical scintillator bars and lead sheets, with seven such modules each in the upstream and central ECals. The ECal region was designed to contain electromagnetic showers occurring within the PØD sub-detector, and as a veto region to reject particle tracks entering from outside the PØD.

The PØD has since been removed from ND280 to make way for a significant upgrade to the detector, discussed in section 4.7. This was partially motivated by the fact the PØD performed somewhat poorly. The analyses presented in this thesis have been performed using Monte Carlo simulations and data generated when the PØD was still present.

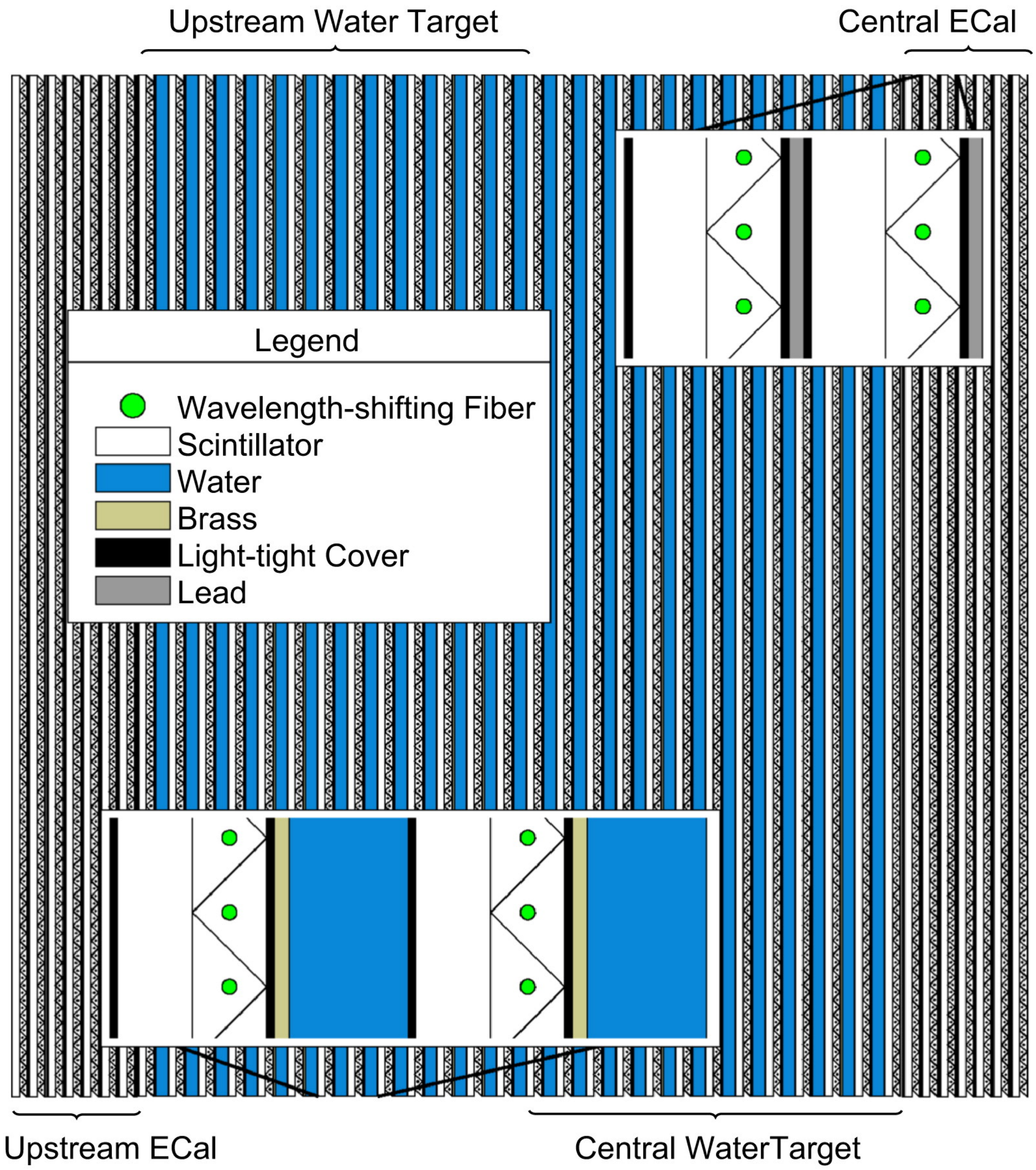

Figure 4.2: Cross-sectional view of the PØD, side on. The blue represents the water-filled bags sandwiched between the brass plates and scintillator layers. The arrangement of the layers in the water region is presented in the bottom-left inset, showing (left to right) vertical scintillator bars, horizontal scintillator bars, the brass sheet and the water layer. Light-tight covers separate the scintillator, bars and water. The top-right inset shows the layers in the ECal regions: vertical scintillator bars, horizontal scintillator bars and lead sheets. Beam direction is left to right. Figure adapted from [72]

.

4.3 Time Projection Chambers

ND280 contains three time-projection chambers (TPCs) [73], placed directly downstream of the PØD with the two fine-grained detectors (see section 4.4) placed between them. These five sub-detectors together make up the "tracking region". The TPCs are designed to accurately track the movement of charged particles, and by measuring their curvature in the magnetic field the momentum can be calculated. Additionally, particle identification is possible by combining the momentum measurement with $\frac{dE}{dx}$ (energy loss E from ionisation for a particle as it passes x distance through a medium). The TPCs consist of an inner box filled with drift gas (Ar:CF_4:C_4H_{10}, ratio 95:3:2), surrounded by an outer box containing CO_2 to electrically insulate the inner box. The outer box has dimensions $2.302 \times 2.400 \times 0.974$ m, while the inner box measures $1.808 \times 2.230 \times 0.854$ m.

The inner box is bisected by a central cathode, which generates a strong electric field between the cathode and the walls of the box. The two inner box walls opposite the plane of the cathode are instrumented with 12 Micromegas detector modules [74], which detect ionised gas particles and collect charge and timing information. Charged particles passing through the drift gas will ionise the molecules, which are then accelerated towards the Micromegas detectors by the electric field. The detector information can then be used to reconstruct the track in 3D, based on the time taken for the ions to drift to the detector modules. The TPCs can provide spatial resolution to < 1 mm and energy deposit resolution to $7.8 \pm 0.2\%$ for minimum ionising particles (particles that deposit close to the minimum possible amount of energy when passing through a medium e.g. muons and electrons at T2K energies). The probability of misidentifying a muon as an electron is just 0.2% at energies < 1 GeV. A cutaway view of the TPC design is shown in figure 4.3.

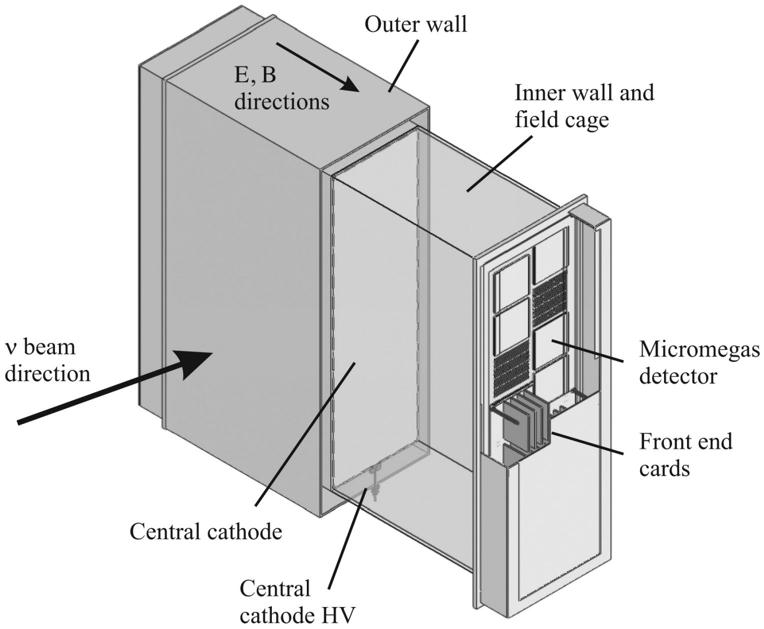

Figure 4.3: Cutaway diagram of the TPC design, showing the main components. Figure adapted from [73].

4.4 Fine-Grained Detectors

The two fine-grained detectors (FGDs) [70] are positioned between the three TPCs in the tracking region. The upstream FGD (FGD1) is composed of layers of scintillator bars in alternating horizontal and vertical orientations, while the downstream FGD (FGD2) has scintillator bar layers in addition to water target modules. A cross-section of FGD1 is shown in figure 4.4.

Each scintillator bar layer is comprised of 192 186.43 × 0.961 × 0.961 cm bars, each threaded with WLS fibre. The fibre is mirrored at one end and coupled to an MPPC at the other. The layers are arranged in pairs of alternating orientation known as "XY modules", each measuring 186.4 × 186.4 × 2.02 cm. FGD1 contains fifteen XY modules, while FGD2 contains seven modules in addition to six water layers. Events in FGD1 and FGD2 can be compared to identify differences in neutrino interactions on oxygen and carbon nuclei.

The criss-cross construction of the FGD allows for the effective 3D reconstruction of charged particles tracks; however, particles moving at a high angle relative to the detector axis can be difficult to reconstruct as they pass through fewer scintillator layers. The FGDs are considered the "target mass" of the detector because the majority of the events reconstructed in the TPCs begin within the plastic scintillator, despite the majority of actual neutrino interactions occurring in denser parts of the detector such as the magnet yoke.

4.5 Electromagnetic Calorimeter

The Electromagnetic Calorimeter (ECal) is a lead-scintillator sampling calorimeter which encloses the PØD, FGDs and TPCs [75]. The primary purpose of the ECal is to measure electromagnetic showers of electrons, positrons and photons. It can be broken down into three main regions: the PØD ECal surrounds the top, bottom and sides of the PØD (not to be confused with the ECal regions within the PØD); the Barrel ECal surrounds the four outer faces of the tracking detectors; and the Downstream (Ds) ECal which covers the downstream face of the last TPC. The top and bottom of the PØD and Barrel ECals are made of two ECal modules separated down the middle of the detector so they come apart with the two halves of the yoke when the detector is opened, meaning there is a total of 13 ECal modules. Each module consists of alternating layers of scintillator bars

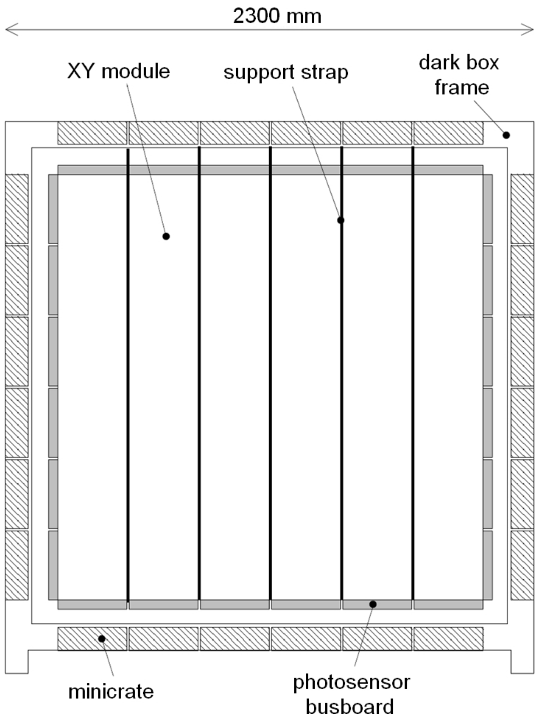

Figure 4.4: Cross-section of FGD1, showing the XY modules and detector casing. Figure adapted from [70].

and lead sheets. The bars are threaded with WLS fibre, and the light is read out to an MPPC at either one or both ends. Fibres with single-ended readout are mirrored at the other end. Ds-ECal fibres have double-ended readout; Barrel ECal fibres running the length of the detector are double-ended, with the other fibres being single-ended; and the PØD ECal fibres are single-ended. As with the FGDs, the scintillator bar orientation alternates between layers.

The barrel ECal modules contain 31 scintillator-lead layers, corresponding to approximately 10 electron radiation lengths (X_0). The scintillator layers are composed of plastic scintillator bars 10 mm thick and 40 mm wide, and the lead sheets are 1.75 mm thick. The Ds ECal has 34 layers (approximately 11 X_0). The PØD ECal modules have only 6 such layers (approximately 4.3 X_0), but significantly thicker lead (4 mm). This reflects the different physics goals in the detector regions: the barrel and Ds ECals are optimised for particle identification and track reconstruction, while the PØD ECal's role is to veto particle interactions occuring outside the PØD and measure the energy of particles leaving the detector.

4.6 Side Muon Range Detector

The side muon range detector (SMRD) is built in to the magnet yoke that surrounds the other sub-detectors. It consists of 440 scintillator modules placed within the 1.7 cm-thick air gaps between the 4.8 cm-thick steel plates which make up the magnet's return yokes. The scintillator modules consist of slabs of plastic scintillator embedded with a wavelength-shifting fibre in a serpentine shape (figure 4.5), each called a scintillation counter. This shape improves the sensitivity of the module compared to a central straight fibre without having to increase the number of scintillator slabs and photosensors, as it reduces the distance between any point in the scintillator and the WLS fibre. The horizontal modules contain four scintillator counters while the vertical modules contain five.

The SMRD is used to identify and measure the momentum of muons that have escaped the detector at high angles relative to the detector axis. It also used to calibrate the detector for backgrounds from cosmic muons and from beam neutrino interactions in the yoke and surrounding walls.

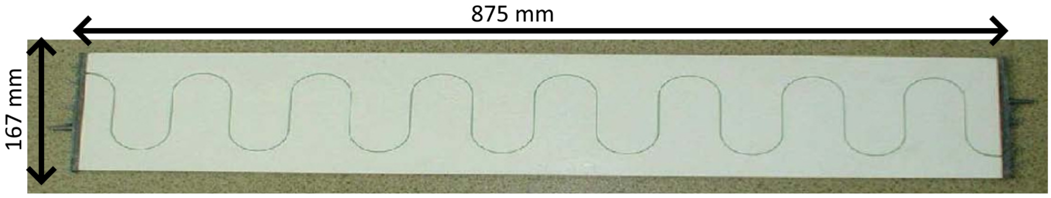

Figure 4.5: SMRD scintillation slab showing serpentine-shaped WLS fibre installation

4.7 ND280 Upgrade

In 2024, a significant upgrade to the ND280 detector was completed, designed to constrain the neutrino interaction cross-sections measurements to reduce the uncertainty in number of predicted events at Super-K from $\sim 6\%$ to $\sim 4\%$. This meets the needs of the next phase of the T2K experiment, T2K-II [76]. In the upgrade, the PØD has been removed and in its place a new suite of sub-detectors has been installed: the SuperFGD (SFGD), two high-angle TPCs (HA-TPCs), and six time-of-flight (TOF) planes. The upstream ECal from the PØD was retained as an independent ECal module. The positioning of the new detectors in ND280 is shown in figure 4.6.

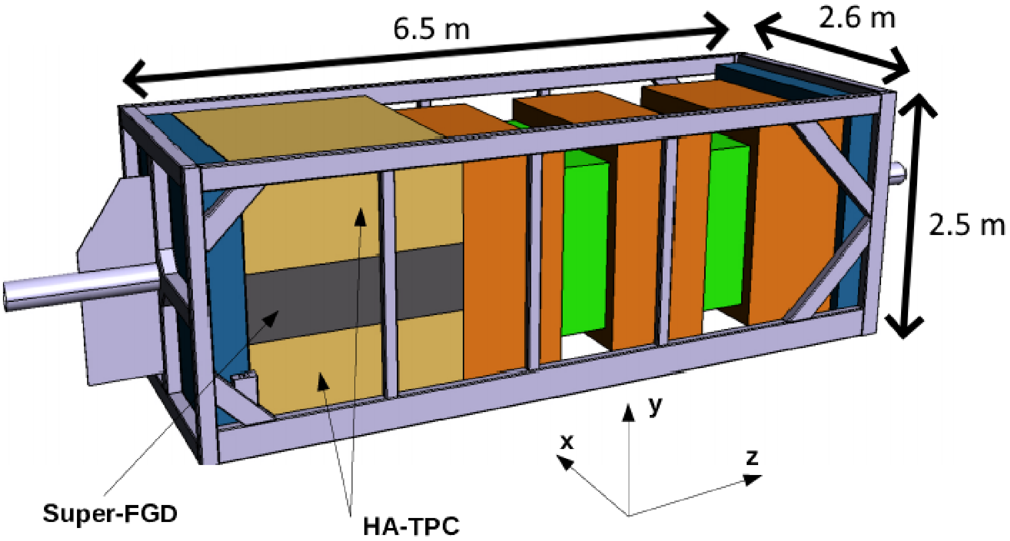

Figure 4.6: Diagram showing the position of the new Super-FGD and High-angle TPCs within the basket, replacing the PØD. Not pictured are the six time-of-flight detectors that surround the six outer faces of the new detectors [76].

4.7.1 SuperFGD

The SuperFGD [77] consists of plastic scintillator threaded with WLS fibre, similar to the two existing FGDs. However, instead of scintillator bars, the SuperFGD is constructed from $1 \times 1 \times 1$ cm^3 optically-independent scintillator cubes. The detector is comprised of a total of 2,064,384 such cubes in a $192 \times 192 \times 56$ cuboid. Each cube is drilled with three holes, allowing WSF to be threaded through each face of the cube and allowing for a three-dimensional measurement with complete sensitivity to high-angle particle tracks. This contrasts with the existing FGDs, which have comparatively poor high-angle tracking as particles may travel through the full length of one FGD bar and leave few distinct scintillator hits across the FGD. Each WLS fibre is connected on one end to an MPPC, for a total of 58,368 readout channels, whilst the opposite end is connected to an LED light injection system for testing and calibrating the MPPCs. The SFGD weighs approximately 2 tons, comparable with the existing FGDs, effectively doubling the main target mass of ND280.

SuperFGD construction posed an interesting challenge as the two million cubes needed to be positioned accurately inside an enclosed box, and threaded with delicate (and expensive) WLS fibre. A method using fishing line was devised: horizontal layers of cubes were assembled by threading them on to thick (1.3 mm) fishing line, then the next layer of cubes was positioned on top of the previous layer and held in place using rigid metal rods through the cubes' vertical holes. This was performed with the bottom and two adjacent sides of the detector's box in position to guide the positioning and threading of the cubes. The remaining sides of the box were then carefully assembled, threading each of the ends of the fishing wire/rods through the corresponding fibre holes in each side. This method proved successful, and all the cubes were positioned correctly within the detector box.

To complete the construction, each strand of fishing line was carefully pulled out and a length of WLS fibre was threaded through the holes in the cubes to the other side of the detector. The length of the fibre (2 m) combined with the inability to adjust the cube alignment once the fishing line was removed called for a careful and methodical approach. The fibres are grouped into 8×8 squares for fitting the MPPC module, so each of these were worked on in an alternating pattern to preserve the integrity of the cube alignment. The MPPC-facing end of each of the fibres has a black plastic optical connector glued to it, and the end is polished with a diamond polisher to improve the optical coupling. A thin foam form was positioned between the box and the fibres' optical connector to cushion the fibre against the MPPC modules. The installation process is shown in figure 4.7. After each set of 16 fibres were inserted, the MPPC module was screwed into place over the optical connectors, and an LED module was used to test that each fibre had acceptable light yield. The SFGD during the construction process is shown in figure 4.8.

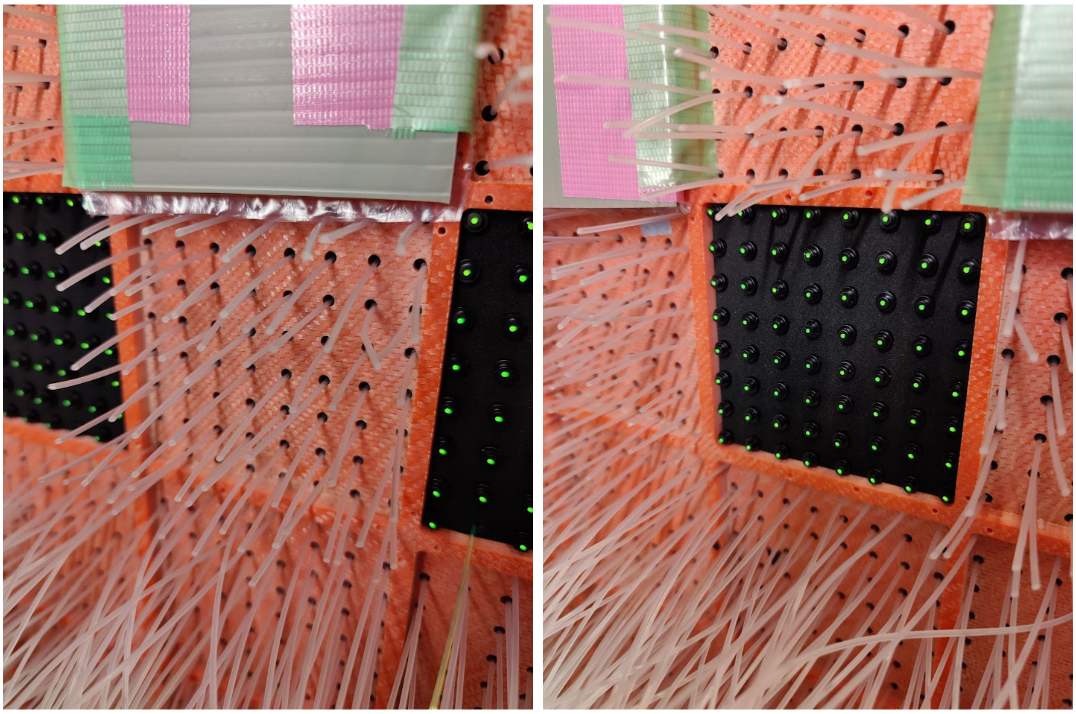

Figure 4.7: Left figure shows group of 16 fibre holes with fishing line still present. Each 8×8 divot is where an MPPC module will be screwed into position. Right figure shows fully inserted set of fibres. Visible are the black plastic optical couplings on the end of each fibre, and the black foam form to protect them against the detector casing. Also visible are grey corrugated plastic squares lined with bubble wrap held in place with pink and green tape, which cover sets of installed fibres to prevent damage.

4.7.2 High-angle TPCs

Two TPCs are positioned above and below the SuperFGD, known as the high-angle TPCs (HA-TPCs) [78] because they cover the high-angle region for particles leaving the SFGD. The HA-TPCs follow a similar design to the existing TPCs, consisting of a box filled with drift gas bisected by a cathode and instrumented with Micromegas detectors. Performance is expected to be similar to the current TPCs, which provide accurate measurements of particle charge and momentum and excel at 3D track reconstruction. Thus, the HA-

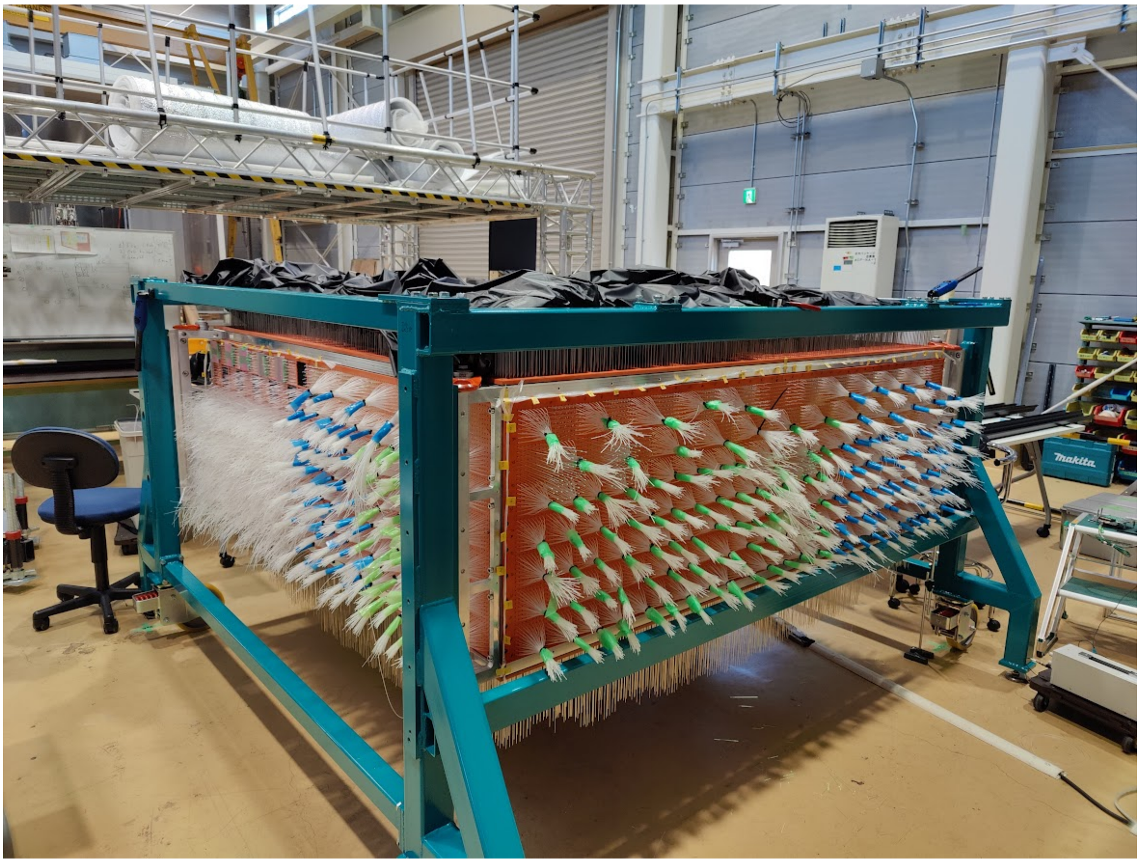

Figure 4.8: The SuperFGD under construction. The bunched-together white fibres are fishing lines used to hold the cubes in position prior to WLS fibre insertion. For the vertical alignment, thin metal rods are used instead.

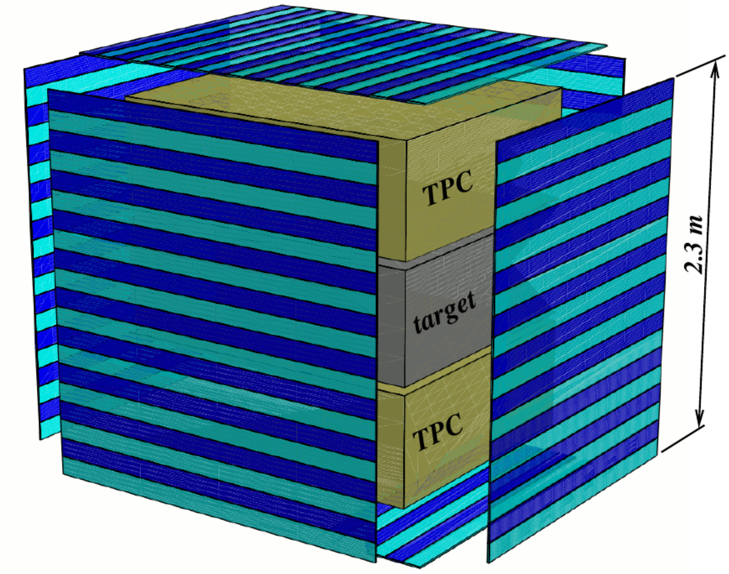

Figure 4.9: Position of time-of-flight planes around the HA-TPCs and SuperFGD. The width and height of the detector is 2.3 m, and the depth is 2 m [76].

TPCs will substantially improve the angular acceptance of the detector whilst maintaining accurate event reconstruction.

4.7.3 Time-of-Flight Planes

The time-of-flight system aims to measure the time taken for a particle to cross the upgraded detector region. The system consists of 6 time-of-flight (ToF) planes that are positioned around the six outer faces of the SuperFGD/HA-TPC "cube", as shown in figure 4.9. Each plane is comprised of 1 layer of plastic scintillator bars with dimensions of $200 \times 1 \times 12$ cm^3 or $230 \times 1 \times 12$ cm^3 depending if the bar will be positioned perpendicular or parallel to the beam direction. Unlike the other scintillator bars within ND280, the ToF bars are not threaded with WLS fibre and are instead coupled directly to MPPCs on both ends. This is to optimise time sensitivity, allowing for a time resolution of around 150 ps over the entire angular coverage. This is enabled by advances in large-area photomultiplier MPPC technology, allowing for compact but highly-sensitive photosensors [79]. These MPPCs are sensitive enough to compensate for the photon degradation in long scintillator bars without WLS fibres. The ToF system can accurately determine particle direction, useful in both 4π solid angle studies and vetoing cosmic muons.

Chapter 5

MC Simulation and Systematics

The Monte Carlo models used to simulate neutrino interactions in the ND280 detector are a central part of the T2K oscillation analysis. The complexities of particle interactions within the detector, combined with the extremely low interaction rate of neutrinos, means the properties of the neutrino beam cannot be read directly from the detector data. This is compounded by the high number of systematic uncertainties in our knowledge of neutrino interactions, beam production, and the detector itself. Thus, Monte Carlo simulations are performed across a wide range of parameters, each corresponding to some systematic uncertainty in the model or experiment setup. These parameters are known as "systematic parameters". The simulation output is then compared with detector data to constrain the uncertainties and improve the overall oscillation measurement. This comparison is known as the near detector fit, and is described in detail in chapter 8 along with the software involved.

This chapter will discuss the models and systematic parameters used in simulating neutrino interactions in the ND280 detector, focusing on the neutrino beam flux (section 5.1), neutrino interactions (section 5.2) and detector response (section 5.3). As fake data studies, the main topic of this thesis, directly affect the interaction parameters, more detail will be given on the neutrino interaction model compared to the flux and detector models. In the remainder of this thesis, "systematics" will be used to refer to the systematic uncertainties of a process.

5.1 Neutrino Flux Model

The neutrino flux model simulates the production of the neutrino beam beginning with the interactions of protons hitting the graphite target, then propagating the resultant particles and decay products through the horns (as described in section 3.1). A replica of the T2K target at the NA61/SHINE experiment at CERN has been used for hadron production measurements [80] [81]. FLUKA is used to simulate interactions inside the target [82], whilst the produced particles and subsequent decay products are tracked through the horn field using the GEANT3-based JNUBEAM package [83].

The MC prediction for pion production is tuned to $\pi^{\pm}$ yields from the NA61/SHINE experiments using the replica target, which further constrains the flux parameters. Pions leaving the target that are within the phase space covered by the NA61/SHINE data (approximately 90%) are given the weight

$$w(p, \theta, z, i) = \frac{\mathrm{d}n^{\mathrm{NA61}}(p, \theta, z, i)}{\mathrm{d}n^{\mathrm{MC}}(p, \theta, z, i)} \tag{5.1}$$

where $\mathrm{d}n$ is the POT-normalised differential yield for data (NA61) and Monte-Carlo simulation (MC), for pions with momentum p, polar angle θ and longitudinal position z along the target, for a particle of type i (π^+, π^-).

For particles leaving the target, no additional tuning is applied for their interactions within the target. Particles not covered by the replica target data and interactions occurring outside the target are tuned using 2009 data taken from the NA61/SHINE experiments on a thin target [84] and other external measurements. The overall uncertainty in the beam flux is show in figure 5.1. It can be seen that uncertainty in hadron interactions is the dominant source of uncertainty across the majority of neutrino energies. The ν_μ neutrino mode is the most significant set of uncertainties, as it is the main neutrino flavour in FHC mode. The neutrino energy peak (600 MeV) has a flux uncertainty of $\sim$ 5%, and at higher energies around the peak region ($\sim$ 1 GeV), the proton beam profile becomes a major source of uncertainty and the uncertainty approaches $\sim$ 8%. The other major set uncertainties, $\bar{\nu_\mu}$ in antineutrino mode, shows similar uncertainties in the peak region.

There are a total of 100 systematics used in the current flux model, which are implemented as a covariance matrix. The parameters are binned according to neutrino energy, flavour (ν_μ , $\bar{\nu}_\mu$, ν_e , $\bar{\nu}_e$) and horn current mode. The same binnings are use for both the near and far detector analyses.

The bin edges for the neutrino energy are defined as follows, in GeV:

- FHC ν_μ: 0, 0.4, 0.5, 0.6, 0.7, 1, 1.5 2.5, 3.5, 5, 7, 30
- FHC $\bar{\nu_\mu}$: 0, 0.7, 1, 1.5, 2.5, 30
- FHC ν_e: 0, 0.5, 0.7, 0.8, 1.5, 2.5, 4, 30
- FHC $\bar{\nu_e}$: 0, 2.5, 30
- RHC $\bar{\nu_\mu}$: 0, 0.4, 0.5, 0.6, 0.7, 1, 1.5 2.5, 3.5, 5, 7, 30
- RHC ν_μ: 0, 0.7, 1, 1.5, 2.5, 30
- RHC $\bar{\nu_e}$: 0, 0.5, 0.7, 0.8, 1.5, 2.5, 4, 30
- RHC ν_e: 0, 2.5, 30

This accounts for 50 parameter bins; both ND280 and Super-K have independent flux parameters so a full oscillation fit has 100 flux parameters. In the case of a single detector fit (as presented in this thesis), the bin values are simply duplicated across for the other detector bins.

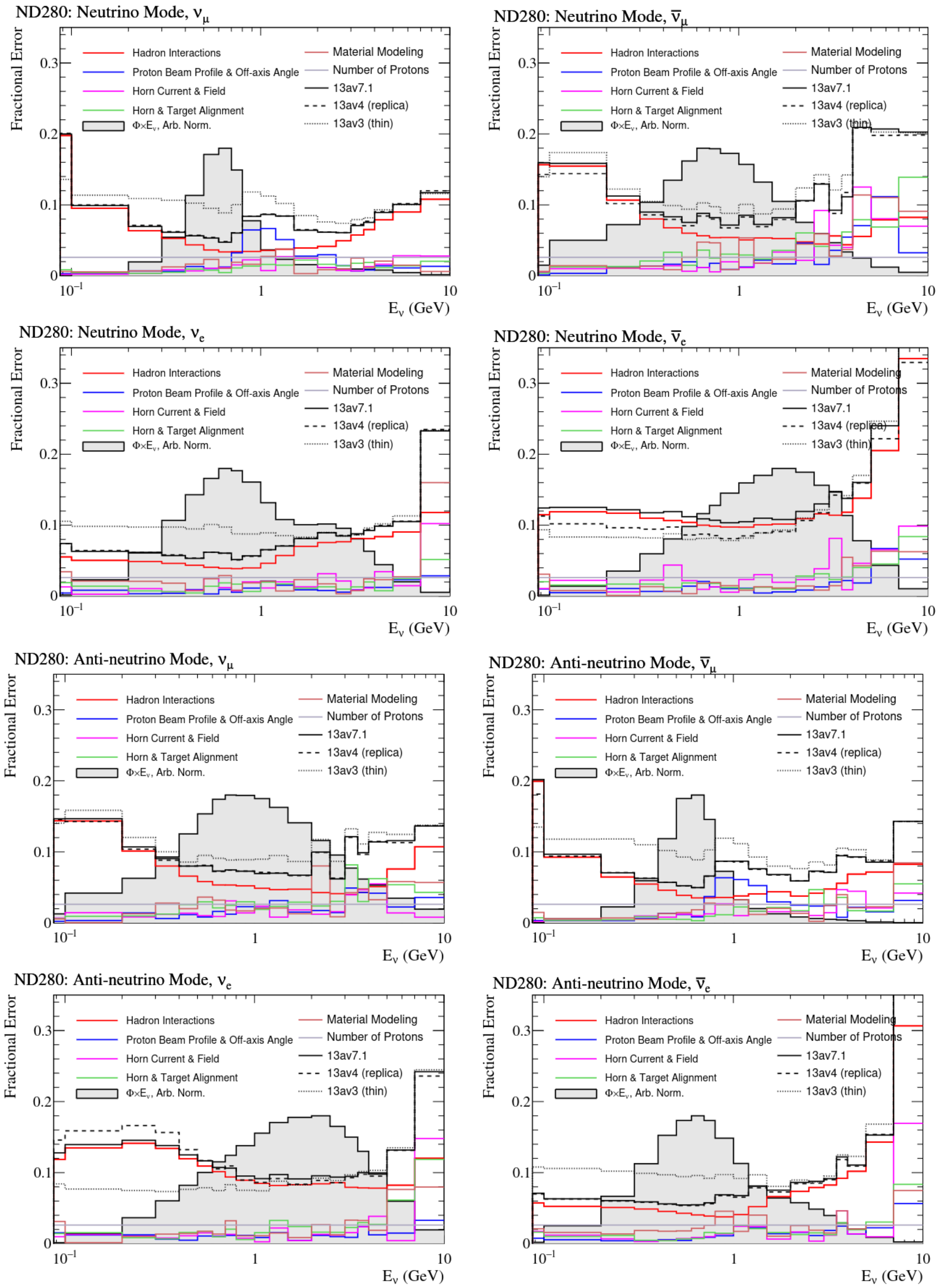

Figure 5.1: Flux uncertainties in ND280 as a function of true neutrino energy. Coloured lines show the contributions to the total, which is in black. The dotted and dashed lines show the total uncertainty based on solely the thin target data and replica target data, respectively. The grey histogram shows the normalised T2K flux energy distribution, in arbitrary units. "13avX" refers to the version of the flux model used; v3 only used thin target data and v4 was the first to use replica target data. Plots adapted from [85].

5.2 Neutrino Interaction Model

The oscillation analysis is heavily dependent on the neutrino interaction model as the oscillation parameters are measured by comparing neutrino interaction rates in the ND280 and Super-K detectors. Interactions are simulated using the NEUT neutrino-nucleus interaction event generator, which uses a variety of theoretical models for the different neutrino interaction channels [53][86][87]. Each of these channels also has associated uncertainty parameters as there are plausible variations in the NEUT model based on theory- and data-driven uncertainties. Additional models not included in this parametrisation are analysed in fake data studies, detailed in section 9. The NEUT interaction channels and their associated systematics are described in the following sections.

5.2.1 Charged-Current Quasi-Elastic (CCQE)

CCQE interactions, also called 1p1h (one-particle one-hole), are interactions where a neutrino interacts with a single nucleon via a charged current ($W^{\pm}$) to produce a charged lepton and eject a single nucleon. An example of this interaction is shown in figure 5.2.

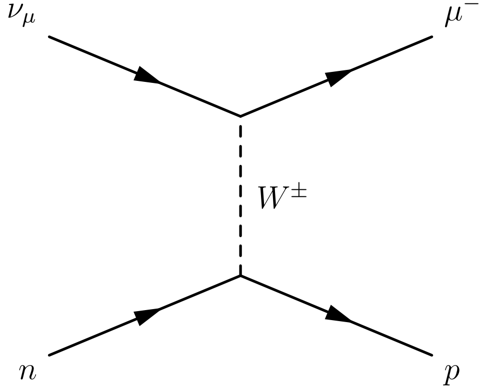

Figure 5.2: Pseudo-Feynman diagram of a charged-current quasi-elastic (CCQE) neutrino interaction.

In NEUT, these are modelled according to a spectral function (SF) model, a two-dimensional distribution describing the probability of finding a nucleon with momentum $|\mathbf{p}|$ and removal energy E_{rmv} (the energy needed to eject the nucleon from the nuclear potential). This distribution is shown in figure 5.3 [53]. CCQE is the dominant interaction at the T2k 2.5° off-axis peak of 600 MeV (see figures 2.3 and 3.7) and is the most important interaction for the oscillation analysis, hence it has a fairly large number of systematic parameters.

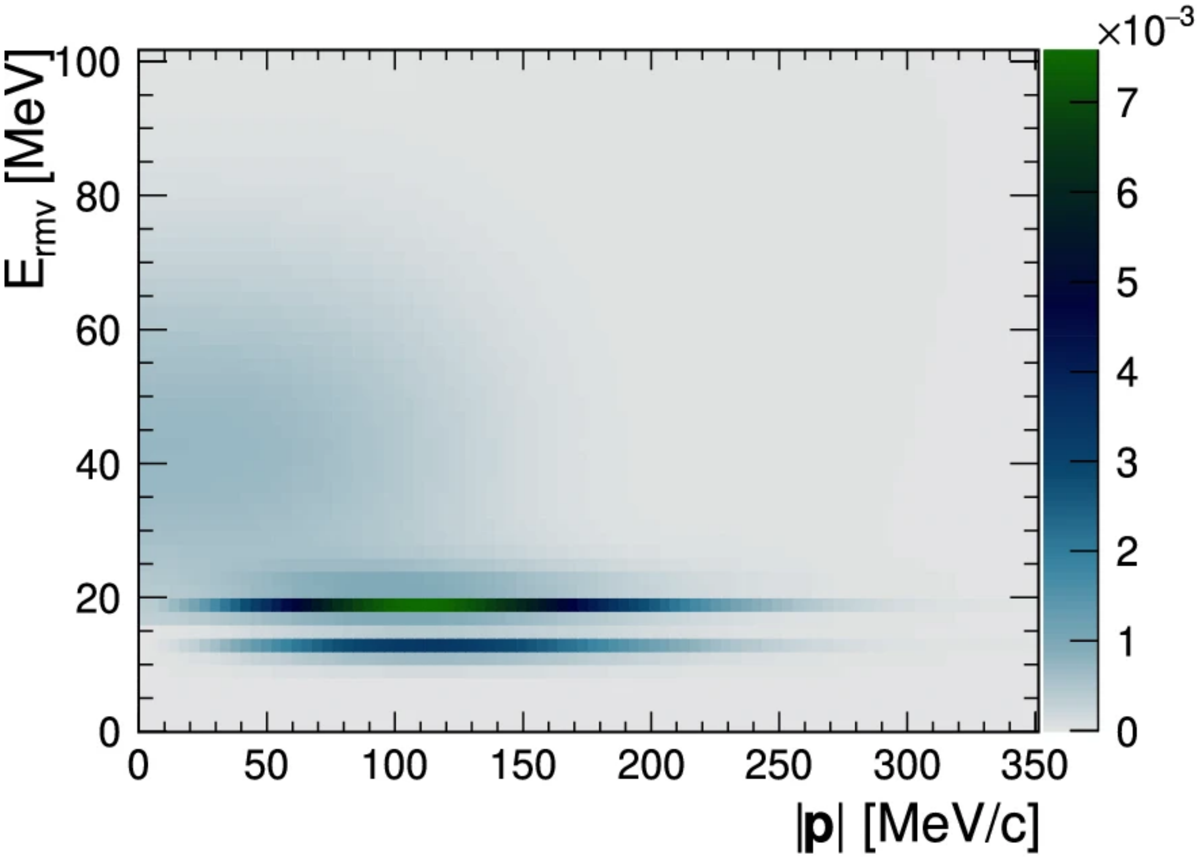

Figure 5.3: Two-dimensional probability density distribution for the oxygen spectral function for the CCQE model in NEUT [53]. In the darker areas, there is a higher probability of finding an initial-state nucleon with a particular removal energy (E_{rmv}) and momentum $|\mathbf{p}|$. The two dark lines show the sharp p-shells at $E_{rmv} \sim 12$ MeV and $E_{rmv} \sim 18$ MeV, while the more diffuse region above shows the larger s-shell.

Parameter	Momentum Range (GeV^2)	Prior
Q2_norm_5	0.25 - 0.5	1 ± 0.11
Q2_norm_6	0.5 - 1	1 ± 0.18
Q2_norm_7	> 1	1 ± 0.4

Table 5.1: Q^2 normalisation parameters in the ND280 MC simulation, showing the momentum range each parameter affects and their prior values.

Parameter	Nuclei	Prior
SF_SRC_Norm_OGraph	Oxygen	1 ± 2
SF_SRC_Norm_CGraph	Carbon	1 ± 2

Table 5.2: Parameters and priors for the short range correlations in the spectral function nuclear model used in the ND280 MC simulation.

The CCQE systematics can be split into the following categories:

- **Axial Mass M_{QE}^A:** The nucleon axial mass parameter M_{QE}^A corresponds to the axial form factor for quasi-elastic neutrino-nucleon interactions. It has a nominal value of 1.03 ± 0.06 GeV, which is determined via bubble chamber [88] and neutrino-deuterium scattering data [89].

- **Q^2 Normalisation Parameters:** The Q^2 normalisation parameters are used to reweight the event rates in certain ranges of the true momentum transfer Q^2 in neutrino-nuclear interactions. There are three parameters, with the momentum ranges and prior values shown in table 5.1.

  These parameters suppress model events rates at low momenta, as experimental data from MINERνA suggest a substantially lower event rate compared to the model [88]. Lower values of Q^2 are covered by Pauli blocking parameters (see below).

- **Short Range Correlation and Mean Field Parameters**

  The short range correlation (SRC) and mean field (MF) parameters are used to adjust the spectral function model used for modelling nuceli. SRC accounts for interactions between two nucleons at very short ranges, while MF describes the nuclear shell structure and the P and S shells of carbon and oxygen nuclei (oxygen P shells are further split into $P_{1/2}$ and $P_{3/2}$). The SRC parameters are shown in table 5.2.

  The MF parameters can be broken down further into normalisation parameters,

Parameter	Type	Nuclei	Prior
SF_PShell_MeanF_Norm_CGraph	Norm	Carbon	0 ± 0.2
SF_SShell_MeanF_Norm_CGraph	Norm	Carbon	0 ± 0.45
SF_PShell_MeanF_PMissShape_CGraph	Shape	Carbon	0 ± 1
SF_SShell_MeanF_PMissShape_CGraph	Shape	Carbon	0 ± 1
SF_P1_2Shell_MeanF_Norm_OGraph	Norm	Oxygen	0 ± 0.45
SF_P3_2Shell_MeanF_Norm_OGraph	Norm	Oxygen	0 ± 0.2
SF_SShell_MeanF_Norm_OGraph	Norm	Oxygen	0 ± 0.75
SF_P1_2Shell_MeanF_PMissShape_OGraph	Shape	Oxygen	0 ± 1
SF_P3_2Shell_MeanF_PMissShape_OGraph	Shape	Oxygen	0 ± 1
SF_SShell_MeanF_PMissShape_OGraph	Shape	Oxygen	0 ± 1

Table 5.3: Mean field parameters and priors for the spectral function nuclear model in the ND280 MC simulation.

which reweight the number of events, and shape parameters, which alter the kinematics of each event. These are shown in table 5.3.

- **Pauli Blocking**

  In the ground state of a nucleus, the Pauli exclusion principle requires that the nucleons occupy different quantum states. Thus, some have a higher energy state than others; the highest nucleon energy is known as the Fermi energy. A neutrino interacting with a nucleon must have enough energy to excite it beyond the Fermi energy, as all the lower energy states are occupied. Neutrino interactions are therefore suppressed at lower energies. All neutrino-nuclear interactions with momentum transfer below 209 MeV are weighted to zero in the default SF model; this is applied for both oxygen and carbon in NEUT. However, as this is somewhat of a “crude estimate” [90], additional parameters are used to shape the momentum distribution. In the MC, parameters are applied to oxygen and carbon nuclei for neutrino and anti-neutrino interactions. Two additional parameters are used for resonant (pion-producing) interactions with each nuclei. Table 5.4 shows the Pauli blocking parameters and their priors.

- **Binding Energy**

  The binding energy (E_b) parameters describe the binding energy in oxygen and carbon nuclei in CCQE interactions. They affect the ν_μ momentum distribution by directly altering the momentum, contrasting with most other parameters which simply reweight the number of events in a given momentum bin. This means the E_b parameters can cause events to migrate between kinematic bins. The binding

Parameter	Interaction	Nuclei	Prior
SF_PBTwkDial_NuclMom_C12_nuGraph	ν_μ	Carbon	0 ± 1
SF_PBTwkDial_NuclMom_O16_nuGraph	ν_μ	Oxygen	0 ± 1
SF_PBTwkDial_NuclMom_C12_nubarGraph	$\bar{\nu}_\mu$	Carbon	0 ± 1
SF_PBTwkDial_NuclMom_O16_nubarGraph	$\bar{\nu}_\mu$	Oxygen	0 ± 1
SF_PBTwkDial_NuclMom_piProd_C12Graph	π-prod.	Carbon	0 ± 1
SF_PBTwkDial_NuclMom_piProd_O16Graph	π-prod.	Oxygen	0 ± 1

Table 5.4: Pauli blocking parameters and priors in the ND280 MC simulation.

Parameter	Interaction	Nuclei	Prior
EB_bin_C_nu	ν_μ	Carbon	2 ± 6
EB_bin_O_nu	ν_μ	Oxygen	4 ± 6
EB_bin_C_nubar	$\bar{\nu}_\mu$	Carbon	0 ± 6
EB_bin_O_nubar	$\bar{\nu}_\mu$	Oxygen	0 ± 6

Table 5.5: Binding energy parameters and priors in the ND280 MC simulation.

energy parameters are shown in table 5.5.

5.2.2 Two-Particle Two-Hole (2p2h)

In a 2p2h interaction, the neutrino interacts with a bound pair of nucleons and ejects both of them from the nucleus. A pseudo-Feynman diagram of this process is shown in figure 5.4. Despite 1p1h being the dominant interaction at T2K energies, 2p2h interactions produce final states that are indistinguishable in the detector from 1p1h but have different lepton kinematics [91]. NEUT uses the Nieves *et al.* model [92], in which the 2p2h cross section peaks in two regions of momentum and energy transfer: quasi-elastic-like (energy transfer $\lesssim$ 0.3 GeV) and Delta-like (energy transfer $\gtrsim$ 0.3 GeV).

The 2p2h model has normalisation parameters for ν and $\bar{\nu}$ interactions, as well as a scaling correction for oxygen nuclei interactions as the nominal model is for carbon nuclei. All have prior values of 1 ± 1. Respectively, these are:

- 2p2h_norm_nu
- 2p2h_norm_nubar
- 2p2h_norm_CtoO

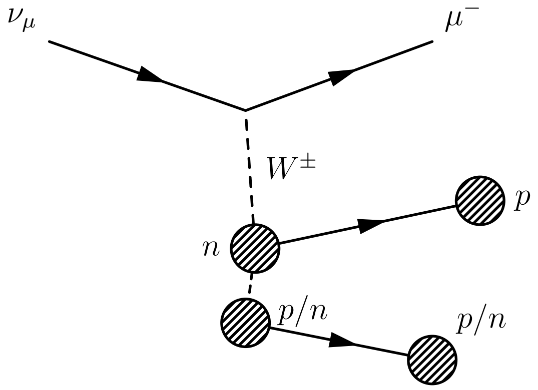

Figure 5.4: Pseudo-Feynman diagram of a two-particle-two-hole (2p2h) neutrino interaction.

Parameter	Interaction	Nuclei	Prior
MECTwkDial_PDDWeight_C12_NPGraph	Neutron-Proton	Carbon	0 ± 3
MECTwkDial_PDDWeight_C12_NNGraph	Neutron-Neutron	Carbon	0 ± 3
MECTwkDial_PDDWeight_O16_NPGraph	Neutron-Proton	Oxygen	0 ± 3
MECTwkDial_PDDWeight_O16_NNGraph	Neutron-Neutron	Oxygen	0 ± 3
MECTwkDial_PNNN_ShapeGraph	NN/NP ratio	-	0 ± 0.33

Table 5.6: Shape parameters and priors for 2p2h interactions.

Additionally, there are shape parameters for neutron-neutron (NN) and neutron-proton (NP) pairs for carbon and oxygen nuclei, as well as a parameter for the ratio of NN to NP interactions. These are shown in table 5.6.

There are also four parameters for the 2p2h energy dependence at high and low energies, for ν and $\bar{\nu}$. These are fixed at the near detector and are not affected by the near detector fit.

5.2.3 Single-Pion Production (SPP)

SPP interactions are neutrino-nucleus interactions that produce a single final-state pion. These are mostly produced by neutrinos exciting nucleons into a baryon resonance that decays into a pion and a nucleon. Figure 5.5 shows some examples of this interaction. NEUT uses an adjusted Rein-Sehgal (R-S) model to describe SPP interactions [93]. Whilst $\Delta(1232)$ resonances are the most common resonance, there are a total of 18 baryonic resonances in the model. Coherent scattering off nuclei also contribute to the SPP cross section, particularly at low momentum transfer; in NEUT, this is modelled with the Berger-Sehgal model [94].

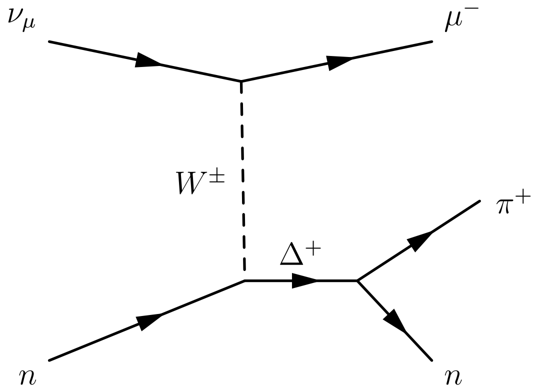

Figure 5.5: Pseudo-Feynman diagram for a single pion production neutrino interaction. This is one of many possible interactions between a neutrino and nucleon which produce a single final-state pion.

Parameter	Description	Prior
CA5RESGraph	Axial form factor at $Q^2 = 0$	1.06 ± 0.1
MaRESGraph	Axial mass	0.91 ± 0.1
BgSclRESGraph	Non-resonant contributions to SPP	1.21 ± 0.27
SPP_Pi0Norm_numu	Normalisation for neutrino events	1 ± 0.3
SPP_Pi0Norm_numubar	Normalisation for antineutrino events	1 ± 0.3
RES_Eb_C_numuGraph	Binding energy in CCRES ν_μ-carbon interactions	25 ± 25
RES_Eb_O_numuGraph	Binding energy in CCRES ν_μ-oxygen interactions	25 ± 25
RES_Eb_C_numubarGraph	Binding energy in CCRES $\bar{\nu}_\mu$-carbon interactions	25 ± 25
RES_Eb_O_numubarGraph	Binding energy in CCRES $\bar{\nu}_\mu$-oxygen interactions	25 ± 25
MDLSPiEjGraph	R-S Δ decay parameter	1 (Flat)

Table 5.7: Parameters and priors for single pion production interactions.

The parameters of the R-S model used in the simulations are shown in table 5.7. The model uses three methods to calculate the kinematics of a resonance: the first method isotropically ejects the pion and nucleon back-to-back in the resonant rest frame, with no preferred direction of either particle; the second considers an intermediate $\Delta(1232)$ resonance, which decays into the final state pion and nucleon [95]. The "MDLSPiEjGraph" (MoDeL Single PIon EJection) parameter is used for the fit to determine the ratio of models used: 0 is purely isotropic; 1 is purely $\Delta(1232)$. There is also the low-momentum antineutrino non-resonant contributions parameter
`BgSclLMCPiBarRES`. This is a flat parameter and is fixed (not altered) in the near detector fit.

Parameter	Description	Prior
MultiPi_Multiplicity_TotXSec	Norm. for multiπ cross section	0 ± 1
MultiPi_Multiplicity_ShapeGrap	Shape for multiπ interactions	0 ± 1
MultiPi_BY_VectorGraph	Normalisation for Bodek-Yang corrections	0 ± 1
MultiPi_BY_AxialGraph		0 ± 1
DIS_BY_corr_on_offGraph		0 ± 1
DIS_BY_corr_on_off_NCGraph	Shape for Bodek-Yang corrections	0 ± 1
MultiPi_BY_corr_on_off_NC		0 ± 1

Table 5.8: Parameters and priors for deep inelastic scattering interactions in the ND280 MC simulation.

5.2.4 Deep Inelastic Scattering (DIS)

DIS interactions occur when a neutrino interacts with a nucleon with sufficient energy to break quarks from the bound state. DIS only becomes dominant at high (≥ 8 GeV) energies (see figure 2.3), but is still present above 1.3 GeV. They are described using the GRV98 Parton Distribution Functions [96], which are extended using Bodek-Yang corrections [97], and applied for interactions with hadronic invariant mass $1.3 < W < 2.0$ GeV. Beyond 2.0 GeV, PYTHIA 5.7 is used [98]. To avoid double-counting with non-resonant SPP, only DIS interactions that produce more than one final-state pion are considered.

The parameters of the DIS model are shown in table 5.8

5.2.5 Final-State Interactions (FSI)

Final-state interactions are interactions between a hadron produced in the initial neutrino interaction, and other hadrons in the nucleus. In NEUT, pion FSI is described with the semi-classical intranuclear cascade model by Salcedo and Oset [99], whilst nucleon FSI uses an analogous cascade model [100]. The parameters associated with FSI are described in table 5.9.

5.2.6 FSI Strength and RPA Strength

The Final State Interaction (FSI) Strength and Random Phase Approximation (RPA) Strength parameters are relatively new, having been introduced for the 2024 oscillation analysis [95]. These are designed to improve the nuclear model at low Q^2 (< 0.4 GeV). The FSI strength parameters replace the former optical potential parameters, and RPA strength replaces an *ad hoc* smearing applied based on fake data studies. The new pa-

Parameter	Description	Prior
PionFSI_QELowMomProb	π QE scattering probability at low momentum	1.069 ± 0.313
PionFSI_QEHighMomProb	π QE scattering probability at high momentum	1.824 ± 0.859
PionFSI_InelProb	π inelastic scattering probability	1 ± 1.1
PionFSI_AbsProb	π absorption probability	1.4 ± 0.432
PionFSI_CExLowMomProb	π charge exchange probability at low momentum	0.697 ± 0.697
PionFSI_CExHighMomProb	π charge exchange probability at high momentum	0.228 ± 1.8
NucleonFSI_Total	FSI scattering probability	1 ± 0.3
NucleonFSI_Single	Single π production probability	1 ± 0.3

Table 5.9: Parameters and priors for final-state interactions in the ND280 MC simulation.

Parameter	Nucleus	Neutrino	Energy (GeV)	Prior
HFPW_toHFTwkDial_C_nu_0Graph	Carbon	ν	$0.05 \leq q < 0.10$	1 ± 1
HFPW_toHFTwkDial_C_nu_1Graph	Carbon	ν	$0.10 \leq q < 0.20$	1 ± 1
HFPW_toHFTwkDial_C_nu_2Graph	Carbon	ν	$0.20 \leq q < 10$	1 ± 1
HFPW_toHFTwkDial_C_anu_0Graph	Carbon	$\bar{\nu}$	$0.05 \leq q < 0.10$	1 ± 1
HFPW_toHFTwkDial_C_anu_1Graph	Carbon	$\bar{\nu}$	$0.10 \leq q < 0.20$	1 ± 1
HFPW_toHFTwkDial_C_anu_2Graph	Carbon	$\bar{\nu}$	$0.20 \leq q < 10$	1 ± 1
HFPW_toHFTwkDial_O_nu_0Graph	Oxygen	ν	$0.05 \leq q < 0.10$	1 ± 1
HFPW_toHFTwkDial_O_nu_1Graph	Oxygen	ν	$0.10 \leq q < 0.20$	1 ± 1
HFPW_toHFTwkDial_O_nu_2Graph	Oxygen	ν	$0.20 \leq q < 10$	1 ± 1
HFPW_toHFTwkDial_O_anu_0Graph	Oxygen	$\bar{\nu}$	$0.05 \leq q < 0.10$	1 ± 1
HFPW_toHFTwkDial_O_anu_1Graph	Oxygen	$\bar{\nu}$	$0.10 \leq q < 0.20$	1 ± 1
HFPW_toHFTwkDial_O_anu_2Graph	Oxygen	$\bar{\nu}$	$0.20 \leq q < 10$	1 ± 1

Table 5.10: FSI Strength parameters used in the ND280 MC simulation.

rameters are physically motivated and provided additional degrees of freedom. These parameters are applied as weights to the nominal SF model.

The FSI strength parameters are calculated as the ratios between the Hartree Fock Plane Wave (HFPW) and Plane Wave (PW) models. They are applied for ν and $\bar{\nu}$ interactions across carbon and oxygen nuclei, and divided into three energy bins for a total of 12 parameters. These are described in table 5.10.

The RPA strength parameters are calculated as the ratio between the Hartree Fock Plane Wave (HFPW) and Continuum Random Phase Approximation Plane Wave (CRPAPW) models. *Continuum* RPA (CRPA) is used over the nominal RPA approach as it significantly reduces the computation complexity by turning many discrete interaction calcu-

Parameter	Nucleus	Neutrino	Energy (GeV)	Prior
HFPW_toCRPAPWTwkDial_C_nu_0Graph	Carbon	ν	$0.05 \leq q < 0.10$	1 ± 1
HFPW_toCRPAPWTwkDial_C_nu_1Graph	Carbon	ν	$0.10 \leq q < 0.20$	1 ± 1
HFPW_toCRPAPWTwkDial_C_nu_2Graph	Carbon	ν	$0.20 \leq q < 10$	1 ± 1
HFPW_toCRPAPWTwkDial_C_anu_0Graph	Carbon	$\bar{\nu}$	$0.05 \leq q < 0.10$	1 ± 1
HFPW_toCRPAPWTwkDial_C_anu_1Graph	Carbon	$\bar{\nu}$	$0.10 \leq q < 0.20$	1 ± 1
HFPW_toCRPAPWTwkDial_C_anu_2Graph	Carbon	$\bar{\nu}$	$0.20 \leq q < 10$	1 ± 1
HFPW_toCRPAPWTwkDial_O_nu_0Graph	Oxygen	ν	$0.05 \leq q < 0.10$	1 ± 1
HFPW_toCRPAPWTwkDial_O_nu_1Graph	Oxygen	ν	$0.10 \leq q < 0.20$	1 ± 1
HFPW_toCRPAPWTwkDial_O_nu_2Graph	Oxygen	ν	$0.20 \leq q < 10$	1 ± 1
HFPW_toCRPAPWTwkDial_O_anu_0Graph	Oxygen	$\bar{\nu}$	$0.05 \leq q < 0.10$	1 ± 1
HFPW_toCRPAPWTwkDial_O_anu_1Graph	Oxygen	$\bar{\nu}$	$0.10 \leq q < 0.20$	1 ± 1
HFPW_toCRPAPWTwkDial_O_anu_2Graph	Oxygen	$\bar{\nu}$	$0.20 \leq q < 10$	1 ± 1

Table 5.11: RPA Strength parameters used in the ND280 MC simulation

Parameter	Description	Prior
nue_numu	cross section ratio for ν_e/ν_μ	1 ± 0.028
nuebar_numubar	cross section ratio for $\bar{\nu}_e/\bar{\nu}_\mu$	1 ± 0.028
CC_misc	Normalisation for misc. CC interactions	1 ± 1
NC_1gamma	Norm. for 1γ NC interactions	1 ± 1
NC_other_near	Norm. for other NC interactions at ND280	1 ± 0.3
NC_other_far	Norm. for other NC interactions at Super-K	1 ± 0.3
CC_Coh_C	CC coherent interactions with carbon	1 ± 0.3
CC_Coh_O	CC coherent interactions with oxygen	1 ± 0.3
CC_norm_nu	Norm. applied to all CC ν interactions	1 ± 0.02
CC_norm_nubar	Norm. applied to all CC $\bar{\nu}$ interactions	1 ± 0.01

Table 5.12: Miscellaneous parameters and their priors.

lations into a single continuum [95]. As with the FSI parameters, there are a total of 12 RPA parameters across nuclei, neutrino type and energy range. These are described in table 5.11.

5.2.7 Miscellaneous

The remaining parameters do not fit into any particular categories. They mainly consist of normalisation parameters that adjust parts of the overall interaction model. These parameters are shown in table 5.12.

5.3 Near Detector Model

Following the simulation of particle interactions within ND280, the particle propagation and detector response is modelled using GEANT4 [101]. The systematics of the near detector model are used to account for the differences between the simulated detector and the real detector, which include detection capabilities as well as the physical properties of the detector itself. Detector systematics are evaluated using dedicated control samples, where comparisons between MC and data are used to assign uncertainties to parameters [102].

The systematics can be grouped into three types: observable, efficiency-like and normalisation. An overview of these categories and the systematics is presented below, but a more in-depth description is available in [103] and [102]. All parameters are assumed to be Gaussian-like.

5.3.1 Observable

Observable systematics affect the properties of reconstructed particles, such as direction and momentum. These parameters are considered "variation-like", as the error is propagated by varying the value of the observable and determining the effect on the analysis samples.

- **B Field distortions**: Uncertainties in modelling the detector's magnetic field, which affects TPC track reconstruction. These parameters use a uniform probabilty density function, not Gaussian like the other parameters.
- **TPC Momentum Scale** and **Resolution**: Uncertainties in momentum reconstruction for particles within the TPCs.
- **TPC PID**: Uncertainties in particle identification within the TPCs.
- **FGD PID**: Uncertainties in particle identification within the FGDs.
- **Time-of-Flight**: Timing of particles passing from one subdetector to another (see section 6.2.2).

5.3.2 Efficiency-like

Efficiency-like systematics correspond to reconstruction and detection probability. These are applied as event-by-event weights, which are applied to events within a certain sample, hence they are less computationally intentive than observable systematics [102].

- **TPC Track Efficiency**: Ability for the TPC to accurately reconstruct a particle's track.
- **TPC Cluster Efficiency**: Ability to reconstruct objects with 19 or more adjacent TPC hits.
- **TPC Charge ID Efficiency**: Ability to determine particle charge, based on TPC track curvature.
- **TPC-FGD Matching Efficiency**: Efficiency in matching tracks for particles propagating between a TPC and FGD.
- **FGD Hybrid Tracking Efficiency**: Ability to reconstruct tracks in FGD in the presence of a long FGD-TPC track.
- **Michel Electron Efficiency**: Detection efficiency of Michel electrons, electrons created by the decay of a muon.

5.3.3 Normalisation

Normalisation systematics affect total event rate and total number of events of certain samples. For most of the systematics, this is to account for differences in simulation and data caused by interactions that are not fully modelled. These systematics are also applied as event-by-event weights.

- **OOFV Event Background**: Correction for background from events occurring outside of fiducial volume but within the detector volume.
- **Sand Event Background**: Correction for background from events occurring between proton beam target and detector.
- **Pile-up**: Correction for multiple neutrino events occurring within the same time window, where the tracks may be misattributed to a single event.
- **Pion secondary interactions**: Interactions where a pion interacts outside of the nucleus it was produced in.
- **FGD Mass**: From uncertainty in the mass of the FGDs.

5.4 Conclusion

The MC model used at T2K is critical for the oscillation analysis, and it is only through the choice of appropriate models and systematic parameters that the neutrino oscillation parameters can be determined via fitting the model to data. The cross section models in particular are continuously evaluated against the wider knowledge of particle interactions from other experiments. The spectral function used in the current CCQE model was implemented for the 2023 oscillation analysis [53], replacing the previous Fermi gas model that presented a large uncertainty in previous analyses [91]. Chapters 9 and 10 present an overview of other candidate models and an investigation into the ability of a new fitter (GUNDAM, see chapter 8) to fit them effectively.

Chapter 6

Data Samples and Selections

ND280 selections are used to distribute reconstructed neutrino interaction events into topological categories (samples) based on the nature of the interaction and its final-state particles. This chapter will mainly discuss the 4π solid-angle (referred to as "numuCC4piMultiPiPhotonProton") selection, which was initially developed by Yongheng Xu [104] but was not fully implemented into the T2K oscillation analysis until after the Production 7 upgrade to the ND280 reconstruction software (see chapter 7). This newer selection introduces angular samples for high-angle and backwards-going events, whereas previous selections (such as numuCCMultiPiPhotonProton) only included forwards-going events. The development of a 4π solid-angle selection allows for better comparison of ND280 data with Super-K, which already has full angle coverage of neutrino events. Each of these samples begins with the construction of the CC-Inclusive sample, which identifies good-quality charged-current events. The CC-Inclusive sample is a fairly typical sample to begin with at T2K, and has been in use for many years.

ND280 selections under development are implemented in the `HighLAND2` (High Level Analysis at the Near Detector version 2) software package [105], which is responsible for accessing variables and event data, and provides advanced plotting tools. `HighLAND2` is built on the `Psyche` (Propagation of SYstematics and CHaracterisation of Events) framework, where the event selection cuts are applied. Fully-developed selections are migrated to `Psyche` in a minimalist format for faster processing; selections under development are defined in `HighLAND2`, which is the case for the numuCC4piMultiPiPhotonProton selection discussed in this chapter. Figure 6.1 gives an overview of how analysis is performed with `HighLAND2` and `Psyche`.

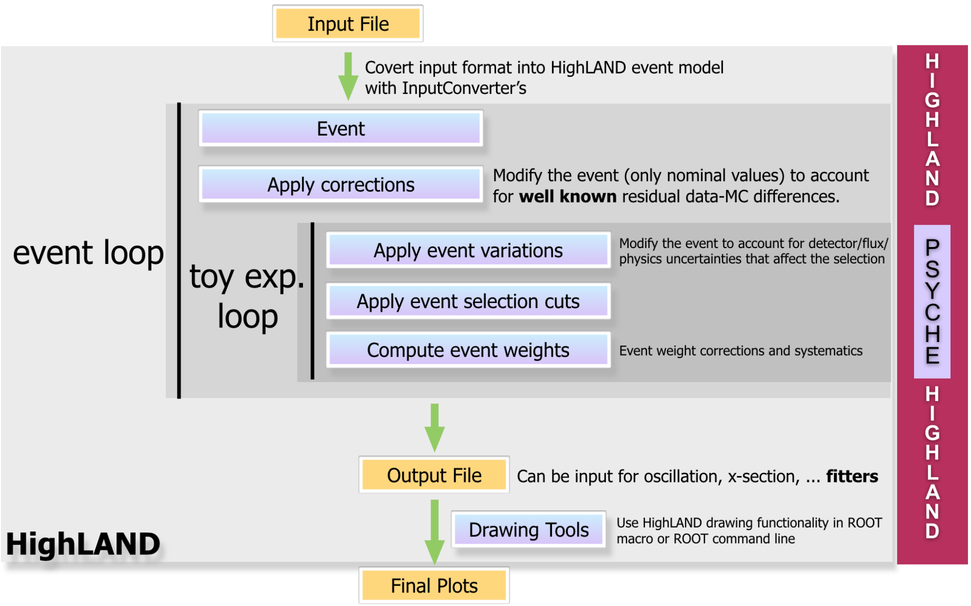

Figure 6.1: Overview of how analysis is performed using the `HighLAND2` and `Psyche` software packages, which forms the basis of high-level event analysis at ND280 [106]. `HighLAND2` accesses event data and applies data-MC corrections, while `Psyche` applies event selections and calculates event weights.

6.1 CC-Inclusive

The CC-inclusive sample is used to identify charged-current interactions that produce a final state muon. The highest-momentum negatively-charged track from an event is always assumed to be the muon. The event vertex is assumed to be at the beginning of the muon track. Cuts are applied across certain criteria to remove poor quality and mis-reconstructed events to produce a high-quality sample. This sample is not used in analysis directly, but is used as a basis for other selections, such as the 4π selection discussed later in this chapter. The cuts used in creating this sample are described below, in the order they are applied.

Event Quality Cut

The neutrino beam is generated by bunches of protons colliding with a graphite target, each bunch having a time window of 15 ns. Neutrino events in ND280 must fall within 4σ (± 60 ns) of the mean bunch time of the bunches or they are cut.

Total Multiplicity Cut

Events must contain at least one reconstructed track crossing through TPC2 or TPC3. This is to ensure that enough data can be collected for momentum measurement and particle identification.

Quality and Fiducial Volume Cut

The beginning of a particle track (the event vertex) must be within the fiducial volume (FV) of FGD1 or FGD2. The FV depends on both the FGD in question and whether the track is categorised as high-angle (HA) with respect to the z-axis (TPC hits ≤ 18) or low-angle (TPC hits > 18). For all cases, the x range is -874.51 mm to 874.51 mm and the y range is -819.51 mm to 929.51 mm. For FGD1, the z range in the low-angle case is 125.75 mm to 447.38 mm and in the high-angle case is 125.75 mm to 437.26 mm. For FGD2, the z range in the low-angle case is 1483.75 mm to 1807.38 mm and in the high-angle case is 1483.75 mm to 1797.26 mm. The z range is reduced in the high-angle case to remove the last FGD layer along the beamline, as these tracks have little to no TPC information [107].

Upstream Background Veto

Reconstruction errors can occur where a muon track is reconstructed as originating in the FGD FV, but actually begins further upstream. If the second-highest momentum track of an event starts more than 150 mm upstream of the muon candidate, the event is vetoed. For FGD2, the event is also vetoed if a secondary track starts within the FGD1 FV.

Broken Track Cut

Another mis-reconstruction can occur when a muon track originating in a FGD FV is split into two components: one fully contained in the FGD (called an isoFGD track), and a second that begins in the final layer of the FGD and passes into a TPC. The latter can be mis-reconstructed as the main muon candidate track. To remove these, muon candidate tracks beginning in the last two layers of an FGD where an isoFGD track is present are cut.

Muon PID Cut

Particle Identification (PID) is the process of identifying the types of particles associated with each track of an event. This is used to select charged-current ν_μ events by identifying the final state μ^-. For low-angle tracks, TPC PID can be applied by measuring the ionisation energy deposited by a particle traversing a TPC. The energy deposited as a function of distance (dE/dx, the rate of change of energy E across distance x) depends on the particle type, so the measurement can be compared against potential particle hypotheses: muon, electron, pion, and proton. Pull values are calculated from these comparisons, which are then used to construct likelihood variables. For a given hypothesised particle i, the pull is defined as:

$$P_i = \frac{dE/dx_{measured} - dE/dx_{expected,i}}{\sigma_{dE/dx}} \tag{6.1}$$

where P_i is the pull value, $dE/dx_{measured}$ is the energy loss rate measured in the TPC for the track, $dE/dx_{expected,i}$ is the expected energy loss rate for the hypothesised particle, and $\sigma_{dE/dx}$ is the uncertainty in the difference between the measured and expected dE/dx value. The pull value is used to define the likelihood $\mathcal{L}_i$:

$$\mathcal{L}_i = \frac{e^{-P_i^2}}{\sum\limits_j e^{-P_j^2}} \tag{6.2}$$

where the summation in the denominator occurs across all particle types considered in the hypothesis: muons, protons, electrons and pions. Additionally, a likelihood for identifying minimum ionising particles (MIPs) is also applied:

$$\mathcal{L}_{MIP} = \frac{\mathcal{L}_\mu + \mathcal{L}_\pi}{1 - \mathcal{L}_p} \tag{6.3}$$

MIPs are particles with dE/dx values close to the minimum required for ionisation in a medium. To select μ^- events for the ν_μ CC selections, the likelihood cuts are applied as:

$$\begin{aligned} &\mathcal{L}_\mu > 0.05 \\ &\mathcal{L}_{MIP} > 0.8 \text{ if } p_\mu < 500 \text{ MeV}/c \end{aligned} \tag{6.4}$$

6.2 The 4π Solid Angle Selection

After the initial set of quality cuts are complete, the remaining events are distributed into samples based on the topology of the event interactions and the direction of the muon track in the detector.

The numuCC4piMultiPiPhotonProton (4π) selection is an evolution of the earlier numuCCMultiPiPhotonProton selection, adding additional samples for high-angle and backwards-going events; previously, only forward-going events were considered. “4π” refers to the 4π radian solid angle the selection will select events from, unlike the numuCCMultiPiPhotonProton sample where “MultiPi” refers to multiple pions. The far detector, Super-K, was already capable of selecting events across the full 4π solid angle, thus introducing a similar capability to ND280 will allow for better comparison of data from the two detectors.

The 4π selection has 10 samples:

- **CC-Photon:** Event contains one or more reconstructed photons or neutral pions.
- **CC1π:** Event contains zero reconstructed photons and a single positively charged pion. The muon produces 19 or more TPC hits and travels in a forward direction.
- **CC1πHA:** Event contains zero reconstructed photons and a single positively charged pion. The muon produces 18 or fewer TPC hits and travels in a forward direction.
- **CC-Other** Event contains zero reconstructed photons or neutral pions, more than one positive pion, or more than zero negative pions.
- **CC0π0γ0pFwd:** Event contains zero reconstructed photons or pions, and zero reconstructed protons. The muon produces 19 or more TPC hits, and travels in a forward direction.
- **CC0π0γNpFwd:** Event contains zero reconstructed photons or pions, and one or more reconstructed protons. The muon produces 19 or more TPC hits, and travels in a forward direction.
- **CC0π0γ0pHA:** Event contains zero reconstructed photons or pions, and zero reconstructed protons. The muon produces 18 or fewer TPC hits, but may travel in a forward or backward direction.
- **CC0π0γNpHA:** Event contains zero reconstructed photons or pions, and one or more reconstructed protons. The muon produces 18 or fewer TPC hits, but may travel in a forward or backward direction.
- **CC0π0γ0pBwd:** Event contains zero reconstructed photons or pions, and zero reconstructed protons. The muon produces 19 or more TPC hits, and travels in a backward direction.
- **CC0π0γNpBwd:** Event contains zero reconstructed photons or pions, and one or more reconstructed protons. The muon produces 19 or more TPC hits, and travels in a backward direction.

Of these samples, the previous numuCCMultiPiPhotonProton selection had only CC-Photon, CC1π, CC-Other, CC0π0γ0pFwd and CC0π0γNpFwd; the total number of samples has doubled. Figure 6.2 displays the process of the selection, highlighting the final samples used in the selection output as well as the intermediate samples which were further broken down.

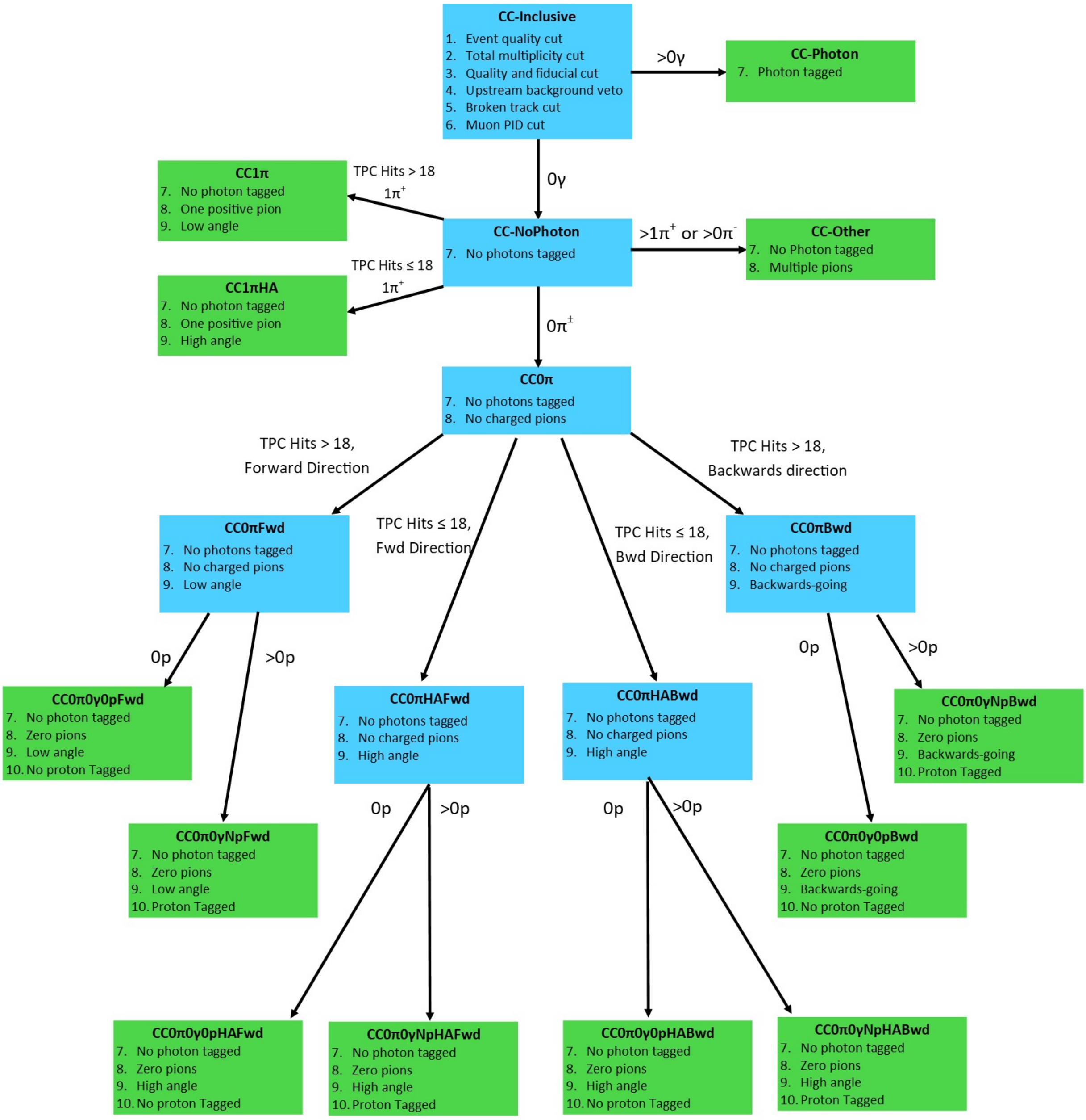

Figure 6.2: The selection process for the numuCC4piMultiPiPhotonProton selection. Green boxes show the samples used in the analysis, while blue boxes show intermediate samples that are further broken down. The cuts in the initial CC-inclusive selection are used to remove poor quality events. In the analysis, the CC0π0γ0pHAFwd and CC0π0γ0pHABwd samples are merged into a single CC0π0γ0pHA sample. This merge is also performed on the CC0π0γNpHA samples.

6.2.1 Particle Identification

The 4π selection separates events based on the particle content of the final state. Cuts are made on photon, pion, and proton content, each requiring a different approach and making use of different subdetectors. The Production 7 software upgrade has changed several aspects of the particle reconstruction and identification methods since the 4π selection was first developed. Additionally, certain parameters have been changed during the validation of this selection for the new software, discussed in detail in chapter 7. This section will discuss particle identification as it is performed Production 7.

Photons

Photons in ND280 mostly come from neutral pion decays, via $\pi^0 \to \gamma\gamma$. They can be identified in the TPCs by $\mathrm{e}^+\mathrm{e}^-$ pair production $\gamma \to e^+e^-$, or the ejection of an electron via Compton scattering. Photons are also detected in the ECal as follows: photon candidates are first identified by finding isolated ECal objects, i.e. reconstructed tracks or showers that are completely contained in the ECal and have no component from another subdetector. The following criteria is then applied for photon identification:

$$\begin{aligned} &\texttt{PIDMipEM} > -7 \\ &\texttt{MostUpStreamLayerHit} < 7 \\ &\texttt{NHits} > 4 \end{aligned} \tag{6.5}$$

PIDMipEM is a likelihood-based parameter constructed to determine whether an ECal object is MIP-like (e.g. muons) or electromagnetic-like (photons, e^-, e^+) [108]. MostUpStreamLayerHit ensures that only tracks which begin sufficiently close to the innermost ECal layer are accepted. This cut is applied to prevent event pile-up, which occurs when an interaction occurring outside the detector's FV produces hits at the same time as an FV interaction, thus making it appear that the FV event produced more hits than in reality. The NHits cut ensures that the reconstructed ECal object has a sufficient number of particle hits for it to be considered good quality.

These parameters values were determined during the validation of the 4π selection, which was required for its implementation into the Production 7 software upgrade. The upgrade introduces multiple changes to the simulation and reconstruction in ND280, especially for ECal reconstruction. The Production 7 changes, selection validation, and determination of these PID parameters are discussed in detail in chapter 7.

Pions

For the TPCs, the method for pion tagging is different for charged and neutral pions. Charged pions can be identified via the ionisation energy loss rate, using the likelihood calculation shown in equation 6.2. The likelihood used for identification is $\mathcal{L}_\pi > 0.3$ in the TPCs. For FGDs, the pull value (equation 6.1) must satisfy $-2 < P_\pi < 2.5$. Neutral pions do not deposit any ionisation energy, but can be identified by their decay products. The main decay for π^0 is $\pi^0 \to \gamma\gamma$ (98.82% [10]), and the photons can be identified from the pair production process $\gamma \to e^+e^-$.

Protons

Positively-charged tracks not tagged as muons or pions are considered proton candidates. For IsoFGD tracks the pull value (equation 6.1) must satisfy $P_p > -4$, and for TPC tracks the likelihood (equation 6.2) must satisfy $\mathcal{L}_p > 0.5$.

6.2.2 Time-of-Flight Discrimination

Discrimination between forwards- and backwards-going events is performed using time-of-flight (ToF) information. A single particle track typically passes through multiple ND280 subdetectors, leaving multiple hits with corresponding timestamps. The timestamps from each subdetector are combined to create a "time mark", which is used to determine the travel time between the subdetectors [104]. For each subdetector, a straight line is fitted to all the hits associated with a single track. The coordinates values for x, y and z of each hit are evaluated using the parametric function

$$\begin{aligned} x &= x_0 + t \times k_x \\ y &= y_0 + t \times k_y \\ z &= z_0 + t \times k_z \end{aligned} \tag{6.6}$$

where x_0, y_0, and z_0 are the coordinates at which the fitted line first intercepts with the detector; t is the timestamp of the hit; and k_x, k_y and k_z are the component gradients of the line. The equation is applied at the coordinates of the first hit in line to obtain the hit's timestamp, T_1, and again at the final hit to obtain the timestamp T_2. The time mark T_{sub} for the subdetector is defined as:

$$T_{sub} = \frac{T_1 + T_2}{2} \tag{6.7}$$

Topology name	Start	End	Non-FGD Hits	TPC Hits
Fgd1Fwd_ToF_DsECal_track	FGD1	DsECal	> 1	> 18
Fgd1Fwd_ToF_DsECal_shower	FGD1	DsECal	1	> 18
Fgd1Bwd_ToF_P0D_track	P0D	FGD1	> 1	> 18
Fgd1Bwd_ToF_P0D_shower	P0D	FGD1	1	> 18
Fgd1Bwd_ToF_ECal_track	BrECal	FGD1	> 1	> 18
Fgd1Bwd_ToF_ECal_shower	BrECal	FGD1	> 1	> 18
Fgd1HAFwd_ToF_ECal_track	FGD1	BrECal	> 1	≤ 18
Fgd1HAFwd_ToF_ECal_shower	FGD1	BrECal	1	≤ 18
Fgd1HABwd_ToF_ECal_track	BrECal	FGD1	> 1	≤ 18
Fgd1HABwd_ToF_ECal_shower	BrECal	FGD1	1	≤ 18
Fgd2Fwd_ToF_ECal_track	FGD2	BrECal	> 1	> 18
Fgd2Fwd_ToF_ECal_shower	FGD2	BrECal	1	> 18
Fgd2Fwd_ToF_DSECal_track	FGD2	DsECal	> 1	> 18
Fgd2Fwd_ToF_DSECal_shower	FGD2	DsECal	1	> 18
Fgd2Bwd_ToF_ECal_track	BrECal	FGD2	> 1	> 18
Fgd2Bwd_ToF_ECal_shower	BrECal	FGD2	1	> 18
Fgd2HAFwd_ToF_ECal_track	FGD2	BrECal	> 1	≤ 18
Fgd2HAFwd_ToF_ECal_shower	FGD2	BrECal	1	≤ 18
Fgd2HABwd_ToF_ECal_track	BrECal	FGD2	> 1	≤ 18
Fgd2HABwd_ToF_ECal_shower	BrECal	FGD2	1	≤ 18
Fgd1Fwd_ToF_FGD2	FGD1	FGD2	N/A	> 18
Fgd2Bwd_ToF_FGD1	FGD2	FGD1	N/A	> 18

Table 6.1: List of all time-of-flight topologies used in the ND280 analysis. The "start" and "end" columns describe which subdetector a track began and ended in. Non-FGD Hits refers to the number of hits associated with a track that occurred outside of an FGD. The number of TPC hits corresponds to whether the topology is considered to be high-angle or not.

The ToF between two subdetectors is the difference in the time mark between them for the track. For instance, between TPC1 and FGD1, the ToF would be

$$\mathrm{ToF}_{TPC1-FGD1} = T_{TPC1} - T_{FGD1} \tag{6.8}$$

From the ToF difference, the direction of the track can be determined by the position of the subdetectors within ND280 and the sign of the time difference. There are a total of 24 track topologies, shown in table 6.1.

The distribution of the ToF for each event in a topology is considered to be double-Gaussian like; the error the ToF measurement is assumed to follow a Gaussian distribution, while the double peaks are the combination of right- and wrong-direction tracks in a sample due to imperfections in the reconstruction and selection process. This is discussed further in section 7.2.

6.3 Conclusion

Selections are used at T2K to identify and remove poor-quality reconstructed events and to categorise events into samples based on interaction topology. This chapter discussed the newly-developed numuCC4piMultiPiPhotonProton selection, which introduces new samples for backwards-going and high-angle events into ND280. This allows for a much more straightforward comparison with neutrino data from Super-K, which already has full 4π solid-angle acceptance.

For this selection to be fully implemented into the main T2K oscillation analysis, it was necessary to validate it for the Production 7 software upgrade, which significantly affects the ND280 reconstruction algorithm. The validation and results are discussed in chapter 7, which constitutes the bulk of the work on the selection by the author.

Chapter 7

P7 Validation

Production 7 (P7) was a significant upgrade for the ND280 reconstruction and simulation software implemented in November 2023, approximately 9 years after the prior Production 6 (P6). P7 includes updates to external software packages (e.g. GEANT4, ROOT), a new TPC reconstruction algorithm (TREx [109]) and significant changes to ECal hit detection and clustering algorithms [110].

The numuCC4piMultiPiPhotonProton (4π) selection described in chapter 6 required validation before it could be used in analyses in P7, as it had been developed in P6. Particularly, the changes to the ECal reconstruction required changes to be made to the selection particle identification methods that relied on ECal PID variables.

The selection validation is discussed in section 7.1. This chapter also discusses the validation of timeslip corrections that are applied to data from Run 8 (section 7.2), and of systematic parameters for the TPC-ECal track matching (section 7.3).

7.1 Selection Validation

This section describes the validation of the numuCC4piMultiPiPhotonProton (also called “4π”) selection, which is currently the main selection used in the T2K oscillation analysis. The validation work was carried out initially with the numuCCMultiPiPhotonProton selection, but moved to the 4π selection as the latter concluded development. As the 4π selection is an evolution of numuCCMultiPiPhotonProton, and has identical CC-inclusive cuts and particle identification selections, the work could be directly carried over with minimal changes. As the numuCCMultiPiPhotonProton selection has since been depreciated, this section will discuss the validation exclusively in terms of the 4π selection.

The process of validation is to ensure the selections can maintain effectiveness with the new reconstruction algorithms. This is done by analysing the efficiency and purity of the samples of the selections. Efficiency and purity are defined as:

$$\text{Efficiency} = \frac{\text{No. of true events correctly sorted into a given sample}}{\text{Total No. of true events that should be in the sample}} \tag{7.1}$$

$$\text{Purity} = \frac{\text{No. of correctly identified events in selected sample}}{\text{Total No. of events in selected sample}} \tag{7.2}$$

The 4π selection merges its 10 samples into five larger samples for efficiency and purity calculations:

- CC0pi0p: Charged-current events with zero pions, zero protons, zero photons.
- CC0piNp: Charged-current events with zero pions, one or more protons, zero photons.
- CC1pi: Charged-current events with one pion, zero protons, zero photons.
- CCOther: Charged-current events with multiple pions, zero photons.
- CCPhoton: Charged-current events with one or more photons.

This allows for direct comparison with P6 results even with the 4π selection as the new angular samples are not applied. High sample purity is somewhat more desirable for the oscillation analysis than high efficiency as the proportion of correct events in a sample is more analytically useful than a greater number of events overall. Naturally, however, high values for both is ideal.

These validations focus on the selection of photons using ECal variables, as the ECal reconstruction was one of the major changes between P6 and P7. The correct selection of photons is important because it improves the purity of the other samples.

7.1.1 Inputs

Table 7.1 shows the lists of all runs used in the analyses presented in this thesis, along with the POT values for MC and data.

Horn Current	Run	MC POT ($\times 10^{20}$)	Data POT ($\times 10^{20}$)
FHC (ν_μ -mode)	2 Air	16.80	0.36
	2 Water	12.04	0.43
	3 Air	30.78	1.59
	4 Air	36.12	1.79
	4 Water	33.30	2.44
RHC ($\bar{\nu}_\mu$ -mode)	5 Water	22.11	0.43
	6 Air	33.03	3.41
	7 Water	33.30	2.44
FHC (ν_μ -mode)	8 Air	44.53	4.15
	8 Water	27.17	1.58
RHC ($\bar{\nu}_\mu$ -mode)	9 Water	45.52	2.06
Total	-	301.40	20.68

Table 7.1: List of T2K data-taking runs with number of protons on target (POT) for MC and data. The run numbering also lists the status of The PØD's water bags during the run, containing water or air. Runs 1 and 10 also exist, but data was only taken from the far detector [53].

This validation of the 4π selection only made use of run 4 air. This is due to limited production of MC and data files for P7 during development; however, this run is still considered representative of all of the neutrino-mode runs. A separate validation was performed for the anti-neutrino selection [111].

7.1.2 ECal PID variables

`PIDMipEM` is a discriminator variable used for particle identification in the ECal. It determines if a reconstructed ECal object is more likely to be caused by a MIP (e.g. muons), or more $\gamma/e^{\pm}$-like (EM-like). The variable is constructed from low-level PID ECal event variables: the circularity, cluster hit charge deviation, layer charge truncated max ratio and dE/dx front-back ratio. These are described in detail in [112].

To select EM-like objects, a cut is applied to remove all objects identified as MIPs. Nominally, this cut would be `PIDMipEM` > 0, but due to the imperfect nature of reconstruction and identification, a cut made at a slightly different value may produce better selection results. The distribution of this value for each event is shown in figure 7.1 across P6 and P7. Events that are more MIP-like have lower values of `PIDMipEM` , while events that are more EM-like have higher values of `PIDMipEM` .

It was initially assumed the cut could remain at the nominal value of `PIDMipEM` > 0, which

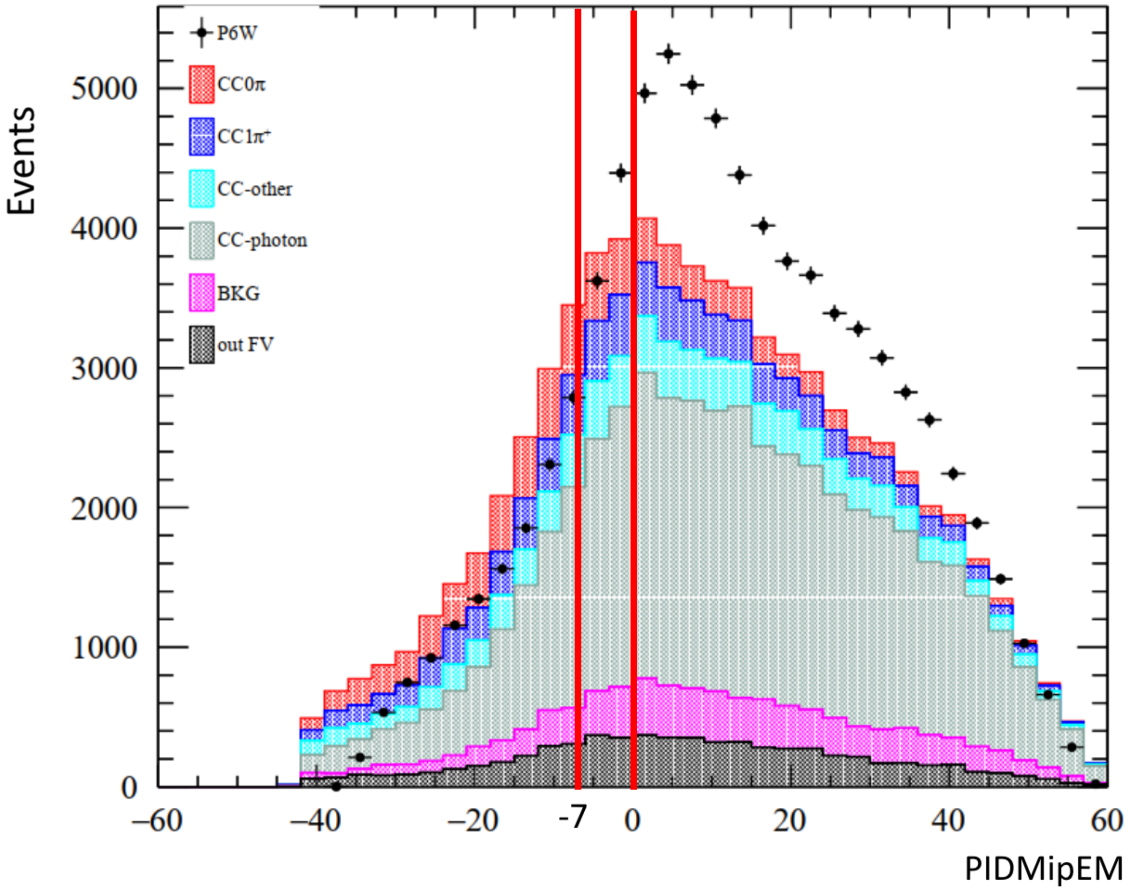

Figure 7.1: Distribution of the `PIDMipEM` variable across events in Production 6 (black points) and Production 7 (filled histogram) MC reconstruction, for the CC-Inclusive sample. Generally speaking, events with `PIDMipEM` < 0 correspond to minimally-ionising particles (e.g. muons) and `PIDMipEM` > 0 correspont to electromagnetic-like (e.g. photons, electrons). Changes to the ECal reconstruction in Production 7 motivated further examination of this variable to identify if a new cut is required, as can be seen in the change of the shape of the distribution. The cut was changed from 0 to −7 following investigation into the effect on the efficiency and purity of samples.

would remove all events with a `PIDMipEM` value less than zero. However, concurrent to this work, the RHC Photon selection was in development which relies on similar PID cuts, and it was determined that keeping only events with `PIDMipEM` > -7 provided a significant improvement in the RHC photon selection. The development of the RHC selection and related cut values is described in detail in [111]. In order to maintain consistency across both selections, an identical cut was implemented in this selection. The changes to the efficiency and purity as a result of this are shown in table 7.2. The overall changes were considered acceptable for validation of the 4π selection. This is because the efficiency and purity of the main samples, CC0pi0p and CC0piNp, were not significantly changed relative to the previous cut of `PIDMipEM` > 0.

`PIDMipEM` > 0			
Sample	Efficiency (%)	Purity (%)	Eff×Pur (Normalised)
CC0pi0p	32.84 ± 0.12	82.83 ± 0.15	27.20
CC0piNp	14.00 ± 0.01	73.76 ± 0.26	10.33
CC1pi	25.31 ± 0.20	64.83 ± 0.36	16.41
CCOther	17.26 ± 0.36	54.84 ± 0.84	9.47
CCPhoton	47.36 ± 0.27	52.61 ± 0.28	24.92

`PIDMipEM` > -7			
Sample	Efficiency (%)	Purity (%)	Eff×Pur (Normalised)
CC0pi0p	32.38 ± 0.12	83.76 ± 0.15	27.12
CC0piNp	13.88 ± 0.09	74.91 ± 0.26	10.40
CC1pi	24.49 ± 0.20	66.27 ± 0.36	16.23
CCOther	15.83 ± 0.35	57.21 ± 0.89	9.06
CCPhoton	50.34 ± 0.27	50.37 ± 0.27	25.36

Table 7.2: Comparison of efficiency and purity across samples for `PIDMipEM` cut at 0 and -7 in P7, as part of the validation for the 4π selection. The cut value of 0 was initially considered; however, validation of the RHC photon selection suggested that a cut at -7 provided a better photon sample and therefore improved the purity for the other samples [111]. The results suggest the change in efficiency and purity is acceptable and the new cut was implemented for both selections.

7.1.3 MostUpstreamLayerHit

The `MostUpStreamLayerHit` variable is used to identify the innermost ECal layer with hits in a reconstructed ECal object. A photon from the inner subdetectors of ND280 is more likely to shower in the innermost layers of the ECal. Conversely, a particle whose

Cut value	Sample	Efficiency	Purity	Eff×Pur
5	CC0pi	46.92 ± 0.13	79.66 ± 0.13	37.38
	CC1pi	25.39 ± 0.20	64.49 ± 0.36	16.37
	CCOther	17.50 ± 0.36	54.51 ± 0.83	9.54
	CCPhoton	46.48 ± 0.27	52.65 ± 0.28	24.46
6	CC0pi	46.84 ± 0.13	79.89 ± 0.13	37.42
	CC1pi	25.31 ± 0.20	64.83 ± 0.36	16.41
	CCOther	17.26 ± 0.36	54.84 ± 0.84	9.47
	CCPhoton	46.36 ± 0.27	52.61 ± 0.28	24.92
7	CC0pi	46.77 ± 0.13	80.05 ± 0.13	37.44
	CC1pi	25.24 ± 0.20	65.10 ± 0.36	16.43
	CCOther	17.15 ± 0.36	55.44 ± 0.84	9.51
	CCPhoton	48.01 ± 0.27	52.49 ± 0.28	25.20
8	CC0pi	46.71 ± 0.13	80.19 ± 0.13	37.45
	CC1pi	25.17 ± 0.20	65.31 ± 0.36	16.44
	CCOther	17.02 ± 0.36	55.99 ± 0.85	9.53
	CCPhoton	48.52 ± 0.27	52.33 ± 0.28	25.39

Table 7.3: Efficiency and purity values for charged-current samples, dependent on value of the `MostUpStreamLayerHit` cut. ECal reconstructed objects that have no hits in the number of ECal layers below the cut value are excluded to reduce pile-up.

reconstructed object only has hits in the outer layers of the ECal is more likely to have come from outside of the detector. These events can cause “pile-up”, which occurs when a background event produces photon-like activity in the ECal within the same time window as a “legitimate” neutrino event from inside the detector, thus producing a false ECal photon tagging rate.

Applying a cut on this variable to remove events originating from the outer layers of the detector reduces the number of pile-up events and improves the overall photon tagging efficiency. In P6, the cut was placed at `MostUpStreamLayerHit` < 6, meaning reconstructed objects with no hits within the innermost 5 layers of the ECal were removed.

For P7, a range of `MostUpStreamLayerHit` values were tested against the efficiency and purity of selections, shown in table 7.3. The cut value for `MostUpStreamLayerHit` was found to have only a minor effect on the efficiency and purity of the samples. Thus, a new cut value of `MostUpStreamLayerHit` < 7 was agreed upon for P7, following comparisons with the RHC selection [111] [102].

7.1.4 ECal Cluster NHits

Changes to the ECal reconstruction algorithm in P7 allow for reconstructed clusters to have fewer detector hits compared to P6 [110]. To ensure that ECal clusters used in the selection would still have a sufficient number of detector hits for a good quality reconstruction, a cut of `ECalNHitsCut` > 4 was introduced to remove clusters composed of four or fewer hits [102].

7.1.5 Validation Results

Following the changes to the selection variables discussed in sections 7.1.2, 7.1.3, and 7.1.4, the final results for the sample efficiency and purity for Production 7 versus Production 6 could be produced. Figures 7.2 and 7.3 show the efficiency and purity of the four main samples as a function of true muon momentum, showing the values for both P6 and P7. It can be seen that the efficiency and purity distribution in P6 has been almost completely recovered in P7 for all of the four samples. Optimisation of the selections to take full advantage of the new reconstruction algorithms is beyond the scope of the work presented here, and will require a more in-depth treatment e.g. redefinition of high-level variables.

The final validation values for efficiency and purity in Production 7 compared to Production 6 are shown in table 7.4. Note that the CC0pi0p and CC0piNp samples have been merged into a single CC0pi sample, as the samples were not separate in P6.

The most significant samples for this validation were CC0pi and CC1pi, as these heavily factor into the oscillation analysis. The P7 efficiency of these two samples has dropped by $\sim 1\%$ compared to P6; however, the purity has risen by a similar amount. As high purity is more preferable than high efficiency (although maximising both is of course strictly best), this is a very good result. The efficiency and purity values were sufficiently high for the selection to be validated, and no further adjustments to the selection variables were made.

The CCOther and CCPhoton samples are less important for the oscillation analysis, but is was still desirable to maintain the efficiency and purity values as they could pull events into an incorrect sample. The purity of these samples has increased, by $\sim 5\%$ for CCOther and $\sim 2\%$ for CCPhoton. The efficiency of CCOther has dropped by $\sim 2\%$ and the efficiency of CCPhoton has increased by $\sim 3\%$, which is sufficiently within the desired range.

The overall increase in purity across all samples in P7 compared to P6 means that the new selection is producing better quality samples than before, which is better for the oscillation analysis.

CC0pi

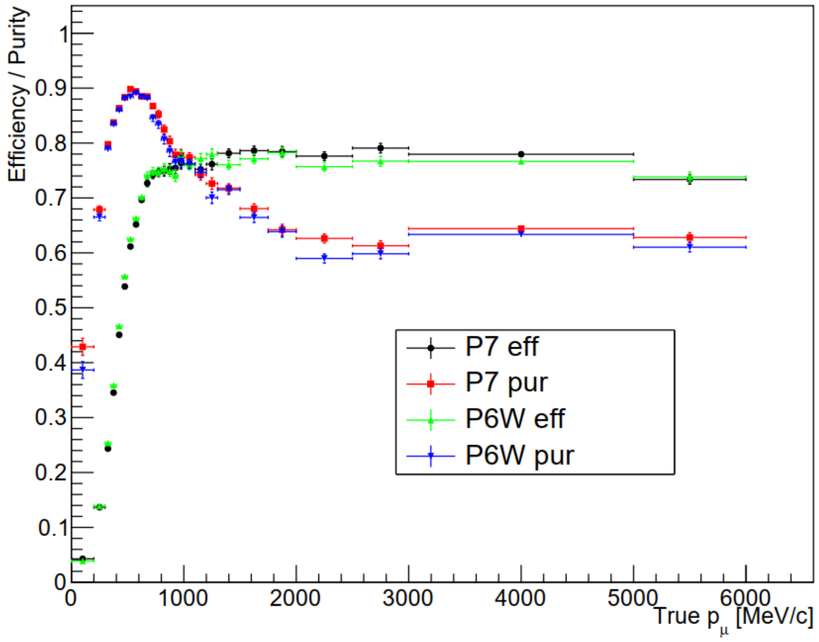

CC1pi

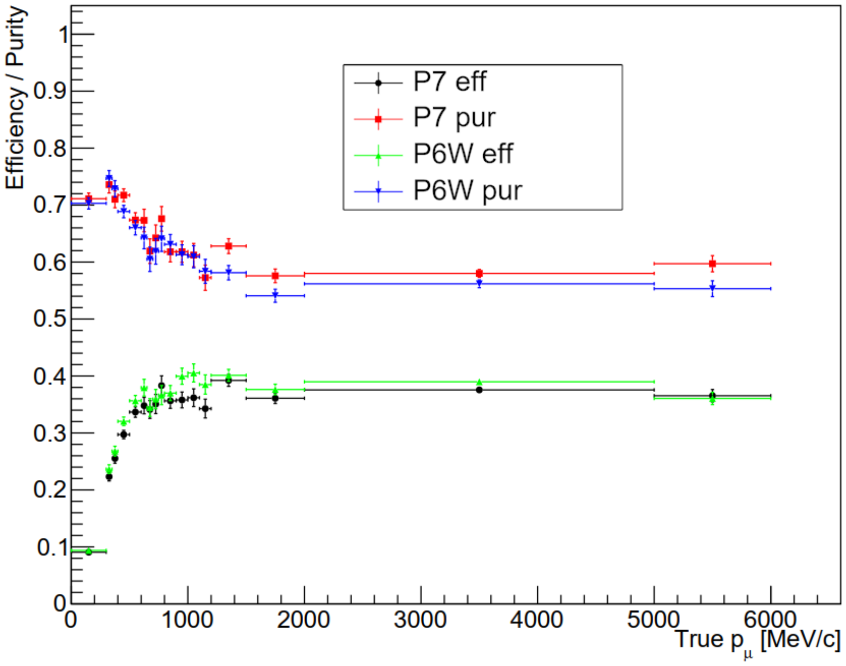

Figure 7.2: Efficiency and purity for CC0pi (top) and CC1pi (bottom) samples as a function of true muon momentum. The black and green points show the sample efficiency in P7 and P6, respectively, and the red and blue points show the sample purity in P7 and P6, respectively. “P6W” refers to the version of P6 this was performed with. The aim of the validation was to recover the P6 values of efficiency and purity for P7, which, as these plots show, was successful. Peak neutrino energy is 600 MeV, hence the finer binning in the region. CC0pi is the most significant sample in the analysis, hence the selection is optimised more specifically towards this sample to maximise its efficiency and purity, particularly in the peak region.

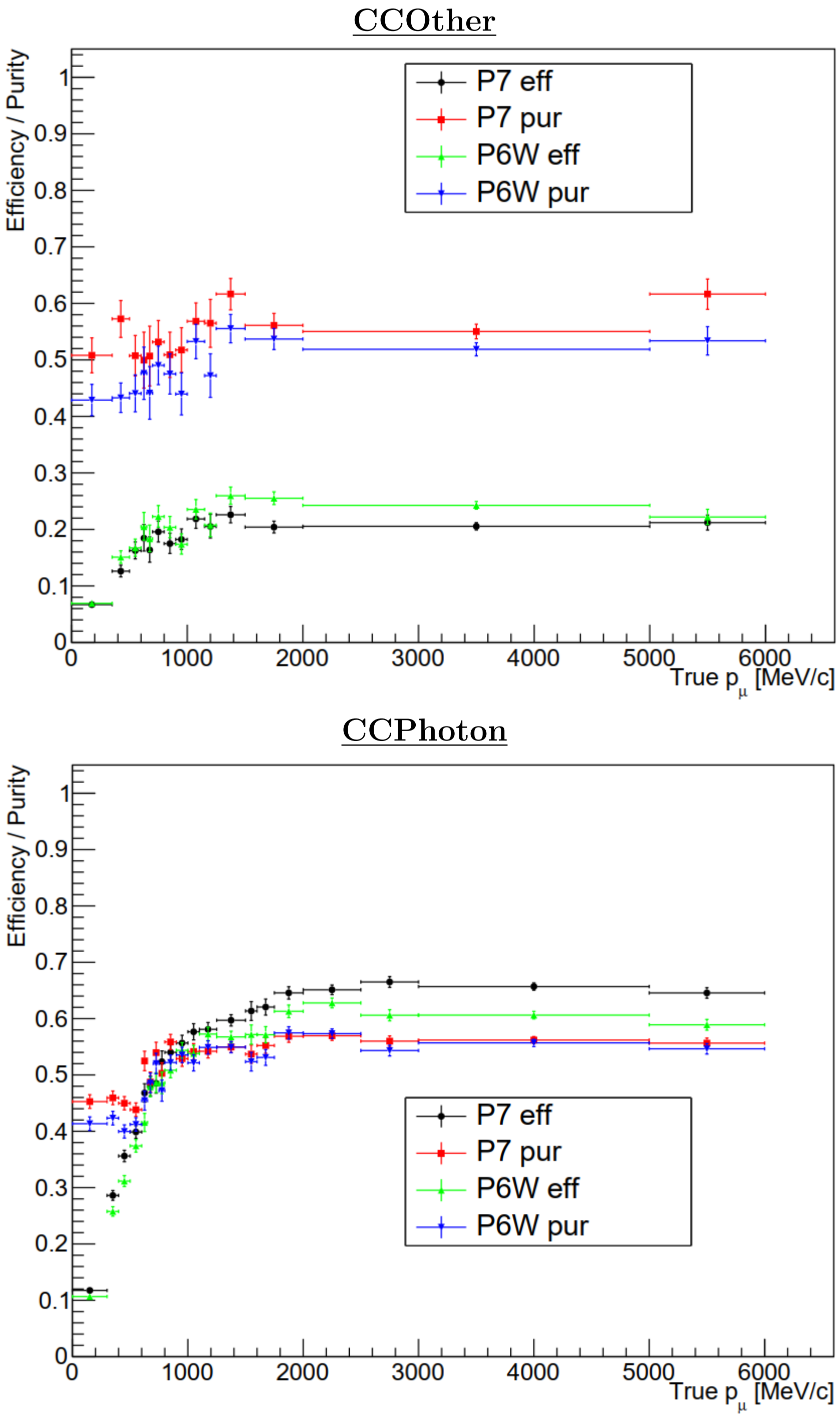
CCOther

CCPhoton

Figure 7.3: Efficiency and purity for CCOther and CCPhoton samples as a function of true muon momentum. The black and green points show the sample efficiency in P7 and P6, respectively, and the red and blue points show the sample purity in P7 and P6, respectively. “P6W” refers to the version of P6 this was performed with. The aim of the validation was to recover the P6 values of efficiency and purity for P7, which, as these plots show, was successful. Peak neutrino energy is 600 MeV, hence the finer binning in the region. Low efficiency for CCOther is not unexpected, as it is not considered critical to the main analysis and exists mostly to “soak up” irrelevant events away from the more important samples (e.g. CC0pi).

Sample	Efficiency (%)		Purity (%)	
	P6	P7	P6	P7
CC0pi	47.49 ± 0.13	46.84 ± 0.13	78.99 ± 0.13	79.89 ± 0.13
CC1pi	26.46 ± 0.21	25.31 ± 0.20	63.02 ± 0.35	64.83 ± 0.36
CCOther	19.68 ± 0.38	17.26 ± 0.36	49.41 ± 0.75	54.84 ± 0.84
CCPhoton	44.12 ± 0.27	47.36 ± 0.27	50.87 ± 0.29	52.61 ± 0.28

Table 7.4: Efficiency and purity values across charged-current samples for the nominal Production 6 selections and post-modification Production 7 selections. Efficiency is the number of true events in the sample against the total number of true events, and purity is the number of true events in the sample against the total number of events in the sample. These efficiency and purity values were deemed sufficient to validate the 4π selection and implement it fully into Production 7.

7.2 Run 8 Timeslip Corrections

Run 8 data from ND280 has a significant discrepancy between MC and data for time-of-flight (ToF) information [113], as demonstrated in figure 7.4. This was caused by a hardware issue during data-taking, and resulted in random time shifts of ±10 ns being applied to some events. The issue was attributed to a unstable connection between the Readout Merger Modules (RMMs) and the Secondary Clock Modules (SCMs) [114]. RMMs combine incoming data from the Trip-T front-end boards (TFBs), which themselves are connected to the readout MPPCs in the detectors. The Secondary Clock Modules (SCM) passes triggers from the Main Clock Module (MCM) to the RMMs to capture the event. The RMMs and SCMs are connected via Xilinx RocketIO transceivers with a phase-lock loop frequency of 100 MHz, 4 times slower than the TFB clocks. This phase-lock can cause shifts of up to 10 ns when a connection between an RMM and SCM is established if there are connection issues with the optical fibres.

Minor timeslips appear all data runs and are typically corrected by a Gaussian smearing correction, where a Gaussian fit is applied to MC and data and the MC is smeared until it resembles the data distribution [114]. Note that the ToF measurements presented in this chapter do not have the track flipping correction applied [115], hence the presence of wrong-direction tracks in ToF topologies.

The run 8 data timeslips were considered significant enough to require a new treatment. A correction algorithm was developed to apply similar “timeslips” to the run 8 MC to reduce the discrepancy between MC and data, and improve the accuracy of the MC simulation [104]. This algorithm was developed in P6 and, given the importance of timing data in the 4π selection, needed to be validated for P7. To achieve this, it was first made sure the correction algorithm was still capable of resolving the run 8 timeslip issues. After a successful test, a new set of correction parameters was produced.

Each ToF topology has some fraction f_1 of events shifted by +10 ns, and some fraction f_2 shifted by −10 ns. A ToF topology of N events can be divided into three groups: events that have no timeslip, $E_0 = N(1 - f_1 - f_2)$; events with a +10 ns timeslip, $E_1 = Nf_1$; and events with a −10 ns timeslip, $E_2 = Nf_2$. The correction algorithm generates a random number f in the range $(0, 1)$ for each event in a topology. If $0 < f < f_1$, +10 ns is applied to the event's ToF value; if $f_1 < f < f_1 + f2$, −10 ns is applied; and for $(f_1 + f_2) < f < 1$, the ToF value is unchanged.

The calculation of f_1 and f_2 is performed by a 5-dimensional fractional fit; this is a complex process, and will only be summarised here. It is explained in detail in [113]. First, the standard Gaussian smearing correction is applied to the nominal MC distribution. This generates a smeared Gaussian fit for the two MC peaks with mean values of $\mu_\pm$ and standard deviations $\sigma_\pm$, where − denotes the backwards-going peak and + denotes the forward-going peak. Is is assumed both peaks follow a similar distribution, so $\sigma_- = \sigma_+ = \sigma$ is applied to reduce the number of degrees of freedom.

The algorithm then loops over all possible values of f_1 and f_2 and applies them to the MC distribution to find the values that minimise the Pearson χ^2 test statistic between the data and MC distributions. This is calculated as

$$\chi^2 = \sum_{i=1}^{N} \frac{(m_i - d_i)^2}{m_i} \tag{7.3}$$

where m_i and d_i are the number of MC and data events in the ith bin, respectively; and N is the number of bins, which is uniformly $N = 119$ across all ToF topologies. The `TFractionFitter` package in ROOT [116] is used as it is optimised to perform fractional fits i.e. fits where some fraction(s) of the distribution is being adjusted, in this case f_1 and f_2.

Applying the correction algorithm to run 8 in P7 shows that it is still able to successfully fit MC to the run 8 data. Figures 7.5 - 7.8 show comparisons between the run 8 data, nominal MC and fitted MC for each of the 24 ToF topologies. Table 7.5 presents the

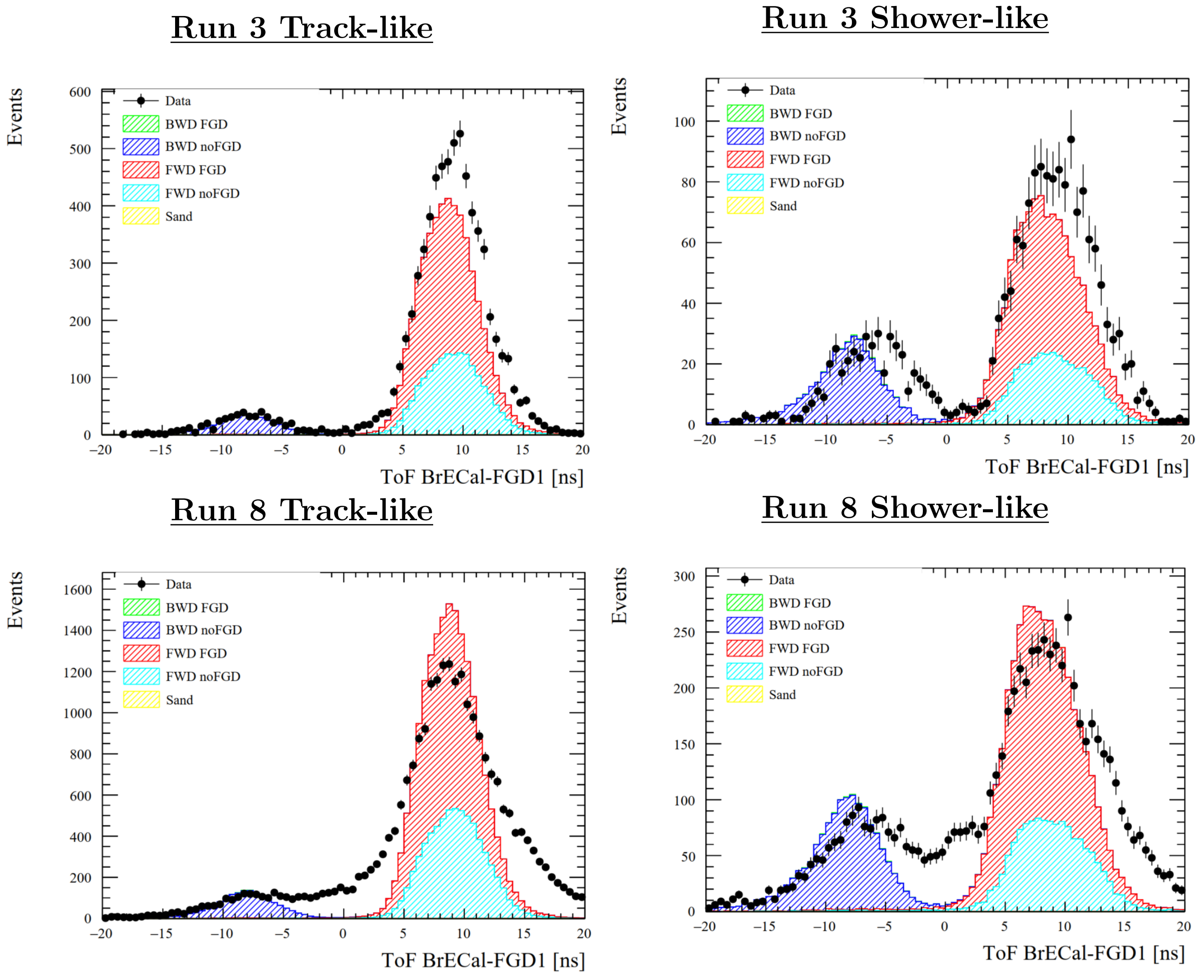

Figure 7.4: Comparison of the forwards-going Barrel ECal to FGD1 track and shower ToF topologies for run 3 (top) and run 8 (bottom), in P6 without any corrections applied. MC with topology breakdown is shown as the filled-in portion, while run data is the black dots. The significant spread in the timing data in run 8 is clear, while run 3 shows a more typical MC-data distribution. Resolving this major discrepancy in run 8 is necessary to make the data useable in the T2K analysis. The double-Gaussian shape shows one peak for backwards-going events and one for forwards-going events. "Track-like" refers tot objects with more than one node in a non-FGD detector, while a "shower-like" object has exactly one node [113]. Plots adapted from [114].

final values for the timeslip correction parameters, which have been implemented into Production 7.

The new timeslip parameter values are comparable with the previous P6 analysis [104], and any differences are considered to be the result of reconstruction changes between P6 and P7. The timeslip plots show that the fitting is being performed extremely well across all topologies. This is true even for backwards-going and high-angle topologies, which have significantly fewer events compared to forwards-going topologies.

The successful validation of this correction allows run 8 data to be used in oscillation analyses with the P7 software. Additionally, the efficacy of the timeslip correction algorithm in run 8 has led it to being applied to all data runs in future analyses, as it is capable of correcting the less prevalent, but still present timeslip errors in the detector data. The implementation of the timeslip correction into the overall analysis will both improve statistics (by inclusion of run 8) and reduce data-MC disagreement (by reducing timeslip differences), and thus improve the constraints on the measurement of the neutrino oscillation parameters at T2K.

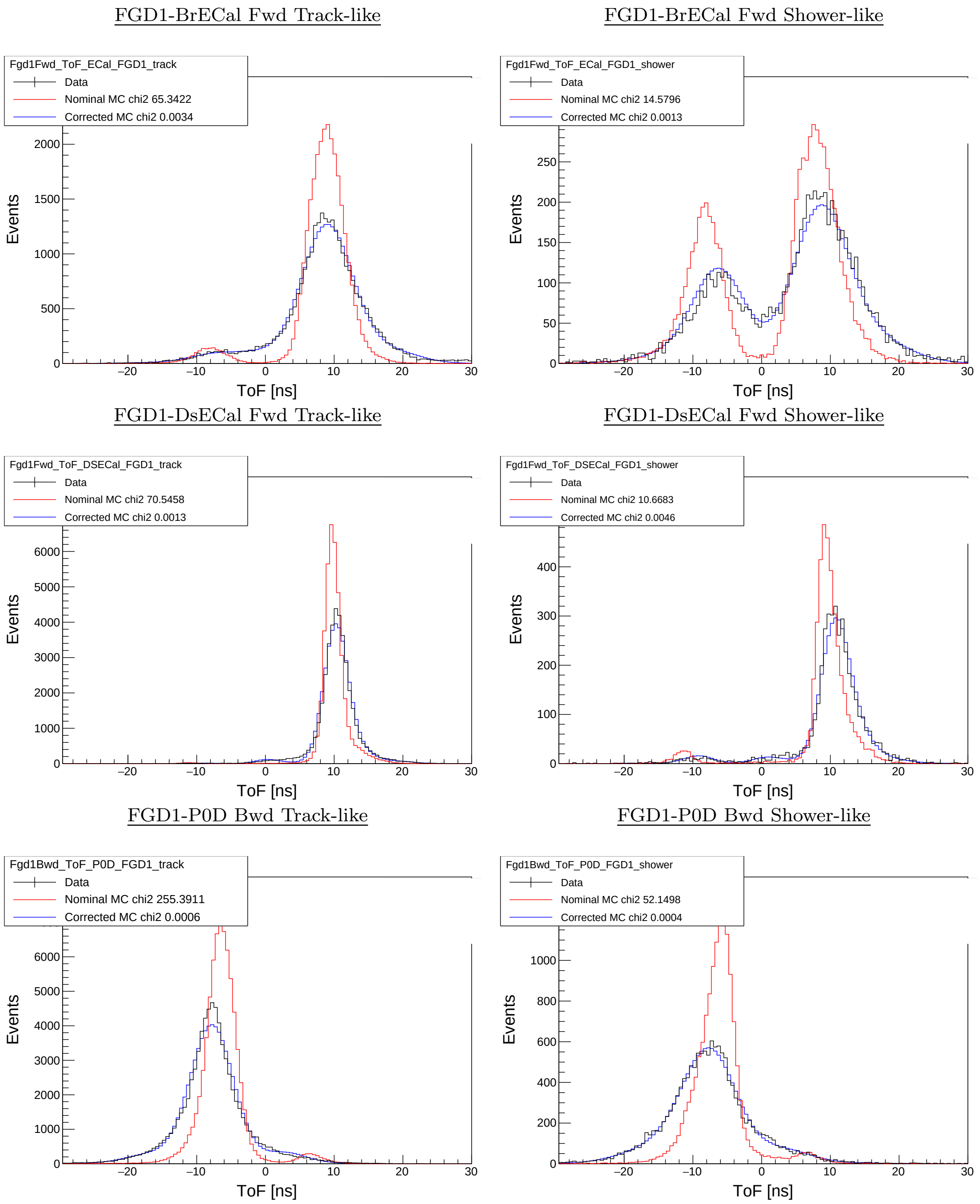

Figure 7.5: Timeslip corrections applied to time-of-flight topologies for run 8. The left plots show track-like topologies and the right plots show shower-like topologies, for FGD1 to barrel ECal forwards (top), FGD1 to downstream ECal forwards (middle) and FGD1 to PØD ECal backwards (bottom). The red line shows the nominal MC while the black line shows the detector data. The blue line shows the MC after the timeslip correction algorithm has been applied. The top-left legend gives the MC-data χ^2 values for before and after the fit.

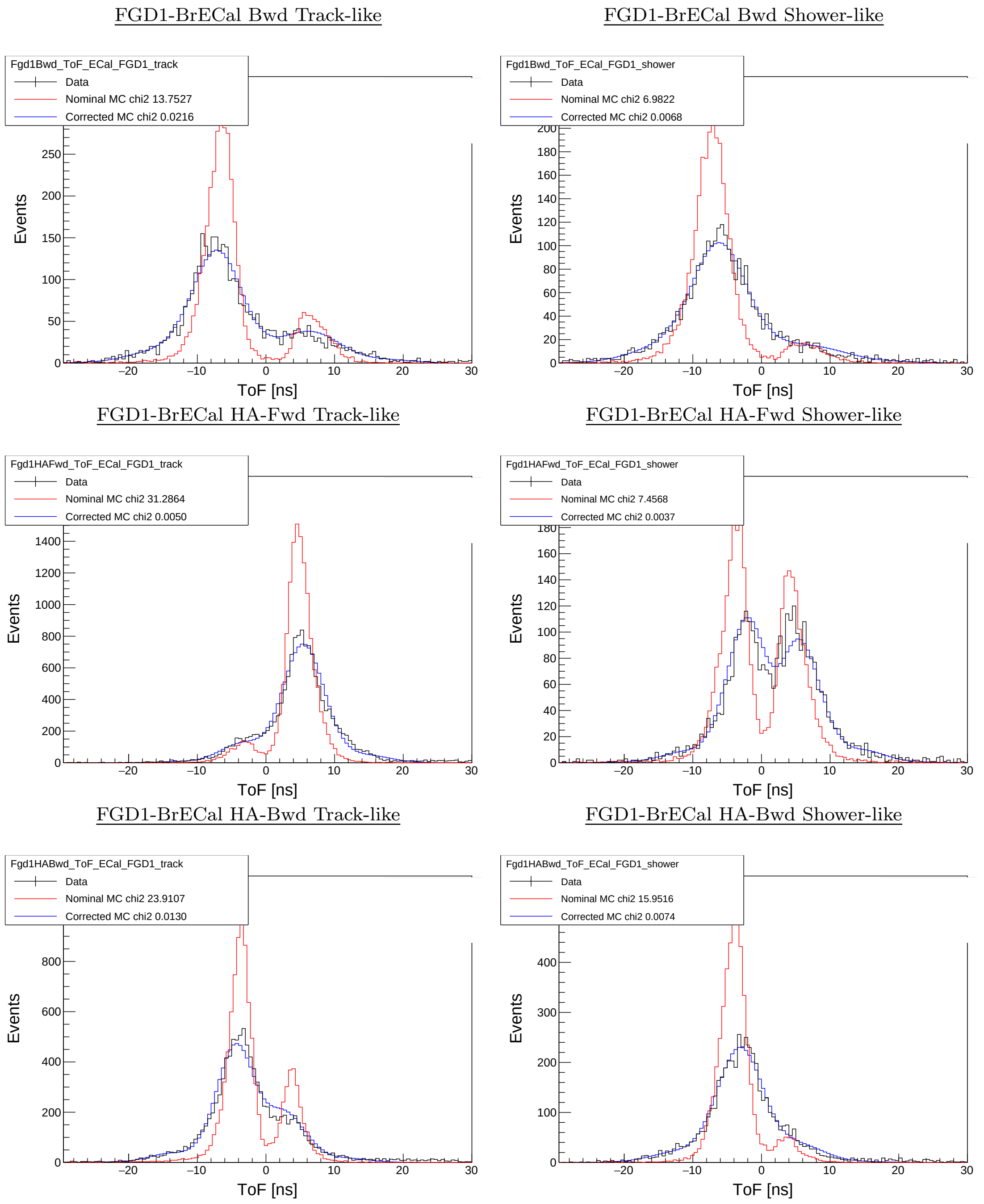

FGD1-BrECal Bwd Track-like

FGD1-BrECal Bwd Shower-like

FGD1-BrECal HA-Fwd Track-like

FGD1-BrECal HA-Fwd Shower-like

FGD1-BrECal HA-Bwd Track-like

FGD1-BrECal HA-Bwd Shower-like

Figure 7.6: Timeslip corrections applied to time-of-flight topologies for run 8. The left plots show track-like topologies and the right plots show shower-like topologies, for FGD1 to barrel ECal backwards (top), FGD1 to barrel ECal high-angle forwards (middle) and FGD1 to barrel ECal high-angle backwards (bottom). The red line shows the nominal MC while the black line shows the detector data. The blue line shows the MC after the timeslip correction algorithm has been applied. The top-left legend gives the MC-data χ^2 values for before and after the fit.

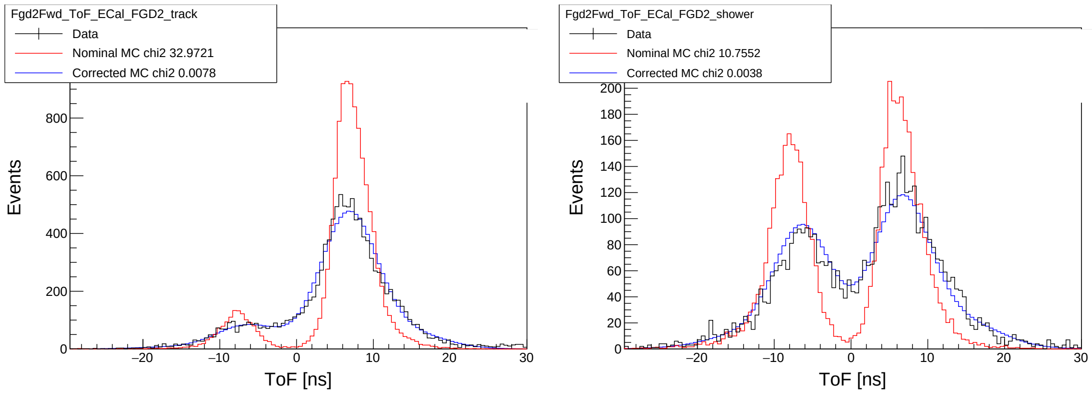
FGD2-BrECal Fwd Track-like

FGD2-BrECal Fwd Shower-like

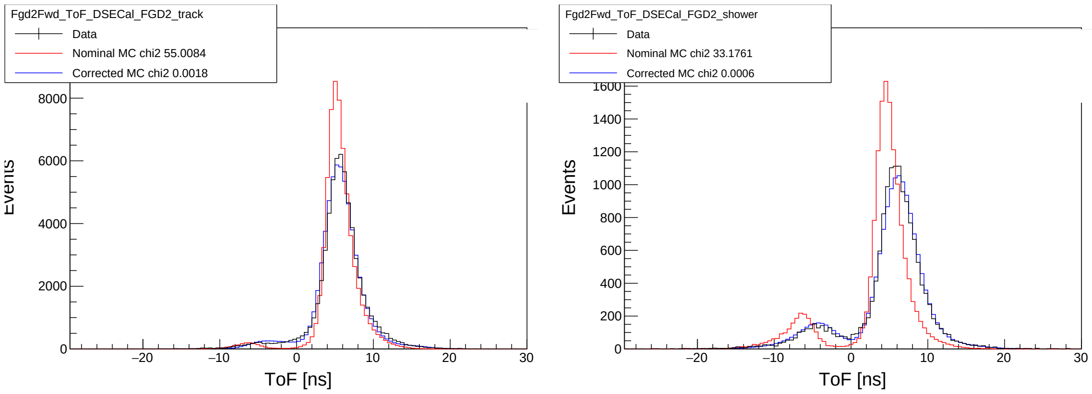
FGD2-DsECal Fwd Track-like

FGD2-DsECal Fwd Shower-like

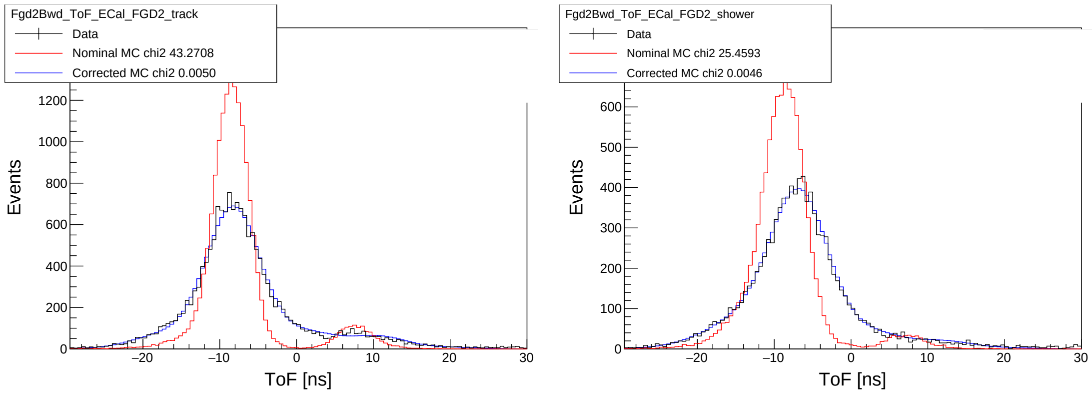
FGD2-BrECal Bwd Track-like

FGD2-BrECal Bwd Shower-like

Figure 7.7: Timeslip corrections applied to time-of-flight topologies for run 8. The left plots show track-like topologies and the right plots show shower-like topologies, for FGD2 to barrel ECal forwards (top), FGD1 to downstream ECal high-angle forwards (middle) and FGD2 to barrel ECal backwards (bottom). The red line shows the nominal MC while the black line shows the detector data. The blue line shows the MC after the timeslip correction algorithm has been applied. The top-left legend gives the MC-data χ^2 values for before and after the fit.

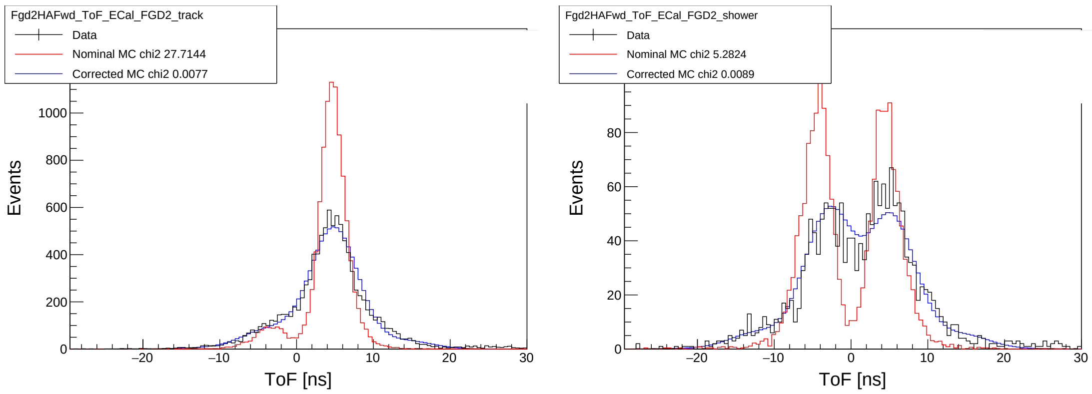
FGD2-BrECal HA-Fwd Track-like

FGD2-BrECal HA-Fwd Shower-like

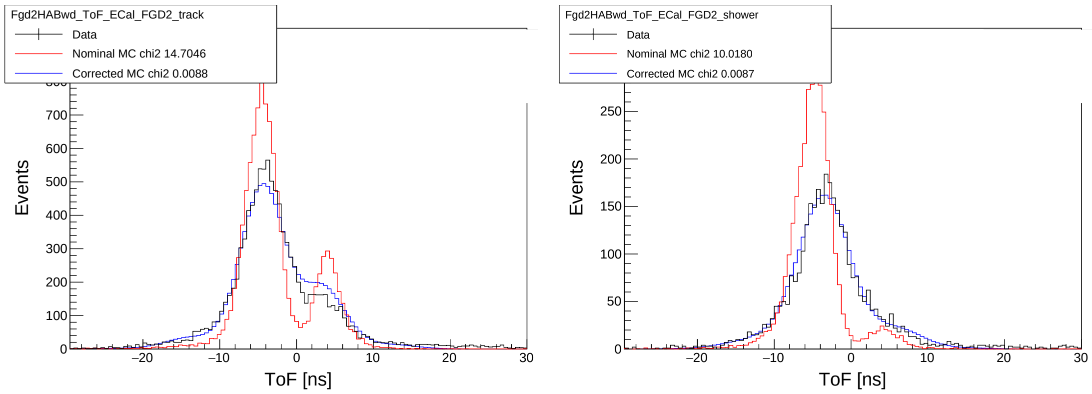
FGD2-BrECal HA-Bwd Track-like

FGD2-BrECal HA-Bwd Shower-like

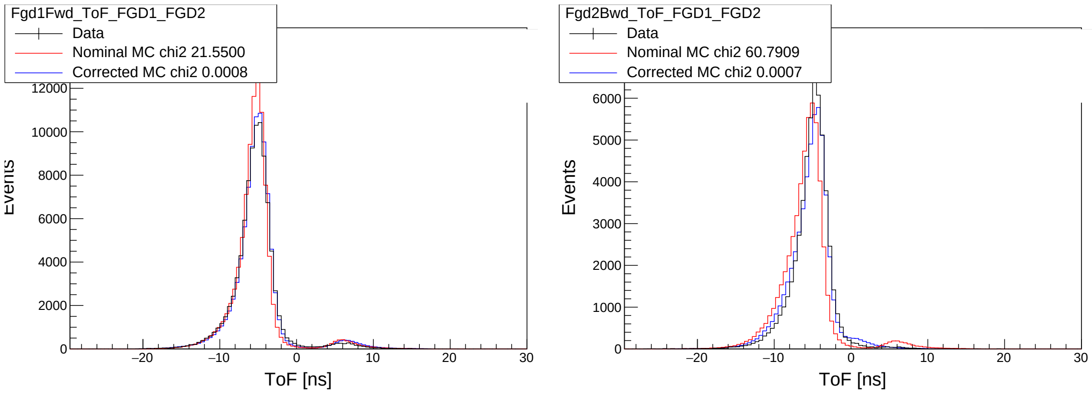
FGD2-BrECal Bwd Track-like

FGD2-BrECal Bwd Shower-like

Figure 7.8: Timeslip corrections applied to time-of-flight topologies for run 8. The left plots show track-like topologies and the right plots show shower-like topologies, for FGD2 to barrel ECal high-angle forwards (top) and FGD2 to barrel ECal high-angle backwards (middle). The bottom two plots show the forwards (left) and backwards (right) for the FGD1 to FGD2 topologies. The red line shows the nominal MC while the black line shows the detector data. The blue line shows the MC after the timeslip correction algorithm has been applied. The top-left legend gives the MC-data χ^2 values for before and after the fit.

Topology	f_1	f_2	σ (ns)	μ_- (ns)	μ_+ (ns)
Fgd1Fwd_ToF_ECal_FGD1_track	0.0570	0.0627	2.8	0.2	0.2
Fgd1Fwd_ToF_ECal_FGD1_shower	0.0184	0.0748	2.8	1.0	1.8
Fgd1Fwd_ToF_DSECal_FGD1_track	0.0273	0.0104	1.4	0.6	1.4
Fgd1Fwd_ToF_DSECal_FGD1_shower	0.0349	0.0096	1.6	1.4	2.2
Fgd1Bwd_ToF_P0D_FGD1_track	0.0451	0.0379	2.4	-1.4	-3.0
Fgd1Bwd_ToF_P0D_FGD1_shower	0.0703	0.0672	3.2	-1.4	-1.4
Fgd1Bwd_ToF_ECal_FGD1_track	0.0605	0.0988	3.0	-0.6	1.0
Fgd1Bwd_ToF_ECal_FGD1_shower	0.0675	0.0799	3.2	1.0	3.4
Fgd1HAFwd_ToF_ECal_FGD1_track	0.0692	0.0453	2.4	0.6	1.0
Fgd1HAFwd_ToF_ECal_FGD1_shower	0.0494	0.0752	2.0	1.0	1.8
Fgd1HABwd_ToF_ECal_FGD1_track	0.0534	0.0696	2.2	-0.6	-1.4
Fgd1HABwd_ToF_ECal_FGD1_shower	0.0650	0.0455	2.8	1.0	1.4
Fgd2Fwd_ToF_ECal_FGD2_track	0.0582	0.0569	3.0	-0.2	0.2
Fgd2Fwd_ToF_ECal_FGD2_shower	0.0421	0.0969	2.8	0.6	1.4
Fgd2Fwd_ToF_DSECal_FGD2_track	0.0319	0.0121	1.2	0.2	5.0
Fgd2Fwd_ToF_DSECal_FGD2_shower	0.0076	0.0089	1.6	1.4	2.2
Fgd2Bwd_ToF_ECal_FGD2_track	0.0596	0.0872	2.8	0.2	3.0
Fgd2Bwd_ToF_ECal_FGD2_shower	0.0749	0.0715	2.8	1.8	5.0
Fgd2HAFwd_ToF_ECal_FGD2_track	0.0696	0.0504	2.6	0.2	1.4
Fgd2HAFwd_ToF_ECal_FGD2_shower	0.0908	0.0806	2.4	0.6	1.8
Fgd2HABwd_ToF_ECal_FGD2_track	0.0457	0.0579	2.0	0.2	-1.0
Fgd2HABwd_ToF_ECal_FGD2_shower	0.0347	0.0577	2.6	1.4	1.0
Fgd1Fwd_ToF_FGD1_FGD2	0.0033	0.0029	0.6	0.2	0.6
Fgd2Bwd_ToF_FGD1_FGD2	0.0000	0.0000	0.2	0.6	-5.0

Table 7.5: Time-of-Flight correction parameters for ND280 run 8 using P7, across all ToF topologies. f_1 is the fraction of events that have has a $+10$ ns correction applied and f_2 is the fraction of events that have a -10 ns correction applied. σ is the standard deviation for the Gaussian distributions, which is applied for both the forwards-going and backwards-going peaks. μ is value of the centre of each peak, μ_- for the backwards-going events and μ_+ for forwards-going. The final topology has f_1 and f_2 values close to zero; this is simply a result of pre-correction distributions already being very similar as this topology does not include the ECal timing; a similar result is observed in the previous analysis [113].

7.3 TPC-ECal Matching Parameters

As part of the Production 7 validation, the systematic uncertainties related to the ND280 ECal were evaluated. This section discusses the TPC-ECal matching efficiencies, which describe how effectively reconstructed tracks which pass between the TPC and ECal can be matched together. Additional work to validate the other ECal systematics was undertaken by others, and is described in [108].

Charged particles travelling from the TPC to the ECal will leave tracks in the TPC and tracks or showers in the ECal. These are reconstructed separately in each subdetector, so need to be matched together as part of the reconstruction process to produce a single particle path. For this analysis, a selection is applied to identify particle tracks leaving the TPC that appear to enter the ECal. This selection makes the following cuts on TPC tracks:

- Good beam and ND280 quality.
- Track starts in an FGD fiducial volume.
- Track has more than 18 TPC nodes in the most downstream TPC it passes through.
- Track appears to enter ECal

Tracks are then divided further depending on particle type, horn current, momentum, and whether the track enters the downstream or barrel ECal.

The efficiency of matching ϵ is calculated as:

$$\epsilon = \frac{\text{Number of tracks passing selection that have an ECal segment}}{\text{Total number of tracks passing selection}} \tag{7.4}$$

The efficiencies are split into separate topologies based on particle type (μ^-, μ^+, p, e^- and e^+), horn current (HC)/beam mode (FHC/ν_μ mode and RHC/$\bar{\nu}_\mu$ mode), and a momentum binning. Track matching efficiencies were calculated for both the DsECal and BrECal. The efficiencies were found for both MC and data, and the results were compared to see if they were acceptable. Tables 7.6 and 7.7 present these efficiencies. The Production 6 efficiencies have been taken from the 2017 ECal study [117]. The previous study used a finer momentum binning, so the efficiency values have been averaged across the new bins. Limited statistics in certain topologies can lead to unusually high data-MC discrepancies. These are present in both the P6 and P7 studies and are generally unavoidable; however, coarser momentum binning implemented in P7 has helped mitigate this to an extent.

The data-MC difference for the P7 topologies show improvements over P6, or at least fall within the uncertainty range. Thus, there were no issues identified with the TPC-ECal matching efficiencies for Production 7, and the validation was approved.

Particle	HC	Momentum (MeV)	Data (%)	MC (%)	**P7** Data-MC (%)	**P6** Data-MC (%)
μ^-	FHC	0 - 400	95.35±0.99	96.24±0.18	-0.89±1.0	2.2±0.8
	FHC	400 - 800	97.20±0.50	97.37±0.10	-0.17±0.51	1.05±0.7
	FHC	800 - 1200	94.95±0.86	97.26±0.15	-2.31±0.87	1.0 ±0.7
	FHC	1200 - 1600	97.10±0.70	96.79±0.18	0.31±0.72	-0.1±0.8
	FHC	> 1600	96.02±0.33	96.78±0.08	-0.76±0.34	0.35±0.5
μ^+	RHC	0 - 400	96.55±2.32	96.83±0.45	-0.28±2.36	-0.3±3.1
	RHC	400 - 800	98.18±1.28	98.24±0.23	-0.06±1.30	0.25±1.9
	RHC	800 - 1200	100.00±0	97.09±0.47	2.91±0.47	1.5 ± 1.3
	RHC	1200 - 1600	93.88±3.50	98.13±0.44	-4.25±3.53	2.5± 1.8
	RHC	> 1600	94.08±1.84	96.99±0.29	-2.91±1.85	1.2± 1.5
p	FHC	0 - 600	81.77±1.96	82.18±0.46	-0.41±2.01	-2.4 ± 3.3
	FHC	> 600	91.18±1.22	92.14±0.26	-0.96±1.25	-2.7 ± 3.8
	RHC	0 - 600	75.00±11.30	77.59±2.49	-2.59±11.58	40 ± 8.2
	RHC	> 600	90.24±4.80	90.91±1.17	-0.67±4.94	0.5 ± 9.7
e^-	FHC	0 - 200	44.09±2.24	45.20±0.58	-1.11±2.31	7.8 ± 4.4
	FHC	> 200	68.67±1.26	69.60±0.33	-0.93±1.31	54.6 ± 17.3
	RHC	0 - 200	38.46±7.68	45.65±2.12	-7.19±7.94	0.6 ± 10.7
	RHC	> 200	72.81±4.09	67.68±1.19	5.13±4.26	6.5 ± 9.6
e^+	FHC	0 - 200	44.93±1.96	46.76±0.55	-1.83±2.04	-1.6 ± 4.3
	FHC	> 200	66.13±1.47	68.05±0.37	-1.92±1.52	1.85 ± 4.2
	RHC	0 - 200	40.54±8.19	47.90±1.91	-7.36±8.41	1.7 ± 10.5
	RHC	> 200	62.50±5.52	69.60±1.31	-7.10±5.68	9.2 ± 12.1

Table 7.6: TPC-ECal matching efficiency comparison in Production 7 for the Downstream ECal, for Data and MC. Values for Production 6 are taken from [117]. For the $\mu^\pm$ topologies, the most significant momentum range is 400-800 as this encapsulates the neutrino beam peak. The matching efficiencies for P7 are similar enough to to P6 values for P7 to be validated.

Particle	HC	Momentum (MeV)	Data (%)	MC (%)	Data-MC (%)	P6 Data-MC (%)
μ^-	FHC	0 - 400	78.43±1.08	80.81±0.25	-2.38±1.11	3.2 ± 3.5
	FHC	400 - 800	91.83±0.77	93.10±0.18	-1.27±0.79	2.0 ± 1.4
	FHC	> 800	90.35±1.02	91.45±0.27	-1.10±1.05	-3.0 ± 3.3
μ^+	RHC	0 - 400	83.33±3.80	80.43±1.03	2.91±3.94	-2.7 ± 4.3
	RHC	400 - 800	86.42±3.91	91.64±0.72	-5.22±3.98	-3.6 ± 6.3
	RHC	> 800	90.00±3.87	82.77±1.39	7.23±4.11	8.55 ± 9
p	FHC	0 - 600	18.30±1.30	19.58±0.34	-1.28±1.35	0.7 ± 4.5
	FHC	> 600	56.09±2.17	49.53±0.51	6.56±2.23	5.3 ± 3.3
	RHC	0 - 600	20.76±5.56	21.47±1.60	-0.71±5.79	27.6 ± 9.4
	RHC	> 600	63.42±7.44	52.82±2.27	10.60±7.78	-47.4 ± 9
e^-	FHC	0 - 200	18.71±1.72	20.92±0.47	-2.21±1.79	-3.3 ± 2.2
	FHC	> 200	70.09±4.46	69.88±1.16	0.21±4.61	-4.4 ± 8.2
	RHC	0 - 200	22.73±6.28	20.85±1.57	1.88±6.48	-10.3 ± 6.1
	RHC	> 200	25.00±24.27	61.72±4.16	-36.72±24.62	-54.6 ± 17.3
e^+	FHC	0 - 200	32.65±2.75	30.71±0.71	1.94±2.84	1.1 ± 2.3
	FHC	> 200	73.40±4.45	67.72±1.21	5.68±4.61	4.2 ± 8.1
	RHC	0 - 200	18.75±9.81	28.93±2.39	-10.18±10.10	-1.5 ± 7.1
	RHC	> 200	66.67±21.60	60.53±4.61	6.14±22.08	-29.8 ± 18.5

Table 7.7: TPC-ECal matching efficiency comparison in Production 7 for the Barrel ECal, for Data and MC. Values for Production 6 are taken from [117]. For the $\mu^\pm$ topologies, the most significant momentum range is 400-800 as this encapsulates the neutrino beam peak. The matching efficiencies for P7 are similar enough to to P6 values for P7 to be validated.

7.4 Conclusion

The Production 7 software upgrade introduced many changes to the reconstruction algorithms used at T2K, thus it was necessary to validate the suite of analysis software to ensure it was still capable of performing at least as well as it did previously in Production 6. The work here focused on the new 4π solid-angle selection (numuCC4piMultiPiPhotonProton), that was developed before the P7 update, but not fully implemented into the analysis, as well as validating the timeslip correction algorithm and the TPC-ECal matching efficiencies.

For the 4π selection, this validation was performed by analysing the efficiency and purity of the selection samples. From these results, certain cut parameters were altered: `PIDMipEM` > 0 was changed to `PIDMipEM` > -7, `MostUpStreamLayerHit` < 0 was changed to `MostUpStreamLayerHit` < 7, and a new `ECalNHitsCut` > 4 cut was introduced. The 4π selection has been fully implemented into the ND280 analysis, allowing for a much better comparison with data from Super-K for all future analyses.

The timeslip correction algorithm was found to still be perfectly functional with P7, and is now implemented across all T2K data runs. The TPC-ECal matching efficiencies were consistent with the P6 results and no action was required.

Future work on the 4π selection (and T2K selection development in general) would take greater advantage of the new reconstruction algorithm, as the work presented here was limited in this scope. For example, the new P7 algorithm allows for ECal clusters to be reconstructed with fewer hits than in P6, but the current selection cuts out these smaller clusters for more straightforward parity to P6.

Chapter 8

The Near Detector Fit

Data from the ND280 detector is used to constrain many of the parameters from the neutrino flux and interaction models used in the oscillation analysis. The near detector (ND) fit adjusts MC simulation data to more closely match data collected from ND280, which in turn constrains the parameters of the model. Depending on the type of fit being performed, the ND fit is either performed simultaneously with the far detector fit, or the constrained parameters from the ND fit are propagated to the far detector fit through a covariance matrix. Either method will constrain the uncertainties across the T2K experiment and reduce the uncertainty in the measurement of the neutrino oscillation parameters.

Two fitters are in use for the T2K oscillation analysis: GUNDAM [118] and MaCh3 [119]. GUNDAM exclusively fits for the near detector, and uses a gradient descent method to tune the parameters. This fitter is discussed in detail in section 8.1. MaCh3 can perform a fit for both the near and far detector data simultaneously, as well as independently for each detector. MaCh3 uses a Markov chain Monte Carlo (MCMC) analysis method [120], which uses a Bayseian statistical approach to maximise the likelihood that the MC model accurately describes the data. Both GUNDAM and MaCh3 are in the process of rigorous testing to ensure that their respective results are in agreement, and that they themselves agree with the previous BANFF fitter [121] [122]. The analysis discussed in this thesis will focus only on GUNDAM.

8.1 The GUNDAM Fitter

The Generalized and Unified Neutrino Data Analysis Methods (GUNDAM) fitter is a software suite that is being developed to perform a variety of analysis tasks, especially near detector fits [122] [118]. The basis of GUNDAM formed from the BANFF near detector fitter, which used a similar gradient-descent method. GUNDAM improves performance and usability compared to BANFF, and was designed to work with the new sub-detectors introduced in the ND280 Upgrade [76]. GUNDAM is also influenced by the Super-xsllhFitter cross section fitter [123], which was itself also inspired by BANFF. Fits in GUNDAM have been shown to be performed up to twelve times faster than in BANFF [122]

8.1.1 The ND280 Test-Statistic

GUNDAM uses a semi-frequentist approach, where a covariance matrix combining the flux, detector, and neutrino cross section systematics provides the nominal values for each parameter. The gradient-descent method relies on the `Minuit2` software package of ROOT to find the set of parameters that minimise the χ^2 test-statistic, defined as

$$\chi^2 \equiv -2\ln\mathcal{L}_{\text{total}} \tag{8.1}$$

where $\mathcal{L}_{\text{total}}$ is the total likelihood across all systematic and statistical components of the fit. A global minimum of the test-statistic maximises the likelihood of the model matching observed data. The generated set of parameters have uncertainties constrained to allow for this maximised likelihood, which is propagated to the far detector fit to produce constraints on the neutrino oscillation parameters.

The likelihood is calculated separately for each selection (see chapter 6). Each selection is binned by reconstructed muon momentum p_μ and the cosine of the muon angle to the detector's z axis, $\cos\theta_\mu$. The likelihood is calculated by finding the minimum $-2\ln\mathcal{L}_{\text{total}}$ of the data and MC across all bins and samples for each set of parameter values. The total likelihood is defined as:

$$-2\ln\mathcal{L}_{\text{total}} = -2\ln\mathcal{L}_{\text{stat}} - 2\ln\mathcal{L}_{\text{syst}} \tag{8.2}$$

where $\mathcal{L}_{\text{stat}}$ is the statistical (Poisson) likelihood and $\mathcal{L}_{\text{syst}}$ is the systematic uncertainty likelihood. Systematic uncertainties come from previous knowledge of approximate parameter values ("priors"), while statistical uncertainties come directly from detector data and MC predictions.

The Barlow-Beeston method [124] has been applied since the 2020 oscillation analysis and is used to account for uncertainties from the difference between the generated MC and the theoretical "true" MC (MC with infinite generated events). The statistical likelihood can be broken down into the MC statistical likelihood $\mathcal{L}_{\text{MC stat}}$ and the Poisson likelihood $\mathcal{L}_{\text{Poisson}}$ for each bin:

$$-2\ln\mathcal{L}_{\text{stat}} = -2\ln\mathcal{L}_{\text{MC stat}} - 2\ln\mathcal{L}_{\text{Poisson}} \tag{8.3}$$

The Poisson term $\mathcal{L}_{\text{Poisson}}$ is expressed as

$$-2\ln\mathcal{L}_{\text{Poisson}} = 2\sum_{j}^{\text{samples}}\sum_{i}^{\text{bins}}\left(N_{\text{MC}} - N_{\text{Data}} + N_{\text{Data}}\ln\frac{N_{\text{Data}}}{N_{\text{MC}}}\right) \tag{8.4}$$

where in each bin j of sample i, N_{MC} is the number of events in a given bin in the generated MC, and N_{Data} is the number of events in the bin from detector data.

To account for the $\mathcal{L}_{\text{MC stat}}$ component, an extra scaling parameter β_i is applied to the ith bin such that the number of events is $N_i^{\text{True}} = \beta_i N_i^{\text{Gen}}$, where N_i^{Gen} is the number of events in the bin from the generated MC (equivalent to N_{MC} in equation 8.4), and N_i^{True} is the theoretical "true" number of events. If the scaling parameter can be determined, the true MC value can be used in the fit.

As this method adds a number of additional fit parameters equal to the number of data bins, this would significantly increase the complexity of the fit. Thus, it is assumed that the number of events in a bin follows an independent Gaussian distribution allowing β to be calculated analytically for each bin:

$$\beta^2 + (\mu\sigma^2 - 1)\beta - n\sigma^2 = 0 \tag{8.5}$$

where μ is the number of generated MC events in the bin, including applied weights w_i such that $\mu = w_i N_i^{\text{Gen}}$; σ^2 is the uncertainty in the number events in the bin, calculated as $\sigma^2 = \sum w_i^2/(\sum w_i)^2$; and n is the number of events in the bin from detector data. This allows β to be calculated without any additional parameters.

This is implemented into the $\mathcal{L}_{\text{MC stat}}$ term as:

$$-2\mathcal{L}_{\text{MC stat}} = 2\sum_{i}^{\text{bins}} \frac{\beta_i - 1}{2\sigma^2_{\beta_i}} \tag{8.6}$$

Thus, the total statistical likelihood (equation 8.3) can found by combining equations 8.4 and 8.6:

$$\begin{aligned} &-2\ln\mathcal{L}_{\text{stat}} = \\ &2\sum_{j}^{\text{samples}}\sum_{i}^{\text{bins}}\left[\left(N_{\text{MC}} - N_{\text{Data}} + N_{\text{Data}}\ln\frac{N_{\text{Data}}}{N_{\text{MC}}}\right) + \frac{(\beta_i - 1)^2}{2\sigma^2_{\beta_i}}\right] \end{aligned} \tag{8.7}$$

The other part of the total likelihood, the systematic uncertainties $\mathcal{L}_{\text{syst}}$, is parametrised as:

$$-2\ln\mathcal{L}_{\text{syst}} = \sum_{i}\sum_{j}(p_i - p_i^{\text{prior}})V_{ij}^{-1}(p_j - p_j^{\text{prior}}) \tag{8.8}$$

where p_i and p_j are the current values of fit parameters i and j, p_i^{prior} and p_j^{prior} are their respective priors, and $\mathbf{V}^{-1}$ is the inverse of the prior covariance matrix. The covariance matrix is constructed from prior knowledge of the systematic parameters, and describes the error for each parameter as well as the correlations between them.

8.1.2 GUNDAM Structure

GUNDAM is centred around the parameter propagation engine, called the `Propagator`. The `Propagator` is in charge of applying parameters to the defined samples. GUNDAM's fitter engine (`FitterEngine`) is built on top of the `Propagator` and only drives the changes to the parameter values, leaving the `Propagator` to update the fit samples independently. An overview of the `Propagator` class structure is shown in figure 8.1, which also shows how the sample events and fit parameters are implemented. The `FitterEngine` interfaces with the minimisation algorithms provided by ROOT, which for the analysis in this thesis was `Minuit2` and its algorithms `Migrad`, `Simplex` and `Hesse`. The `FitterEngine` applies the minimisation algorithms to the test-statistic discussed in section 8.1.1 to perform the fit.

GUNDAM is designed to be highly flexible and function as a multi-purpose fitter [125]. It is configured via a collection YAML/JSON files, which set options such as the input files, minimisation strategy, and maximum number of calls.

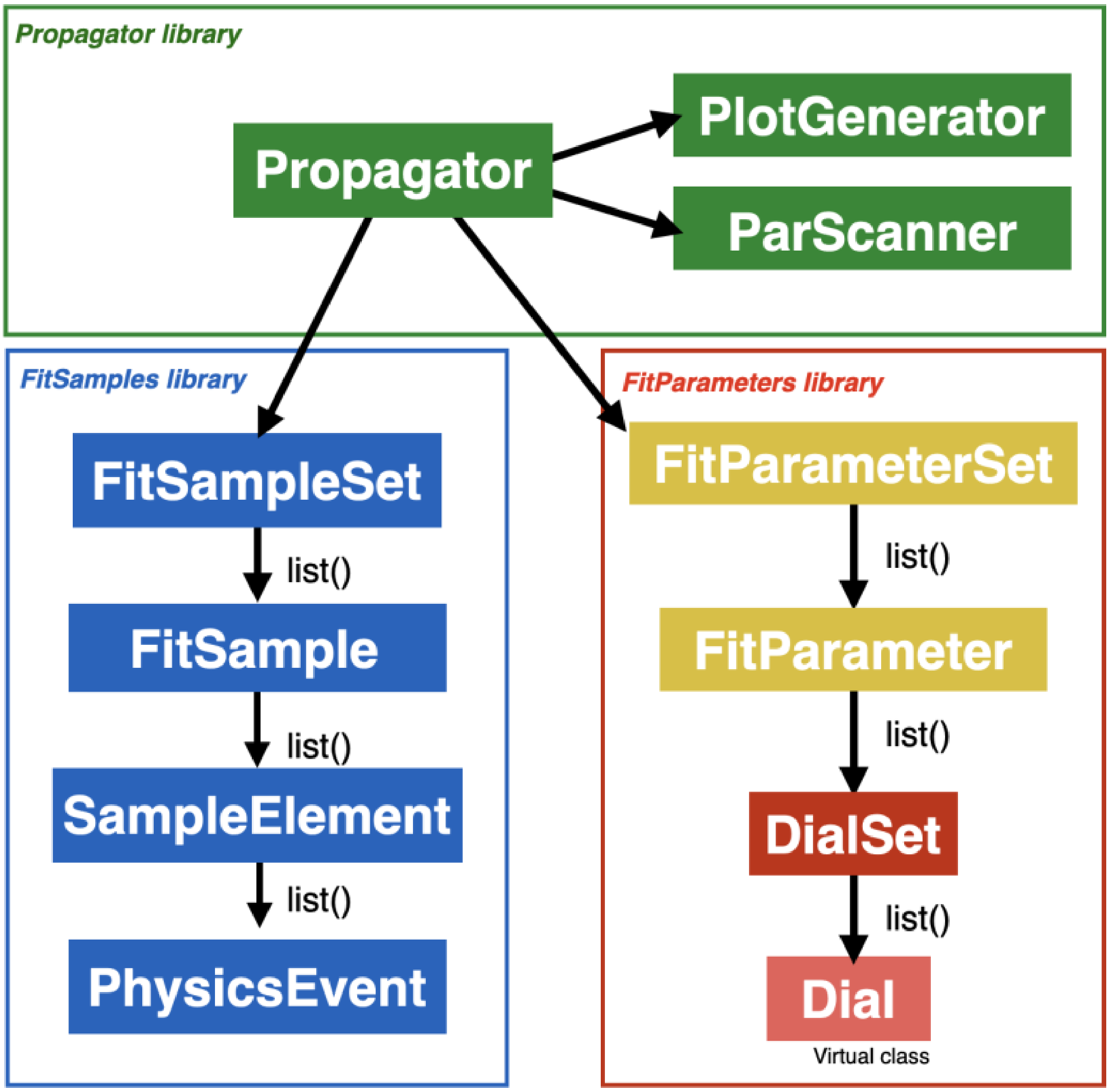

Figure 8.1: Overview of the class structure in the GUNDAM fitter [125]. The `Propagator` class owns the `FitSamples` and `FitParameters` libraries, which contain the physics events sorted by samples and the fit parameters, respectively. The `Propagator` is responsible for propagating changes in the parameters to the events. The parameter changes themselves are fed down to the `Propagator` by the `FitterEngine` (not pictured), which interfaces with the minimisation algorithm.

Chapter 9

Fake Data Studies

The T2K experiment uses the NEUT [87] framework to model neutrino interactions for the Monte Carlo simulations. No perfect model exists that would describe these interactions with perfect accuracy. Thus, the simulations are inherently limited in accuracy and the impact this has on the measurement of the neutrino oscillation parameters must be studied. The nominal model used by NEUT is discussed in chapter 5; however, multiple alternative models exist for different aspects of the interaction. “Fake data sets” are used for this analysis, where the nominal simulation data is reweighted to imitate data generated by these alternative models. These changes may be beyond the typical uncertainties applied when performing a data fit.

In a fake data study, the nominal MC is fitted to the fake data using the GUNDAM fitter (see chapter 8) to identify the differences in the momentum and angle distributions of the final-state muons, as well as parameter values, between the fitted MC and the fake data. It is possible that some fake data models mirror reality more accurately than the current NEUT models, so it must be determined if the fitter is capable of fitting these alternative models given the prior parameter values and their uncertainties in the nominal MC.

A full fake data analysis would include the production of fake data sets for both the near and far detector, and an oscillation analysis with each set to determine any bias in the oscillation parameters caused by the alternative models [125]. This is outside the scope of the analysis presented here, which only focuses on the ND280 detector.

At T2K, there are currently 19 fake data sets. Each fake data study is implemented

Fake Data Study	Model Component	Description	Results
SF to LFG	Nuclear Model	9.1.1	10.4.1
SF to CRPA	Nuclear Model	9.1.1	10.4.2
SF to SuSAv2	Nuclear Model	9.1.1	10.4.3
Z-Expansion AFF	CCQE	9.1.2	10.5.1
3-Component AFF	CCQE	9.1.2	10.5.2
LQCD Z-Expansion	CCQE	9.1.3	10.5.3
SPP Matrix Element	CC1π	9.1.4	10.6.1
SPP Adversarial;	CC1π	9.1.5	10.6.2
RS to Martini	CC1π	9.1.6	10.6.3
Low Q^2 SPP	CC1π	9.1.7	10.6.4
CC0π Non-QE	CC0π	9.1.8	10.7.1
2p2h Eb Correction	2p2h	9.1.9	10.7.2
MultiPi Multiplicity	DIS	9.1.10	10.7.3

Table 9.1: List of fake data studies and the component of the model they affect, with link to relevant sections for descriptions and fit results. Certain studies have been merged in this table (e.g. SPP Matrix Element has two associated fake data studies) hence fewer than 19 studies are listed.

as parameter tweaks in `NIWGReWeight`, which are applied to the nominal MC files. The parameter settings used for each study are given in Appendix A. The nominal MC is initially in FlatTree file format, which is used as an input for `OAGenWeightsApps`, which interfaces with `NIWGReWeight` via `T2KReWeight`. This reweighting process produces files in spline format, which are used as the input for GUNDAM. The spline format and how it is used in GUNDAM is discussed in section 10.2.

9.1 List of Fake Data Sets

Fake data sets (FDS) are generated from nominal MC by applying weights to certain dials, the weight values depending on the specific FDS. The nominal parameter values and uncertainties in the MC files are converted to splines when this weighting is applied, which are used as the input for the GUNDAM fitter. There are a total of 19 fake data sets used in this analysis, which are described in the following sections. Each of the FDS presented here are motivated by a theoretical model or experimental result, often from other neutrino experiments. Some are considered “extreme” compared to T2K results (i.e. far beyond any measurement made at T2K), but each represents some plausible physical reality. Table 9.1 highlights which part of the interaction model they affect, and the numbering of the relevant sections where the description and fit results are provided.

9.1.1 Nuclear Models: LFG, CRPA and SuSAv2

Nuclear effects constitute one of the largest uncertainties in CCQE neutrino interactions [125]. As such, exploring the effects of alternative models via fake data studies allow the robustness of the analysis to realistic changes in the CCQE model predictions to be tested. Local Fermi Gas (LFG), Continuum Random Phase approximation (CRPA) and SuperScaling Approach V2 (SuSAv2) are models that predict different ν_μ cross sections as a function of energy, different ν_μ /$\bar{\nu}_\mu$ cross section asymmetries, different carbon/oxygen cross section ratios, and changes to the ν_μ /ν_e cross section difference. Figure 9.1 shows the effects of these models on the ν_μ cross section.

The reweighting is performed by finding the ratios of the differential cross sections as a function of (anti)neutrino flavour, nucleus type, neutrino energy, lepton momentum, and lepton angle. For LFG, these cross sections are read from pre-calculated histograms created from 100 million NEUT events. For CRPA, the cross sections are calculated from hadron tensor tables. As the non-relativistic assumptions in CRPA are invalid at high energy transfer, the CRPA fake data set reweights to SuSAv2 for energy transfers above 1 GeV. In the $0.5 - 1$ GeV range, there is a transition between the models [126].

These models are applied only to carbon and oxygen nuclear interactions as the majority of detected interactions occur in plastic scintillator or water targets.

9.1.2 Axial Form Factors: Z-Expansion and 3-component

The axial part of the electroweak nucleon form factor lacks strong experimental motivation for a specific parametrisation so a nominal model with a single dipole is used, made by analogy with electromagnetic form factors [128]. NEUT uses such a model, with additional parameters for high Q^2 interactions ($Q^2 > 0.25$ GeV). However, experimental evidence suggests that a single free parameter is insufficient to describe the relevant range for Q^2 transfer [125]. As there are multiple possible parametrisations, two different models are used in this analysis: z-expansion and 3-component.

Z-expansion is a model-independent parametrisation based on QCD sum rules [129], while the 3-component model expands the simple dipole model to have three free parameters,

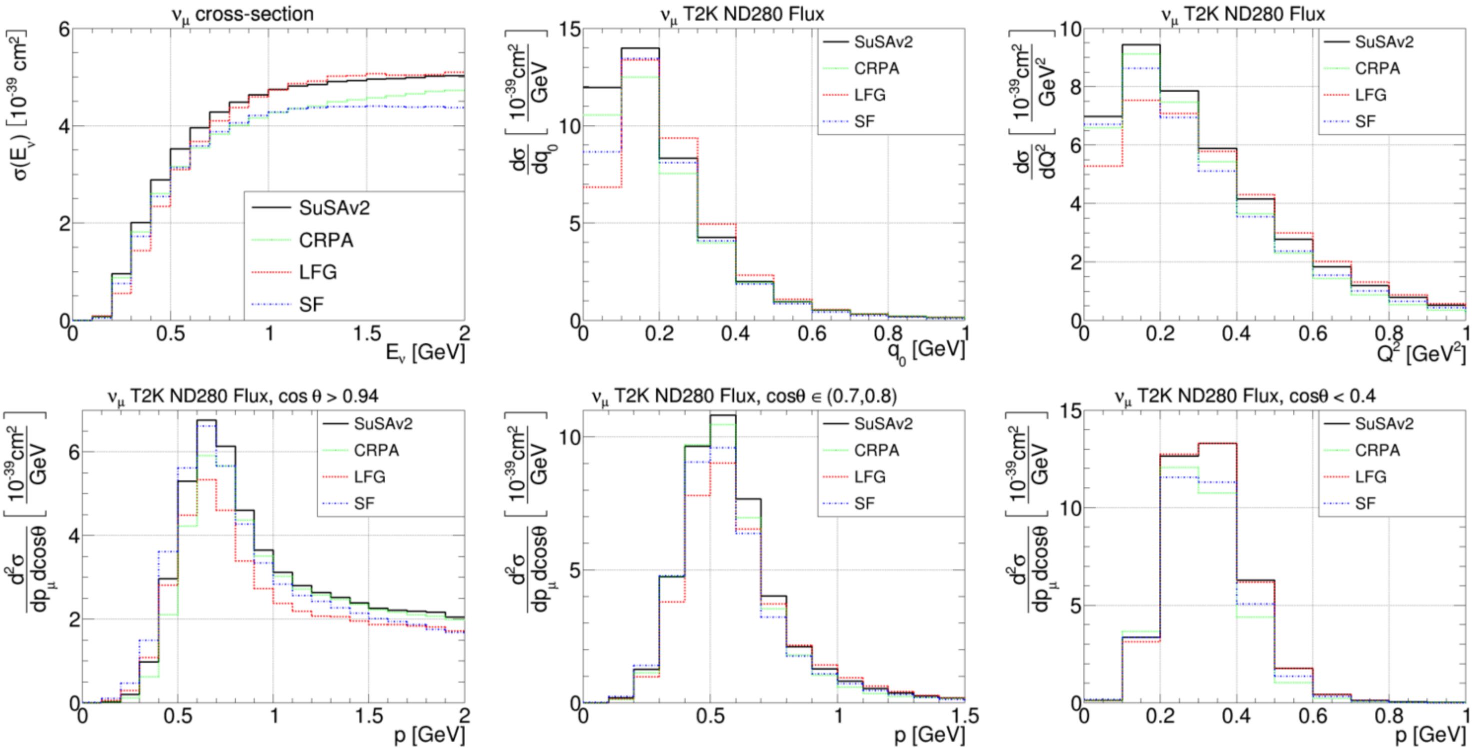

Figure 9.1: Comparison of the muon neutrino cross section for the various nuclear models used in the fake data studies. The top left plot shows the total cross section as a function of energy, while the other plots show the differential cross section averaged over the neutrino flux. The nominal NEUT model is a spectral function (SF) is the dashed blue line, while the alternative models are SuSAv2, continuum random phase approximation (CRPA) and local Fermi gas (LFG), shown in solid black, dashed green, and dashed red lines, respectively. These are shown as a function of energy and four-momentum transfer (top row) and outgoing muon momentum and angle from the detector's longitudinal axis (bottom row). Plots from [127]

so has more freedom at low Q^2 compared to the nominal model. Each model has three associated fake data sets: one nominal model, and one each for $\mp 1\sigma$ (standard deviation) shifts in the uncertainty of the model.

9.1.3 Lattice QCD Z-Expansion

The lattice QCD z-expansion fake data set follows a similar model to the z-expansion study described above, but uses lattice QCD to calculate the form factor and uncertainties [130]. This model has two associated fake data sets: the nominal model and -1σ.

9.1.4 Single Pion Production Matrix Element -1/+1σ

In the NEUT model, the single pions produced in $\Delta(1232)$ resonance decays resulting in a 1π and a nucleon have a high degree of uncertainty in their kinematics. These two fake data sets uses a $\mp 1\sigma$ variation of the Δ matrix element to vary the pion kinematics, without affecting the outgoing lepton distribution. Despite what the name might suggest, this is actually achieved by varying certain parameters (see appendix A) by $\mp 3\sigma$. This name is purely due to convention, and is somewhat arbitrary. The -1σ set has the effect of increasing the cross section at low pion momentum ($p_\pi < 160$ MeV) by $\sim 20 - 30\%$ and decreasing it by a similar amount at higher momenta. For $+1\sigma$ this effect is reversed.

This fake data study is not expected to significantly change the near detector fit as the overall μ^- momentum/angle distribution should remain the same, but would have a more significant effect at the far detector.

9.1.5 SPP Adversarial

Contrasted to the theory-driven approach to pion kinematics described in section 9.1.4, the SPP adversarial data set is data-driven. ND280 and SK measurements show discrepancies in low-momentum pion production [131]. For TPC pions this is concentrated at low energies ($<$ 300 MeV) and high angles, where the prediction underestimates the detector data. Michel-tagged pions show a postfit overestimation of $\sim$ 20% (see figure 9.2). A scaling factor has been calculated for each pion topology to change the shape of the spectra while preserving the cross section: all CC1π events are re-weighted by a factor of 0.7 if the highest momentum final-state pion has a momentum of less than 0.3GeV/c [132]

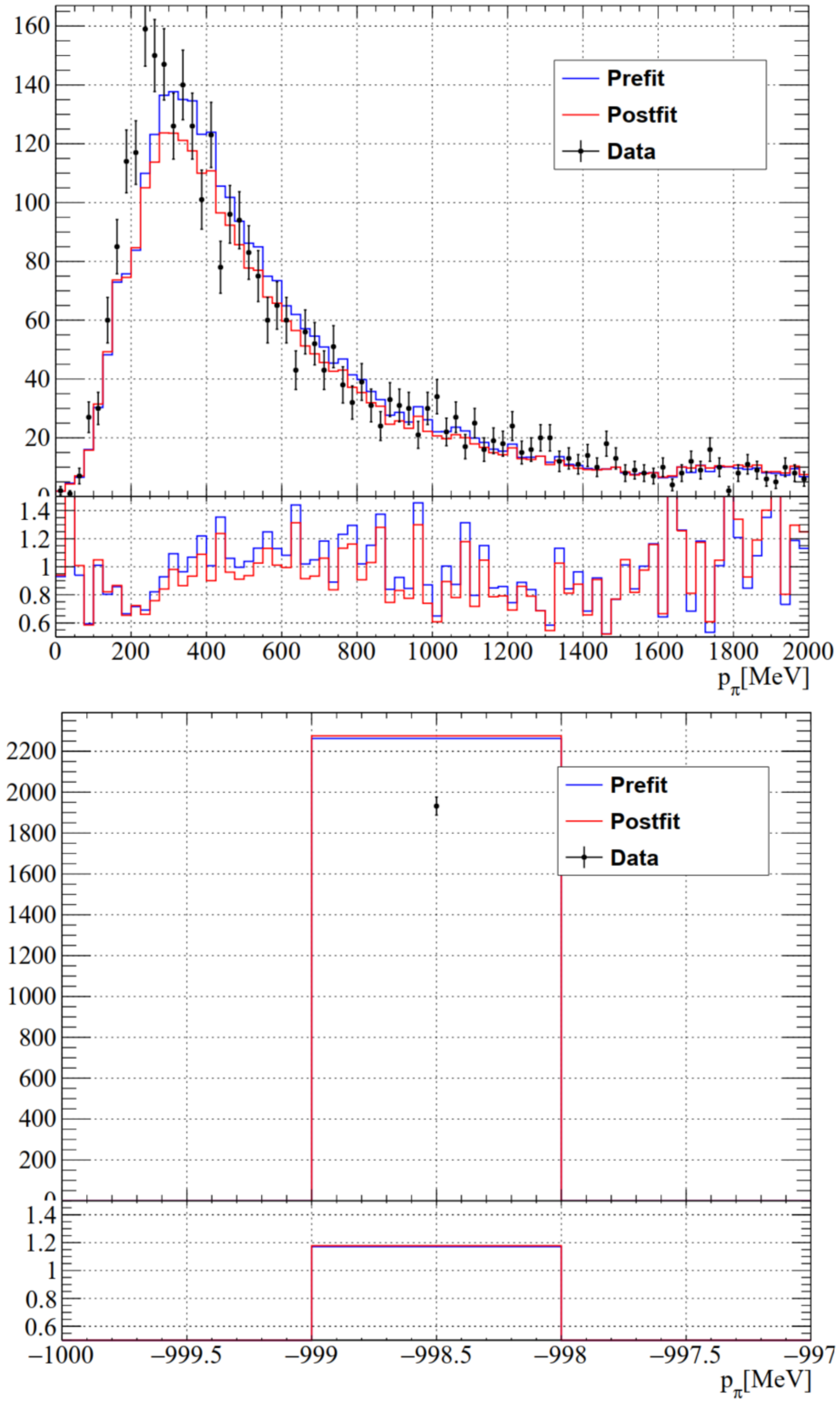

Figure 9.2: Momentum distributions for pre/postfit and reconstructed data for TPC tagged pions (top) and Michel tagged pions (bottom) for FGD1 CC1π selection [125]. Data is shown as black dots, prefit in solid blue, and postfit in solid red. The TPC plot shows a deficit in postfit compared to data in the peak region, while the Michel plot shows an excess in postfit compared to data. This discrepancy is what has motivated the SPP adversarial fake data study. −999 MeV is the nominal value used for Michel electrons in the analysis.

9.1.6 RS to Martini Model

The RS to Martini fake data set is based off a neutrino-nucleus interaction model developed by Martini and collaborators, built on a random phase approximation approach to nuclear responses, and includes Δ-resonance excitations [133]. NEUT's nominal Rein-Sehgal model only models neutrino-nucleon interactions, with corrections for nuclear effects added in afterwards. The Martini model, on the other hand, describes the neutrino interaction with the entire nucleus. Currently, this fake data study only applies the model's effects to 1π production, but can potentially be extended to other interaction channels.

9.1.7 Low Q^2 Suppression Single Pion Production

This FDS significantly suppresses single pion production at lower Q^2, a suppression of roughly 20% at the Q^2 peak. This has been motivated by analysis of MINERνA pion production results and the GENIE event generator [134]. However, no substantial evidence suggests that it is applicable to the NEUT framework used by T2K given that there are significant differences in the base single pion production models, especially in the low-Q^2 region. Additionally, the T2K pion production data itself does not suggest a need for such low-Q^2 suppression [79]. Nevertheless, this is useful as an extreme fake data study to test the behaviour of the fit under very large changes.

9.1.8 CC0π Non-QE

The CCQE model is given much freedom to correct differences between data and simulation in CC0π (charged current neutrino interactions that produce zero pions) samples due to the large number of uncertainties assigned to it. Thus, inadequacies in the models of other (non-QE) contributions to this sample (e.g. 2p2h, pion absorption) are potentially "soaked up" by the CC0π model. The CC0π Non-QE fake data set ascribes almost all variation in CCQE caused by QE parameters to the non-QE models. This is achieved by performing a fit, resetting the CCQE portion of the postfit simulation back to its prefit values, then altering only the CC0π non-QE contributions to restore the fit.

9.1.9 2p2h Eb Correction

The 2p2h (see section 5.2.2) Eb correction fake data study introduces a correction for the nuclear binding energy *Eb* which includes the mean field potential responsible for binding the nuclear system [135].

9.1.10 MultiPi Multiplicity

The nominal MC uses a custom DIS model for multiple pion production, with a multiplicity model used to determine the number of pions produced. However, external datasets for multi-pion production can differ significantly, leading to a high degree of variability in the choice of model [127] [136]. This fake data set uses an alternative model which adjusts the cross section as a function of the neutrino energy, the hadronic invariant mass, and the multiplicity probability for a given hadronic mass range. This has the effect of increasing the ν_μ -nucleon cross section for multiple pion production compared to the nominal NEUT model, as shown in figure 9.3.

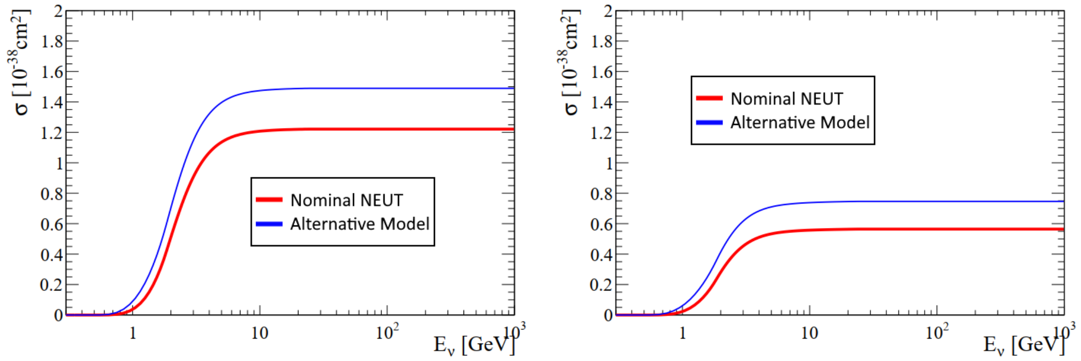

Figure 9.3: Effect of the alternative pion multiplicity model on the cross sections in the NEUT multipi model, for ν_μ interactions on neutron (left) and proton (right) target nucleons. The increased cross section, especially at higher energies, will increase the number of events producing multiple pions. Plot adapted from [127].

9.2 Conclusion

Fake data studies are an important part of the T2K analysis, as they allow us to test our analysis tools against alternative particle interaction models, beyond just the nominal NEUT model used in the main MC simulation. This chapter has presented details on 19 fake data studies that are analysed in this thesis, which cover a range of different components in the model, including the nuclear model, CCQE interactions, and CC1π interactions. Some of these models represent very plausible alternatives to the nominal model, such as the Z-expansion and 3-component axial form factors. Others, such as the low Q^2 SPP suppression, represent a reality far outside of what has been measured at T2K, but are useful in testing the capabilities of our analysis tools.

The results of the fake data analysis, using the GUNDAM fit, is presented in chapter 10.

Chapter 10

Fake Data Fit Results and Analysis

This chapter presents and discusses the results of the GUNDAM fit analysis of the fake data studies (FDS). First, the generation of the fake data input files for GUNDAM is discussed, including particular idiosyncrasies for specific studies. Next, the interpolation types used for different systematic parameters and the effect they have on the fit are explored. Finally, the full results for each of the 19 fake data studies are presented and analysed in detail.

10.1 Inputs

This analysis was performed over the set of MC files for runs 2 to 9. These runs and their associated POT values, horn current, etc were previously described in section 7.1.1. Sand events (events from particles created between the proton target and ND280 detector) were not included in this analysis.

Parameter inputs for GUNDAM are formatted as splines. A spline is a mathematical object consisting of a piecewise function produced by interpolating across some number of points, called knots. The interpolation is performed separately between each knot, and must be continuous between the functions at each knot. This contrasts to fitting with a single polynomial, where the curve is defined by just one global function. In GUNDAM, the parameter priors are defined as event weights for variations of $\pm 3\sigma$, $\pm 2\sigma$ and $\pm 1\sigma$ around a central value, for a total of seven knots. Splines are discussed further in section 10.2.

The GUNDAM input splines are generated from the nominal MC flat tree files using the programs in the `OAGenWeightsApps` software package, which also applies the fake data reweighting. Within the `OAGenWeightsApps` software, the `ND280GenWeights` program is used first to apply the FDS weights to the cross section parameters and to convert the flat trees to spline format. These splines are then used as inputs to `makeND280SystSplines` which converts the detector systematics to splines. Finally, `GetPOTweight` is used in conjunction with the real data splines (generated similarly to MC splines, but with real data flat trees) to reweight the FDS spline POT values to match the data values.

Certain fake data studies require certain parameter values to be set at the beginning of the GUNDAM fit, when the FDS spline files are first loaded. All studies which affect the nuclear model or nuclear form factor need the axial mass parameter M_A^{QE} to be changed from 1.03 GeV to 1.21 GeV. The MC simulation initially sets the parameter to 1.21 GeV, but the spline production process changes it to 1.03 GeV, which is preferable for a fit of the nominal MC to real data. However, these particular fake data studies are calibrated around $M_A^{QE} = 1.21$ GeV, hence it needed changed back to the nominal NEUT value used when it was originally generated.

There is a further exception for the three fake data studies which change the nuclear model: SF to LFG, SF to CRPA, and SF to SuSAv2. The parameter values for the carbon and oxygen nuclear binding energies, `EB_bin_C_nu` and `EB_bin_O_nu`, respectively, must be reset to 0. However, this cannot be performed as a parameter change when the spline files are loaded into GUNDAM. Instead, a “dry run” of GUNDAM first is performed to convert the spline files into raw histograms, without performing any fit. The binding energy parameter change is applied at this stage, and the new histogram files can be fed back into GUNDAM as inputs for a full fit.

The fit was performed with mirroring applied to certain parameters, meaning that parameter values that would go beyond physical boundaries are “reflected” to a value of the same magnitude on the other side of the boundary. This affects the parameters for FSI strength, RPA strength, 2p2h shape, CC resonant interactions, and Δ decays.

10.2 Splines and Interpolation

As previously mentioned, the inputs for GUNDAM are formatted as splines, which are piecewise functions interpolated between knots. For the ND fit, the interpolation is generally performed by a cubic function, defined as a “spline” type parameter in the configuration, or a linear function, defined as a “graph” type parameter. The cubic interpolation is modified with “not-a-knot”, which ensures second-derivative continuity for the first and last interior knots. Also, for certain parameters, the cubic interpolation is further modified as “monotonic” or “catmull-rom monotonic”. The former preserves monotonicity for knots strictly increasing or decreasing, and the latter makes a point on a curve depend on the nearest four knots instead of the nearest two. These are applied to FSI and RPA strength parameters and Bodek-Yang DIS correction parameters, respectively.

The effect of the interpolation method on individual parameters can be significant. Early attempts to fit fake data with GUNDAM used linear interpolation for the FSI strength and RPA strength parameters, which was shown to be ineffective and produced poor results. Figure 10.1 shows the effect of this change on the FSI strength parameters for the SF to LFG fake data study. Previously, when using the linear interpolation, certain parameters showed negligible changes in the central parameter value and the uncertainties had disappeared completely. It was initially thought to be a plotting error, but changing from linear to cubic interpolation recovered the uncertainties and produced results closer to what was expected. The interpolations methods used in this analysis are from the latest (at time of writing) GUNDAM configuration, which are optimised for MC to real data fits.

10.3 Fake Data Results

The following sections discuss the results of the GUNDAM fit for the 19 fake data studies. Comparisons between the fake data and the nominal/fitted MC is presented as 2D ratio plots across the momentum and angular distributions of reconstructed muons, in samples from the 4π selection. The value of each bin in the ratio plots, $R_{MC/FD}$, is calculated as

$$R_{MC/FD} = \frac{\text{Number of events in MC bin (nominal or fitted)}}{\text{Number of events in fake data bin}} \tag{10.1}$$

The χ^2 value for each plot is calculated as:

$$\chi^2 = \sum_i \frac{(N_i^{\text{Data}} - N_i^{\text{MC}})^2}{N_i^{\text{MC}}} \tag{10.2}$$

where N_i^{Data} is the number of events in bin i in the fake data distribution and N_i^{MC} is the number of events in bin i in the MC distribution (nominal or fitted, depending if plot is prefit or postfit). The number of degrees of freedom (DoF) in the fit is 4137. As this is

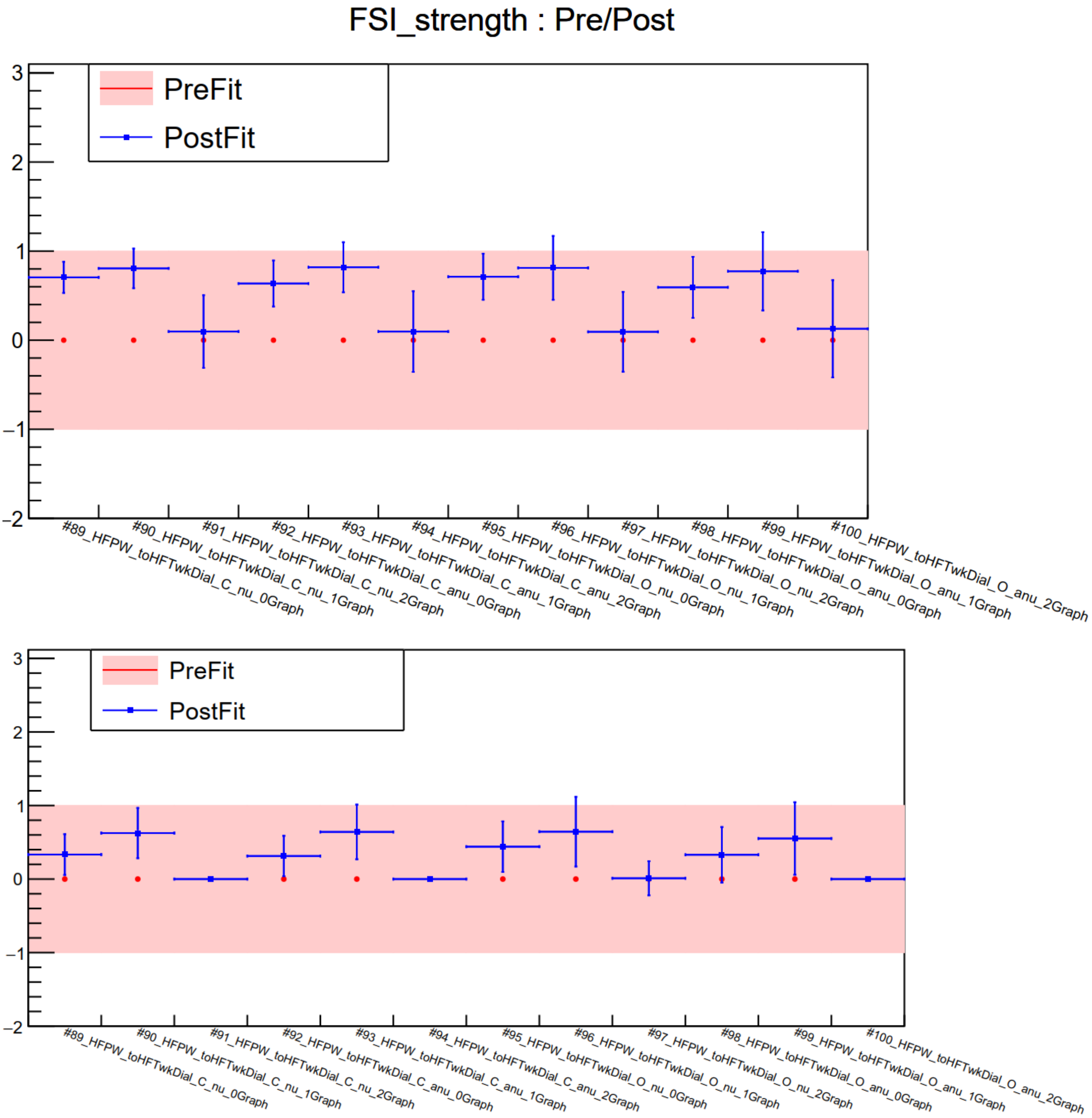

Figure 10.1: Effect on FSI strength parameters for the SF to LFG fake data set GUNDAM fit, showing the current (cubic) interpolation method (top plot) versus the old (linear) method (bottom plot). The central values of the prefit are shown as red points, with pink shading showing the uncertainties. The postfit values are shown as blue points with uncertainties as error bars. The old method produced fitting errors, such as the disappearance of the error bars for some parameters.

very large compared with the χ^2 values calculated, they are not normalised against the DoF for readability, and primarily is to illustrate the quality of the postfit compared to the prefit.

The sensitivity of each of the 4π samples (described in chapter 6.2) to a fake data study can differ significantly depending on which part of the model the study affects. For the following sections, the primary focus will be on the “most significant” sample for each study, which were identified in the previous BANFF analysis [125]. For example, the CC0pi0p0γFwd sample is the most sensitive to studies affecting the nuclear model and axial form factors. New studies not present in the previous analysis will use whichever sample the study is expected to affect the most. The previous work also analyses how each fake data study affects the oscillation parameters; however, this is outside the scope of the work presented here, which focuses exclusively on the near detector. All prefit and postfit samples for each fake data study are available in appendix B.

The fits were performed using the 1.8.X LTS (long-term support) version of GUNDAM. As GUNDAM is still under development, this version was chosen as it provides all necessary analysis tools and bugfix updates, without the potential instability of newly-released versions.

10.4 Nuclear Models

This section discusses the results for the fake data studies that affect the nuclear model: SF to LFG in section 10.4.1, SF to CRPA in section 10.4.2, and SF to SuSAv2 in section 10.4.3. These models are described in detail in section 9.1.1. Given the wide range of interactions this study can affect, the CC0pi0p0γFwd sample has been chosen as the most significant sample for these studies. It is one of the most important samples used in the oscillation analysis and is the dominant sample in terms of number of events [53]. It is comprised mainly of CCQE events, which is the dominant form of neutrino interactions near the beam energy peak of $\sim$ 600 MeV.

10.4.1 SF to LFG

The Spectral Function to Local Fermi Gas fake data fit is shown in figure 10.2, showing the 2D distributions of momentum and $\cos\theta$ for reconstructed muons before and after the GUNDAM fit as the left and right plots, respectively. As the majority of muon tracks are angled close to the detector's central axis, the region around $\cos\theta_\mu = 1$ is considered the most significant; this also applied for the other fake data studies. To reflect this, the axis for the angular distribution has a lower limit of $\cos\theta_\mu = 0.6$. From the prefit, it can be seen that the fake data reweighting shows a high $R_{MC/FD}$ ratio at low four-momentum transfer squared (Q^2) and low $R_{MC/FD}$ at high-Q^2. The low-Q^2 region of neutrino events at ND280 ($Q^2 < 0.25$ GeV) roughly corresponds to the red shaded region on the prefit plot. This region corresponds to events producing forward-going ($\cos\theta_\mu \approx 1$) muons, as well as higher-angle muons at relatively low energies. High-energy interactions have smaller scattering angles than low-energy due to conservation of linear momentum, hence high- and low-Q^2 events have distinct regions in both the momentum and angular distributions. The distribution produced for this analysis shows strong similarities with the 2021 BANFF analysis (BANFF being the predecessor to GUNDAM), shown in figure 10.3, except that the newer plots have much coarser binning. These binning changes are the result of optimisations to BANFF's binning performed by Ewan Miller in 2023 [137]. The optimised binning increased the bin size to ensure a sufficient number of data and MC events are in each bin for a more effective analysis. The newer binning has been copied across to GUNDAM, as the similarities between GUNDAM and BANFF mean the optimisation should still apply. However, this change makes it difficult for a direct comparison with the old binning used in the previous fake data analysis.

The postfit results show that the difference between the fitted MC and the fake data is significantly reduced, as expected. This result is, by inspection, very similar to the 2021 fit with both showing the largest difference to be $\lesssim 5\%$. The GUNDAM fit was calculated to have a χ^2 of 2.321, which is significantly lower than the χ^2 of 39.8 seen in the 2021 analysis. This is likely to be the result of the binning changes, hence the difficulty in making a direct comparison. The prefit for this analysis has a χ^2 value of 180.7.

The effect of the fit on the systematic parameters for the cross section are shown in figures 10.4, 10.5 and 10.6. There are significant changes in the values of the CCQE parameters and very little change in the SPP, DIS, and Misc parameter values; however, all plots show the reduction in uncertainties, which is the main point of the ND fit. The flux parameters show only small changes, and the postfit values are all within the uncertainties of the prefit. This shows that the cross section parameters are capable of compensating for the majority of the fake data-MC difference, suggesting that the cross section model has sufficient degrees of freedom to fit data in a universe where the "true" nuclear model is local Fermi gas. The parameter adjustments for the FSI and RPA strength are very large for the low-energy parameters (parameters ending in `0Graph` and `1Graph`), which correlates with the significant change in low-energy event numbers seen in the prefit plot in figure 10.2.

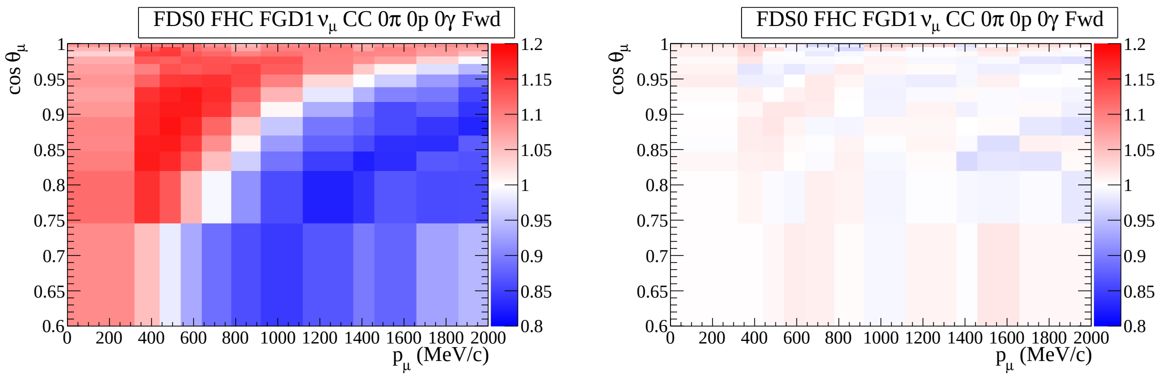

Figure 10.2: Prefit (left) and postfit (right) plots for the SF to LFG fake data study, showing the CC0π0p0γFwd sample. The colour of each bin shows the value of the ratio $R_{MC/FD}$. The prefit has a χ^2 value of 180.7 and the postfit has a value of 2.321. There is strong similarity in the prefit to the 2021 BANFF analysis (below, figure 10.3), and the postfit shows an improvement over the 2021 result, demonstrating GUNDAM can successfully fit this fake data at least as well as the previous BANFF fitter.

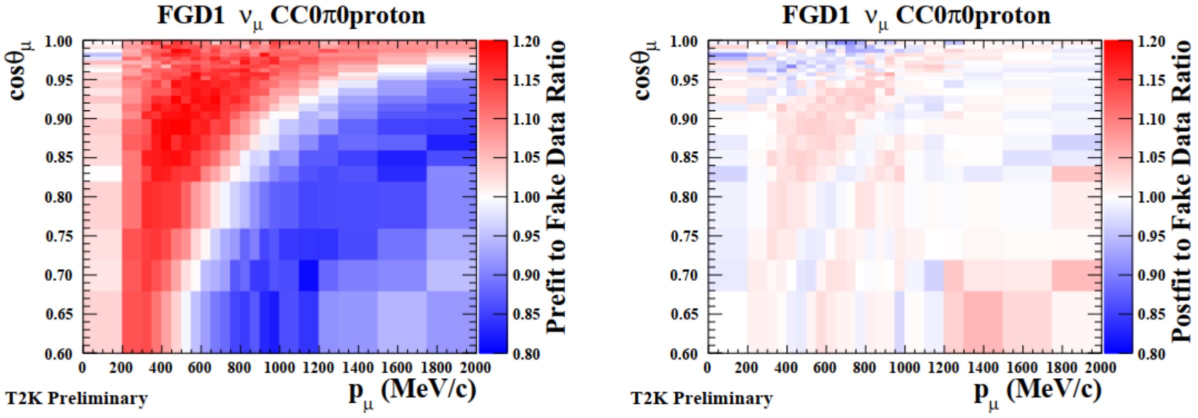

Figure 10.3: Prefit (left) and postfit (right) for the SF to LFG fake data study in the 2021 BANFF fake data analysis, showing the CC0π0γFwd sample. The colour of each bin shows the value of the ratio $R_{MC/FD}$. Plot adapted from [125].

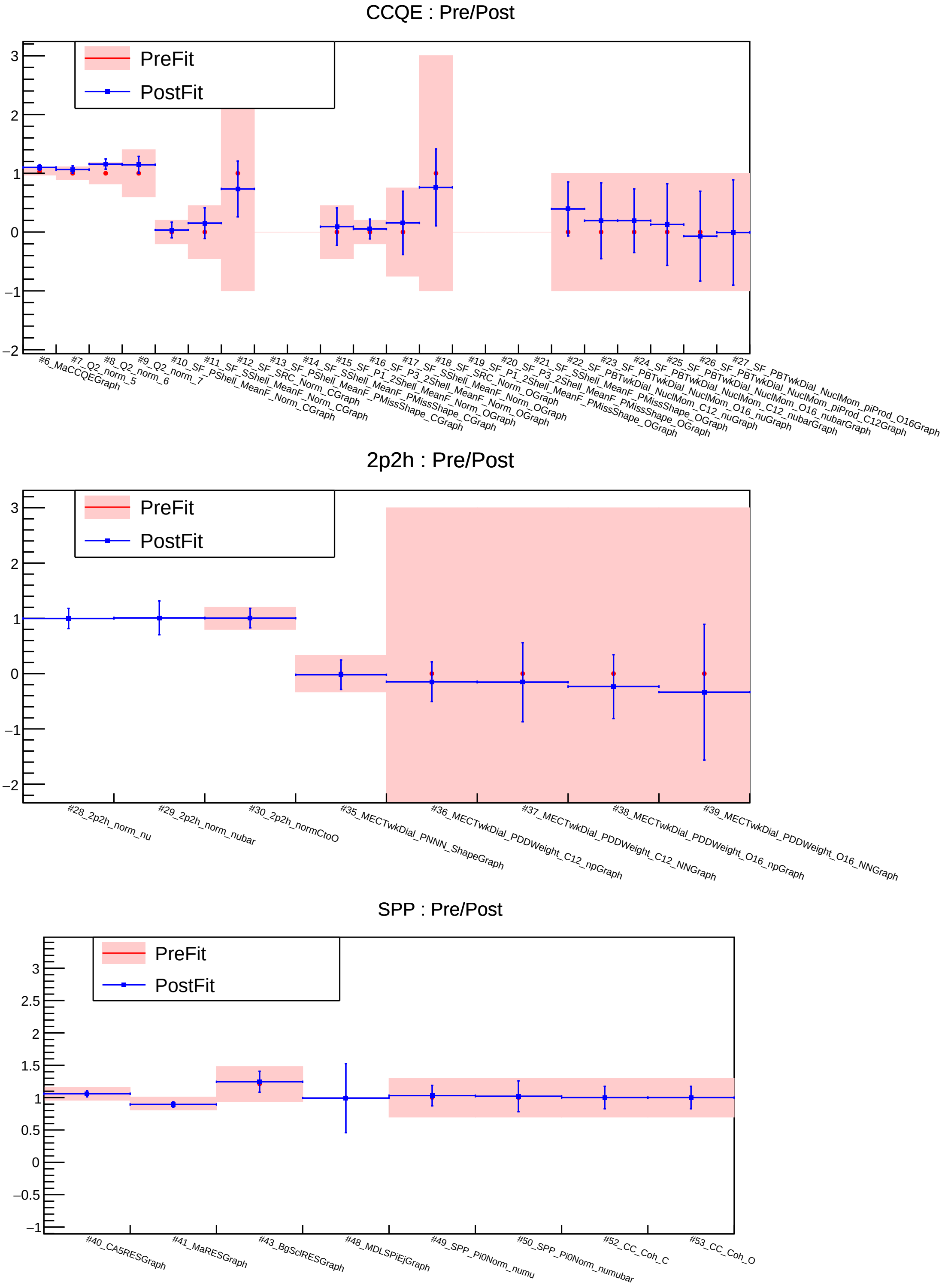

Figure 10.4: Cross section systematic parameters from the GUNDAM fit for the SF to LFG fake data study, showing CCQE (top), 2p2h (middle), and single pion production (bottom). The central values of the prefit are shown as red points, with pink shading showing the uncertainties. The postfit values are shown as blue points with uncertainties as error bars. The blank areas correspond to parameters that are fixed in the fit as they were expected to have a very low sensitivity to the fit [90], hence they have no postfit.

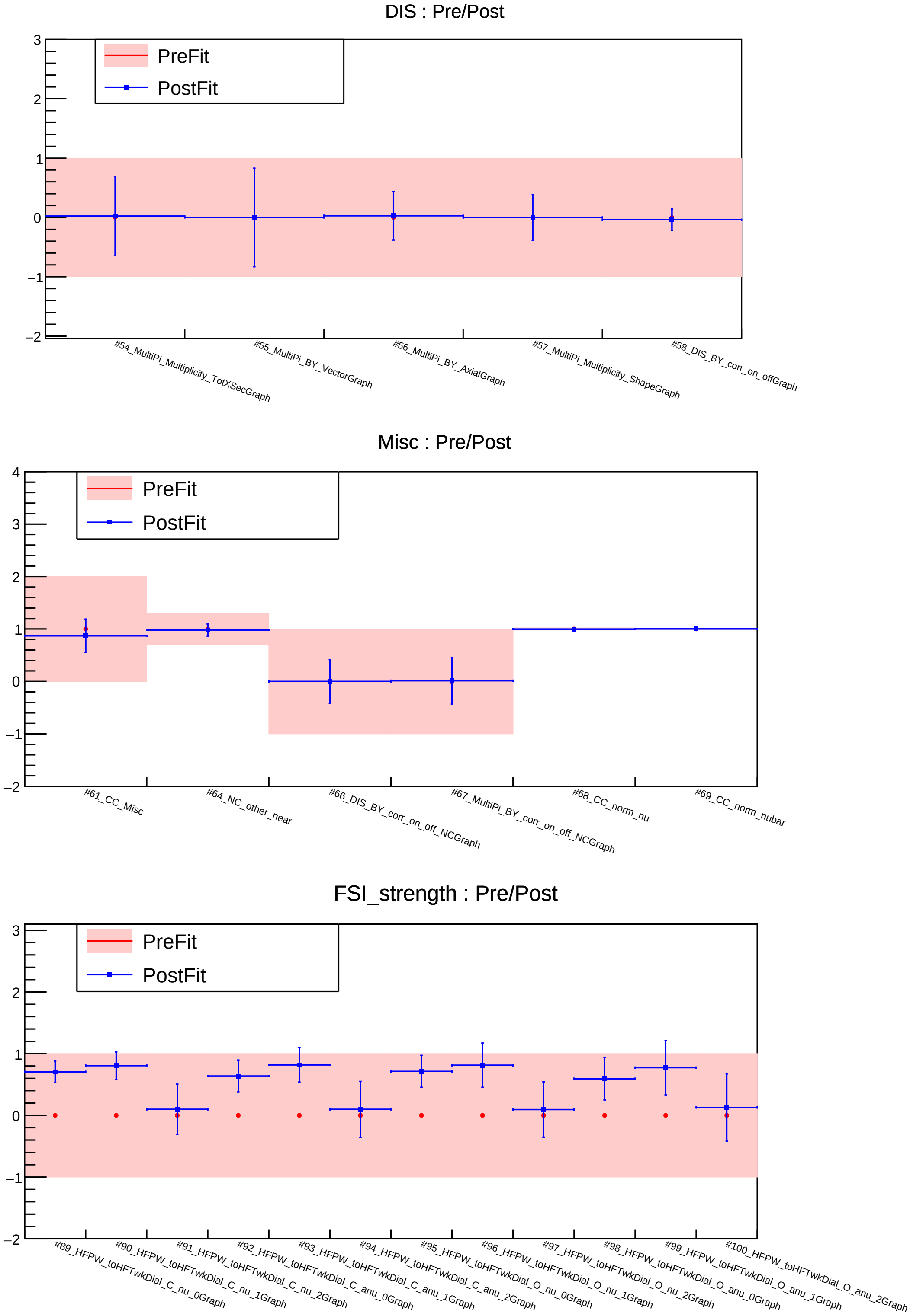

Figure 10.5: Cross section systematic parameters from the GUNDAM fit for the SF to LFG fake data study, showing DIS (top), miscellaneous parameters (middle), and FSI strength (bottom). The central values of the prefit are shown as red points, with pink shading showing the uncertainties. The postfit values are shown as blue points with uncertainties as error bars. The postfit parameters are shown to be within the uncertainty ranges of the prefit, which suggests the existing priors are sufficient for fitting for this fake data study.

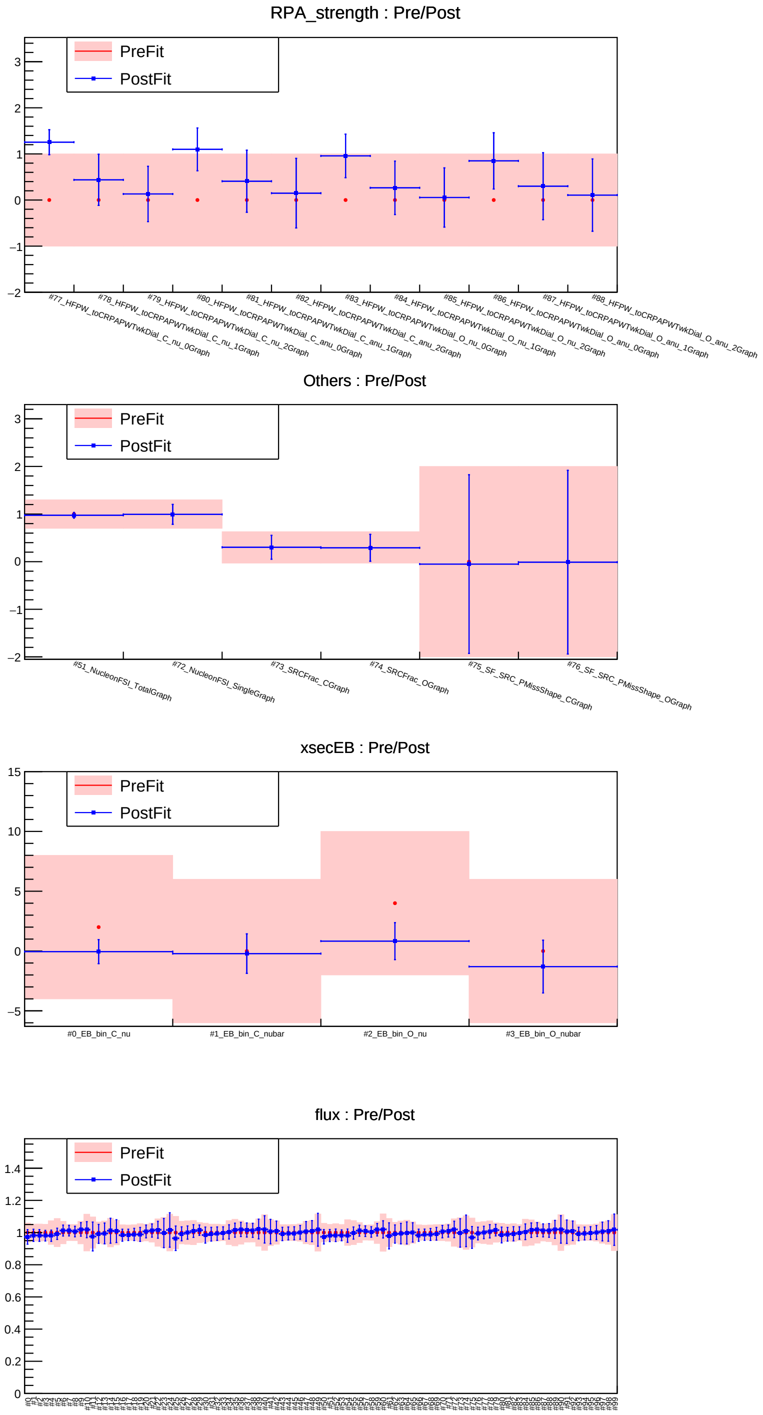

Figure 10.6: Cross section systematic parameters from the GUNDAM fit for the SF to LFG fake data study. From top to bottom: RPA strength, other parameters, binding energy, and beam flux. The central values of the prefit are shown as red points, with pink shading showing the uncertainties. The postfit values are shown as blue points with uncertainties as error bars. The postfit parameters are shown to generally be within the uncertainty ranges of the prefit, which suggests the existing priors are sufficient for fitting for this fake data study.

10.4.2 SF to CRPA

The Spectral Function to Continuum Random Phase Approximation fake data fit is shown in figure 10.7, showing the 2D distributions of momentum and $\cos\theta$ for reconstructed muons before and after the GUNDAM fit. The prefit plot shows an increase in $R_{MC/FD}$ at low muon momentum around $\cos\theta_\mu = 1$ and a decrease in $R_{MC/FD}$ at higher muon momentum, suggesting a decreased cross section at low-Q^2 and an increase at high-Q^2. This is similar to the SF to LFG study, but the effect covers a smaller Q^2 range. Also visible is an increase in $R_{MC/FD}$ in the range $p_\mu = 1000 - 1200$ MeV. Both of these features are also visible in the 2021 analysis, shown in figure 10.8. The GUNDAM fit does not fully resolve the postfit-to-fake-data difference, as there is still a strong excess in muons in the fitted MC compared to the nominal MC around $\cos\theta_\mu = 1$. Similar results were seen in the 2021 analysis, but it can be seen the GUNDAM results show an improvement as the largest differences have been reduced from $\sim 20\%$ to $\sim 10\%$. This is an expected improvement due to the changes to fit parameters (new FSI strength and RPA strength parameters designed for low-Q^2 events), so the improved fit is a positive sign. However, it must be noted that the current binning is much coarser compared to the old analysis, so large differences over a narrow momentum range might be absorbed into larger bins.

The parameter changes from the fit are shown in figures 10.9, 10.10, and 10.11. There is a significant increase for some of the Pauli blocking parameters, the last six in the CCQE parameter plot, which is opposite to what was observed in the 2021 analysis, shown in figure 10.12. However, there have been major changes to the parameters used in the analysis, as the Optical Potential has been removed and FSI and RPA strength parameters introduced, so it is expected for there to be differences in the two analyses.

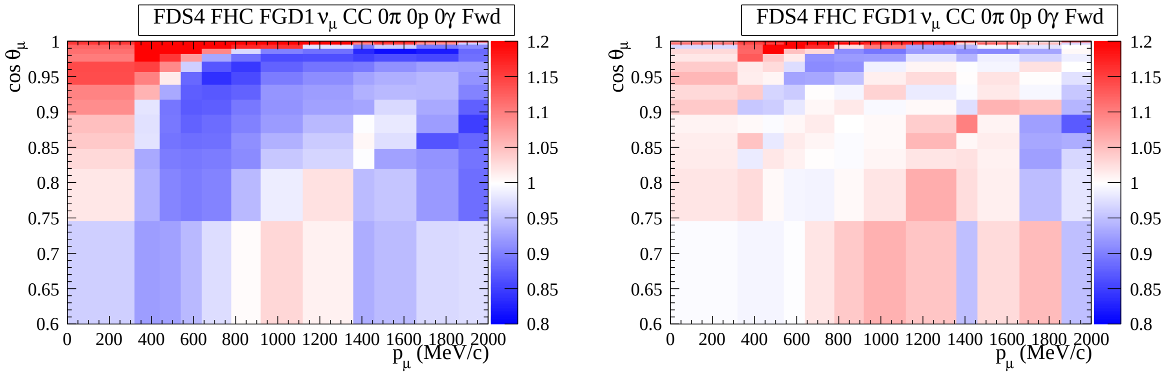

Figure 10.7: Comparisons between prefit (left) and postfit (right) for the SF to CRPA fake data study in the CC0π0p0γFwd sample. The colour of each bin shows the value of the ratio $R_{MC/FD}$. The prefit has a χ^2 value of 193.0 and the postfit has a value of 32.6. the fit has not been able to fully resolve the data-MC difference, and there is still some significant differences between the MC and the fitted fake data. However, similar results were observed in the 2021 analysis (figure 10.8), so this at least an indication the new fitter and parameter changes have not made things any worse.

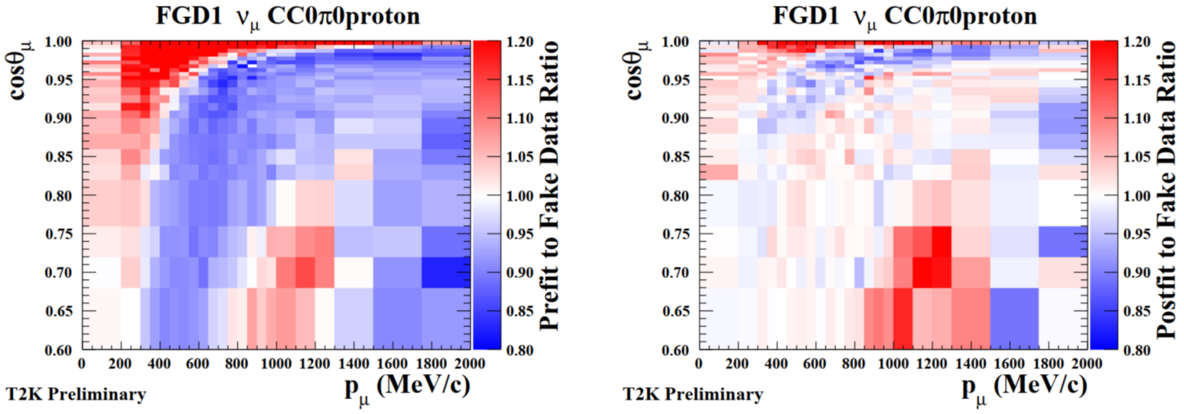

Figure 10.8: Prefit (left) and postfit (right) for the SF to CRPA fake data study in the 2021 BANFF fake data analysis, showing the CC0π0p sample. The colour of each bin shows the value of the ratio $R_{MC/FD}$. Plots adapted from [125].

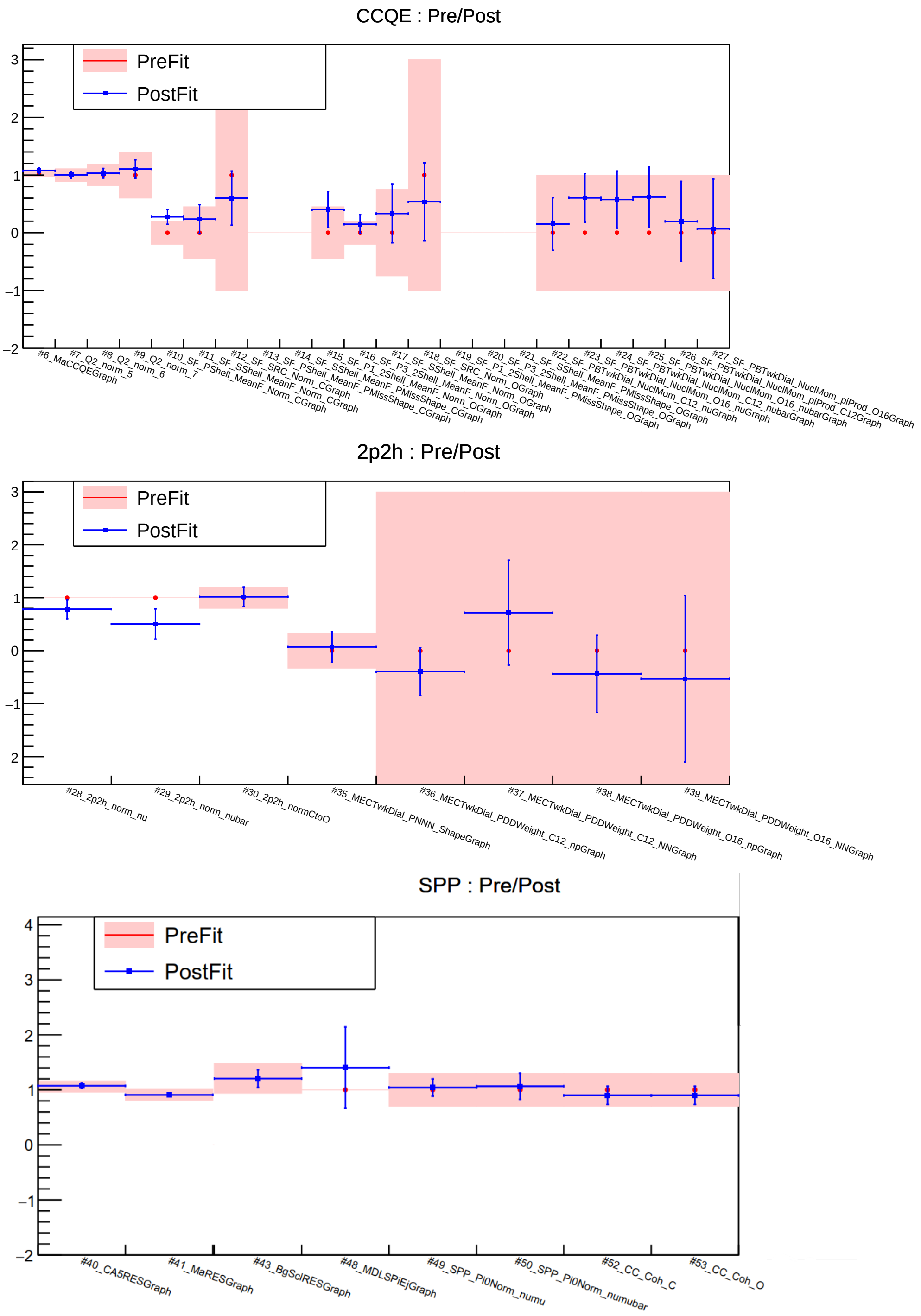

Figure 10.9: Cross section systematic parameters from the GUNDAM fit for the SF to CRPA fake data study, showing CCQE (top), 2p2h (middle), and single pion production (bottom). The central values of the prefit are shown as red points, with pink shading showing the uncertainties. The postfit values are shown as blue points with uncertainties as error bars. The blank areas correspond to parameters that are fixed in the fit as they were expected to have a very low sensitivity to the fit [90], hence they have no postfit. There is strong pulling in the 2p2h normalisation parameters (#28 and #29), as well as the Δ decay parameter (#48). These parameters are fairly weakly constrained, so this is not necessarily a problem but is worth further analysis in the future.

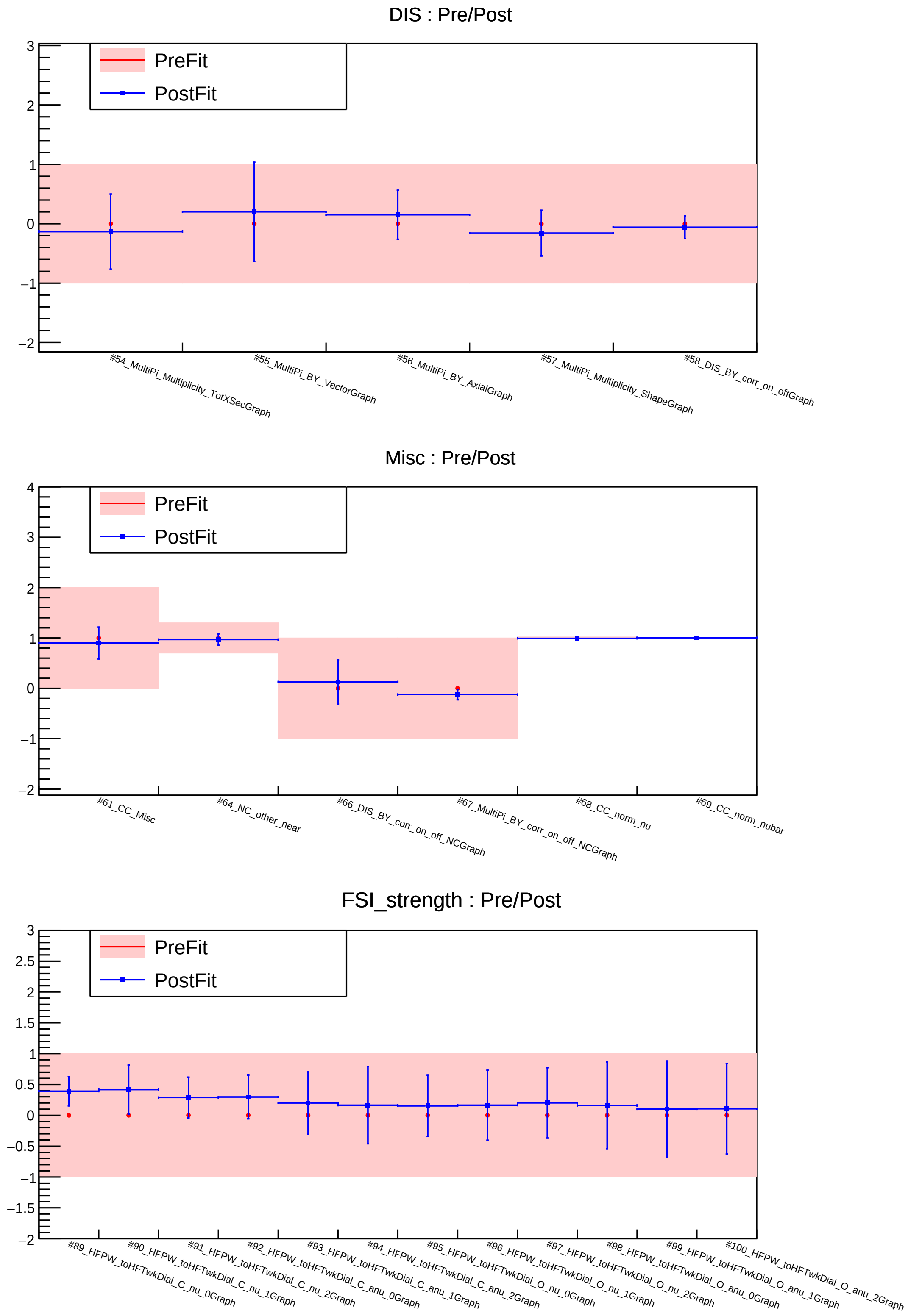

Figure 10.10: Cross section systematic parameters from the GUNDAM fit for the SF to CRPA fake data study, showing DIS (top), miscellaneous parameters (middle), and FSI strength (bottom). The central values of the prefit are shown as red points, with pink shading showing the uncertainties. The postfit values are shown as blue points with uncertainties as error bars. The postfit parameters are shown to generally be within the uncertainty ranges of the prefit, which suggests the existing priors are sufficient for fitting for the fake data study. The relatively small parameter pulls suggest most are not particularly sensitive to this fake data study.

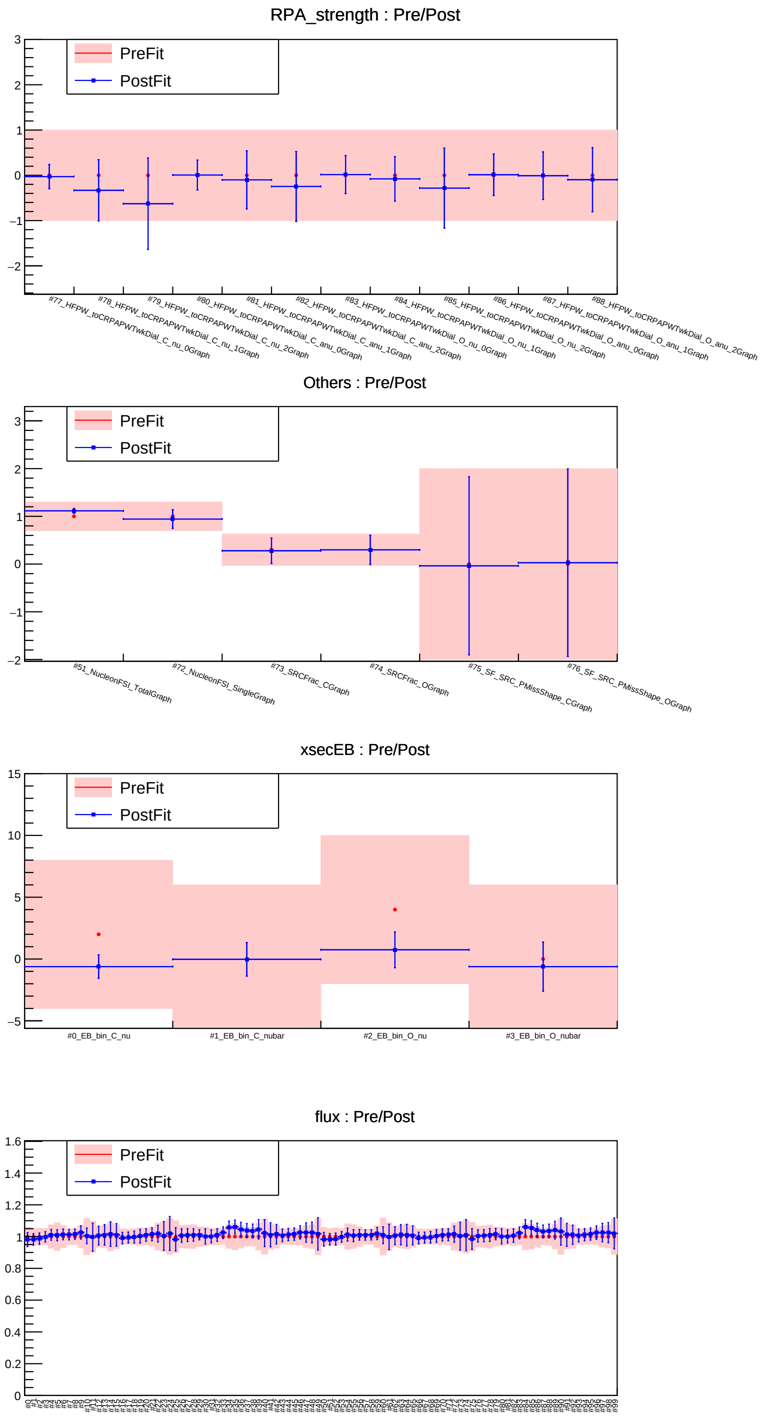

Figure 10.11: Cross section systematic parameters from the GUNDAM fit for the SF to CRPA fake data study. From top to bottom: RPA strength, other parameters, binding energy, and beam flux. The central values of the prefit are shown as red points, with pink shading showing the uncertainties. The postfit values are shown as blue points with uncertainties as error bars. The postfit parameters are shown to generally be within the uncertainty ranges of the prefit, which suggests the existing priors are sufficient for fitting for the fake data study. The flux parameters show a some pulling in the #35-#40 region, corresponding to higher-energy range (> 1 GeV) of the RHC $\bar{\nu}_\mu$ flux. As this is a relatively low-statistics region, this is not a concern, and falls within prior uncertainties anyway.

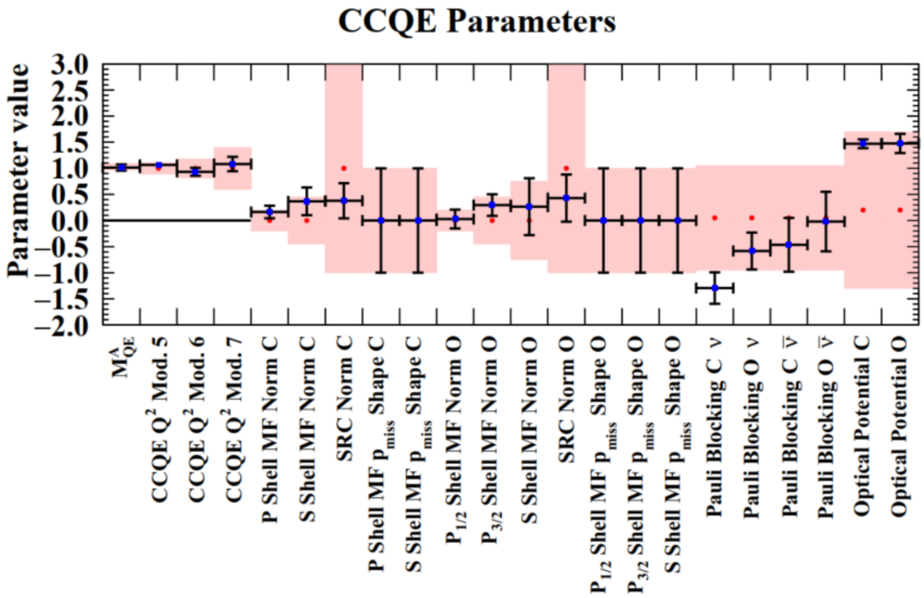

Figure 10.12: CCQE parameter values for the BANFF fit of the SF to CRPA fake data study, from the 2021 fake data analysis. The central values of the prefit are shown as red points, with pink shading showing the uncertainties. The postfit values are shown as blue points with uncertainties as black error bars. The Pauli blocking parameters are pulled down rather than up as seen in the current analysis. However, the removal of Optical Potential and the introduction of FSI/RPA strength mean the changes are compensated for in different parameters. Plot adapted from [125].

10.4.3 SF to SuSAv2

The Spectral Function to SuperScaling Approach V2 fake data fit is shown in figure 10.13. Similar to the other studies on nuclear models, the prefit shows increase in $R_{MC/FD}$ at lower muon momentum, as well in bins close to $\cos\theta_\mu = 1$, corresponding to a reduced cross section at low-Q^2. Meanwhile, $R_{MC/FD}$ has a very low value across most of the momentum range for $\cos\theta_\mu \lesssim 1$, corresponding to an increased cross section at high-Q^2. The postfit shows a significant improvement across the majority of bins. This is a new fake data study for the current oscillation analysis, so there are no previous BANFF studies for comparison. The fit parameters are shown in figures 10.14, 10.15, and 10.16. Similar to the SF to CRPA study, there is relatively little parameter change for the FSI and RPA strength parameters, and there is significant difference in the Pauli blocking parameters. Greater changes in the FSI and RPA strength parameters was expected for the two studies as they should have a strong effect in the low-Q^2 region in CC interactions.

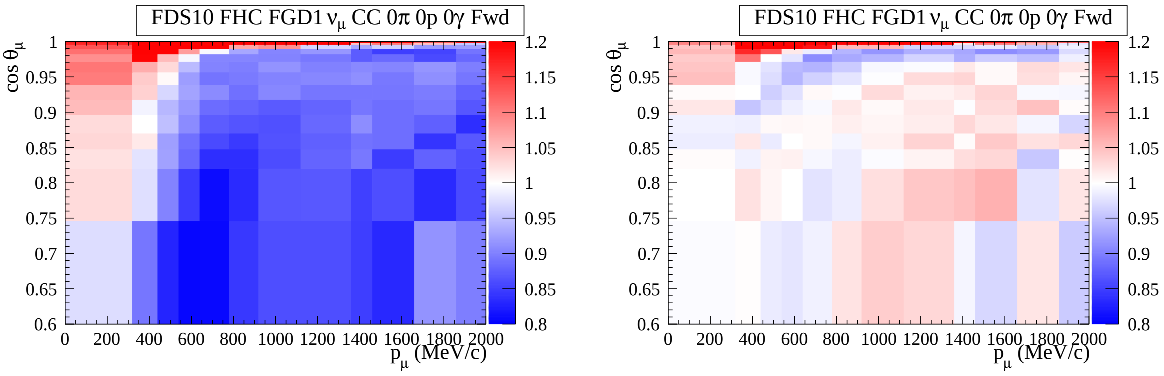

Figure 10.13: Comparisons between prefit (left) and postfit (right) for the SF to SuSAv2 fake data study in the CC0π0p0γFwd sample. The colour of each bin shows the value of the ratio $R_{MC/FD}$. The prefit has a χ^2 value of 296.0 and the postfit has a value of 25.8. The fit quality is generally good, showing that GUNDAM is capable of fitting this fake data set effectively.

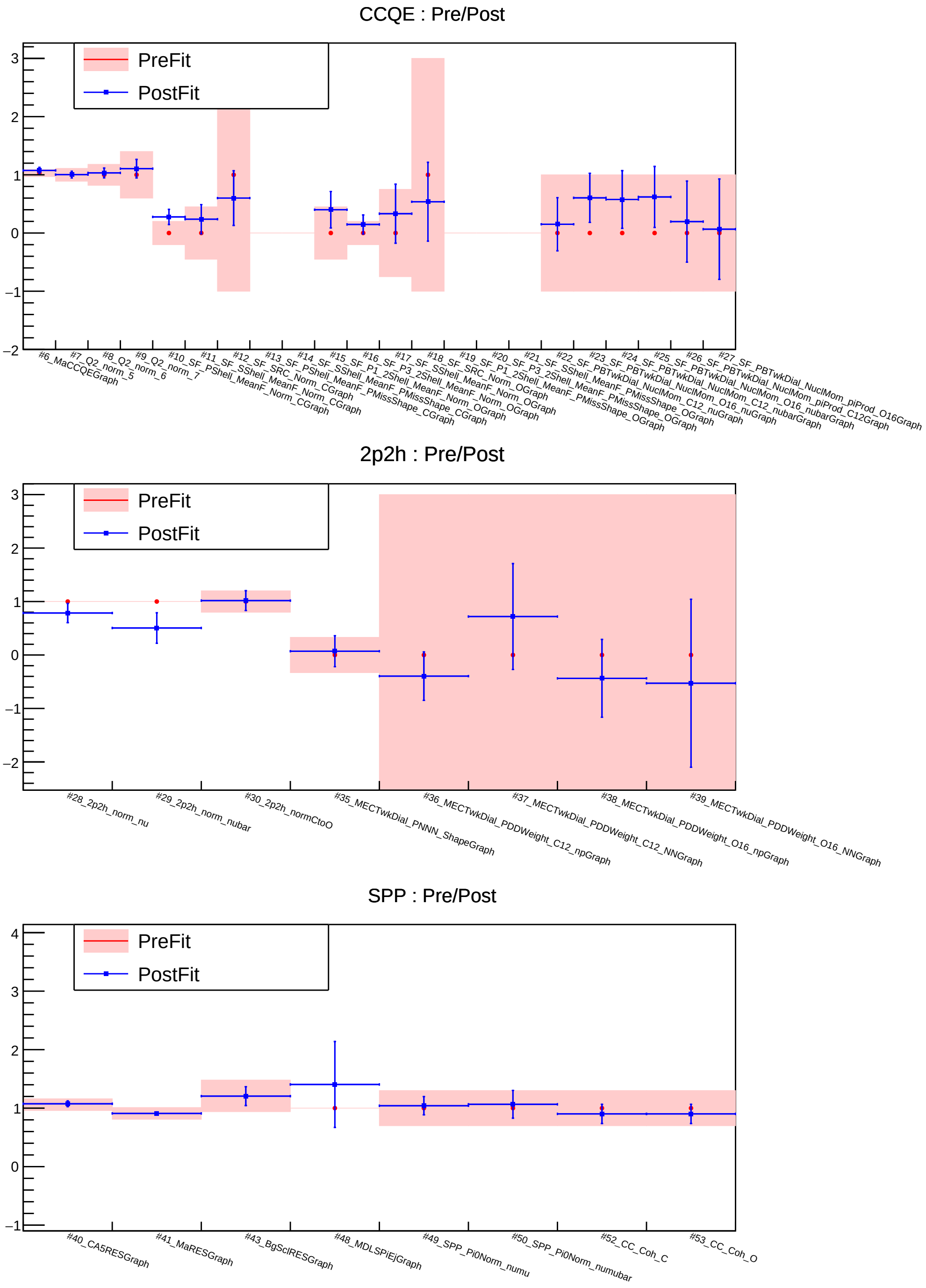

Figure 10.14: Cross section systematic parameters from the GUNDAM fit for the SF to SuSAv2 fake data study in the CC0π0p0γFwd sample, showing CCQE (top), 2p2h (middle), and single pion production (bottom). The central values of the prefit are shown as red points, with pink shading showing the uncertainties. The postfit values are shown as blue points with uncertainties as error bars.The blank areas correspond to parameters that are fixed in the fit as they were expected to have a very low sensitivity to the fit [90], hence they have no postfit. There is strong pulling in the 2p2h normalisation parameters (#28 and #29), as well as the Δ decay parameter (#48). These parameters are fairly weakly constrained, so this is not necessarily a problem but is worth further analysis in the future.

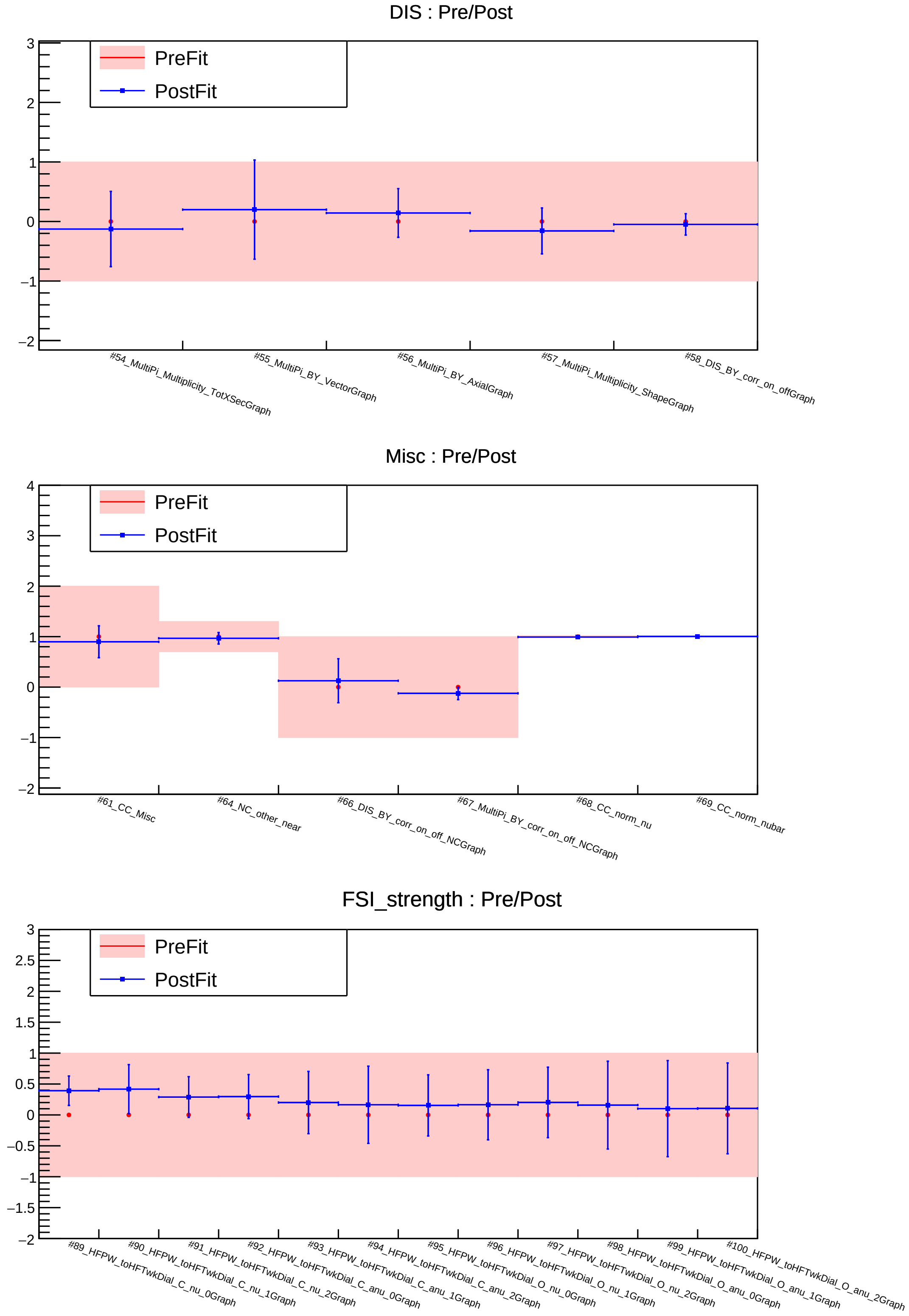

Figure 10.15: Cross section systematic parameters from the GUNDAM fit for the SF to SuSAv2 fake data study in the CC0π0p0γFwd sample, showing DIS (top), miscellaneous parameters (middle), and FSI strength (bottom). The central values of the prefit are shown as red points, with pink shading showing the uncertainties. The postfit values are shown as blue points with uncertainties as error bars.

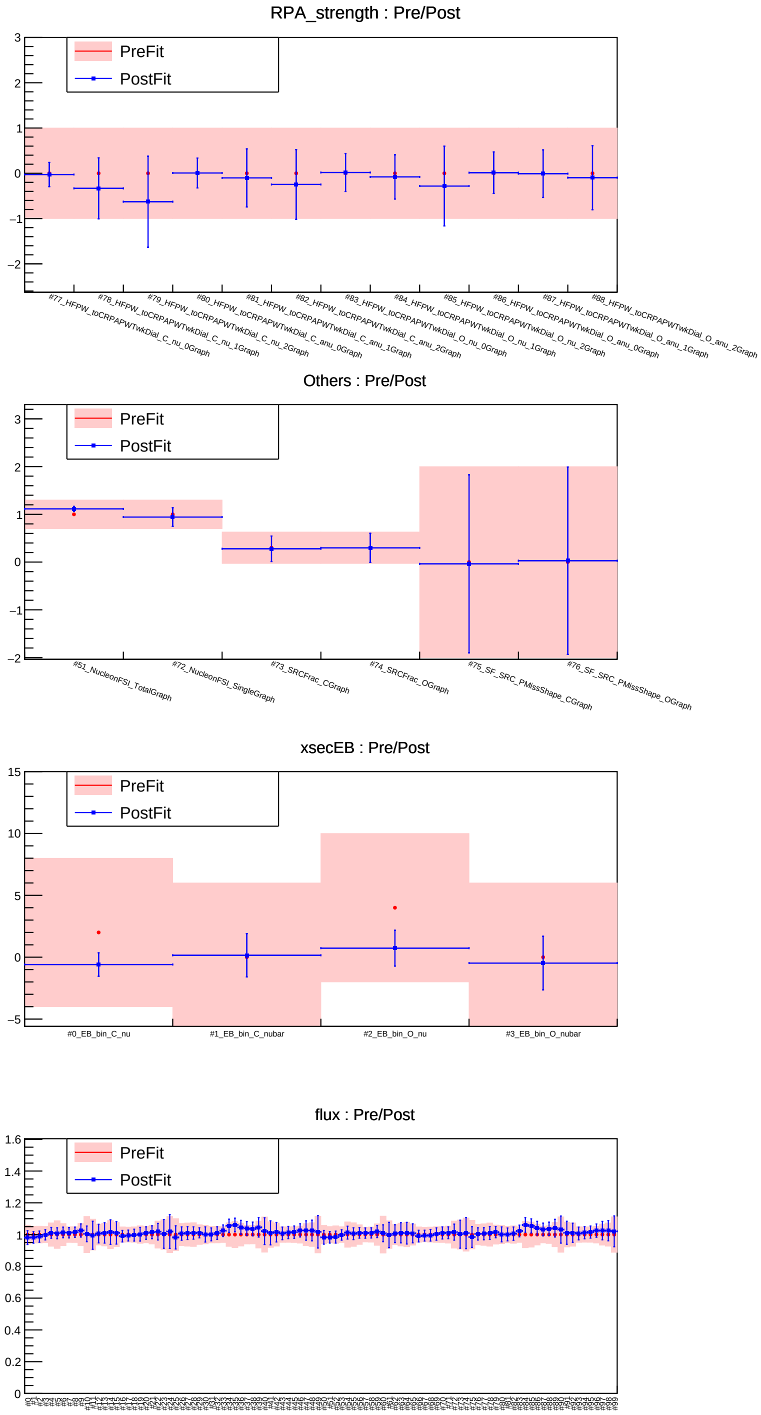

Figure 10.16: Cross section systematic parameters from the GUNDAM fit for the SF to SuSAv2 fake data study in the CC0π0p0γFwd sample. From top to bottom: RPA strength, other parameters, binding energy, and beam flux. The central values of the prefit are shown as red points, with pink shading showing the uncertainties. The postfit values are shown as blue points with uncertainties as error bars. The postfit parameters are shown to generally be within the uncertainty ranges of the prefit, which suggests the existing priors are sufficient for fitting for this fake data study.

10.5 Axial Form Factors

This section discusses the results for the fake data studies that affect the axial form factor of the nucleus: Z-Expansion (subsection 10.5.1), 3-Component(subsection 10.5.2), and LQCD Z-Expansion (subsection 10.5.3). The first two models have -1σ, nominal, and $+1\sigma$ studies, while the LQCD model has nominal and -1σ only, for a total of eight fake data studies. These models are described in detail in section 9.1.2. The CC0pi0p0γFwd sample has been chosen as the most significant sample for these studies, and is presented in the ratio plots comparing MC and fake data.

Contrasting to the nuclear model studies in the previous section, these fake data studies have a greater effect in the high-Q^2 region. The systematics analysis will focus on the CCQE parameters for brevity, as these are more heavily affected compared to other parameter groups.

10.5.1 Z-Expansion

The three Z-Expansions fake data fits, -1σ, nominal, and $+1\sigma$, are shown in figure 10.17. The prefit plots show that the -1σ study increases $R_{MC/FD}$ in high-momentum, high-angle bins (reduces the high-Q^2 cross section), while the $+1\sigma$ study significantly decreases it (increases the high-Q^2 cross section). Note that, for these particular studies, the z-axis range has been extended from $0.8 - 1.2$ to $0.5 - 1.5$; the $+1\sigma$ study produces a data-MC difference far beyond any reasonable real data result, especially in the given momentum range. The nominal study has only very slight change compared to the nominal MC, with a change of $\sim 5\%$ at most for any bin.

The postfit plots show that reasonably good agreement has been achieved for the -1σ and nominal Z-Expansion studies. The $+1\sigma$ study still shows some significant difference and, curiously, shows an increase in $R_{MC/FD}$ between the fitted MC and the fake data in some bins. This suggests GUNDAM has some difficulty with large changes between data and MC at $p_\mu \gtrsim 1000$ MeV/c. However, this is not unexpected as there are fewer parameters for adjusting high-momentum muons as these are already relatively well-modelled in the MC, thus the GUNDAM fit is better designed for differences at lower momentum. A similar result was observed in the 2021 analysis [125].

The parameter changes for the CCQE systematics are shown in figure 10.18. As the plots in figure 10.17 suggest, there is relatively little change in the -1σ and nominal studies (top and middle plots, respectively). The $+1\sigma$ study shows significant changes in the axial mass (`MACCQEGraph`) and Q^2 normalisation (`Q2_norm`) parameters. Particularly, `Q2_norm_7`, which corresponds to events with $Q^2 > 1000$ MeV/c, has completely diverged from the nominal value. This is consistent with what is observed in the ratio plots.

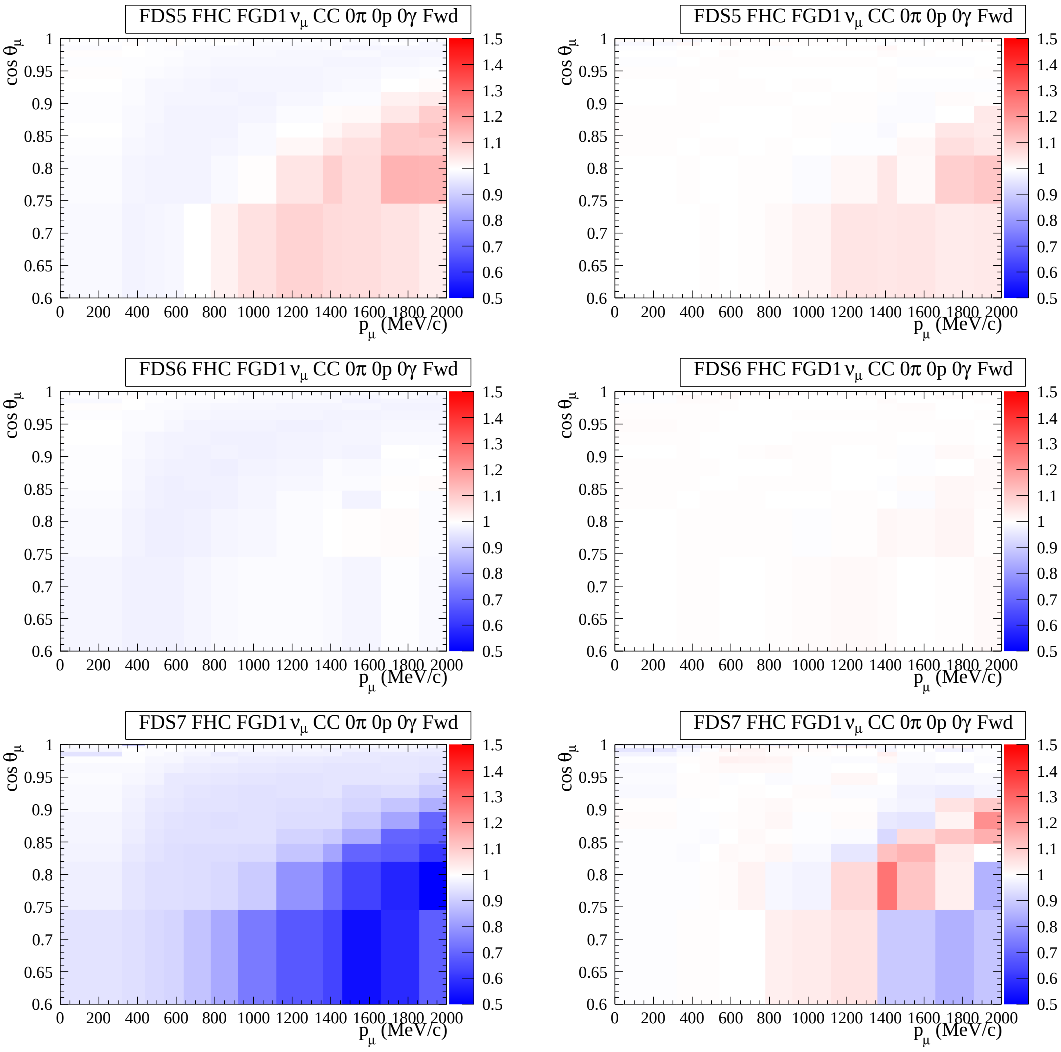

Figure 10.17: Comparisons between prefit (left) and postfit (right) for the Z-expansion AXFF fake data study, with -1σ, nominal, and $+1\sigma$ top, middle and bottom, respectively, in the CC0π0p0γFwd sample. The colour of each bin shows the value of the ratio $R_{MC/FD}$. The prefit distributions have χ^2 values of 17.3, 14.9 and 272.7, respectively, while the postfits have χ^2 values of 9.17, 4.39 and 21.3. Note that, compared to similar plots for other fake data studies, the z-axis range has been extended to $0.5 - 1.5$ as the study has a very strong effect especially at high Q^2. The fit quality is generally good, showing that GUNDAM is capable of fitting this fake data set effectively.

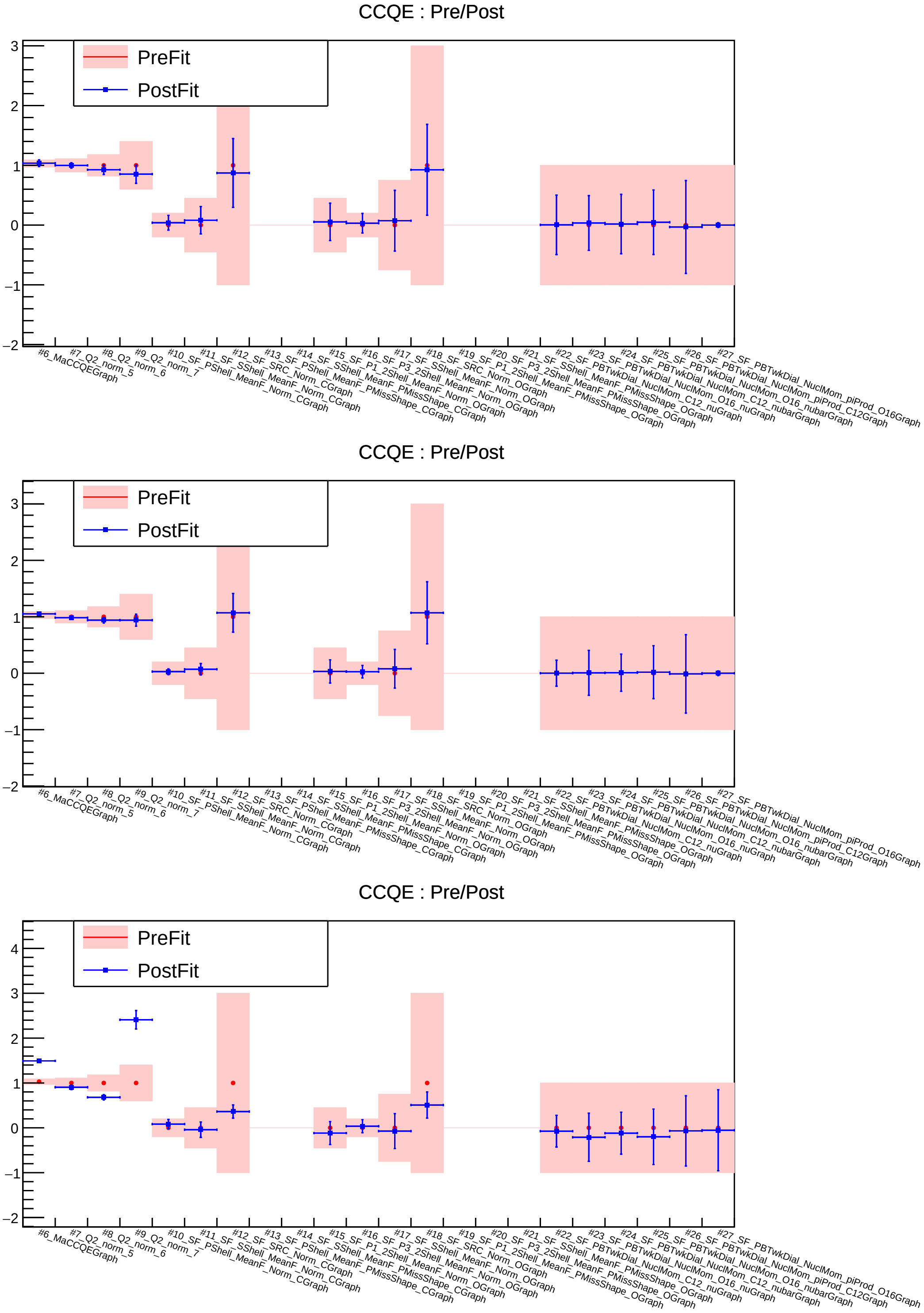

Figure 10.18: CCQE cross section systematic parameters from the GUNDAM fit for the AXFF Z-Expansion fake data studies. The central values of the prefit are shown as red points, with pink shading showing the uncertainties. The postfit values are shown as blue points with uncertainties as error bars. The -1σ, nominal and $+1\sigma$ studies are top, middle, and bottom respectively. There is generally minor parameter pulling from the nominal values in the -1σ and nominal models, but the $+1\sigma$ shows major pulling in the high-energy Q^2 normalisation bin (#9, corresponding to > 1 GeV). This is consistent with the large data-MC difference observed in this region (see figure 10.17).

10.5.2 3-Component

The ratio plots for the 3-component -1σ, nominal and $+1\sigma$ fake data studies are shown in figure 10.19. There is relatively little difference between the prefit plots for three studies in this model, with all reducing $R_{MC/FD}$, and thus increasing the cross section, at medium-to-high muon momentum compared to the nominal MC. The postfit shows good agreement across the three studies. The systematics plots in figure 10.20 show relatively small changes in the fit parameters, with the largest being the `Q2_norm_7` parameter, which affects the expected momentum range ($Q^2 > 1000$ MeV).

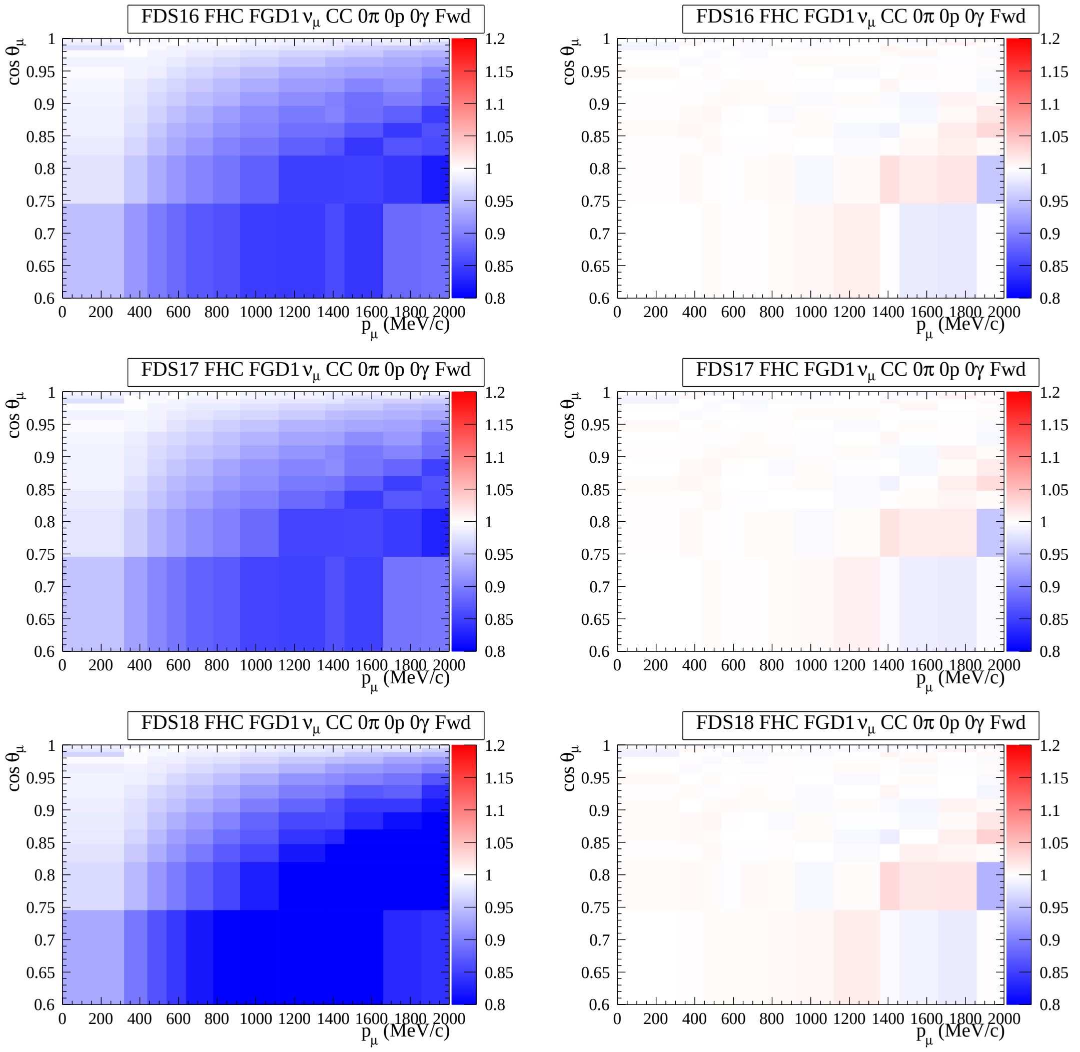

Figure 10.19: Comparisons between prefit (left) and postfit (right) for the 3-component AXFF fake data study, with -1σ, nominal, and $+1\sigma$ top, middle and bottom, respectively, in the CC0π0p0γFwd sample. The colour of each bin shows the value of the ratio $R_{MC/FD}$. The prefit χ^2 values are 113.5, 96.3 and 231.9, respectively, while the postfit χ^2 values are 0.61, 0.41 and 0.70. The fit quality here is very high even for the major fake data-MC difference in the low-Q^2 region.

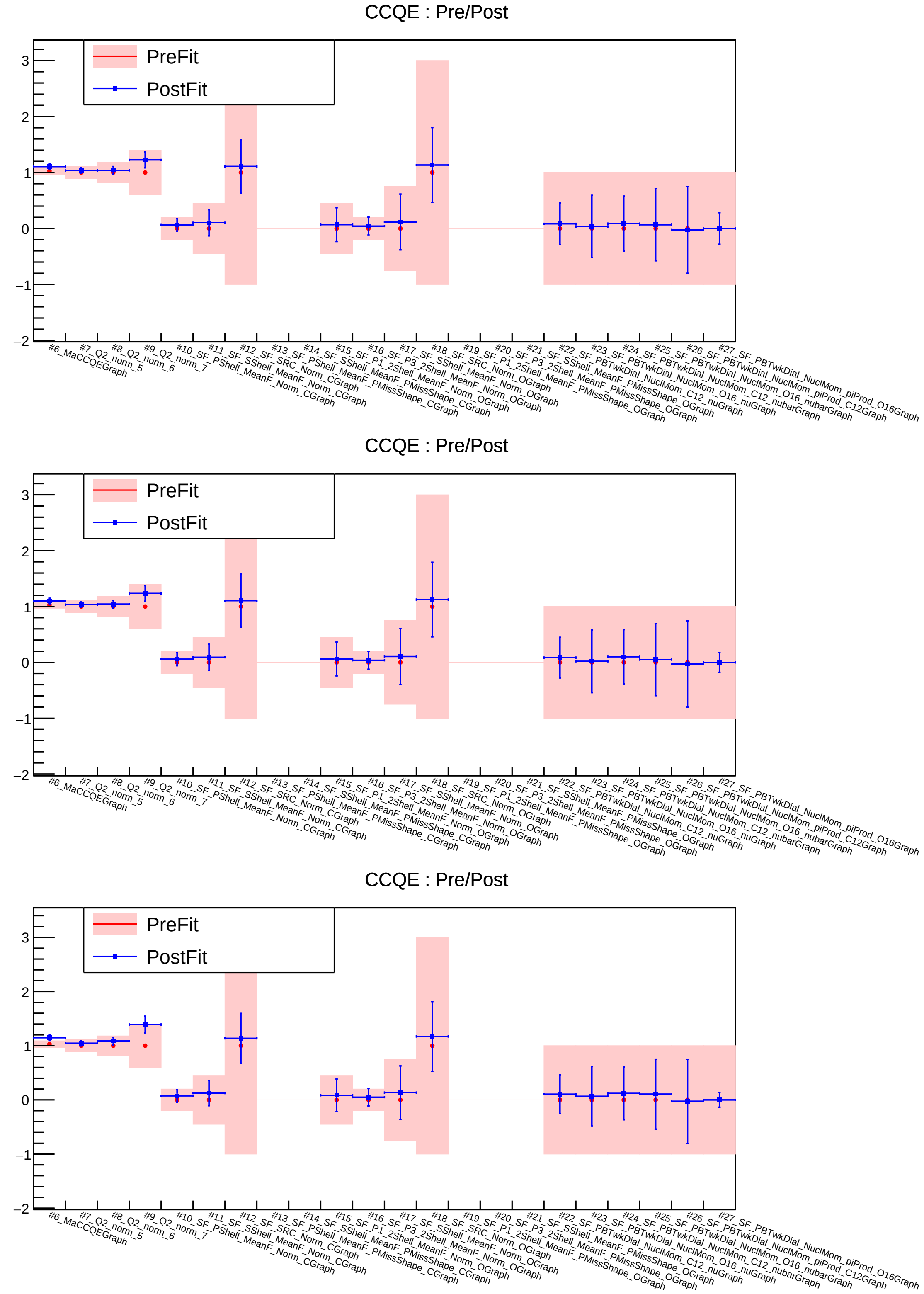

Figure 10.20: CCQE cross section systematic parameters from the GUNDAM fit for the AXFF 3-Component fake data studies. The central values of the prefit are shown as red points, with pink shading showing the uncertainties. The postfit values are shown as blue points with uncertainties as error bars. The -1σ, nominal and $+1\sigma$ studies are top, middle, and bottom respectively. The blank areas correspond to parameters that are fixed in the fit as they were expected to have a very low sensitivity to the fit [90], hence they have no postfit. The largest parameter pull is for the $Q^2 > 1$ GeV normalisation parameter (#9), which is consistent with what is observed in figure 10.5.2, showing the largest data-MC difference corresponds to this region.

10.5.3 LQCD Z-Expansion

Figure 10.21 shows the ratio plots for the nominal and -1σ LQCD Z-Expansion fake data studies. This fake data study is a modification of the Z-Expansion model discussed previously, so there are similarities between the two. The z-axis has range also been expanded to from $0.8 - 1.2$ to $0.5 - 1.5$ for these plots, as the difference between the fake data and the nominal MC is much greater than in other studies, especially in the high-Q^2 region. The nominal study shows only slight changes between the nominal MC and the fake data, while the -1σ study shows a large decrease in $R_{MC/FD}$ in the high-Q^2 region. The postfit plots show reasonable fit quality, although GUNDAM continues to struggle fitting particularly large changes at high Q^2. The systematics plots, shown in figure 10.22, show very small changes in the nominal study, and a significant change in the `Q2_nom_7` parameter for the -1σ study, which is expected.

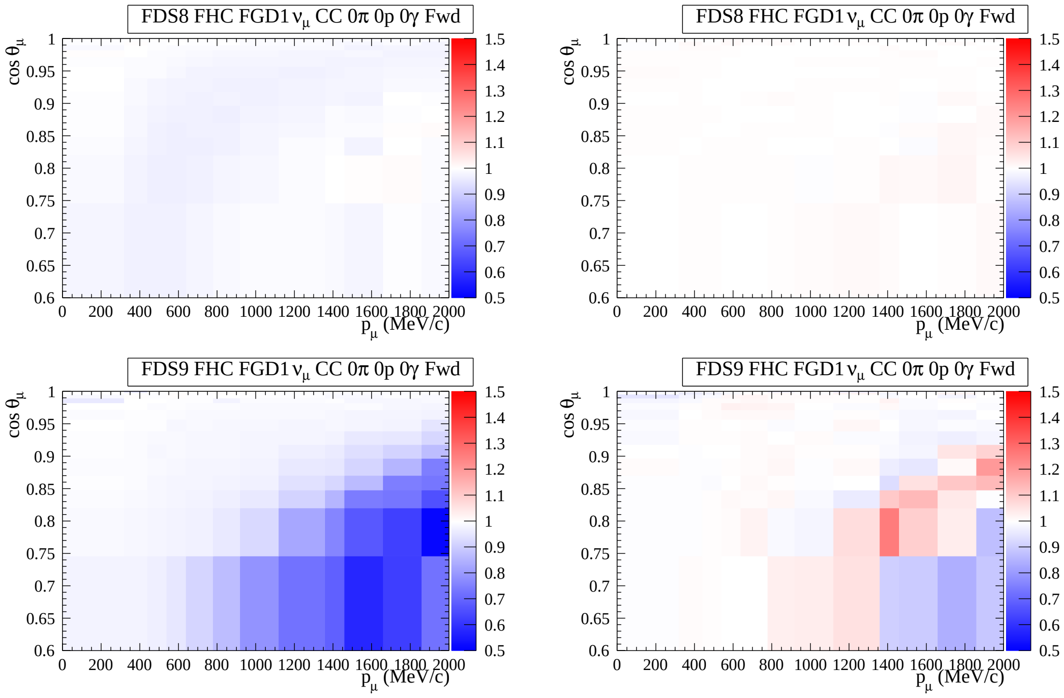

Figure 10.21: Comparisons between prefit (left) and postfit (right) for the Z-expansion LQCD AXFF fake data study, with nominal and -1σ studies top and bottom, respectively. The colour of each bin shows the value of the ratio $R_{MC/FD}$. Note that, compared to similar plots for other fake data studies, the z-axis range has been extended to $0.5 - 1.5$ as the study has a very strong effect especially at high Q^2. The prefit χ^2 values are 15.0 and 150.6, respectively, while the postfit χ^2 values are 4.39, and 19.0. The fit quality is generally good, showing that GUNDAM is capable of fitting this fake data set effectively, especially considering the very large difference in the high-Q^2 region compared to most other fake data studies.

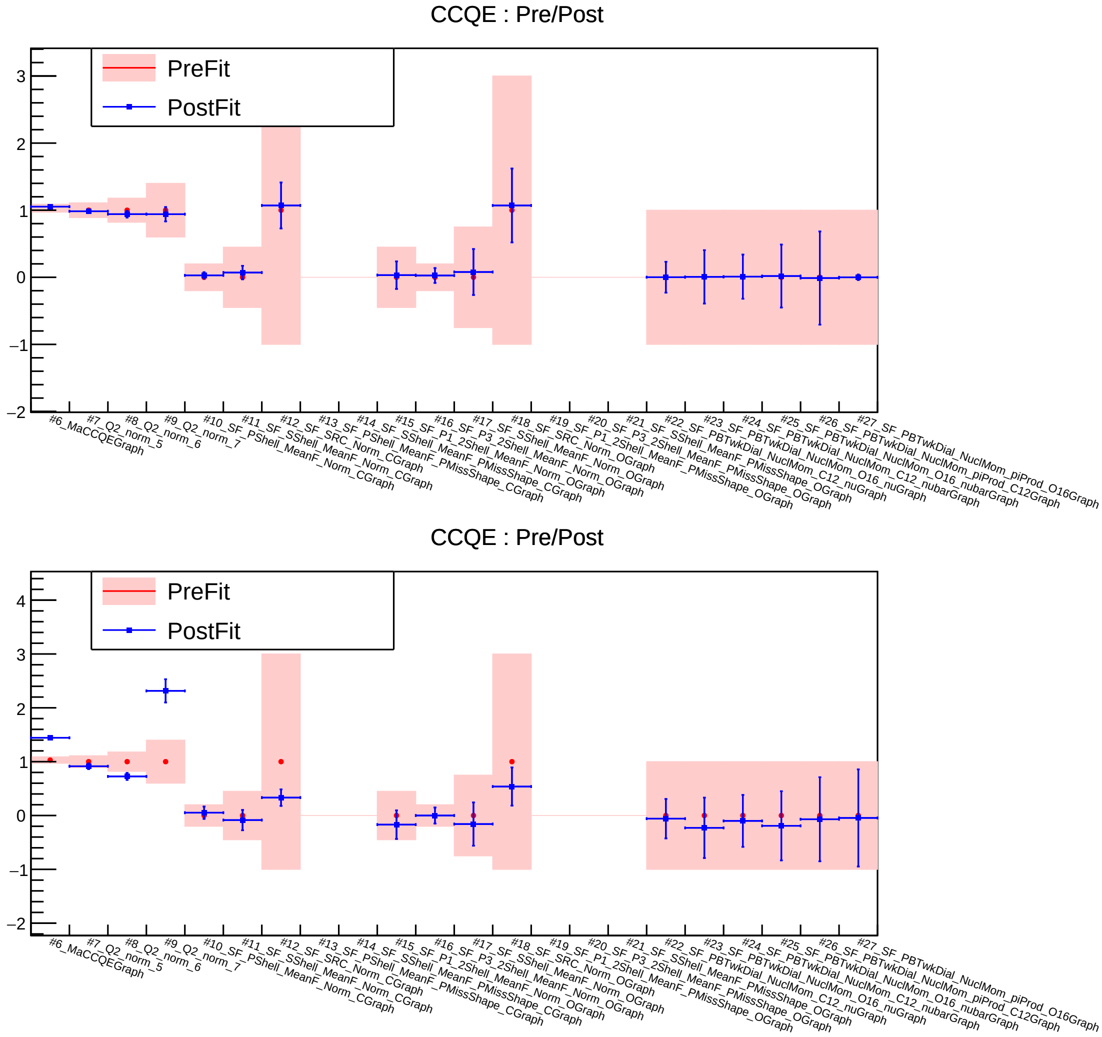

Figure 10.22: Cross section systematic parameters from the GUNDAM fit for the LQCD Z-Expansion fake data studies, with -1σ and nominal studies top and bottom, respectively. The central values of the prefit are shown as red points, with pink shading showing the uncertainties. The postfit values are shown as blue points with uncertainties as error bars. The blank areas correspond to parameters that are fixed in the fit as they were expected to have a very low sensitivity to the fit [90], hence they have no postfit. The nominal model shows major pulling in the high-energy Q^2 normalisation bin (#9, corresponding to > 1 GeV). This is consistent with the large data-MC difference observed in this region (see figure 10.21).

10.6 Single Pion Production

This section covers the fake data studies that affect the single pion production model: SPP Matrix Element $-1\sigma/+1\sigma$ (subsection 10.6.1), SPP Adversarial (subsection 10.6.2), RS to Martini (subsection 10.6.3), and Low-Q^2 SPP (subsection 10.6.4). For these studies, the CC$1\pi0\gamma$Fwd sample has been chosen for the prefit and postfit ratio plots as this sample contains the majority of single pion production events. Similarly, the parameter analysis will focus on the single pion production systematics.

10.6.1 SPP Matrix Element

For these fake data studies, the single pion production matrix element is shifted by $\pm1\sigma$; the ratios between the prefit and postfit MC against fake data are shown in figure 10.23. The plots show the expected effect in the prefits, with the -1σ study decreasing $R_{MC/FD}$ across the momentum range (corresponding to an decrease in cross section), and the $+1\sigma$ increasing $R_{MC/FD}$ (corresponding to an increase in cross section). Notes that the angular bin below $\cos\theta_\mu = 0.85$ extend below the limit of the plot to $\cos\theta_\mu = -1$, so the values $R_{MC/FD}$ must be taken with this in mind. The postfit plots show a successful fit, with the largest difference between the fitted MC and fake data being $< 5\%$.

The change in systematics in the fits are shown in figure 10.24. Of particular note is the anomalously large uncertainty on the MDLSPiEjGraph parameter in the $+1\sigma$ study, which extend $\sim \pm4$ beyond the central value. This suggests some significant issue in fitting this parameter for this study. This does not appear in any of the other studies, and there is not obvious reason it would appear here. It is possible the choice of interpolation method may resolve this, or it may be a minor bug in GUNDAM. This will be explored in future work as GUNDAM continues to be developed.

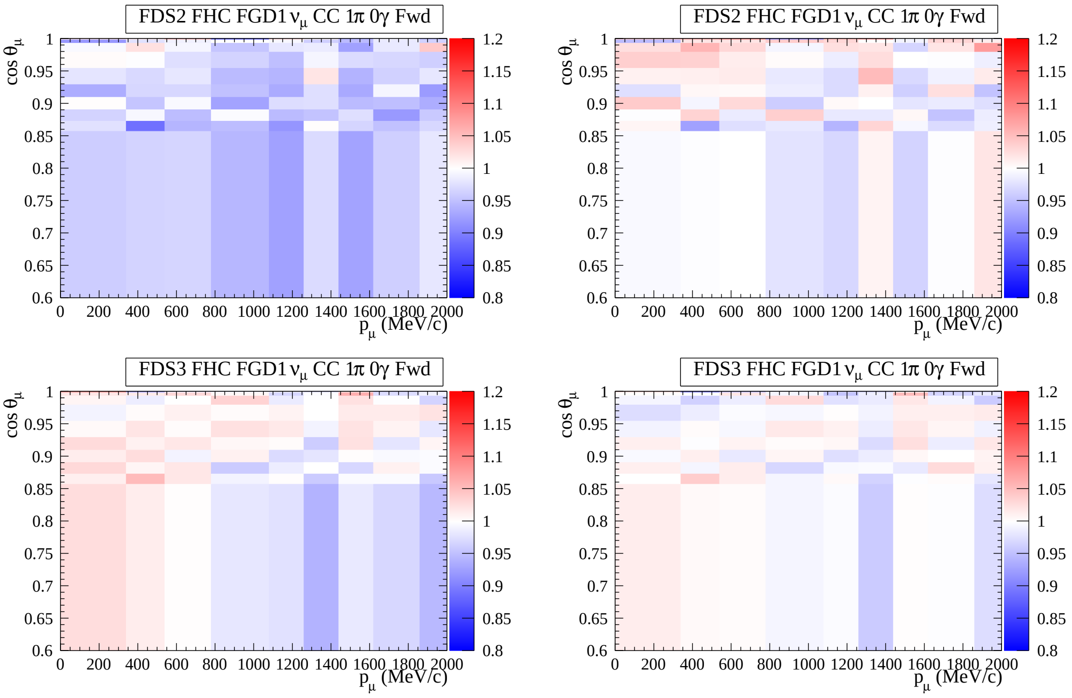

Figure 10.23: Comparisons between prefit (left) and postfit (right) for the SPP Matrix Element fake data study for the CC1π0γFwd sample, with -1σ and $+1\sigma$ top and bottom, respectively. The colour of each bin shows the value of the ratio $R_{MC/FD}$. The prefit χ^2 values are 11.5 and 2.28, respectively, while the postfit χ^2 values are 2.51 and 1.18. The fit quality is good, showing that GUNDAM is capable of fitting this fake data set effectively.

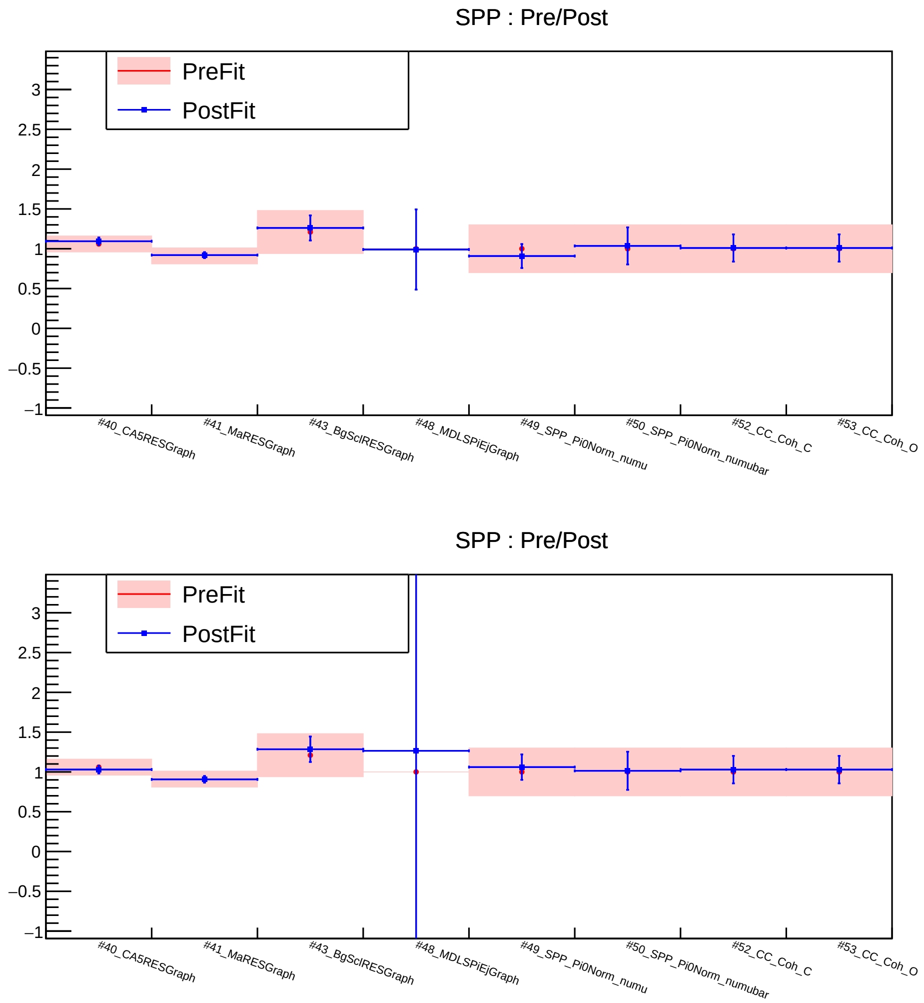

Figure 10.24: Cross section systematic parameters from the GUNDAM fit for the SPP Matrix Element fake data studies. The central values of the prefit are shown as red points, with pink shading showing the uncertainties. The postfit values are shown as blue points with uncertainties as error bars. The -1σ and $+1\sigma$ studies are top and bottom, respectively. The Δ decay parameter (#48) has a very large uncertainty, especially in the $+1\sigma$ study. It is unknown why the uncertainties are so large here, but it is not considered to have compromised the overall fit quality. Otherwise, the other fit parameters are as expected, showing only small changes as the effects of the study on the momentum/angular distribution is relatively minor (figure 10.23.

10.6.2 SPP Adversarial

Figure 10.25 shows the prefit and postfit ratio plots for the SPP Adversarial fake data study. The prefit shows a decrease in $R_{MC/FD}$ across the entire plot, which is expected for the study as the fake data reweighting applies a scaling factor to increase pion production events compared to the nominal MC. The postfit shows a successful fit, with the ratio across all bins being $< 5\%$. The SPP parameter changes are shown in figure 10.26.

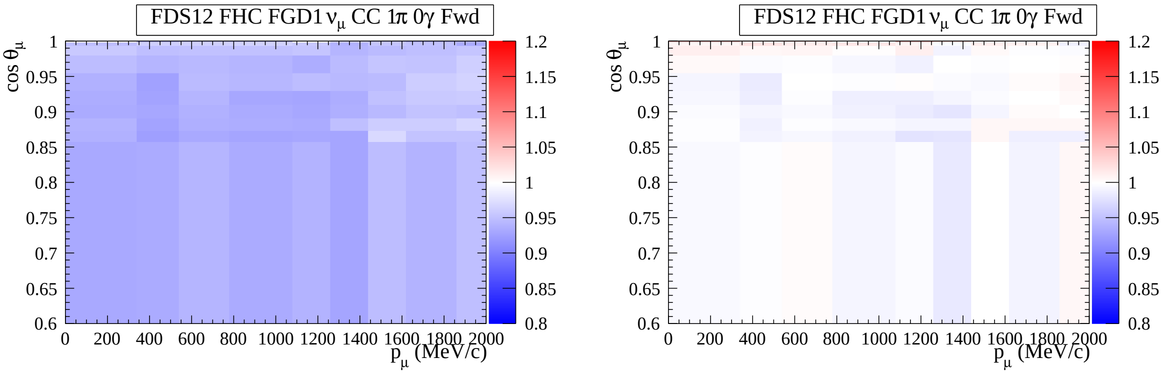

Figure 10.25: Comparisons between prefit (left) and postfit (right) for the SPP Adversarial fake data studies in the CC1π0γFwd sample. The colour of each bin shows the value of the ratio $R_{MC/FD}$. The prefit χ^2 value is 22.2 and the postfit χ^2 value is 0.34. The fit quality is good, showing that GUNDAM is capable of fitting this fake data set effectively.

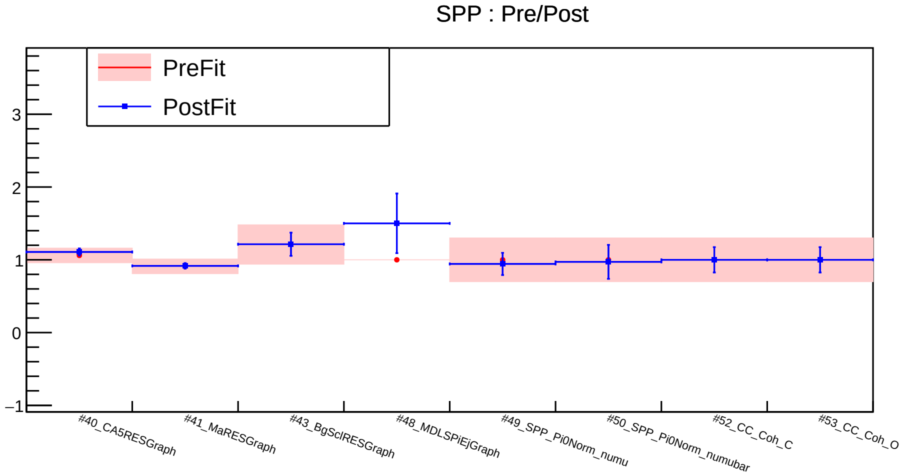

Figure 10.26: Singe Pion Production cross section systematic parameters from the GUNDAM fit for the SPP Adversarial fake data study. The central values of the prefit are shown as red points, with pink shading showing the uncertainties. The postfit values are shown as blue points with uncertainties as error bars. The majority of fitted parameters are within the uncertainties of the priors, suggesting the current priors are acceptable for fitting this study. The large uncertainty in the Δ decay parameter (#48) has been discussed previously (see 10.6.1) and is believed to be a minor fitting error that will be investigated in the future.

10.6.3 RS to Martini

Figure 10.27 shows the prefit and postfit ratio plots for the RS to Martini fake data study. The prefit shows this study significantly increases $R_{MC/FD}$ at low-Q^2, corresponding to a heavy suppression of 1π events in the fake data compared to the nominal MC. The postfit shows a successful fit, with the ratio across all bins being $< 5\%$. The SPP parameter changes are shown in figure 10.28.

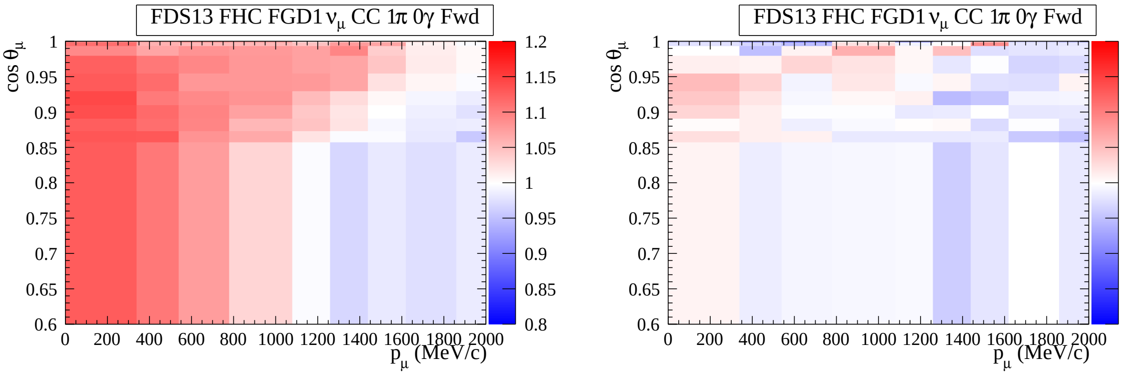

Figure 10.27: Comparisons between prefit (left) and postfit (right) for the RS to Martini fake data study in the CC$1\pi0\gamma$Fwd sample. The colour of each bin shows the value of the ratio $R_{MC/FD}$. The prefit χ^2 value is 29.7 and the postfit χ^2 value is 2.52. The fit quality is good, showing that GUNDAM is capable of fitting this fake data set effectively.

10.6.4 Low Q^2 Suppression Single Pion Production

Figure 10.29 shows the prefit and postfit ratio plots for the Low-Q^2 Suppression Single Pion Production fake data study. As expected, there is a significant increase in $R_{MC/FD}$ (corresponding to a reduction in fake data events in the associated bins compared to nominal MC) in the low-Q^2 region, far beyond what would be expected in a reasonable real data-MC difference. The postfit plot shows GUNDAM can still effectively perform a fit in this extreme circumstance, showing $< 5\%$ difference between the fitted MC and fake data.

The SPP parameter changes are shown in figure 10.30. The `MDLSPiEjGraph` parameter shows an unusually large uncertainty, which further suggests issues with fitting this particular parameter as this was previously seen in the SSP Matrix Element $+1\sigma$ study. The CCQE parameters are also included here to highlight that the π-production Pauli blocking parameters (two rightmost parameters) are increased in this fit, as the CCQE parameters only show very slight changes in the other SPP-focused fake data studies.

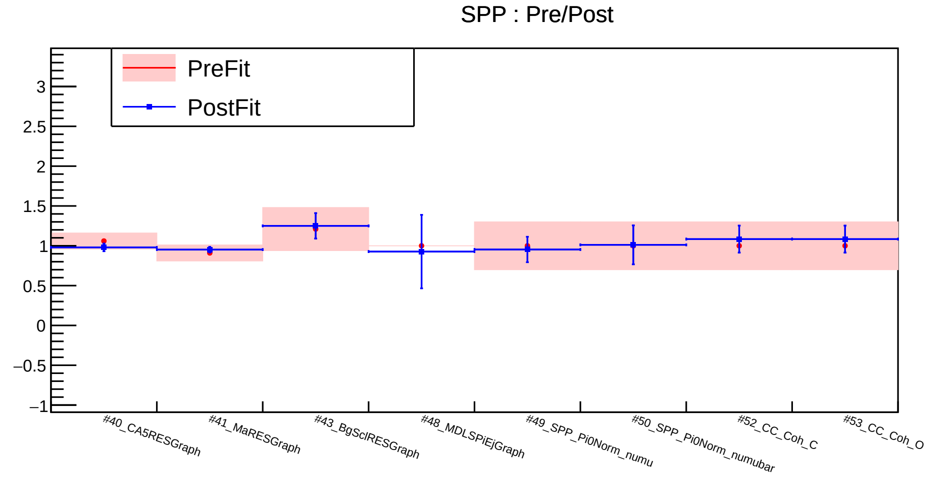

Figure 10.28: Cross section systematic parameters from the GUNDAM fit for the RS to Martini fake data study. The central values of the prefit are shown as red points, with pink shading showing the uncertainties. The postfit values are shown as blue points with uncertainties as error bars. The majority of fitted parameters are within the uncertainties of the priors, suggesting the current priors are acceptable for fitting this study.

As Pauli blocking heavily affects low-momentum neutrino interactions, this change is not unexpected.

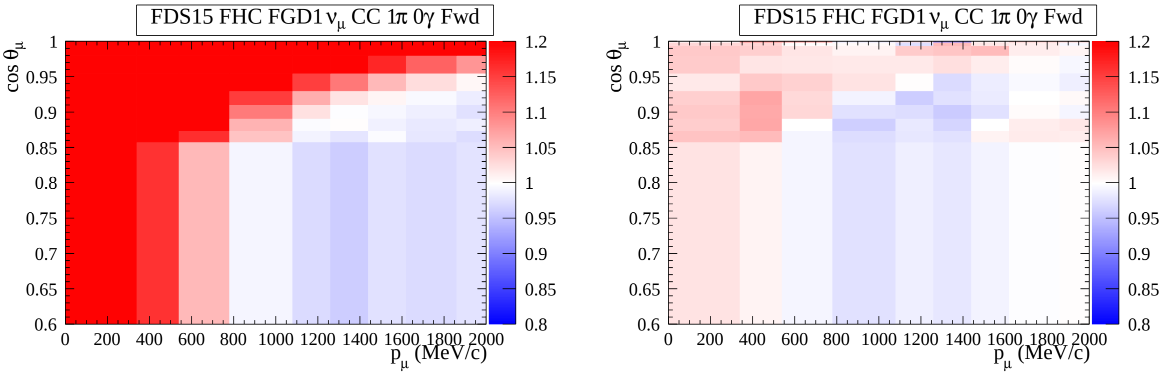

Figure 10.29: Comparisons between prefit (left) and postfit (right) for the Low-Q^2 Suppression Single Pion Production fake data study in the CC1π0γFwd sample. The colour of each bin shows the value of the ratio $R_{MC/FD}$. The prefit χ^2 value is 206.5 and the postfit χ^2 value is 2.29. The large fake data-MC difference represented by the red region in the prefit is almost completely resolved in the postfit, showing GUNDAM is capable of fitting such a large discrepancy.

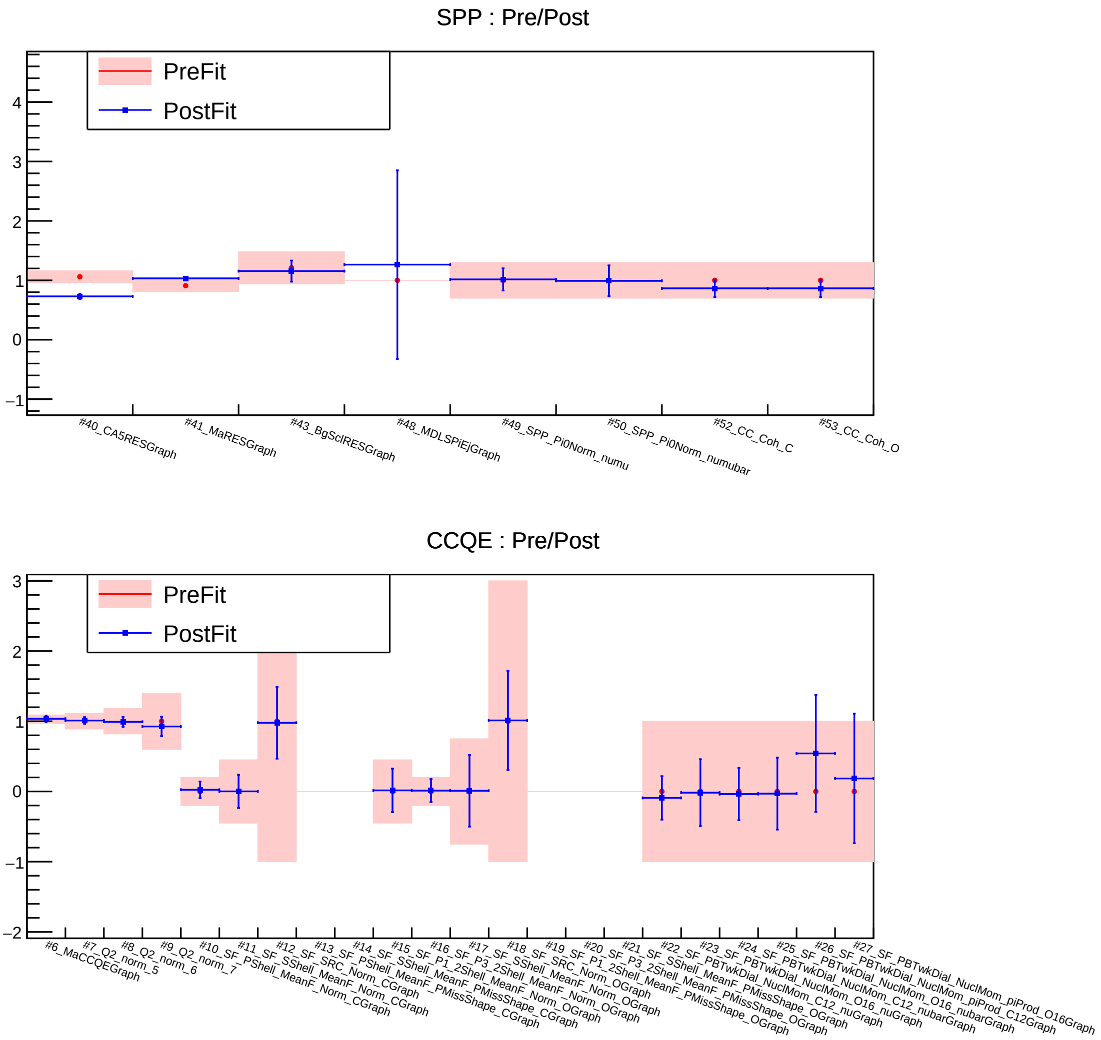

Figure 10.30: Cross section systematic parameters from the GUNDAM fit for the Low-Q^2 Suppression Single Pion Production fake data study. The central values of the prefit are shown as red points, with pink shading showing the uncertainties. The postfit values are shown as blue points with uncertainties as error bars. The SPP parameters are shown above, and the CCQE parameters below. The large pulling of the CA5RES parameter (#40 in the SPP plot) is expected as this parameter corresponds to the axial form factor at low energies thus a large change is not unexpected. Similarly, the Pauli blocking parameters affecting pion production (#26 and #27 on the CCQE plot) are pulled heavily as well, but still within prior uncertainties. The large uncertainty in the Δ decay parameter (#48) has been discussed previously (see 10.6.1) and is believed to be a minor fitting error that will be investigated in the future.

10.7 Other Studies

The following fake data studies do not fall within a larger group, so are gathered in this section. The studies discussed here are CC0pi Non-QE (subsection 10.7.1), 2p2h Eb Correction (subsection 10.7.2) and MultiPi Multiplicity (subsection 10.7.3).

10.7.1 CC0π Non-QE

Figure 10.31 shows the prefit and postfit ratio plots for the CC0pi Non-QE fake data study. As this study has effects across the CC0pi samples, the plots for the CC0π0γ0pFwd and CC0π0γNpFwd samples are given. The prefit plots show an increase in $R_{MC/FD}$ at low Q^2, and a decrease at high Q^2. The postfit for the CC0π0γ0pFwd sample shows good agreement between the fitted MC and fake data, with the largest difference being $< 5\%$. The CC0π0γNpFwd postfit shows worse agreement, with the largest difference being $\sim 10\%$. However, these results are comparable with the 2021 fake data analysis results, shown in figure 10.32, suggesting that the current GUNDAM fit is at least as successful as the previous BANFF fit. Additionally, the samples have postfit χ^2 values of 2.99 and 8.51, respectively, (compared to prefit values of 68.0 and 115.3) which suggests a good fit.

The parameter changes are shown in figures 10.33, 10.34, and 10.35. Generally, the systematics appear as expected; however, the RPA strength parameters show little to no change from their nominal value and in some cases the uncertainties have grown larger. As these are new parameters for this analysis, and there have been previous issues with interpolation methods for the FSI strength and RPA strength parameters (see section 10.2), this is not wholly unexpected, but the specific cause is not fully known at this moment. This will be explored in future GUNDAM analyses.

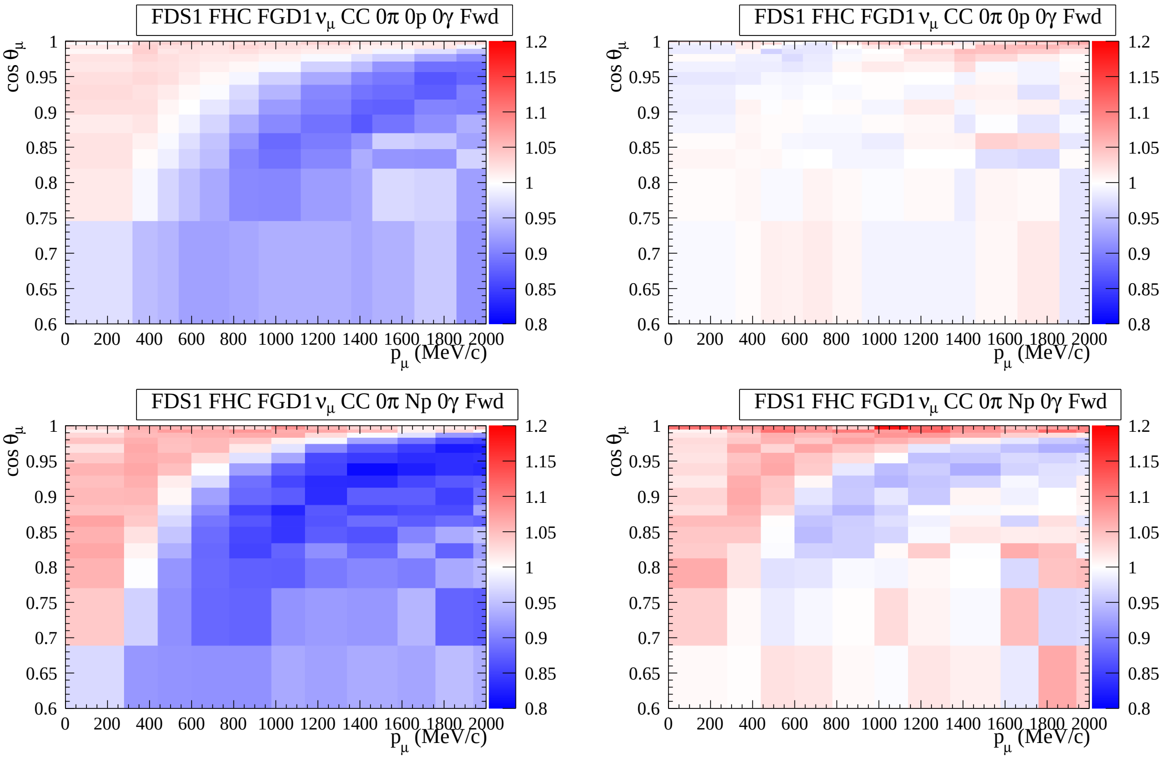

Figure 10.31: Comparisons between prefit (left) and postfit (right) for the CC Non-QE fake data study in the CC1π0γ0pFwd (top) and CC1π0γNpFwd (bottom) samples.The colour of each bin shows the value of the ratio $R_{MC/FD}$. The prefit χ^2 value are 68.0 and 115.3 for CC1π0γ0pFwd and CC1π0γNpFwd, respectively, and the postfit χ^2 values are 2.99 and 8.51. For the zero-proton sample, fit quality is very good. However, the N-proton sample still shows an imperfect fit. The zero-proton sample is much more significant for the oscillation analysis, so this is not a major concern, and the N-proton sample is still fitting to $\sim 5\%$. Both samples are comparable to the previous results from the 2021 analysis (10.32, so the fit quality is still at least as good.

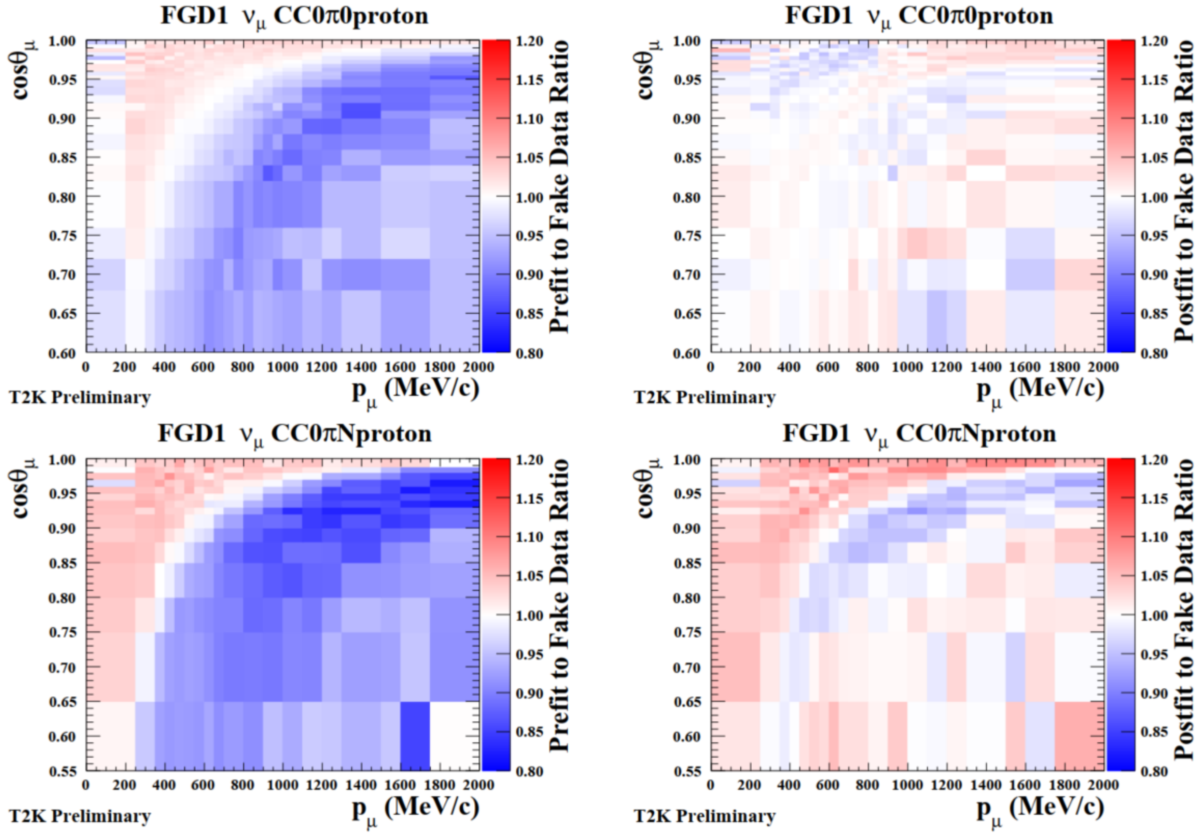

Figure 10.32: 2021 fake data analysis results, showing comparisons between prefit (left) and postfit (right) for the CC Non-QE fake data study in the CC1π0γ0pFwd (top) and CC1π0γNpFwd (bottom) samples. The colour of each bin shows the value of the ratio $R_{MC/FD}$. Plots adapted from [125].

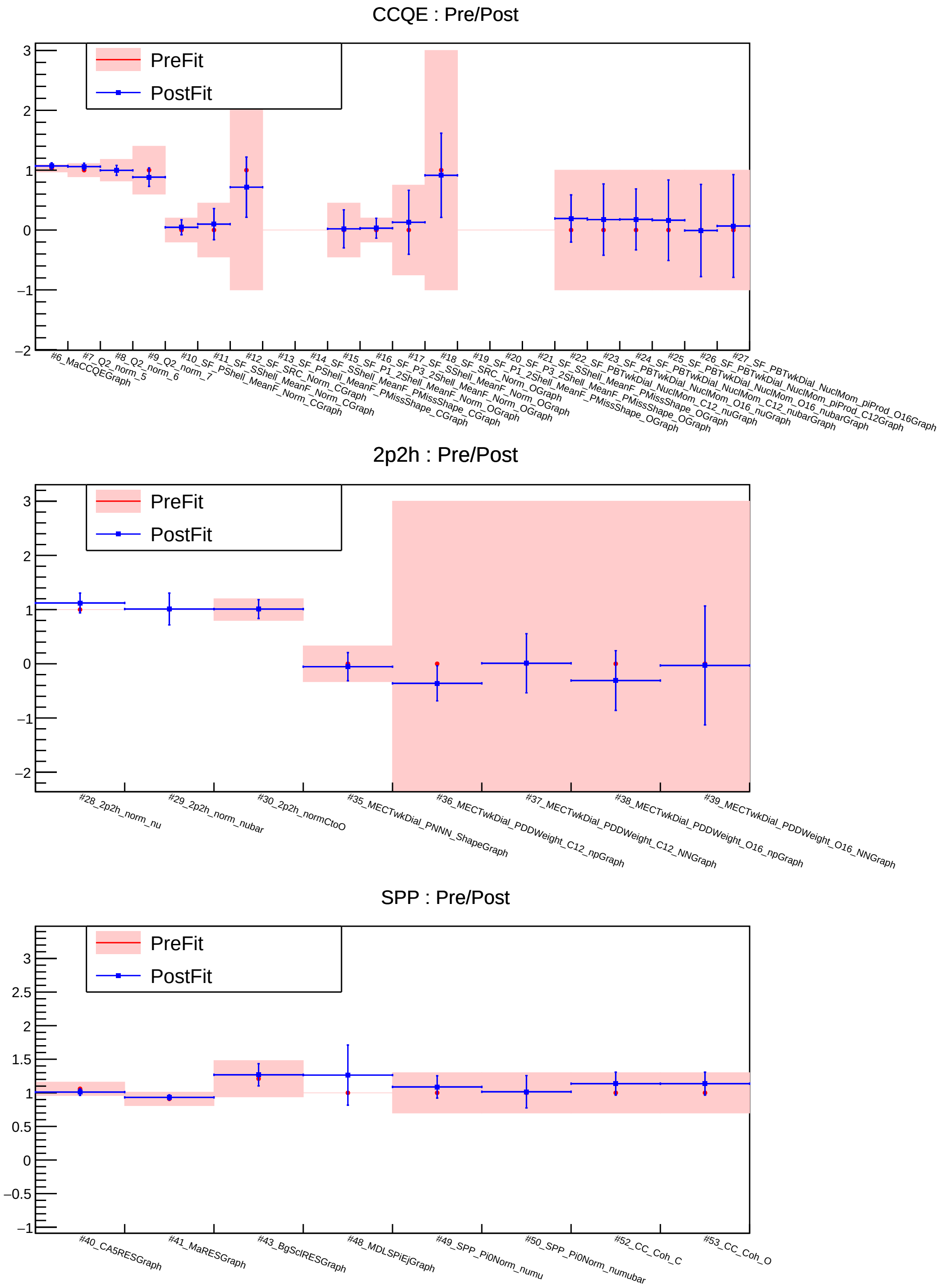

Figure 10.33: Cross section systematic parameters from the GUNDAM fit for the CC0pi Non-QE fake data study, showing CCQE (top), 2p2h (middle), and single pion production (bottom). The central values of the prefit are shown as red points, with pink shading showing the uncertainties. The postfit values are shown as blue points with uncertainties as error bars. The blank areas correspond to parameters that are fixed in the fit as they were expected to have a very low sensitivity to the fit [90], hence they have no postfit. All fitted parameters are within the prior uncertainties (except in cases where no prior uncertainty is set e.g. the 2p2h_norm parameters), suggesting the current priors are sufficient.

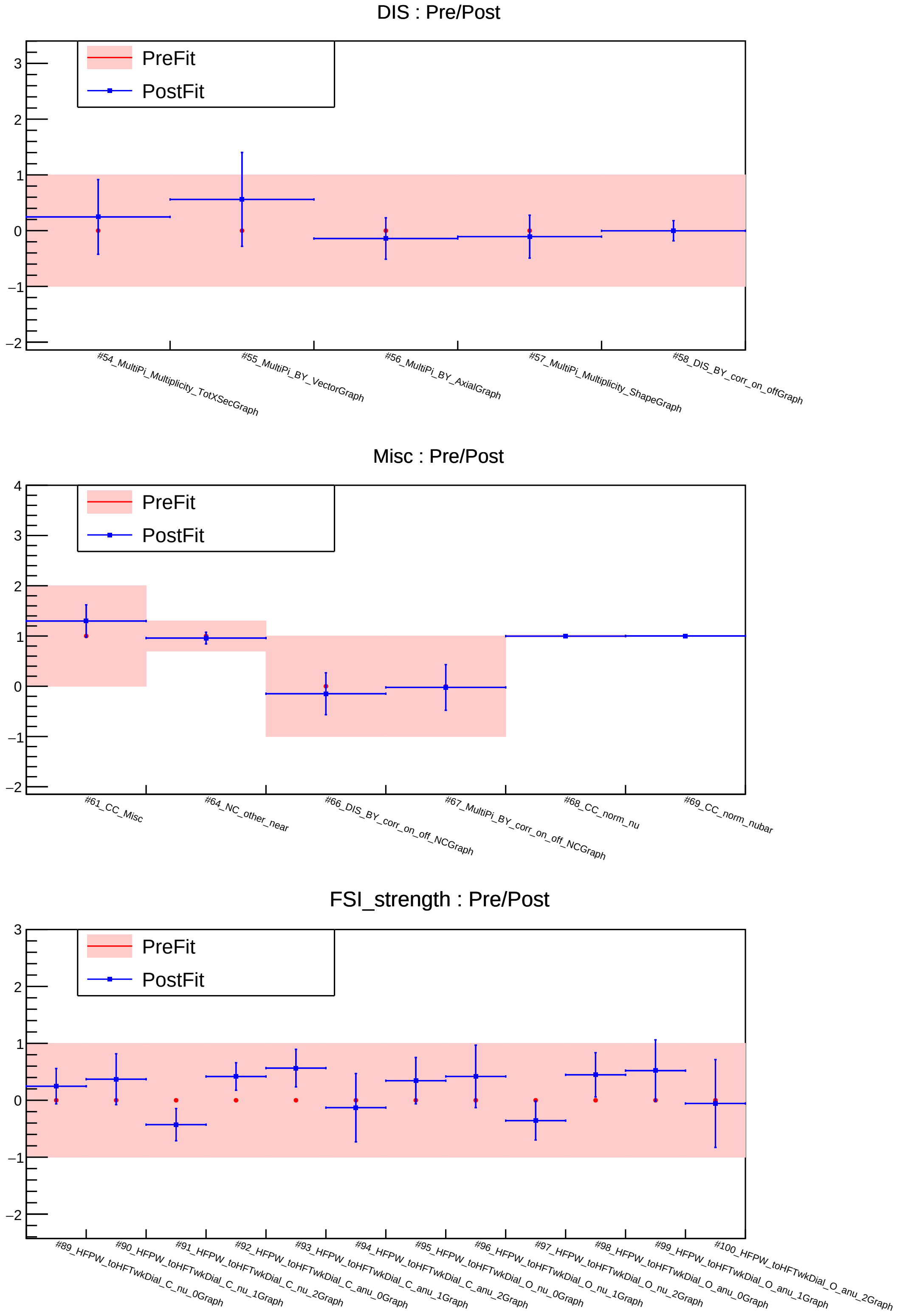

Figure 10.34: Cross section systematic parameters from the GUNDAM fit for the CC0pi Non-QE fake data study, showing DIS (top), miscellaneous parameters (middle), and FSI strength (bottom). The central values of the prefit are shown as red points, with pink shading showing the uncertainties. The postfit values are shown as blue points with uncertainties as error bars. All fitted parameters are within the prior uncertainties, suggesting the current priors are sufficient.

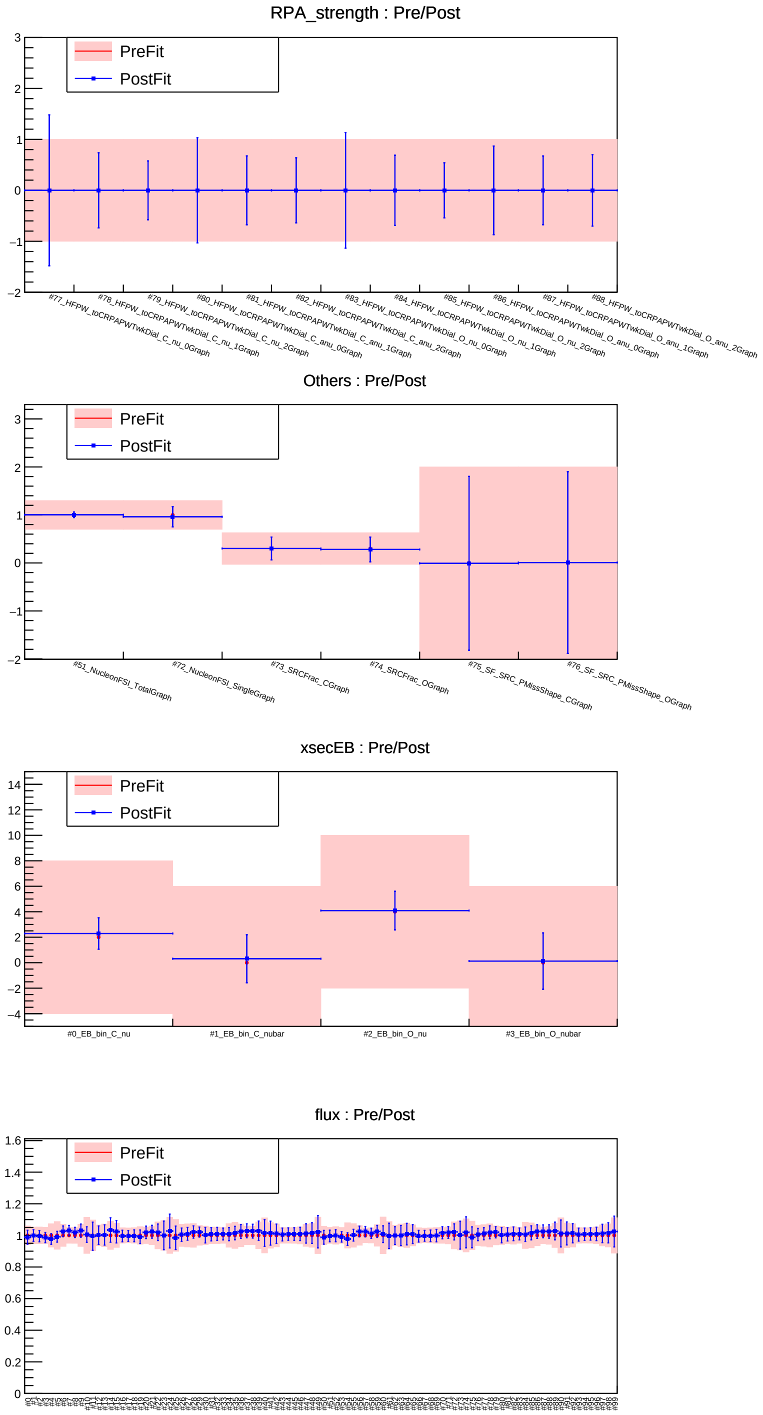

RPA_strength : Pre/Post

Others : Pre/Post

xsecEB : Pre/Post

flux : Pre/Post

Figure 10.35: Cross section systematic parameters from the GUNDAM fit for the CC0pi Non-QE fake data study. From top to bottom: RPA strength, other parameters, binding energy, and beam flux. The central values of the prefit are shown as red points, with pink shading showing the uncertainties. The postfit values are shown as blue points with uncertainties as error bars. The majority of fitted parameters are within the prior uncertainties, suggesting the current priors are sufficient.

10.7.2 2p2h Eb Correction

Figure 10.36 shows the prefit and postfit ratio plots for the 2p2h Eb Correction fake data study, for the CC$0\pi0\gamma$0pFwd sample. The prefit plot shows an increase in $R_{MC/FD}$ across all muon momenta and angles plotted, meaning the study reduces the number of events in almost all fake data bins compared to nominal MC. As the effect is relatively straightforward, it is unsurprising to see the postfit MC almost completely matches the fake data.

Figure 10.37 shows the values for the 2p2h parameters. As expected, there is a reduction in the normalisation parameters `2p2h_norm_nu` and `2p2h_norm_nubar`. The normalisation parameters are most heavily affected, which is expected given the nature of the fit.

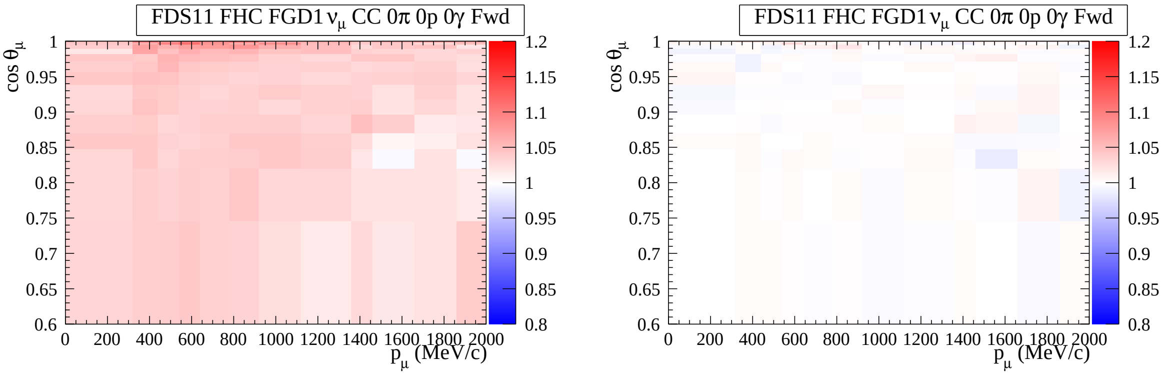

Figure 10.36: Comparisons between prefit (left) and postfit (right) for the 2p2h Eb Correction fake data study in the CC$0\pi0\gamma$0pFwd sample. The colour of each bin shows the value of the ratio $R_{MC/FD}$. The prefit χ^2 value is 21.8 and the postfit χ^2 value is 0.24. The fit quality is almost perfect across the full angle and momentum range, which is not unexpected given the fairly uniform nature of the prefit.

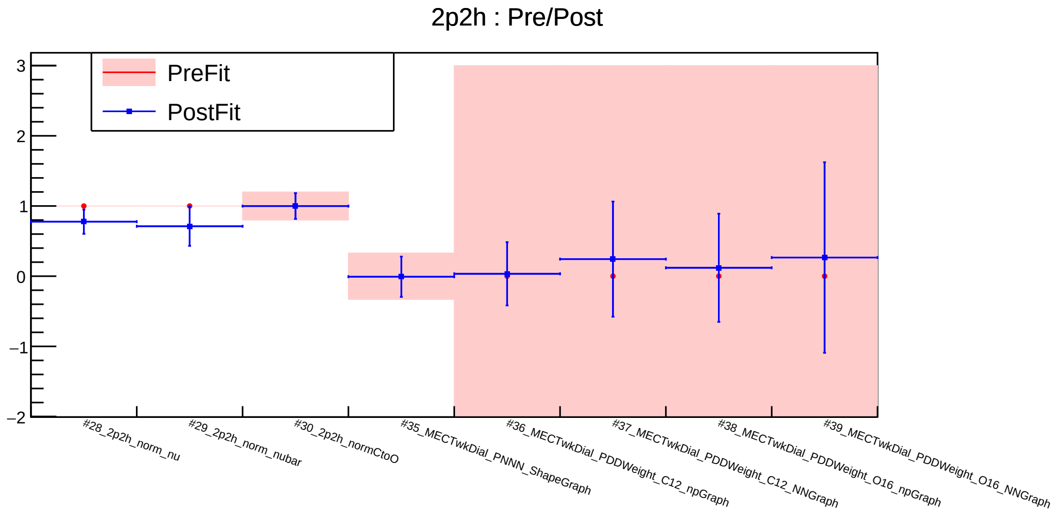

Figure 10.37: Cross section systematic parameters from the GUNDAM fit for the 2p2h Eb Correction fake data study. The central values of the prefit are shown as red points, with pink shading showing the uncertainties. The postfit values are shown as blue points with uncertainties as error bars. The normalisation parameters #28 and #29 are most heavily affected, which is expected given the nature of the fit affecting the full angular/momentum range.

10.7.3 MultiPi Multiplicity

Figure 10.38 shows the prefit and postfit ratio plots for the MultiPi Multiplicity fake data study, for the CC1π0γFwd sample. This sample was chosen because the study directly affects pion production. The prefit shows an decrease in $R_{MC/FD}$ across all muon momenta and angles compared to the nominal MC. In the postfit, the fitted MC closely matches the fake data, with a difference generally $< 5\%$.

The systematic values for the DIS parameters are presented in figure 10.39; this parameter group contains the multiπ-production-related systematics, hence contains the most significant parameters for this study. As expected, there is significant increase in the normalisation parameters `MultiPi_Multiplicity_TotXSecGraph` and `MultiPi_BY_VectorGraph`.

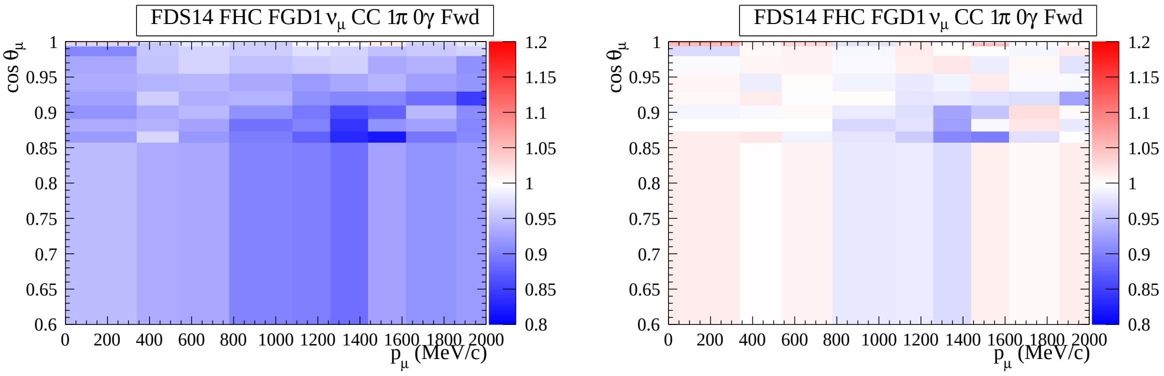

Figure 10.38: Comparisons between prefit (left) and postfit (right) for the MultiPi Multiplicity fake data study in the CC1π0γFwd sample. The colour of each bin shows the value of the ratio $R_{MC/FD}$. The prefit χ^2 value is 38.3 and the postfit χ^2 value is 2.54. The fit quality is generally good, showing that GUNDAM is capable of fitting this fake data set effectively.

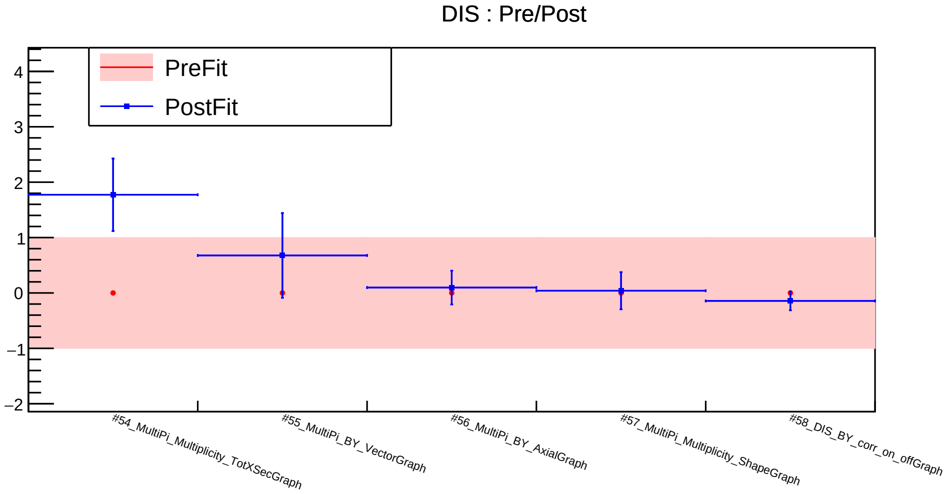

Figure 10.39: Cross section systematic parameters from the GUNDAM fit for the MultiPi Multiplicity fake data study. The central values of the prefit are shown as red points, with pink shading showing the uncertainties. The postfit values are shown as blue points with uncertainties as error bars. There is very strong pulling for the normalisation parameters #54 and #55, which is expected given the fake data has a consistent effect across the total momentum and angle range.

10.8 Fake Data Fit Results Summary

This analysis aimed to determine if the GUNDAM fitter was capable of fitting nominal MC to a wide range of fake data sets, some of which had extreme differences to the nominal MC that are highly unlikely to appear in real data. These extreme fake data studies are still useful as they allow us to test the fitter in situations beyond what it is optimised for, and as all fake data studies are motivated by some theoretical or observed result, none are strictly impossible.

GUNDAM is relatively new software and remains under development, so its ability to fit fake data was unknown but was expected to perform similarly to the previous fitter, BANFF. This work presents the first set of fake data studies performed using GUNDAM, where it was expected to be able to recover the fit quality of the 2021 fake data study [125], which used BANFF.

This new analysis also includes several other changes compared to 2021: new FSI strength and RPA strength parameters have replaced optical potential in the interaction model, and a new binning for the angular and momentum distributions have been introduced. These changes were primarily motivated to improve the real data fit, but it was unknown how the fake data fit would be affected, hence the need for this new analysis.

As there have been significant changes affecting the fit since the previous BANFF analysis, a direct comparison is difficult. Thus, a one-to-one comparison is not featured in this analysis. Comparisons with BANFF have been performed if the GUNDAM fit is apparently relatively poor (for example, in the SF to CRPA study), as in these cases similar results were observed in the BANFF fit.

The χ^2 values for each prefit and postfit plot presented above is summarised in table 10.1. All postfits show a very significant decrease in χ^2 compared to the prefits. The majority of the postfits have $\chi^2 < 10$, which is very low and these can be considered "well-fitted" without further comment. There are a number of exceptions, but these are not necessarily indicative of issues with GUNDAM. The SF to CRPA study (section 10.4.2) has a high postfit χ^2 of 32.6, but it can be seen from the fit plots in the 2021 analysis that the fit quality is no worse than is the previous BANFF fit. However, it was expected that the new FSI/RPA parameters implemented since 2021, which were actually motivated by this fake data set [95], would show noticeable improvements. This is currently still under investigation, but may be a result of the interpolation methods used for these new parameters, which are still in the process of being tuned.

The SF to SuSAv2 has a high postfit χ^2 of 25.8, but it is a new study so lacks a 2021 equivalent. However, it is known from the SF to CRPA study that fitters can struggle with changes to the nuclear model (this is not seen in SF to LFG as more work has been performed to correctly fit that study even before GUNDAM), so the results do not suggest an inherent flaw in GUNDAM's fitting capabilities and will probably need changes to the model itself to fully resolve. The Z-Expansion -1σ studies (sections 10.5.1 and 10.5.3) also show similar results to the 2021 fit.

It is worth reiterating that, as fake data sets, these studies deliberately diverge from what we expect from real detector data. The high quality of the fits show that GUNDAM and the MC model parameters are flexible enough to fit MC to data that is substantially different from the nominal model. All fits successfully converged, and there are no major bugs or issues in running the fit.

A future analysis for the fake data studies would be a full fake data oscillation analysis, using far detector fake data in conjunction with the fits presented here to analyse how the fake data affects the oscillation parameters themselves. At time of writing, no fake data oscillation analysis with GUNDAM has been performed. The software is still in the process of being validated against near detector fits, which must be completed before it can be used to generate any meaningful oscillation results.

Study	**Sample**	**Prefit χ^2**	**Postfit χ^2**
SF to LFG	CC0π0γ0pFwd	180.7	2.32
SF to CRPA	CC0π0γ0pFwd	193.0	32.6
SF to SuSAv2	CC0π0γ0pFwd	296.0	25.8
Z-Expansion -1σ	CC0π0γ0pFwd	17.3	9.17
Z-Expansion Nominal	CC0π0γ0pFwd	14.9	4.39
Z-Expansion +1σ	CC0π0γ0pFwd	272.7	21.3
3-Component -1σ	CC0π0γ0pFwd	113.5	0.61
3-Component Nominal	CC0π0γ0pFwd	96.3	0.41
3-Component $+1\sigma$	CC0π0γ0pFwd	231.9	0.70
LQCD Z-Expansion Nominal	CC0π0γ0pFwd	15.0	4.39
LQCD Z-Expansion -1σ	CC0π0γ0pFwd	150.6	19.0
SPP Matrix Element -1σ	CC1π0γFwd	11.5	2.51
SPP Matrix Element $+1\sigma$	CC1π0γFwd	2.28	1.18
SPP Adversarial	CC1π0γFwd	22.2	0.34
RS to Martini	CC1π0γFwd	29.7	2.52
Low-Q^2 Suppression SPP	CC1π0γFwd	206.5	2.29
CC0π Non-QE	CC0π0γ0pFwd	68.0	2.99
	CC0π0γNpFwd	115.3	8.51
2p2h Eb Correction	CC0π0γ0pFwd	21.8	0.24
MultiPi Multiplicity	CC1π0γFwd	38.3	2.54

Table 10.1: Comparison of prefit and postfit χ^2 values for fake data sets across samples presented in this chapter. Sets with postfit χ^2 values below 10 can be considered well-fitted. For those over 10, there has been discussion on how these are still within expected limits.

Chapter 11

Conclusions and the Future

The field of neutrino physics continues to advance at pace, and precise measurements and accurate analyses are more important than ever as more data is taken and statistical uncertainties decrease. Experiments current and future will push further into particle physics beyond the standard model, and explore new physics on scales from quantum to cosmological. The T2K experiment is a long-baseline neutrino experiment which provides world-leading results on neutrino oscillation parameter measurements. The continuation of its success relies on an ongoing program of upgrades to its detectors and analysis software.

This thesis presents only a few parts of the work that continues to be done for T2K, but represents significant promise for the ND280 near detector analysis. The Production 7 software upgrade, and the validation of the associated analysis tools presented in chapter 7, provides major improvements to main parts of the detector's reconstruction algorithms. The implementation of the 4π selection alongside it allows for a stronger comparison in beam composition between the near and far detectors, as both can analyse events across the full 4π solid-angle range. The efficiency and purity of the major samples of CC0pi, CC1pi, CCPhoton and CCOther has been preserved across P6 to P7, following necessary adjustments to certain selection parameters. It has also been shown that the TPC-ECal matching efficiencies are still at acceptable values. The run 8 timeslip correction algorithm has been shown to work fully in P7, even for topologies with low systematic uncertainties.

The GUNDAM fitter is a significant upgrade to the previous BANFF fitter, and presents improvements to efficacy, usability, and speed. As it is still under development, further testing and validation must be completed before it can be fully integrated into the T2K analysis. Despite the relatively early stages of the project, it has been shown here to be fully capable of performing accurate fits over extreme fake data studies far in excess of what could be expected for real detector data. Additionally, all fit results show acceptable χ^2 values for comparisons between the prefit and postfit momentum and $\cos\theta$ distributions. The GUNDAM fitter typically reduces the fake data-MC difference to less than 5% for all 19 fake data sets across the muon $\cos\theta$ and momentum phase space, and shows similar or improved results when compared with the 2021 BANFF analysis. This successful first exploration into fake data studies with GUNDAM will pave the way towards more in-depth analyses. A full oscillation analysis in conjunction with far detector fake data studies will be necessary in the future.

Beyond the software work presented in this thesis, the completion of the ND280++ in the 2024 upgrade marks a tremendous improvement in the detector's capabilities. The PØD has been replaced by multiple new subdetectors: the top and bottom high-angle TPCs, the superFGD, and six time-of-flight panels. These additions to the detector will require further analysis to fully capitalise on the trove of new data they are providing, but will considerably reduce uncertainties in neutrino measurements.

At the other end of the neutrino beamline, Super-Kamiokande's successor, Hyper-Kamiokande (Hyper-K), is currently under construction [34]. The new far detector will have a fiducial volume eight times that of Super-K, providing improved neutrino detection and many more neutrino events. Hyper-K, like Super-K, will also be used for other areas of neutrino research beyond T2K, including measuring neutrinos from astrophysical sources such as supernovae and the Sun. Hyper-K expects to begin data-taking in 2027. This is in conjunction with ongoing upgrades to the T2K neutrino beam, improving beam energy, number of protons on target, and faster beam spills [138].

To summarise, the work performed by the author has contributed significantly to the ND280 upgrade. This includes the assistance in construction of the new SuperFGD subdetector; the validation of multiple parts for the Production 7 software upgrade, including implementation of the new 4π solid-angle selection, validation of the timeslip correction algorithm, and ECal systematics; and the very first investigation into fake data studies that uses the new GUNDAM fitter. The P7 validation has been able to preserve the efficiency and purity of the main CC0π sample (P6 Eff: 47.49 ± 0.13 P7 Eff: 46.84 ± 0.13; P6 Pur: 78.99 ± 0.13 P7 Pur: 79.89 ± 0.13) despite major changes to the reconstruction algorithms introduced in P7. The GUNDAM work has show a high quality of fitting across almost all fake data sets, with the majority of postfit χ^2 values being < 10.

Bibliography

[1] J. Chadwick. "The intensity distribution in the magnetic spectrum of β particles from radium (B + C)". In: *Verh. Phys. Gesell.* 16 (1914), pp. 383–391.

[2] W. Pauli. "Dear radioactive ladies and gentlemen". In: *Phys. Today* 31N9 (1978), p. 27.

[3] E. Fermi. "Versuch einer Theorie der β-Strahlen. I". In: *Zeitschrift für Physik* 88 (1934), pp. 161–177. URL: `https://api.semanticscholar.org/CorpusID:125763380`.

[4] C. L. Cowan et al. "Detection of the Free Neutrino: a Confirmation". In: *Science* 124.3212 (1956), pp. 103–104. DOI: `10.1126/science.124.3212.103`. eprint: `https://www.science.org/doi/pdf/10.1126/science.124.3212.103`. URL: `https://www.science.org/doi/abs/10.1126/science.124.3212.103`.

[5] Ivan V. Anicin. *The Neutrino - Its Past, Present and Future.* 2005. arXiv: `physics/0503172 [physics.hist-ph]`. URL: `https://arxiv.org/abs/physics/0503172`.

[6] G. Danby et al. "Observation of High-Energy Neutrino Reactions and the Existence of Two Kinds of Neutrinos". In: *Physical Review Letters* 9 (1962), pp. 36–44. URL: `https://api.semanticscholar.org/CorpusID:120314867`.

[7] M. L. Perl et al. "Evidence for Anomalous Lepton Production in $e^+ - e^-$ Annihilation". In: *Phys. Rev. Lett.* 35 (22 Dec. 1975), pp. 1489–1492. DOI: `10.1103/PhysRevLett.35.1489`. URL: `https://link.aps.org/doi/10.1103/PhysRevLett.35.1489`.

[8] K. Kodama et al. "Observation of tau neutrino interactions". In: *Physics Letters B* 504.3 (2001), pp. 218–224. ISSN: 0370-2693. DOI: `https://doi.org/10.1016/S0370-2693(01)00307-0`. URL: `https://www.sciencedirect.com/science/article/pii/S0370269301003070`.

[9] C. Burgess and G. Moore. *The Standard Model: A Primer.* Cambridge University Press, 2006.

[10] S. Navas et al. “Review of particle physics”. In: *Phys. Rev. D* 110.3 (2024), p. 030001. DOI: `10.1103/PhysRevD.110.030001`.

[11] The Standard Model, TikZ.net. URL: `https://tikz.net/sm_particles/`.

[12] J. N. Bahcall and R. Davis. “Solar Neutrinos: A Scientific Puzzle”. In: *Science* 191.4224 (1976), pp. 264–267. DOI: `10.1126/science.191.4224.264`. eprint: `https://www.science.org/doi/pdf/10.1126/science.191.4224.264`. URL: `https://www.science.org/doi/abs/10.1126/science.191.4224.264`.

[13] J. N. Bahcall et al. “Solar neutrino flux”. In: *Astrophys. J.* 137 (1963), pp. 344–346. DOI: `10.1086/147513`.

[14] N. Prakash. *Dark Matter, Neutrinos, and Our Solar System.* World Scientific Publishing, 2013.

[15] D. Vignaud. “The GALLEX solar neutrino experiment”. In: *Nuclear Physics B - Proceedings Supplements* 60.3 (1998), pp. 20–29. ISSN: 0920-5632. DOI: `https://doi.org/10.1016/S0920-5632(97)00498-2`. URL: `https://www.sciencedirect.com/science/article/pii/S0920563297004982`.

[16] K. Nakamura. “Present status and future of Kamiokande”. In: *Conf. Proc. C* 890928 (1989), p. 297.

[17] A. Bellerive et al. “The Sudbury Neutrino Observatory”. In: *Nuclear Physics B* 908 (2016). Neutrino Oscillations: Celebrating the Nobel Prize in Physics 2015, pp. 30–51. ISSN: 0550-3213. DOI: `https://doi.org/10.1016/j.nuclphysb.2016.04.035`. URL: `https://www.sciencedirect.com/science/article/pii/S0550321316300736`.

[18] Q. R. Ahmad et al. “Direct Evidence for Neutrino Flavor Transformation from Neutral-Current Interactions in the Sudbury Neutrino Observatory”. In: *Phys. Rev. Lett.* 89 (1 June 2002), p. 011301. DOI: `10.1103/PhysRevLett.89.011301`. URL: `https://link.aps.org/doi/10.1103/PhysRevLett.89.011301`.

[19] Takaaki Kajita. “Atmospheric neutrinos and discovery of neutrino oscillations”. In: *Proceedings of the Japan Academy, Series B: Physical and Biological Sciences* 86.4 (2010), pp. 303–321. DOI: `10.2183/pjab.86.303`.

[20] B. Pontecorvo. “Mesonium and Antimesonium”. In: *Soviet Journal of Experimental and Theoretical Physics* 6 (1958), p. 429.

[21] Ziro Maki, Masami Nakagawa, and Shoichi Sakata. "Remarks on the Unified Model of Elementary Particles". In: *Progress of Theoretical Physics* 28.5 (Nov. 1962), pp. 870–880. ISSN: 0033-068X. DOI: `10.1143/PTP.28.870`. eprint: `https://academic.oup.com/ptp/article-pdf/28/5/870/5258750/28-5-870.pdf`. URL: `https://doi.org/10.1143/PTP.28.870`.

[22] B. Pontecorvo. "Neutrino Experiments and the Problem of Conservation of Leptonic Charge". In: *Soviet Journal of Experimental and Theoretical Physics* 26 (May 1968), p. 984.

[23] Steve Boyd. *Neutrino Oscillations*. Neutrino Lecture Series. URL: `https://warwick.ac.uk/fac/sci/physics/staff/academic/boyd/stuff/neutrinolectures/`.

[24] S. P. Mikheyev and A. Yu. Smirnov. "Resonance enhancement of oscillations in matter and solar neutrino spectroscopy". In: *Yadernaya Fizika* 42 (Jan. 1985). Provided by the SAO/NASA Astrophysics Data System, pp. 1441–1448. URL: `https://ui.adsabs.harvard.edu/abs/1985YaFiz..42.1441M`.

[25] L. Wolfenstein. "Neutrino oscillations in matter". In: *Physical Review D (Particles and Fields)* 17.9 (May 1978). Provided by the SAO/NASA Astrophysics Data System, pp. 2369–2374. DOI: `10.1103/PhysRevD.17.2369`. URL: `https://ui.adsabs.harvard.edu/abs/1978PhRvD..17.2369W`.

[26] X. Qian and P. Vogel. "Neutrino mass hierarchy". In: *Progress in Particle and Nuclear Physics* 83 (July 2015), pp. 1–30. ISSN: 0146-6410. DOI: `10.1016/j.ppnp.2015.05.002`. URL: `http://dx.doi.org/10.1016/j.ppnp.2015.05.002`.

[27] Maria Prado Rodriguez. "Neutrino Mass Ordering with IceCube DeepCore". In: *Physical Sciences Forum* 8.1 (2023). ISSN: 2673-9984. DOI: `10.3390/psf2023008007`. URL: `https://www.mdpi.com/2673-9984/8/1/7`.

[28] Stefano Gariazzo et al. "Neutrino mass and mass ordering: no conclusive evidence for normal ordering". In: *Journal of Cosmology and Astroparticle Physics* 2022.10 (Oct. 2022), p. 010. ISSN: 1475-7516. DOI: `10.1088/1475-7516/2022/10/010`. URL: `http://dx.doi.org/10.1088/1475-7516/2022/10/010`.

[29] Super-Kamiokande et al. *First joint oscillation analysis of Super-Kamiokande atmospheric and T2K accelerator neutrino data*. 2024. arXiv: `2405.12488 [hep-ex]`. URL: `https://arxiv.org/abs/2405.12488`.

[30] KATRIN Collaboration et al. "Direct neutrino-mass measurement based on 259 days of KATRIN data". In: *Science* 388.6743 (2025), pp. 180–185. DOI: `10.1126/science.adq9592`. eprint: `https://www.science.org/doi/pdf/10.1126/science.adq9592`. URL: `https://www.science.org/doi/abs/10.1126/science.adq9592`.

[31] K. Abe et al. "Results from the T2K Experiment on Neutrino Mixing Including a New Far Detector μ-like Sample". In: *Physical Review Letters* 135.26 (Dec. 2025). ISSN: 1079-7114. DOI: `10.1103/gh5j-5cwv`. URL: `http://dx.doi.org/10.1103/gh5j-5cwv`.

[32] NOvA Website. URL: `https://novaexperiment.fnal.gov/`.

[33] The NOvA Collaboration et al. *Precision measurement of neutrino oscillation parameters with 10 years of data from the NOvA experiment.* 2025. arXiv: `2509.04361 [hep-ex]`. URL: `https://arxiv.org/abs/2509.04361`.

[34] Hyper-Kamiokande Proto-Collaboration et al. *Hyper-Kamiokande Design Report.* 2018. arXiv: `1805.04163 [physics.ins-det]`. URL: `https://arxiv.org/abs/1805.04163`.

[35] DUNE Website. URL: `https://www.dunescience.org/`.

[36] L.J. Wen, J. Cao, and Y.F. Wang. "Reactor Neutrino Experiments: Present and Future". In: *Annual Review of Nuclear and Particle Science* 67.1 (Oct. 2017), pp. 183–211. ISSN: 1545-4134. DOI: `10.1146/annurev-nucl-101916-123318`. URL: `http://dx.doi.org/10.1146/annurev-nucl-101916-123318`.

[37] Jun Cao and Kam-Biu Luk. "An overview of the Daya Bay reactor neutrino experiment". In: *Nuclear Physics B* 908 (2016). Neutrino Oscillations: Celebrating the Nobel Prize in Physics 2015, pp. 62–73. ISSN: 0550-3213. DOI: `https://doi.org/10.1016/j.nuclphysb.2016.04.034`. URL: `https://www.sciencedirect.com/science/article/pii/S0550321316300724`.

[38] H. de Kerret et al. "The Double Chooz antineutrino detectors". In: *The European Physical Journal C* 82.9 (Sept. 2022). ISSN: 1434-6052. DOI: `10.1140/epjc/s10052-022-10726-x`. URL: `http://dx.doi.org/10.1140/epjc/s10052-022-10726-x`.

[39] RENO Collaboration and J. K. Ahn. *RENO: An Experiment for Neutrino Oscillation Parameter θ_{13} Using Reactor Neutrinos at Yonggwang.* 2010. arXiv: `1003.1391 [hep-ex]`. URL: `https://arxiv.org/abs/1003.1391`.

[40] Daya Bay Collaboration. *A Precision Measurement of the Neutrino Mixing Angle θ_{13} using Reactor Antineutrinos at Daya Bay.* 2007. arXiv: `hep-ex/0701029 [hep-ex]`. URL: `https://arxiv.org/abs/hep-ex/0701029`.

[41] Daya Bay collaboration et al. *Precision measurement of reactor antineutrino oscillation at kilometer-scale baselines by Daya Bay.* 2022. arXiv: `2211.14988 [hep-ex]`. URL: `https://arxiv.org/abs/2211.14988`.

[42] M Patrick Decowski and (forthe KamLand Collaboration). "KamLAND's precision measurement of neutrino oscillation parameters". In: *Journal of Physics: Conference Series* 136.2 (Nov. 2008), p. 022005. DOI: `10.1088/1742-6596/136/2/022005`. URL: `https://doi.org/10.1088/1742-6596/136/2/022005`.

[43] K. Eguchi et al. "First Results from KamLAND: Evidence for Reactor Antineutrino Disappearance". In: *Physical Review Letters* 90.2 (Jan. 2003). ISSN: 1079-7114. DOI: `10.1103/physrevlett.90.021802`. URL: `http://dx.doi.org/10.1103/PhysRevLett.90.021802`.

[44] R. Abbasi et al. "Measurement of atmospheric neutrino mixing with improved IceCube DeepCore calibration and data processing". In: *Phys. Rev. D* 108 (1 July 2023), p. 012014. DOI: `10.1103/PhysRevD.108.012014`. URL: `https://link.aps.org/doi/10.1103/PhysRevD.108.012014`.

[45] J. A. Formaggio and G. P. Zeller. "From eV to EeV: Neutrino cross sections across energy scales". In: *Reviews of Modern Physics* 84.3 (Sept. 2012), pp. 1307–1341. ISSN: 1539-0756. DOI: `10.1103/revmodphys.84.1307`. URL: `http://dx.doi.org/10.1103/RevModPhys.84.1307`.

[46] SNO+ Website. URL: `https://snoplus.phy.queensu.ca/`.

[47] NuDoubt^{++}. URL: `https://nudoubt.uni-mainz.de/scientific.php`.

[48] S. Bilenky. *Neutrinos: Majorana or Dirac?* 2020. arXiv: `2008.02110 [hep-ph]`. URL: `https://arxiv.org/abs/2008.02110`.

[49] A. Alavi-Harati et al. "Observation of Direct CP Violation in $K_{S,L} \to \pi\pi$ Decays". In: *Phys. Rev. Lett.* 83 (1 July 1999), pp. 22–27. DOI: `10.1103/PhysRevLett.83.22`. URL: `https://link.aps.org/doi/10.1103/PhysRevLett.83.22`.

[50] Helen O'Keeffe. "Status and plans for T2K neutrino oscillation analyses". In: *NuFact.* 2025.

[51] Hiroshi Nunokawa, Stephen Parke, and José W.F. Valle. "CP violation and neutrino oscillations". In: *Progress in Particle and Nuclear Physics* 60.2 (Apr. 2008), pp. 338–402. ISSN: 0146-6410. DOI: `10.1016/j.ppnp.2007.10.001`. URL: `http://dx.doi.org/10.1016/j.ppnp.2007.10.001`.

[52] K. Abe et al. "The T2K experiment". In: *Nuclear Instruments and Methods in Physics Research Section A: Accelerators, Spectrometers, Detectors and Associated Equipment* 659.1 (Dec. 2011), pp. 106–135. ISSN: 0168-9002. DOI: `10.1016/j.nima.2011.06.067`. URL: `http://dx.doi.org/10.1016/j.nima.2011.06.067`.

[53] K. Abe et al. "Measurements of neutrino oscillation parameters from the T2K experiment using 3.6×10^{21} protons on target". In: *The European Physical Journal C* 83.9 (Sept. 2023). ISSN: 1434-6052. DOI: `10.1140/epjc/s10052-023-11819-x`. URL: `http://dx.doi.org/10.1140/epjc/s10052-023-11819-x`.

[54] S. Igarashi et al. "Accelerator design for 1.3-MW beam power operation of the J-PARC Main Ring". In: *Progress of Theoretical and Experimental Physics* 2021.3 (Feb. 2021), 033G01. ISSN: 2050-3911. DOI: `10.1093/ptep/ptab011`. eprint: `https://academic.oup.com/ptep/article-pdf/2021/3/033G01/36647732/ptab011.pdf`. URL: `https://doi.org/10.1093/ptep/ptab011`.

[55] S. Nagamiya. "The entire view of J-PARC". URL: `https://commons.wikimedia.org/wiki/File:The_entire_view_of_J-PARC.jpg`.

[56] K. Matsuoka et al. "Design and performance of the muon monitor for the T2K neutrino oscillation experiment". In: *Nuclear Instruments and Methods in Physics Research Section A: Accelerators, Spectrometers, Detectors and Associated Equipment* 624.3 (Dec. 2010), pp. 591–600. ISSN: 0168-9002. DOI: `10.1016/j.nima.2010.09.074`. URL: `http://dx.doi.org/10.1016/j.nima.2010.09.074`.

[57] University of Warwick T2K Scientific Overview. URL: `https://warwick.ac.uk/fac/sci/physics/research/epp/exp/t2k/overview_scientific/`.

[58] K. Abe et al. "Measurements of the T2K neutrino beam properties using the INGRID on-axis near detector". In: *Nuclear Instruments and Methods in Physics Research Section A: Accelerators, Spectrometers, Detectors and Associated Equipment* 694 (Dec. 2012), pp. 211–223. ISSN: 0168-9002. DOI: `10.1016/j.nima.2012.03.023`. URL: `http://dx.doi.org/10.1016/j.nima.2012.03.023`.

[59] T2K Official Latest INGRID Diagram. URL: `https://www.t2k.org/docs/plotsx/general/nd280/ingrid/latest_diagram`.

[60] Pablo Fernandez. “Recent results from the long-baseline (LBL) neutrino oscillation experiments”. In: *SciPost Physics Proceedings* (Sept. 2019), pp. 24–28. DOI: `10.21468/SciPostPhysProc.1.029`.

[61] T. Ovsiannikova et al. “The new experiment WAGASCI for water to hydrocarbon neutrino cross section measurement using the J-PARC beam”. In: *Journal of Physics: Conference Series* 675.1 (Jan. 2016), p. 012030. DOI: `10.1088/1742-6596/675/1/012030`. URL: `https://dx.doi.org/10.1088/1742-6596/675/1/012030`.

[62] M. Antonova et al. “Baby MIND: a magnetized segmented neutrino detector for the WAGASCI experiment”. In: *Journal of Instrumentation* 12.07 (July 2017), pp. C07028–C07028. ISSN: 1748-0221. DOI: `10.1088/1748-0221/12/07/c07028`. URL: `http://dx.doi.org/10.1088/1748-0221/12/07/C07028`.

[63] Naoki Otani. *The Preparation Status and Plan for the Next Physics Run of the NINJA Experiment*. 2025. arXiv: `2501.04119 [physics.ins-det]`. URL: `https://arxiv.org/abs/2501.04119`.

[64] T2K Official Latest WAGASCI/Baby MIND Diagram. URL: `https://www.t2k.org/docs/plotsx/general/nd280/wagasci-baby-mind/diagram`.

[65] S. Fukuda et al. “The Super-Kamiokande detector”. In: *Nuclear Instruments and Methods in Physics Research Section A: Accelerators, Spectrometers, Detectors and Associated Equipment* 501.2 (2003), pp. 418–462. ISSN: 0168-9002. DOI: `https://doi.org/10.1016/S0168-9002(03)00425-X`. URL: `https://www.sciencedirect.com/science/article/pii/S016890020300425X`.

[66] Supernova Early Warning System Website. URL: `https://snews2.org/`.

[67] K. Abe et al. “Evidence for the Appearance of Atmospheric Tau Neutrinos in Super-Kamiokande”. In: *Physical Review Letters* 110.18 (May 2013). ISSN: 1079-7114. DOI: `10.1103/physrevlett.110.181802`. URL: `http://dx.doi.org/10.1103/PhysRevLett.110.181802`.

[68] A. Nath and Ng. K. Francis. “Detection techniques and investigation of different neutrino experiments”. In: *International Journal of Modern Physics A* 36.13 (Apr. 2021), p. 2130008. ISSN: 1793-656X. DOI: `10.1142/s0217751x21300088`. URL: `http://dx.doi.org/10.1142/S0217751X21300088`.

[69] K. Abe et al. "First gadolinium loading to Super-Kamiokande". In: *Nuclear Instruments and Methods in Physics Research Section A: Accelerators, Spectrometers, Detectors and Associated Equipment* 1027 (2022), p. 166248. ISSN: 0168-9002. DOI: `https://doi.org/10.1016/j.nima.2021.166248`. URL: `https://www.sciencedirect.com/science/article/pii/S0168900221010883`.

[70] P.-A. Amaudruz et al. "The T2K fine-grained detectors". In: *Nuclear Instruments and Methods in Physics Research Section A: Accelerators, Spectrometers, Detectors and Associated Equipment* 696 (Dec. 2012), pp. 1–31. ISSN: 0168-9002. DOI: `10.1016/j.nima.2012.08.020`. URL: `http://dx.doi.org/10.1016/j.nima.2012.08.020`.

[71] M. Yokoyama et al. "Performance of multi-pixel photon counters for the T2K near detectors". In: *Nuclear Instruments and Methods in Physics Research Section A: Accelerators, Spectrometers, Detectors and Associated Equipment* 622.3 (Oct. 2010), pp. 567–573. ISSN: 0168-9002. DOI: `10.1016/j.nima.2010.07.070`. URL: `http://dx.doi.org/10.1016/j.nima.2010.07.070`.

[72] S. Assylbekov et al. "The T2K ND280 off-axis pi–zero detector". In: *Nuclear Instruments and Methods in Physics Research Section A: Accelerators, Spectrometers, Detectors and Associated Equipment* 686 (Sept. 2012), pp. 48–63. ISSN: 0168-9002. DOI: `10.1016/j.nima.2012.05.028`. URL: `http://dx.doi.org/10.1016/j.nima.2012.05.028`.

[73] T2K ND280 TPC collaboration. *Time Projection Chambers for the T2K Near Detectors*. 2010. arXiv: `1012.0865 [physics.ins-det]`. URL: `https://arxiv.org/abs/1012.0865`.

[74] I. Giomataris et al. "Micromegas in a bulk". In: *Nuclear Instruments and Methods in Physics Research Section A: Accelerators, Spectrometers, Detectors and Associated Equipment* 560.2 (May 2006), pp. 405–408. ISSN: 0168-9002. DOI: `10.1016/j.nima.2005.12.222`. URL: `http://dx.doi.org/10.1016/j.nima.2005.12.222`.

[75] D. Allan et al. "The electromagnetic calorimeter for the T2K near detector ND280". In: *Journal of Instrumentation* 8.10 (Oct. 2013), P10019–P10019. ISSN: 1748-0221. DOI: `10.1088/1748-0221/8/10/p10019`. URL: `http://dx.doi.org/10.1088/1748-0221/8/10/P10019`.

[76] K. Abe et al. *T2K ND280 Upgrade – Technical Design Report*. 2020. arXiv: `1901.03750 [physics.ins-det]`. URL: `https://arxiv.org/abs/1901.03750`.

[77] T. Kikawa. "The SuperFGD for the upgraded T2K near detector — Operation and performance". In: *Nuclear Instruments and Methods in Physics Research Section A: Accelerators, Spectrometers, Detectors and Associated Equipment* 1080 (2025), p. 170616. ISSN: 0168-9002. DOI: `https://doi.org/10.1016/j.nima.2025.170616`. URL: `https://www.sciencedirect.com/science/article/pii/S0168900225004176`.

[78] S. Levorato. "Technical challenges for the new T2K ND280 High-Angle Time Projection Chambers". In: *Nuclear Instruments and Methods in Physics Research Section A: Accelerators, Spectrometers, Detectors and Associated Equipment* 1080 (2025), p. 170709. ISSN: 0168-9002. DOI: `https://doi.org/10.1016/j.nima.2025.170709`. URL: `https://www.sciencedirect.com/science/article/pii/S0168900225005108`.

[79] C. Betancourt et al. "Application of large area SiPMs for the readout of a plastic scintillator based timing detector". In: *Journal of Instrumentation* 12.11 (Nov. 2017), P11023–P11023. ISSN: 1748-0221. DOI: `10.1088/1748-0221/12/11/p11023`. URL: `http://dx.doi.org/10.1088/1748-0221/12/11/P11023`.

[80] N. Abgrall et al. "Measurements of $\pi^{\pm}$ differential yields from the surface of the T2K replica target for incoming 31 GeV/c protons with the NA61/SHINE spectrometer at the CERN SPS". In: *The European Physical Journal C* 76.11 (2016), p. 617. ISSN: 1434-6052. DOI: `10.1140/epjc/s10052-016-4440-y`. URL: `https://doi.org/10.1140/epjc/s10052-016-4440-y`.

[81] L. Berns et al. "Flux Prediction and Uncertainty with NA61/SHINE 2010 Replica Target Measurements". T2K Technical Note 401. 2022.

[82] A. Ferrari et al. "FLUKA: A multi-particle transport code (Program version 2005)". In: (Oct. 2005). DOI: `10.2172/877507`.

[83] K. Abe et al. "T2K neutrino flux prediction". In: *Phys. Rev. D* 87 (1 2013), p. 012001. DOI: `10.1103/PhysRevD.87.012001`. URL: `https://link.aps.org/doi/10.1103/PhysRevD.87.012001`.

[84] N. Abgrall et al. "Measurements of $\pi^{\pm}$, $K^{\pm}$, K^0_S, Λ and proton production in proton–carbon interactions at 31 GeV/c with the NA61/SHINE spectrometer at the CERN SPS". In: 76.2 (2016), p. 84.

[85] L. Berns et al. "Flux Prediction and Uncertainty with NA61/SHINE 20091 Replica-Target Data". T2K Technical Note 354. 2020.

[86] L. Alvarez-Ruso et al. “NuSTEC1 1Neutrino Scattering Theory Experiment Collaboration http://nustec.fnal.gov. White Paper: Status and challenges of neutrino–nucleus scattering”. In: *Progress in Particle and Nuclear Physics* 100 (2018), pp. 1–68. ISSN: 0146-6410. DOI: `https://doi.org/10.1016/j.ppnp.2018.01.006`. URL: `https://www.sciencedirect.com/science/article/pii/S0146641018300061`.

[87] L. Pickering Y. Hayato. “The NEUT neutrino interaction simulation program library”. In: *Phys. J. Spec. Top.* 230 (24 2021), pp. 4469–4481. DOI: `10.1140/epjs/s11734-021-00287-7`. URL: `https://doi.org/10.1140/epjs/s11734-021-00287-7`.

[88] E. Atkin et al. “NIWG model and uncertainties for 2019-2020 oscillation analysis”. T2K Technical Note 344. 2019.

[89] P. Stowell et al. “NUISANCE: a neutrino cross-section generator tuning and comparison framework”. In: *Journal of Instrumentation* 12.01 (Jan. 2017), P01016. DOI: `10.1088/1748-0221/12/01/P01016`. URL: `https://dx.doi.org/10.1088/1748-0221/12/01/P01016`.

[90] C. Bronner et al. “NIWG model and uncertainties for 2021 oscillation analysis”. T2K Technical Note 441. 2021.

[91] K. Abe et al. “Improved constraints on neutrino mixing from the T2K experiment with 3.3×10^{21} protons on target”. In: *Physical Review D* 103.11 (June 2021). ISSN: 2470-0029. DOI: `10.1103/physrevd.103.112008`. URL: `http://dx.doi.org/10.1103/PhysRevD.103.112008`.

[92] J. Nieves, I. Ruiz Simo, and M.J. Vicente Vacas. “The nucleon axial mass and the MiniBooNE quasielastic neutrino–nucleus scattering problem”. In: *Physics Letters B* 707.1 (2012), pp. 72–75. ISSN: 0370-2693. DOI: `https://doi.org/10.1016/j.physletb.2011.11.061`. URL: `https://www.sciencedirect.com/science/article/pii/S0370269311014407`.

[93] D. Rein and L. M. Sehgal. “Neutrino-excitation of baryon resonances and single pion production”. In: *Annals of Physics* 133.1 (1981), pp. 79–153. ISSN: 0003-4916. DOI: `https://doi.org/10.1016/0003-4916(81)90242-6`. URL: `https://www.sciencedirect.com/science/article/pii/0003491681902426`.

[94] Ch. Berger and L. M. Sehgal. “Partially conserved axial vector current and coherent pion production by low energy neutrinos”. In: *Phys. Rev. D* 79 (5 Mar. 2009), p. 053003. DOI: `10.1103/PhysRevD.79.053003`. URL: `https://link.aps.org/doi/10.1103/PhysRevD.79.053003`.

[95] C. Bronner et. al. "NIWG Model and Uncertainty Recommendation for the 2024 Oscillation Analysis". T2K Technical Note 493. 2024.

[96] M Glück, E Reya, and A Vogt. "Dynamical parton distributions revisited". In: *The European Physical Journal C - Particles and Fields* 5.3 (1998), pp. 461–470.

[97] A. Bodek and U. K. Yang. "Modeling Neutrino and Electron Scattering Cross Sections in the Few GeV Region with Effective LO PDFs". In: *AIP Conference Proceedings* 670.1 (June 2003), pp. 110–117. ISSN: 0094-243X. DOI: `10.1063/1.1594324`. eprint: `https://pubs.aip.org/aip/acp/article-pdf/670/1/110/11879340/110\_1\_online.pdf`. URL: `https://doi.org/10.1063/1.1594324`.

[98] T. Sjöstrand. "High-energy-physics event generation with PYTHIA 5.7 and JETSET 7.4". In: *Computer Physics Communications* 82.1 (1994), pp. 74–89. ISSN: 0010-4655. DOI: `https://doi.org/10.1016/0010-4655(94)90132-5`. URL: `https://www.sciencedirect.com/science/article/pii/0010465594901325`.

[99] L.L. Salcedo et al. "Computer simulation of inclusive pion nuclear reactions". In: *Nuclear Physics A* 484.3 (1988), pp. 557–592. ISSN: 0375-9474. DOI: `https://doi.org/10.1016/0375-9474(88)90310-7`. URL: `https://www.sciencedirect.com/science/article/pii/0375947488903107`.

[100] Y. Hayato. "A neutrino interaction simulation program library NEUT". In: *Acta Phys. Polon. B* 40 (2009). Ed. by Arthur Ankowski and Jan Sobczyk, pp. 2477–2489.

[101] S. Agostinelli et al. "Geant4—a simulation toolkit". In: *Nuclear Instruments and Methods in Physics Research Section A: Accelerators, Spectrometers, Detectors and Associated Equipment* 506.3 (2003), pp. 250–303. ISSN: 0168-9002. DOI: `https://doi.org/10.1016/S0168-9002(03)01368-8`. URL: `https://www.sciencedirect.com/science/article/pii/S0168900203013688`.

[102] T. Doyle et al. "FHC and RHC Event Selections with ND280 for the 2024 Oscillation Analysis Inputs: Run 2-9 with Production 7E NEUT 5.6.4.1 p7c1". T2K Technical Note 488. 2024.

[103] P. Bartet et al. "NIWG model and uncertainties for 2019-2020 oscillation analysis". T2K Technical Note 212. 2015.

[104] Y. Xu. "Constraining neutrino interaction parameters using the T2K off-axis near detector ND280 with a 4π solid angle sample selection". PhD thesis. Lancaster University, 2023.

[105] HighLAND2 GitLab Repository. URL: `https://git.t2k.org/nd280/highland2Software`.

[106] The HighLAND framework. URL: `https://nd280.lancs.ac.uk/highland/3.19/highlandDoc_2.5/dox/index.html#HighLAND_framework`.

[107] Danaisis Vargas et al. "numuCC1pi+ interaction on Carbon (FGD1) with 4pi acceptance". T2K Technical Note 390. 2019.

[108] T. Doyle et al. "Evaluation of the ND280 ECal Systematic Uncertainties for Production 7". T2K Technical Note 487. 2022.

[109] E. Larkin et al. "TREx: A new TPC reconstruction code". T2K Technical Note 236. 2016.

[110] A. Finch, D. R. Hadley, and T. Wachala. "ND280 Reconstruction for Production 7". T2K Technical Note 329. 2022.

[111] M. Lamers James. "Development of a boosted decision tree antineutrino photon near detector sample for T2K, and design of th Hyper-Kamiokande outer detector and DAQ". PhD thesis. Lancaster University, 2024.

[112] G. Barker et al. "Implementation of the Second Generation PID for the ND280 Tracker ECals". T2K Technical Note 111. 2012.

[113] Y. Xu. "ν_μ CC selection with improved acceptance for the near detector fits". T2K Technical Note 453. 2022.

[114] S. J. Jenkins, H. M. O'Keeffe, and R. P. Litchfield. "Assessment of the Systematic Uncertainty on ND280 Timeslips". T2K Technical Note 400. 2021.

[115] P. Bartet et al. "ν_μ CC event selections in the ND280 tracker using Run 2+3+4 data". T2K Technical Note 245. 2017.

[116] Rene Brun and Fons Rademakers. "ROOT — An object oriented data analysis framework". In: *Nuclear Instruments and Methods in Physics Research Section A: Accelerators, Spectrometers, Detectors and Associated Equipment* 389.1 (1997). New Computing Techniques in Physics Research V, pp. 81–86. ISSN: 0168-9002. DOI: `https://doi.org/10.1016/S0168-9002(97)00048-X`. URL: `https://www.sciencedirect.com/science/article/pii/S016890029700048X`.

[117] D. Brailsford et al. "Study of the tracker ECal systematic uncertainties". T2K Technical Note 279. 2017.

[118] GUNDAM GitHub Repository. URL: `https://github.com/gundam-organization/gundam`.

[119] MaCh3 GitHub Repository. URL: `https://github.com/t2k-software/MaCh3/`.

[120] C. Bojechko and A. Kaboth. "Muon neutrino disappearance simultaneous fit of ND280 and SK with Run 1+2+3 data using Markov Chain Monte Carlo analysis". T2K Technical Note 140. 2013.

[121] P. de Perio1 et al. "Constraining the Flux and Cross Section Models with Data from the ND280 Detector for the 2012a Oscillation Analysis". T2K Technical Note 106. 2012.

[122] A. Blanchet et al. "GUNDAM: Generic fitter for Upgraded Near Detector Analysis Methods". T2K Technical Note 458. 2023.

[123] Super-xsllhFitter GitHub Repository. URL: `https://gitlab.com/cuddandr/xsLLhFitter`.

[124] R. Barlow and C. Beeston. "Fitting using finite Monte Carlo samples". In: *Computer Physics Communications* 77.2 (1993), pp. 219–228. ISSN: 0010-4655. DOI: `https://doi.org/10.1016/0010-4655(93)90005-W`. URL: `https://www.sciencedirect.com/science/article/pii/001046559390005W`.

[125] T.C. Deiminger et al. "Assessing out-of-model cross-section effects with fits to simulated data". T2K Technical Note 441. 2023.

[126] T. Dieminger and S. Dolan. "NIWGReWeight- Spectral Function to Hadron Tensor Reweighting". T2K Technical Note 434. 2021.

[127] L. Berns et al. "Fake data studies for the T2K+SK atmospheric joint analysis". T2K Technical Note 457. 2023.

[128] A. V. Butkevich and D. Perevalov. "Determination of the axial nucleon form factor from the MiniBooNE data". In: *Physical Review D* 89.5 (Mar. 2014). ISSN: 1550-2368. DOI: `10.1103/physrevd.89.053014`. URL: `http://dx.doi.org/10.1103/PhysRevD.89.053014`.

[129] B. Bhattacharya, R. J. Hill, and G. Paz. "Model-independent determination of the axial mass parameter in quasielastic neutrino-nucleon scattering". In: *Physical Review D* 84.7 (Oct. 2011). ISSN: 1550-2368. DOI: `10.1103/physrevd.84.073006`. URL: `http://dx.doi.org/10.1103/PhysRevD.84.073006`.

[130] A. S. Meyer. *Neutrino Oscillation and Lattice QCD*. 2023. arXiv: `2301.04616 [hep-lat]`. URL: `https://arxiv.org/abs/2301.04616`.

[131] L. Munteanu. “SPP Adversarial Fake Data”. Internal NIWG Meeting Slides. 2022. URL: `https://t2k.org/asg/xsec/meetings/2022/110222/spp_adversarial_fakeData/view`.

[132] Nicholas A. Latham et al. “Measurement of the Electron Neutrino Charged Current Pion Production Cross Section in FGD1 of the ND280 Tracker”. T2K Technical Note 450. 2021.

[133] M. Martini et al. “Unified approach for nucleon knock-out and coherent and incoherent pion production in neutrino interactions with nuclei”. In: *Phys. Rev. C* 80 (6 2009), p. 065501. DOI: `10.1103/PhysRevC.80.065501`. URL: `https://link.aps.org/doi/10.1103/PhysRevC.80.065501`.

[134] P. Stowell et al. “Tuning the genie pion production model with MINERνA data”. In: *Phys. Rev. D* 100 (7 2019), p. 072005. DOI: `10.1103/PhysRevD.100.072005`. URL: `https://link.aps.org/doi/10.1103/PhysRevD.100.072005`.

[135] B. Bourguille, J. Nieves, and F. Sánchez. “Inclusive and exclusive neutrino-nucleus cross sections and the reconstruction of the interaction kinematics”. In: *Journal of High Energy Physics* 2021.4 (Apr. 2021). ISSN: 1029-8479. DOI: `10.1007/jhep04(2021)004`. URL: `http://dx.doi.org/10.1007/JHEP04(2021)004`.

[136] K. S. Kuzmin and V. A. Naumov. “Mean charged multiplicities in charged-current neutrino scattering on hydrogen and deuterium”. In: *Phys. Rev. C* 88 (6 Dec. 2013), p. 065501. DOI: `10.1103/PhysRevC.88.065501`. URL: `https://link.aps.org/doi/10.1103/PhysRevC.88.065501`.

[137] Ewan Miller. “Constraining the Flux and Cross Section Uncertainties for the T2K Experiment Using ND280 Data”. PhD thesis. King’s College London, 2024.

[138] T2K and Beyond. 2021. URL: `https://t2k-experiment.org/beyond-t2k/`.

Appendix A

NIWGReWeight Fake Parameters

This appendix lists the parameter values set for each fake data set. These are applied to the nominal MC flattree files via `NIWGReWeight`.

SF To LFG:
`SF_toLFGTwkDial = 1`

$M_A^{QE} = 1.21$ GeV^2, `EB_bin_C_nu` = 0, `EB_bin_C_nu` = 0 is applied during the GUNDAM fit

Non-QE:
```
nonQETwk_LowQ2recWeight_1 = 0.881677
nonQETwk_LowQ2recWeight_2 = 0.998662
nonQETwk_LowQ2recWeight_3 = 1.3174
nonQETwk_LowQ2recWeight_4 = 1.48727
nonQETwk_LowQ2recWeight_5 = 1.57654
nonQETwk_HighQ2recWeight_1 = 1.80654
nonQETwk_HighQ2recWeight_2 = 1.74901
nonQETwk_HighQ2recWeight_3 = 1.4276
nonQETwk_anu_LowQ2recWeight_1 = 0.658032
nonQETwk_anu_LowQ2recWeight_2 = 0.742947
nonQETwk_anu_LowQ2recWeight_3 = 1.21484
nonQETwk_anu_LowQ2recWeight_4 = 1.21891
nonQETwk_anu_LowQ2recWeight_5 = 1.37637
nonQETwk_anu_HighQ2recWeight_1 = 1.85244
nonQETwk_anu_HighQ2recWeight_2 = 1.63018
nonQETwk_anu_HighQ2recWeight_3 = 1.49767
```

SPP Matrix Element -1σ:
`ROM3M3 = -3`σ
`ROM1M1 = 3`σ
`ROM1M3 = -3`σ
`MDLSPiERj = 1`

SPP Matrix Element $+1\sigma$:
`ROM3M3 = 3`σ
`ROM1M1 = -3`σ
`ROM1M3 = -3`σ
`MDLSPiERj = 1`

SF to CRPA:
`SF_toCRPASuSAv2HybridTwkDial = 1`

$M_A^{QE} = 1.21$ GeV^2, `EB_bin_C_nu` $= 0$, `EB_bin_C_nu` $= 0$ is applied during the GUNDAM fit

Z-Expansion -1σ:
`AxlFFCCQE = 5`
`FAZExp_A1 = 2.28`
`FAZExp_A2 = 0.5403666485`
`FAZExp_A3 = -3.601593719`
`FAZExp_A4 = 2.350915679`

$M_A^{QE} = 1.21$ GeV^2 is applied during the GUNDAM fit

Z-Expansion Nominal:
`AxlFFCCQE = 5`
`FAZExp_A1 = 2.28`
`FAZExp_A2 = 0.26`
`FAZExp_A3 = -5.2`
`FAZExp_A4 = 2.6`

$M_A^{QE} = 1.21$ GeV^2 is applied during the GUNDAM fit

Z-Expansion $+1\sigma$:
`AxlFFCCQE = 5`
`FAZExp_A1 = 2.231420552`
`FAZExp_A2 = -0.514799999`
`FAZExp_A3 = -9.829468312`
`FAZExp_A4 = 5.506347821`

$M_A^{QE} = 1.21$ GeV^2 is applied during the GUNDAM fit

LQCD Z-Expansion Nominal:
`AxlFFCCQE = 5`
`FAZExp_A1 = 2.28`
`FAZExp_A2 = 0.26`
`FAZExp_A3 = -5.2`
`FAZExp_A4 = 2.6`

$M_A^{QE} = 1.21$ GeV^2 is applied during the GUNDAM fit

LQCD Z-Expansion -1σ:
`AxlFFCCQE = 5`
`FAZExp_A1 = 2.069086266`
`FAZExp_A2 = -0.8883496854`
`FAZExp_A3 = -6.024137229`
`FAZExp_A4 = 2.332464989`

$M_A^{QE} = 1.21$ GeV^2 is applied during the GUNDAM fit

SF to SuSAv2:
`SF_toSuSAv2TwkDial = 1`

$M_A^{QE} = 1.21$ GeV^2, `EB_bin_C_nu` $= 0$, `EB_bin_C_nu` $= 0$ is applied during the GUNDAM fit

2p2h Eb Correction:
`MECTwkDial_Eb_C12_nu = 1`
`MECTwkDial_Eb_O16_nu = 1`
`MECTwkDial_Eb_C12_nubar = 1`
`MECTwkDial_Eb_O16_nubar = 1`
`FAZExp_A4 = 2.332464989`

SPP Adversarial:
`SPPTwk_SPPAdversarial2022 = 1`

RS to Martini:
`RS_toMartiniTwkDial = 1`

MultiPi Multiplicity:
`MultiPi_Multiplicity_FDS = 1`

Low Q^2 SPP:
`SPPTwk_LowQ2Suppression = 1`
`SPPTwk_LowQ2SuppressionForm = 0`

3-Component -1σ:

```
AxlFFCCQE = 4
FAxlCCQEAlpha = 0.1584532369
FAxlCCQEBeta = 1.092163679
FAxlCCQEGamma = 0.4165094425
FAxlCCQETheta = -0.6049211041
```

$M_A^{QE} = 1.21$ GeV^2 is applied during the GUNDAM fit

3-Component Nominal:

```
AxlFFCCQE = 4
FAxlCCQEAlpha = 0.23
FAxlCCQEBeta = 1.22
FAxlCCQEGamma = 0.44
FAxlCCQETheta = -0.26
```

$M_A^{QE} = 1.21$ GeV^2 is applied during the GUNDAM fit

3-Component $+1\sigma$:

```
AxlFFCCQE = 4
FAxlCCQEAlpha = 0.1351120969
FAxlCCQEBeta = 1.229616897
FAxlCCQEGamma = 0.409450104
FAxlCCQETheta = -0.133810261
```

$M_A^{QE} = 1.21$ GeV^2 is applied during the GUNDAM fit

Appendix B

GUNDAM Fit Comparisons Across All Fake Data Studies

Prefit:

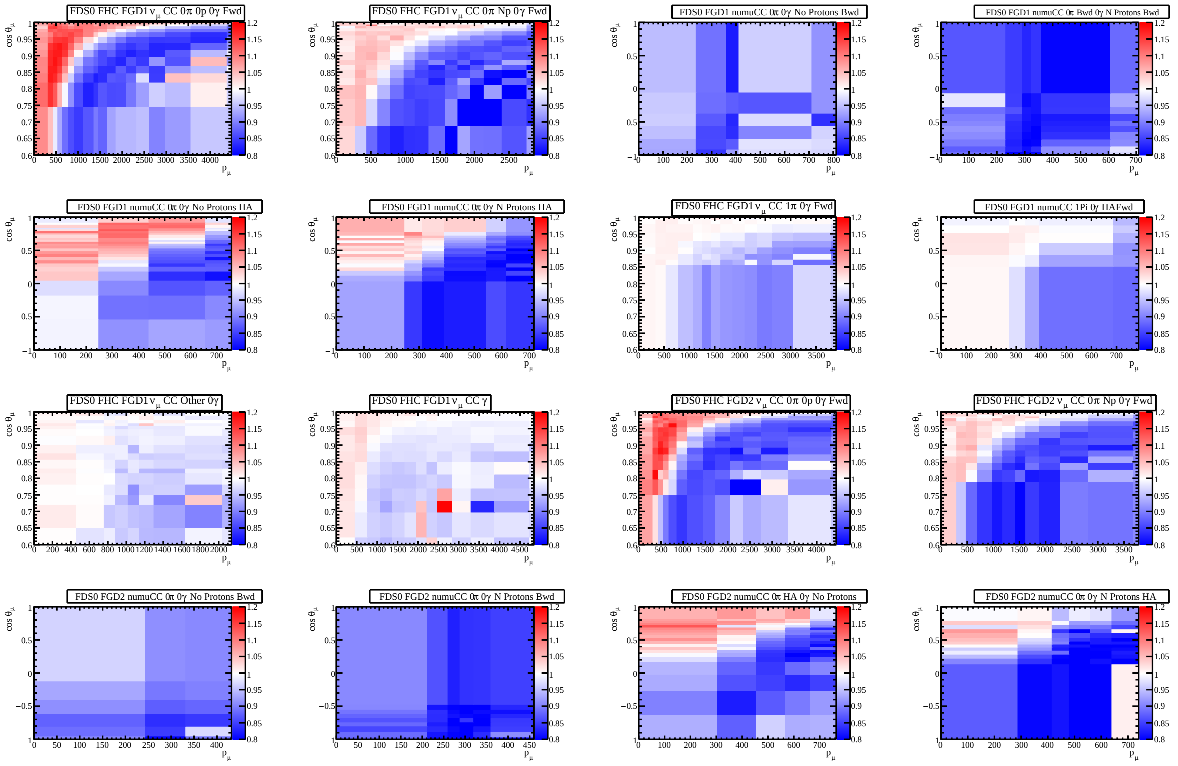

Postfit:

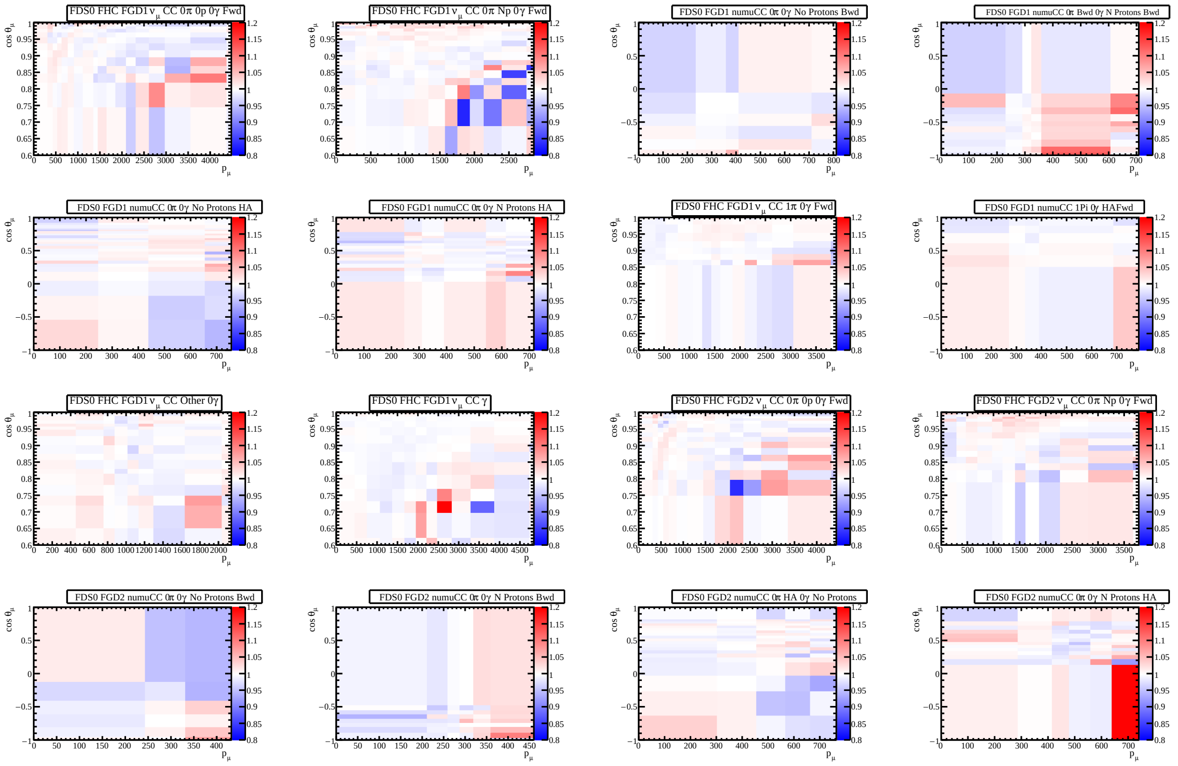

Figure B.1: Prefit (top 16) and postfit (lower 16) results for the SF to LFG fake data set, showing the ratio of the angular and momentum distributions between the fitted MC and the nominal fake data across 4π selection samples.

Prefit:

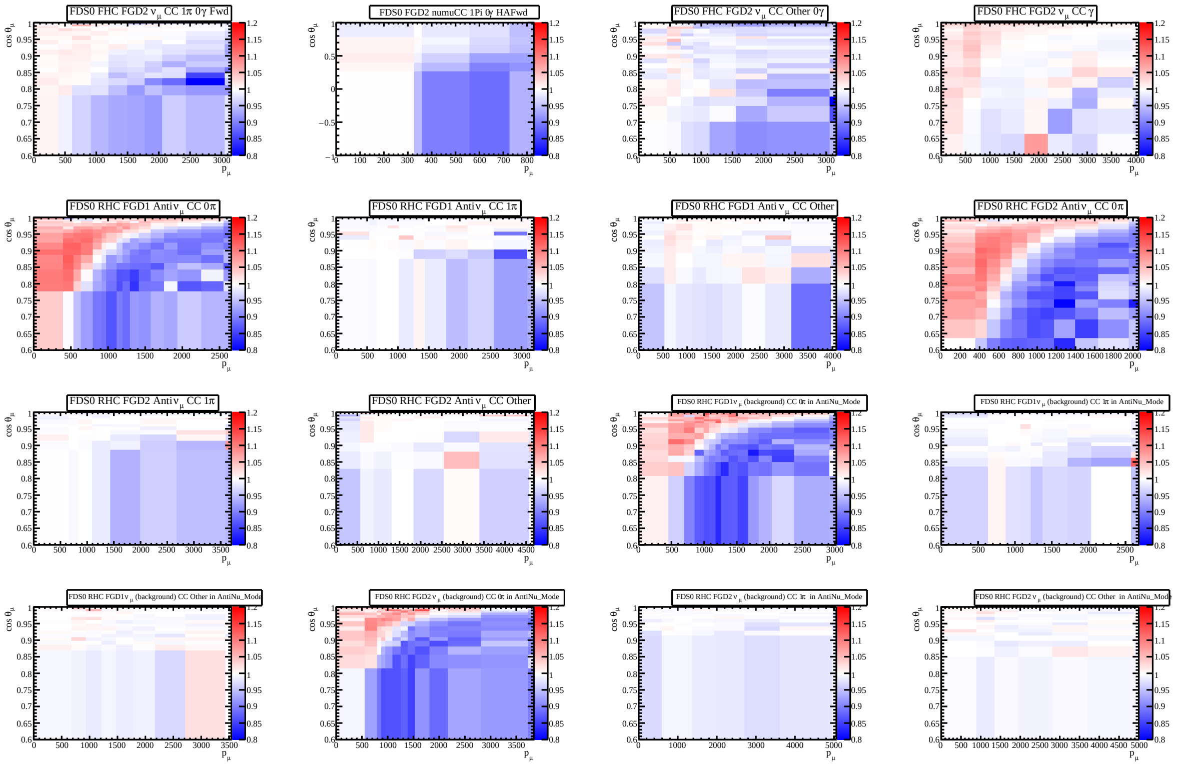

Postfit:

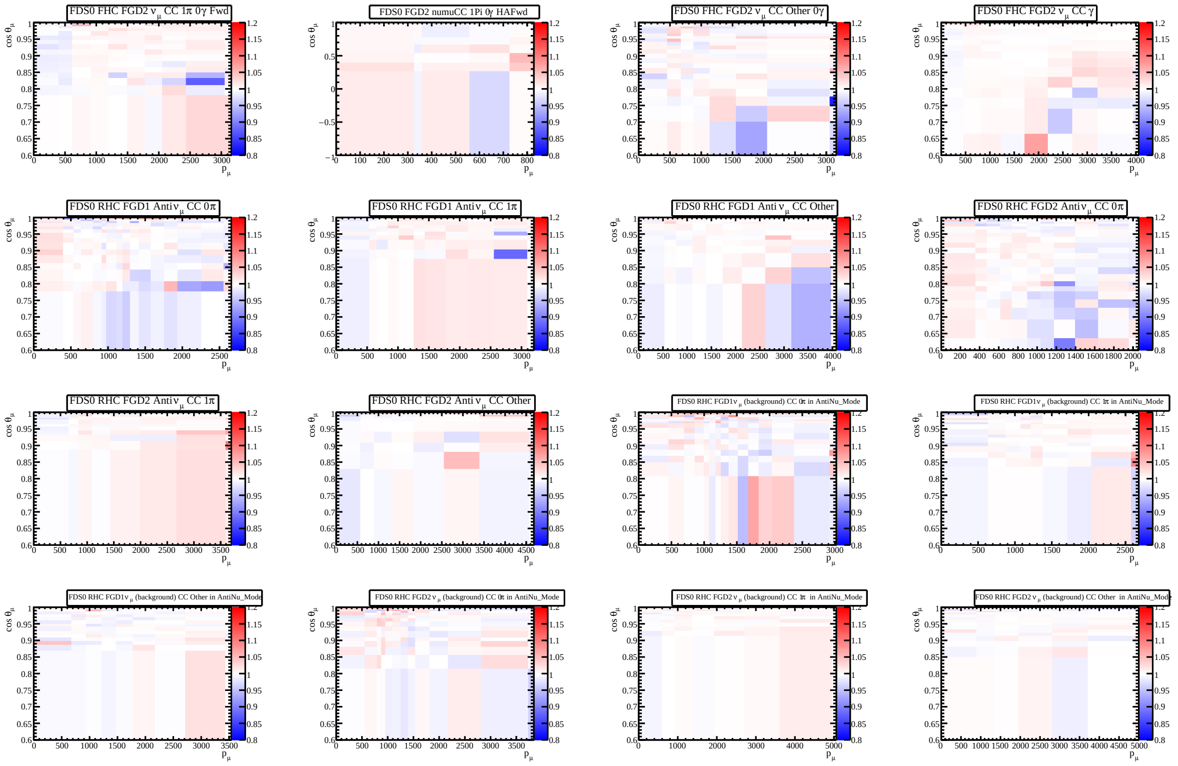

Figure B.2: Prefit (top 16) and postfit (lower 16) results for the SF to LFG fake data set, showing the ratio of the angular and momentum distributions between the fitted MC and the nominal fake data across 4π selection samples.

Prefit:

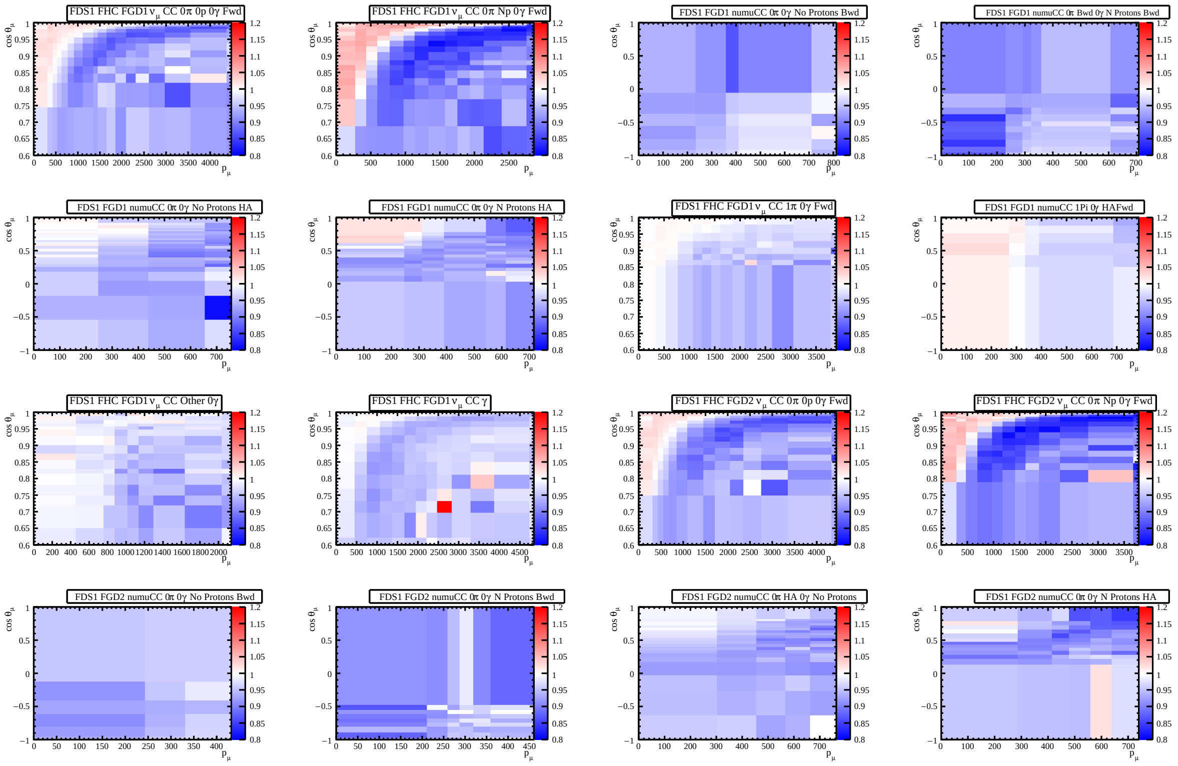

Postfit:

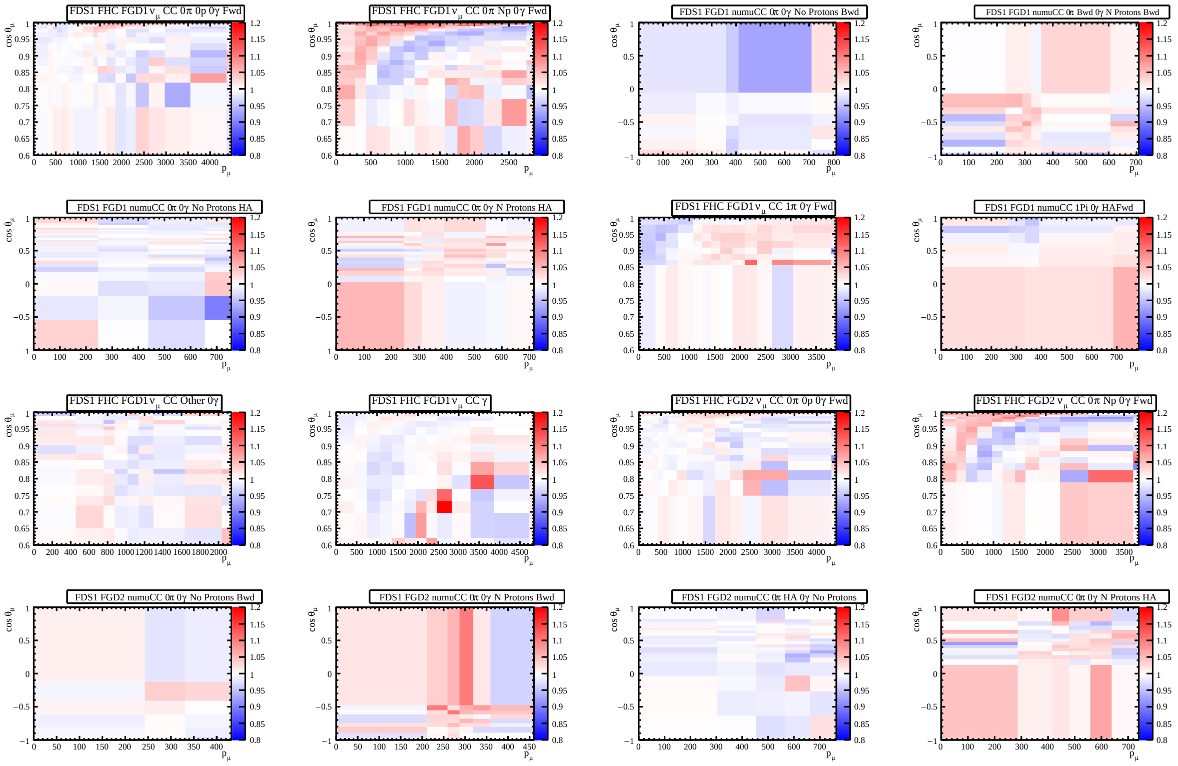

Figure B.3: Prefit (top 16) and postfit (lower 16) results for the Low Q^2 SPP fake data set, showing the ratio of the angular and momentum distributions between the fitted MC and the nominal fake data across 4π selection samples.

Prefit:

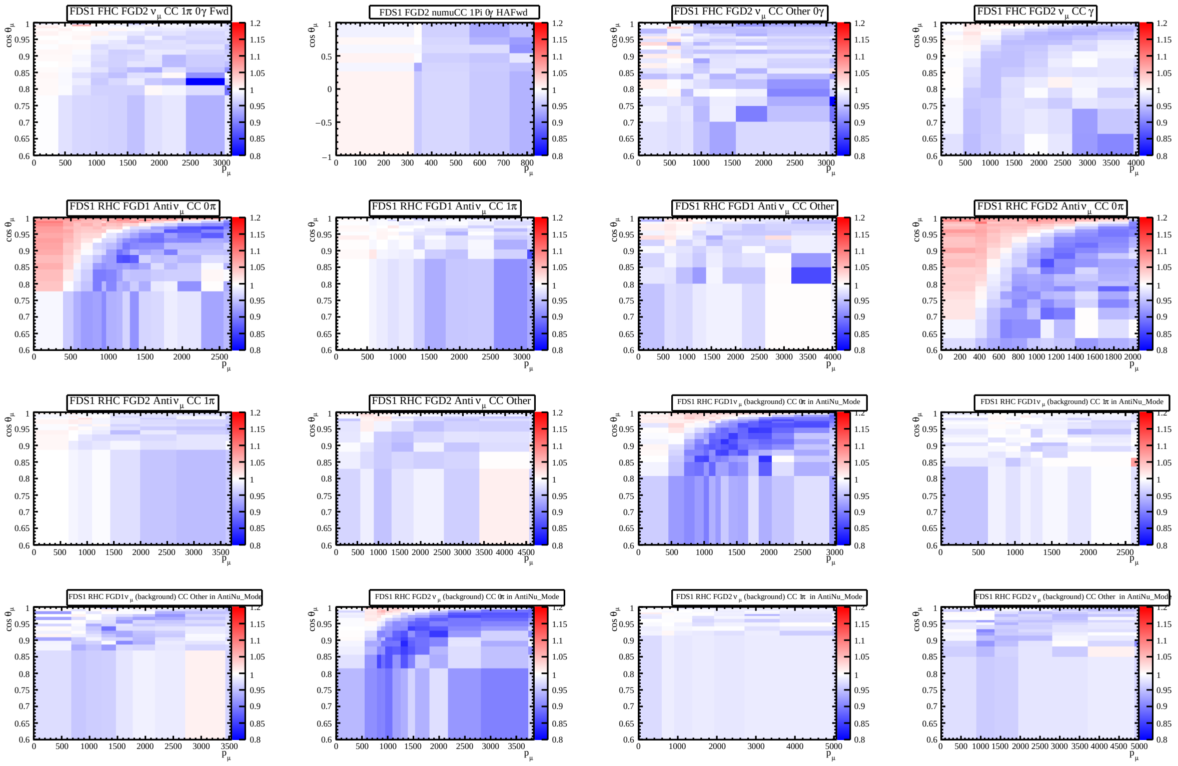

Postfit:

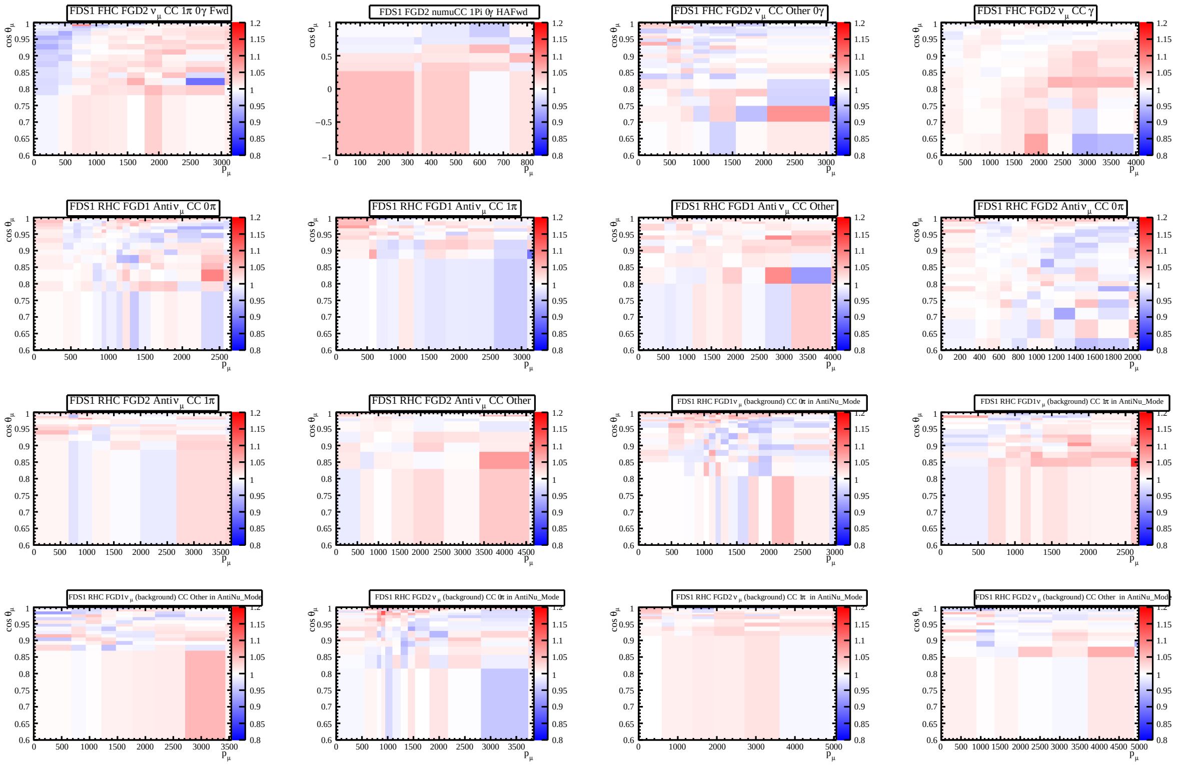

Figure B.4: Prefit (top 16) and postfit (lower 16) results for the Low Q^2 SPP fake data set, showing the ratio of the angular and momentum distributions between the fitted MC and the nominal fake data across 4π selection samples.

Prefit:

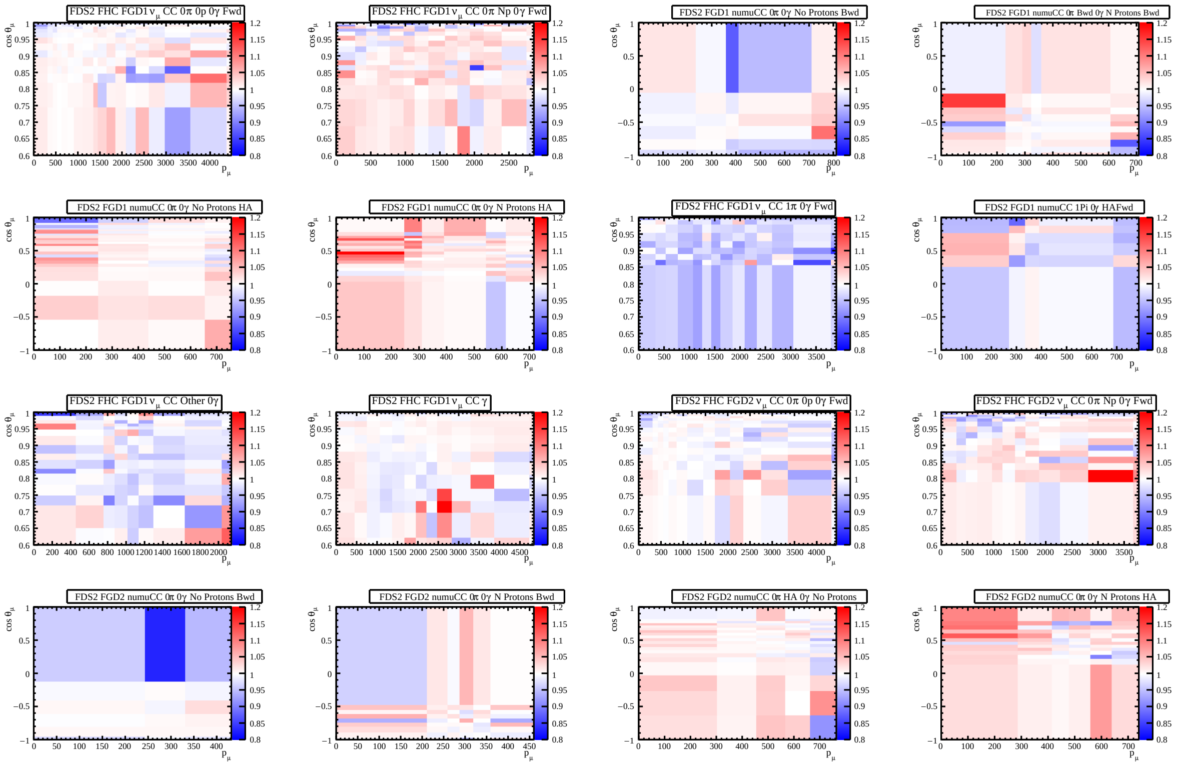

Postfit:

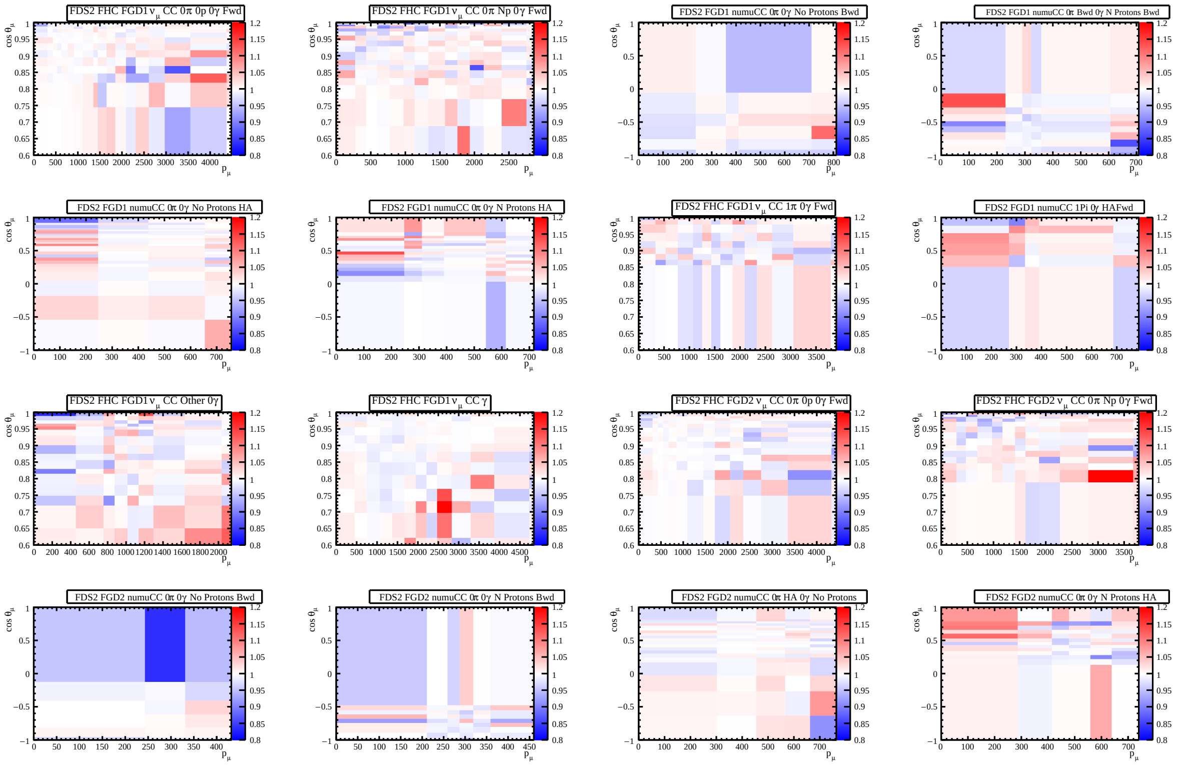

Figure B.5: Prefit (top 16) and postfit (lower 16) results for the SPP MatrixEl M1sig fake data set, showing the ratio of the angular and momentum distributions between the fitted MC and the nominal fake data across 4π selection samples.

Prefit:

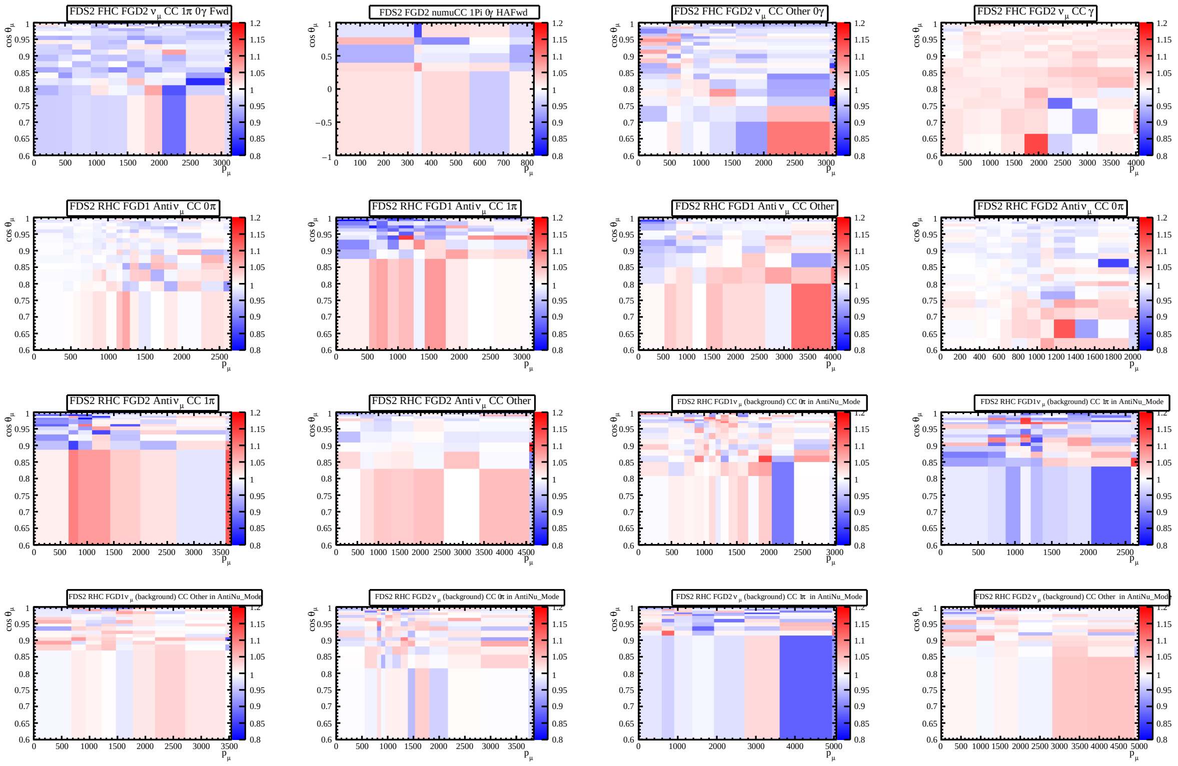

Postfit:

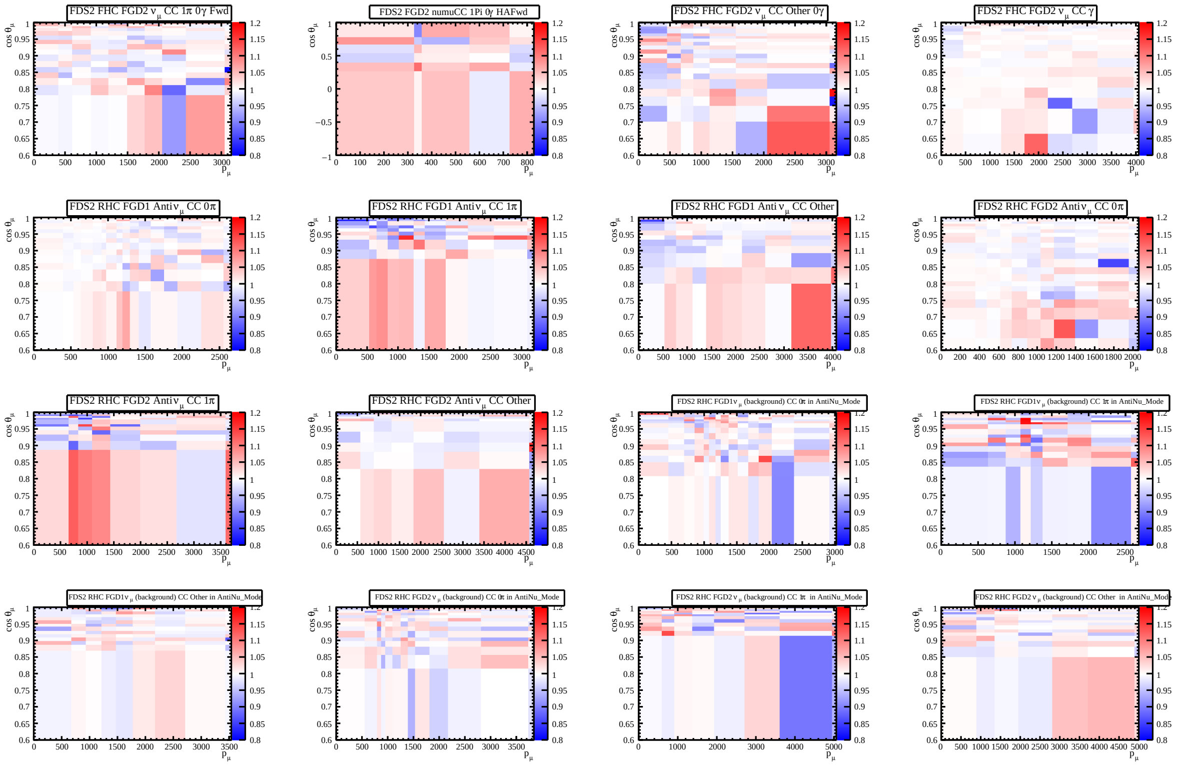

Figure B.6: Prefit (top 16) and postfit (lower 16) results for the SPP MatrixEl M1sig fake data set, showing the ratio of the angular and momentum distributions between the fitted MC and the nominal fake data across 4π selection samples.

Prefit:

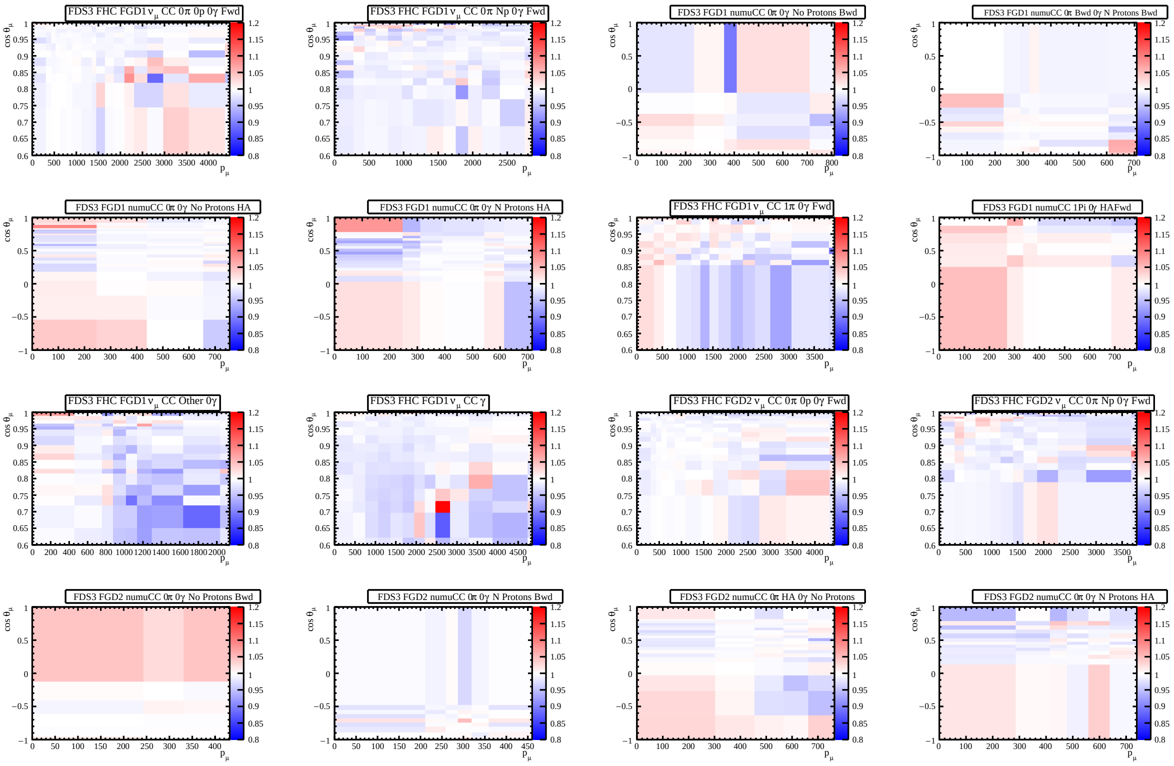

Postfit:

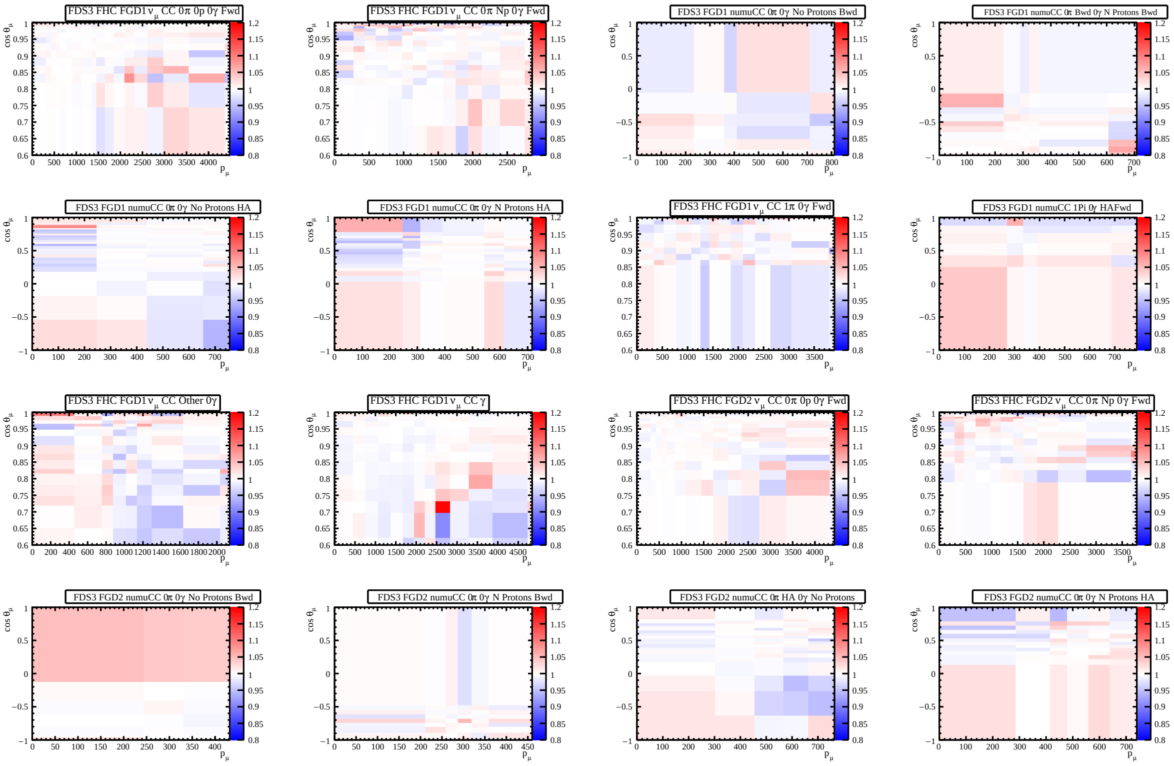

Figure B.7: Prefit (top 16) and postfit (lower 16) results for the SPP MatrixEl P1sig fake data set, showing the ratio of the angular and momentum distributions between the fitted MC and the nominal fake data across 4π selection samples.

Prefit:

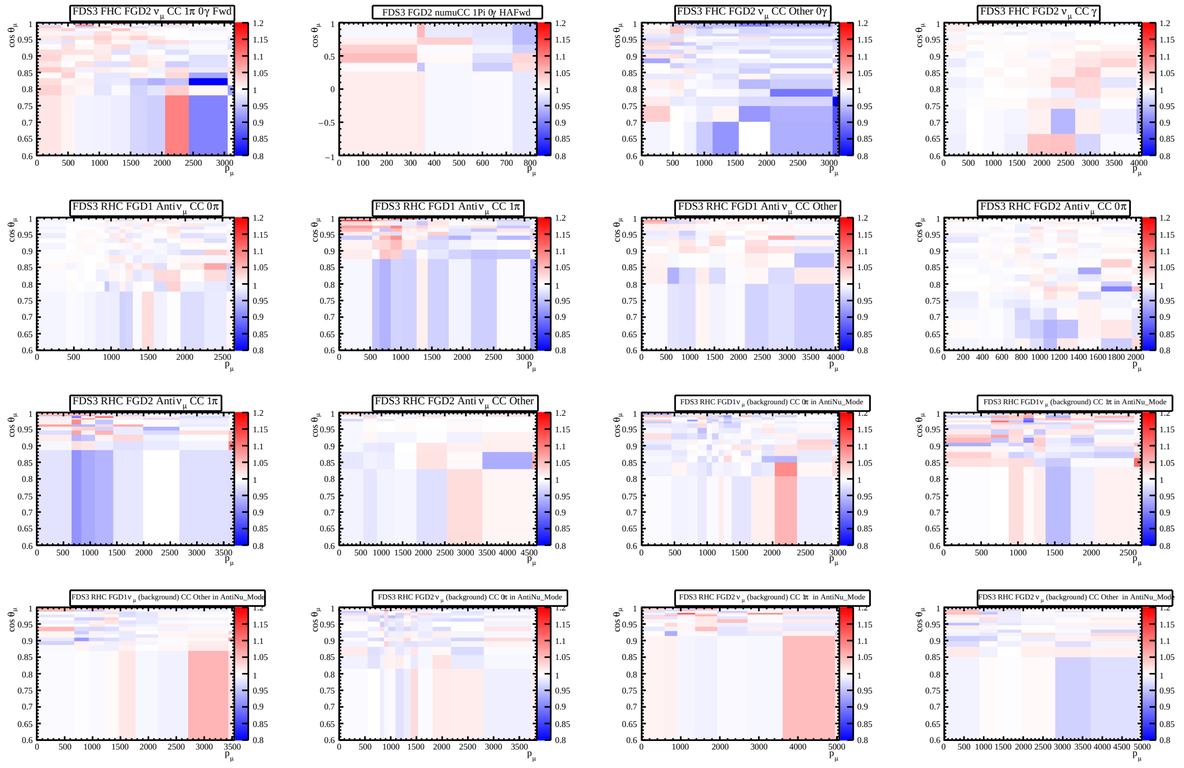

Postfit:

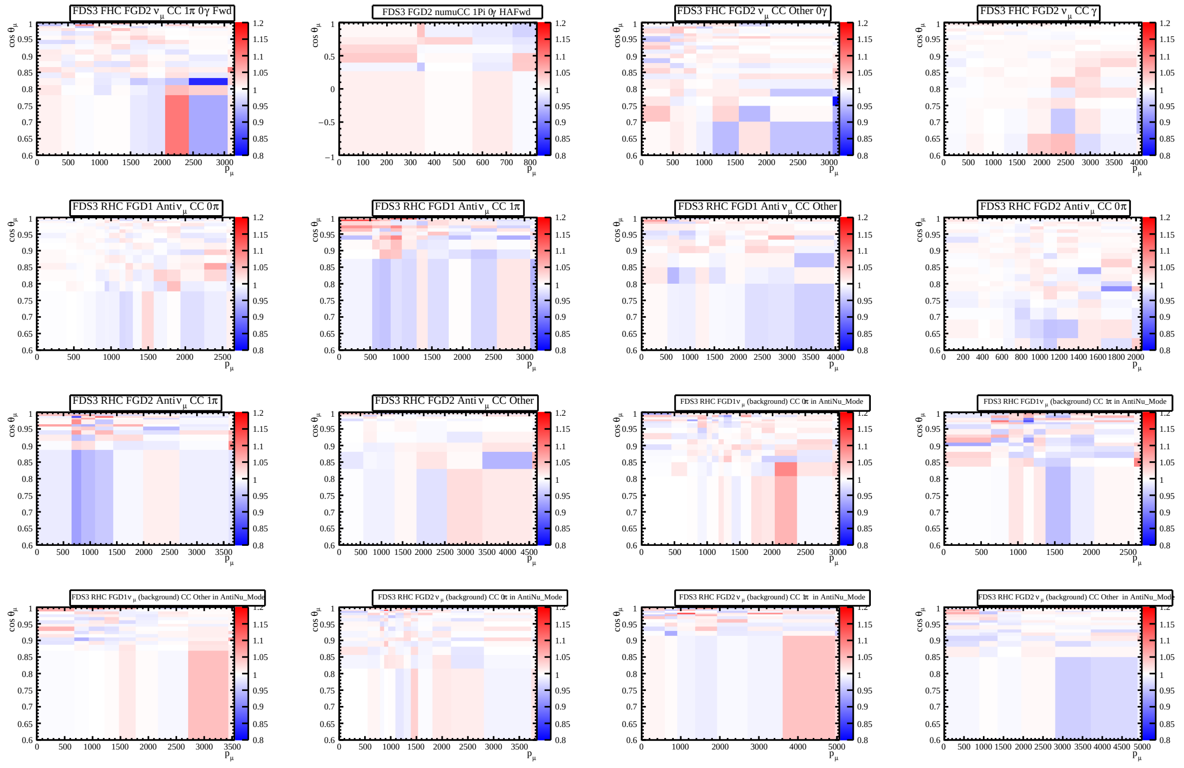

Figure B.8: Prefit (top 16) and postfit (lower 16) results for the SPP MatrixEl P1sig fake data set, showing the ratio of the angular and momentum distributions between the fitted MC and the nominal fake data across 4π selection samples.

Prefit:

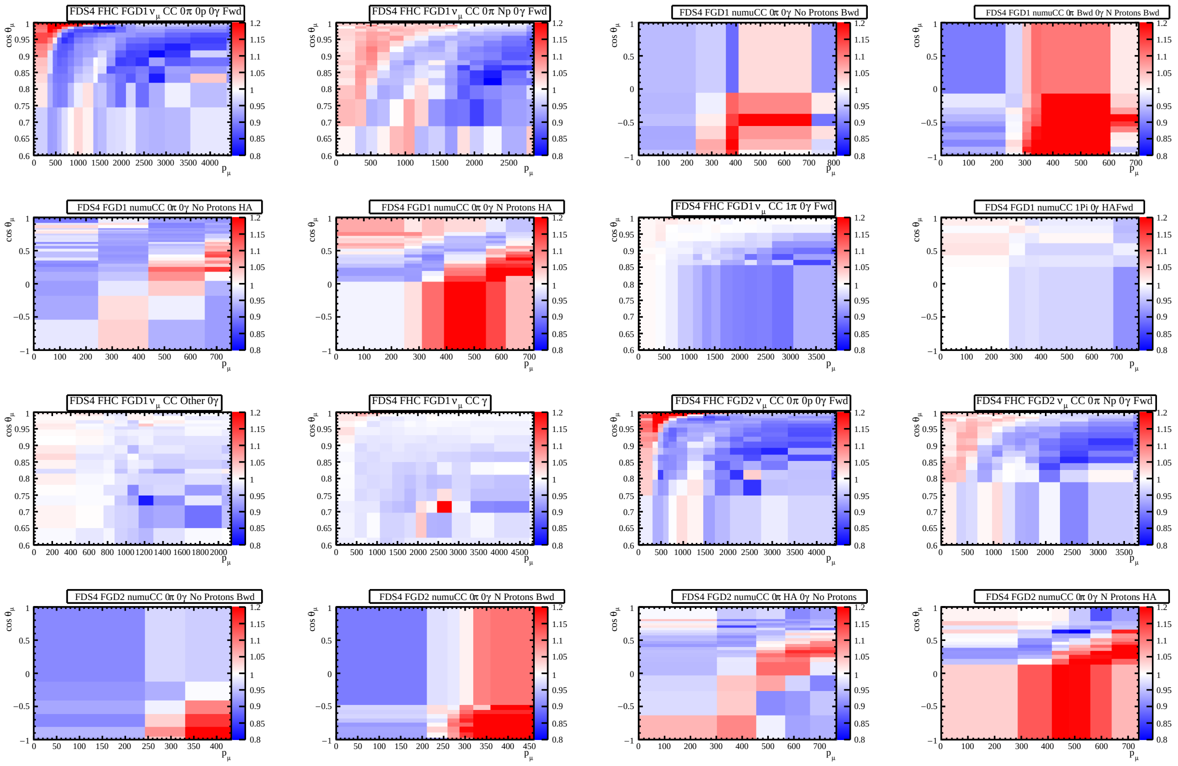

Postfit:

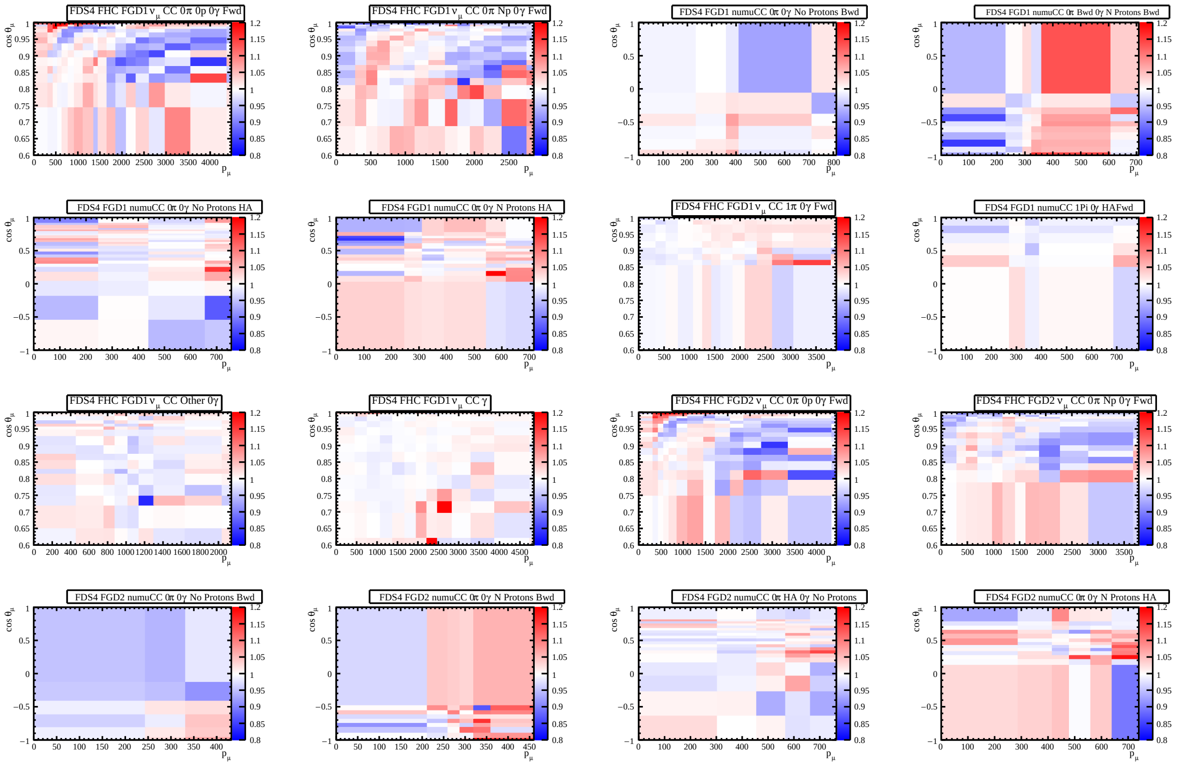

Figure B.9: Prefit (top 16) and postfit (lower 16) results for the SF to CRPA fake data set, showing the ratio of the angular and momentum distributions between the fitted MC and the nominal fake data across 4π selection samples.

Prefit:

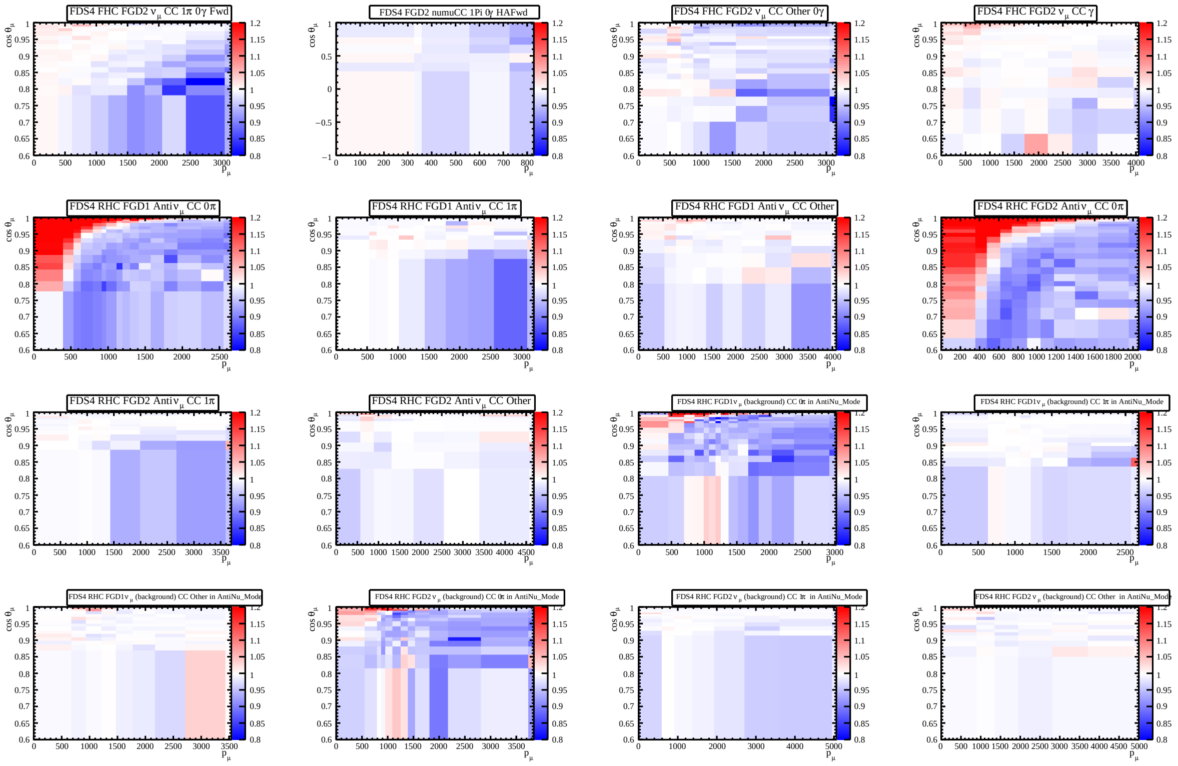

Postfit:

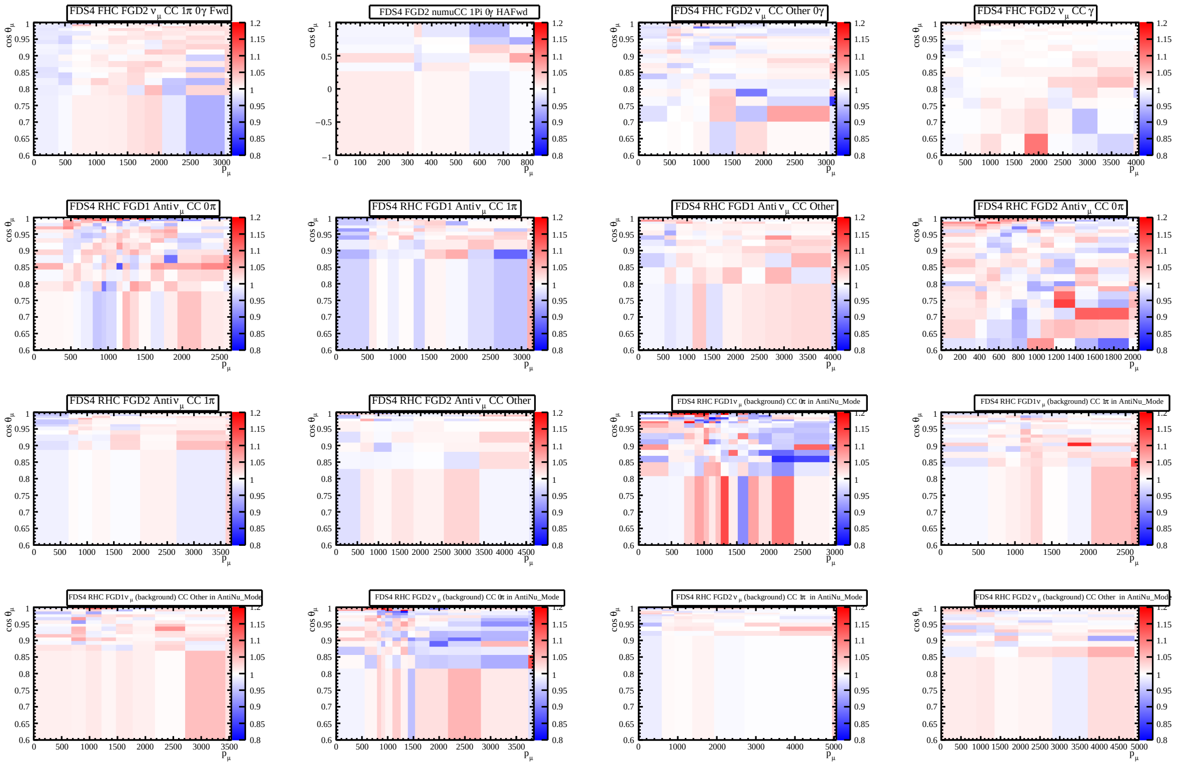

Figure B.10: Prefit (top 16) and postfit (lower 16) results for the SF to CRPA fake data set, showing the ratio of the angular and momentum distributions between the fitted MC and the nominal fake data across 4π selection samples.

Prefit:

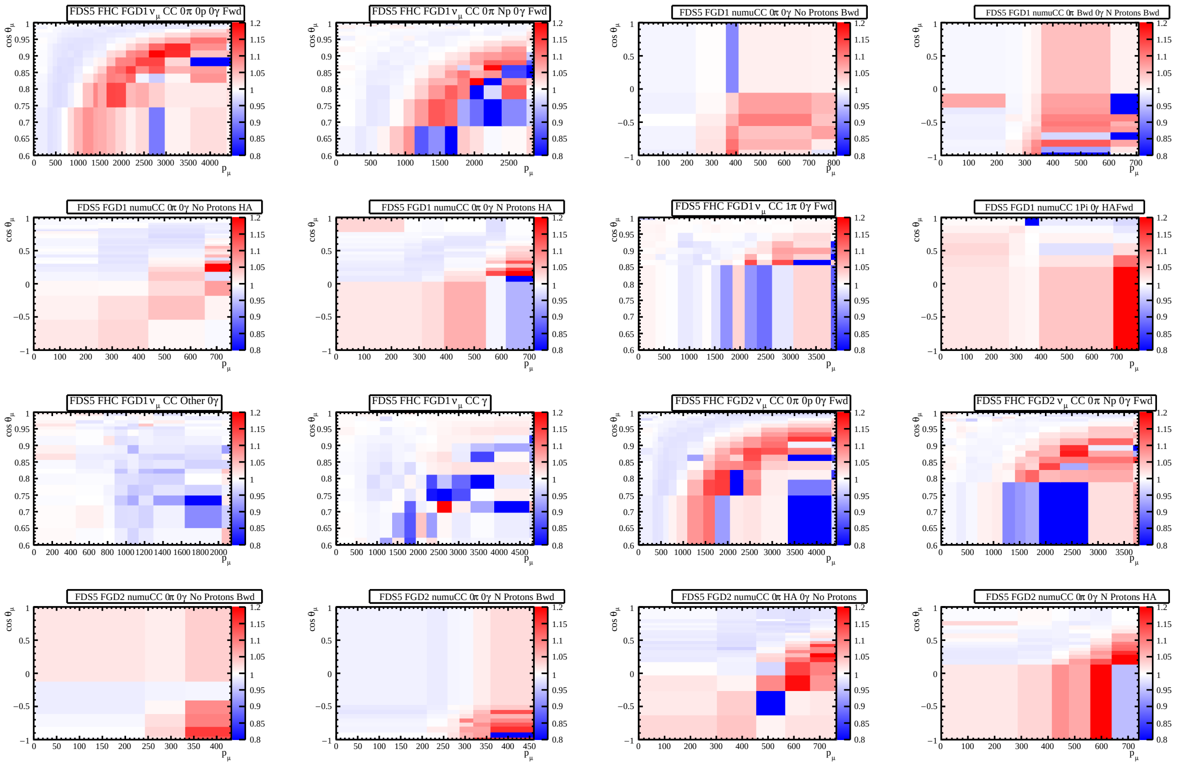

Postfit:

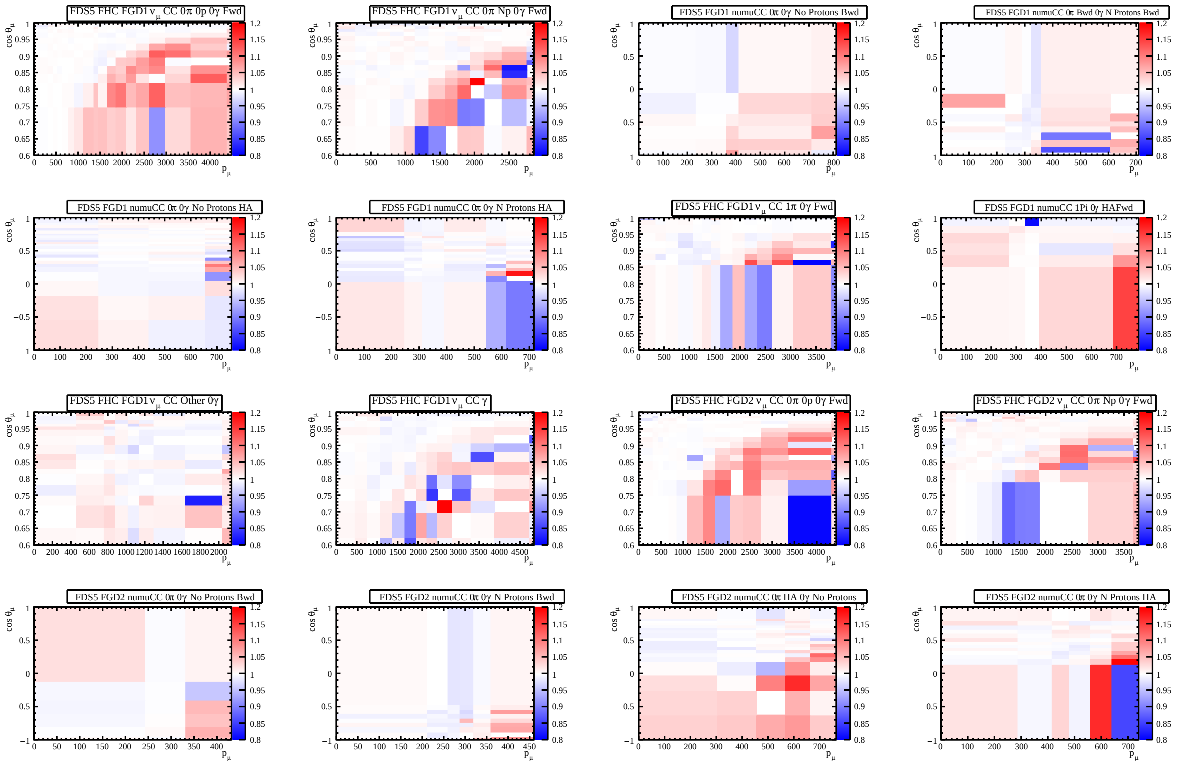

Figure B.11: Prefit (top 16) and postfit (lower 16) results for the AXFF ZExp M1sig fake data set, showing the ratio of the angular and momentum distributions between the fitted MC and the nominal fake data across 4π selection samples.

Prefit:

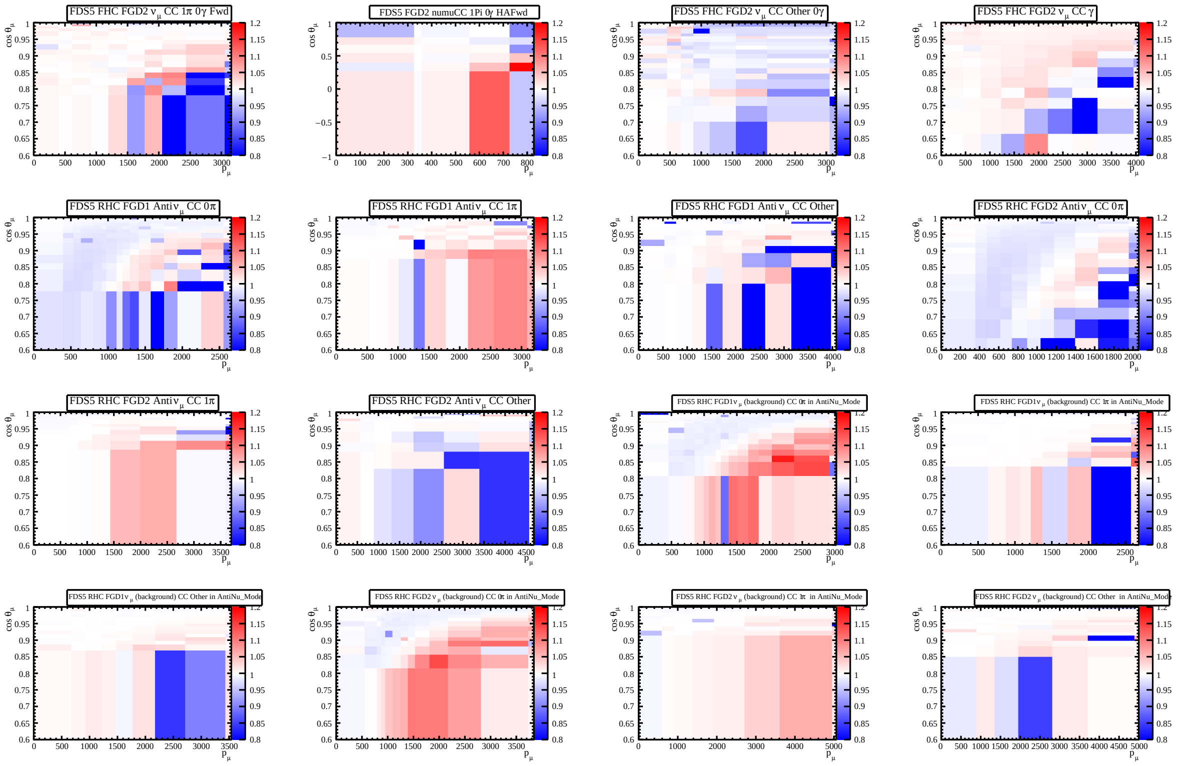

Postfit:

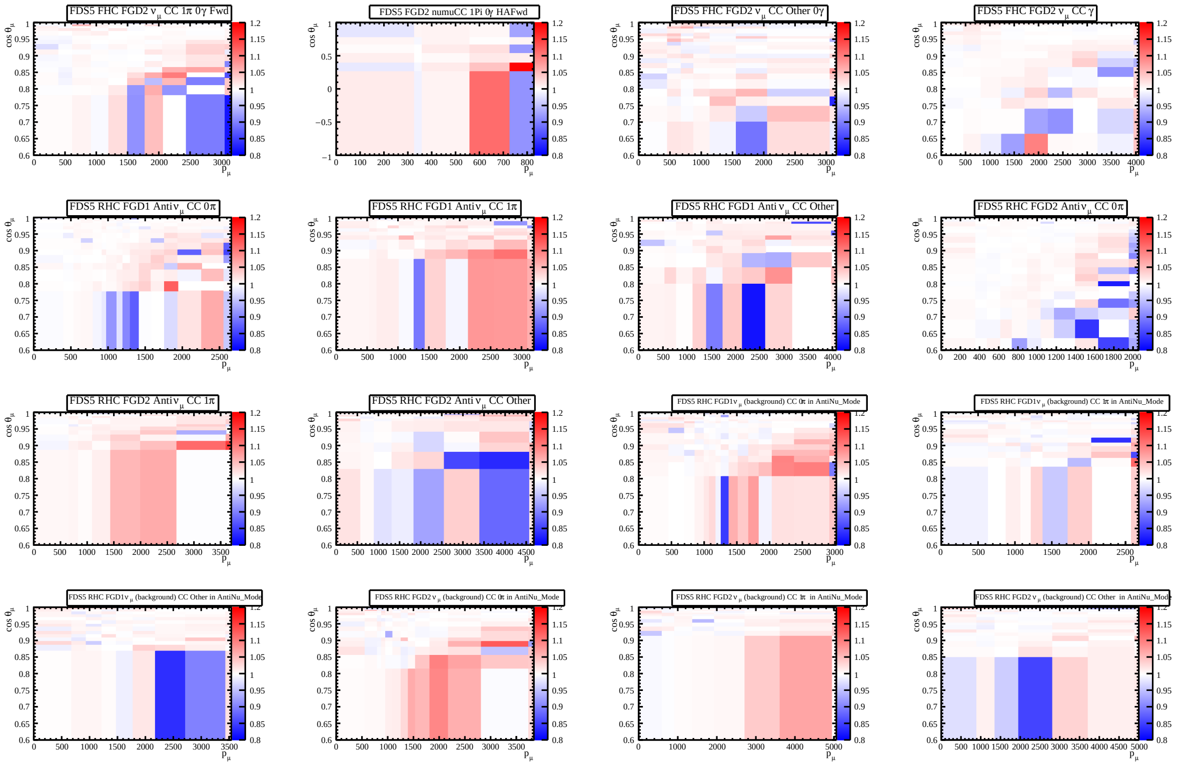

Figure B.12: Prefit (top 16) and postfit (lower 16) results for the AXFF ZExp M1sig fake data set, showing the ratio of the angular and momentum distributions between the fitted MC and the nominal fake data across 4π selection samples.

Prefit:

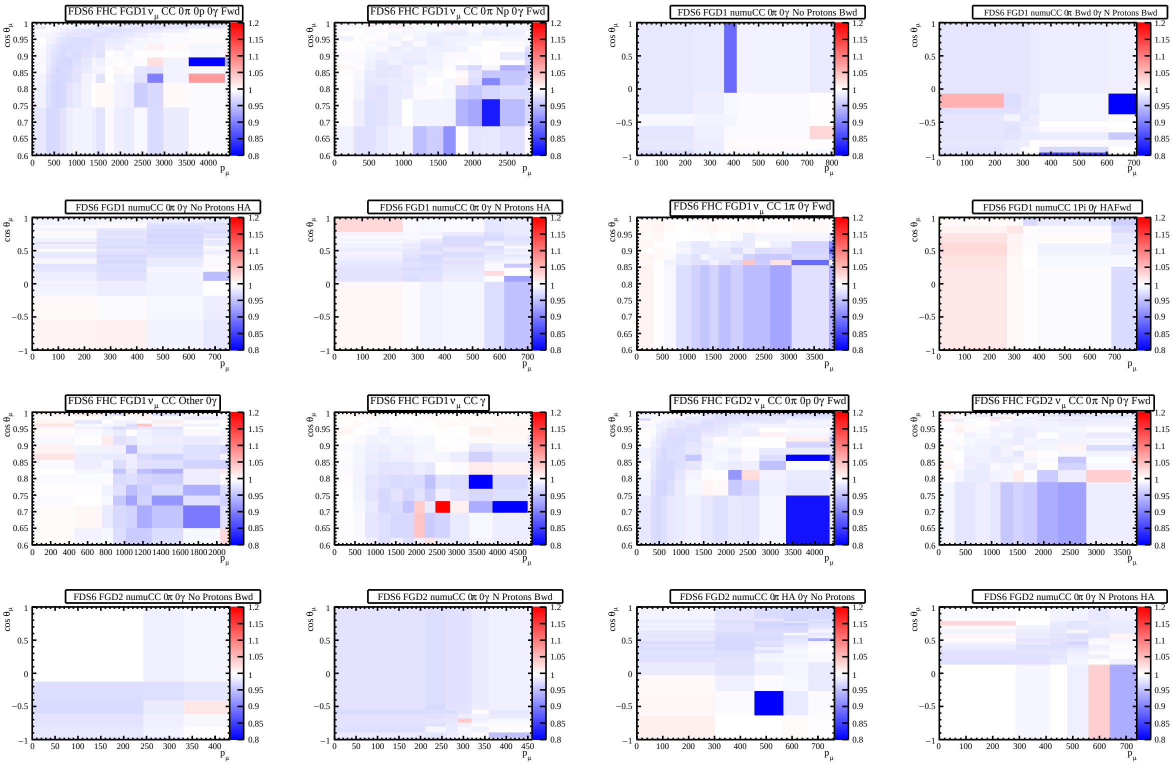

Postfit:

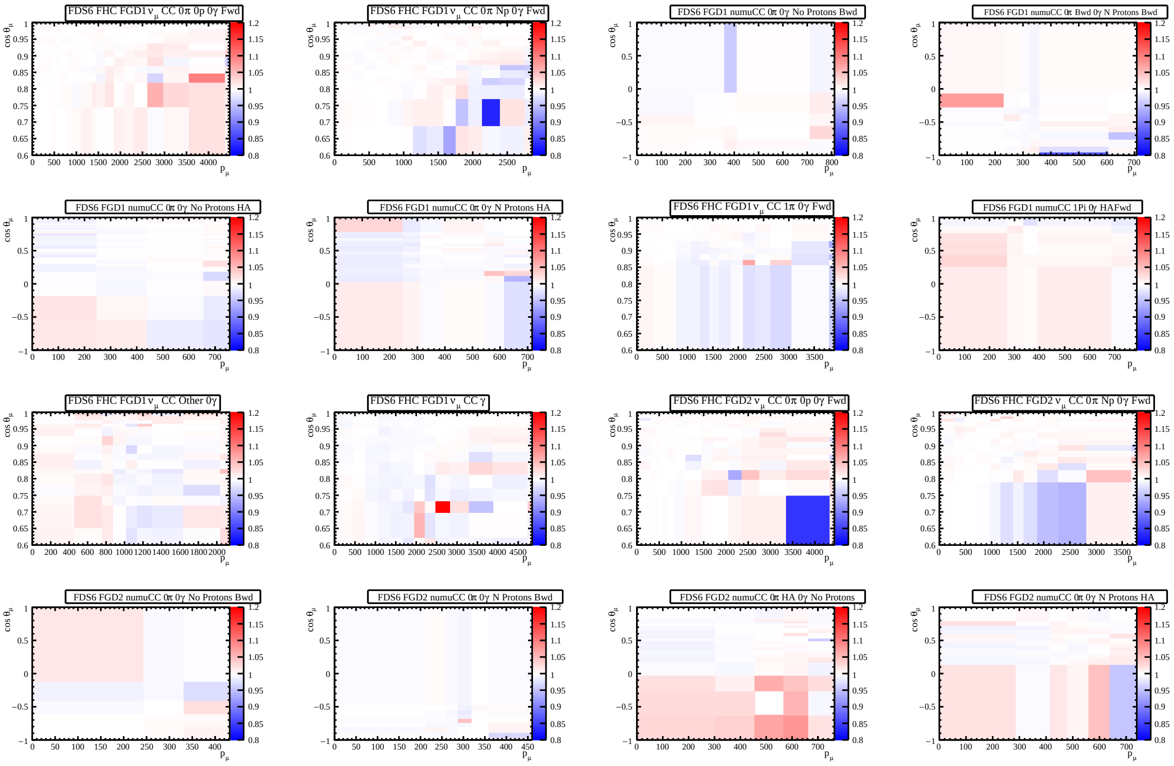

Figure B.13: Prefit (top 16) and postfit (lower 16) results for the AXFF ZExp Nom fake data set, showing the ratio of the angular and momentum distributions between the fitted MC and the nominal fake data across 4π selection samples.

Prefit:

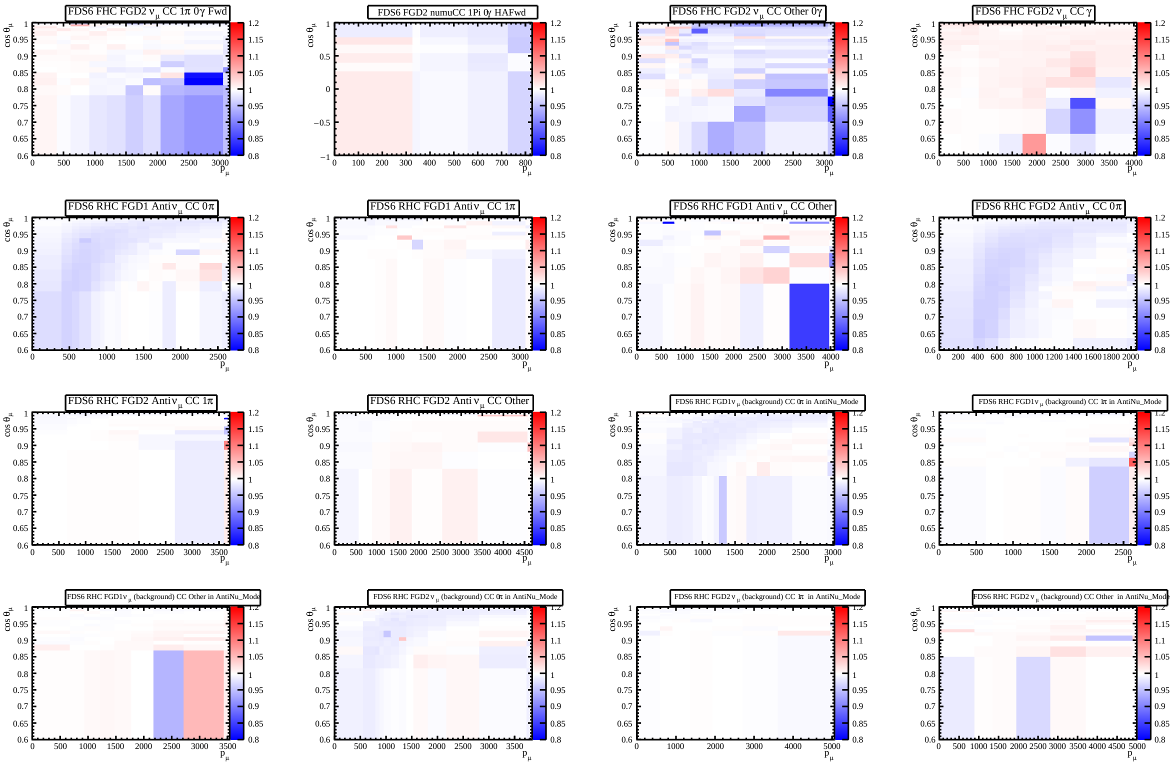

Postfit:

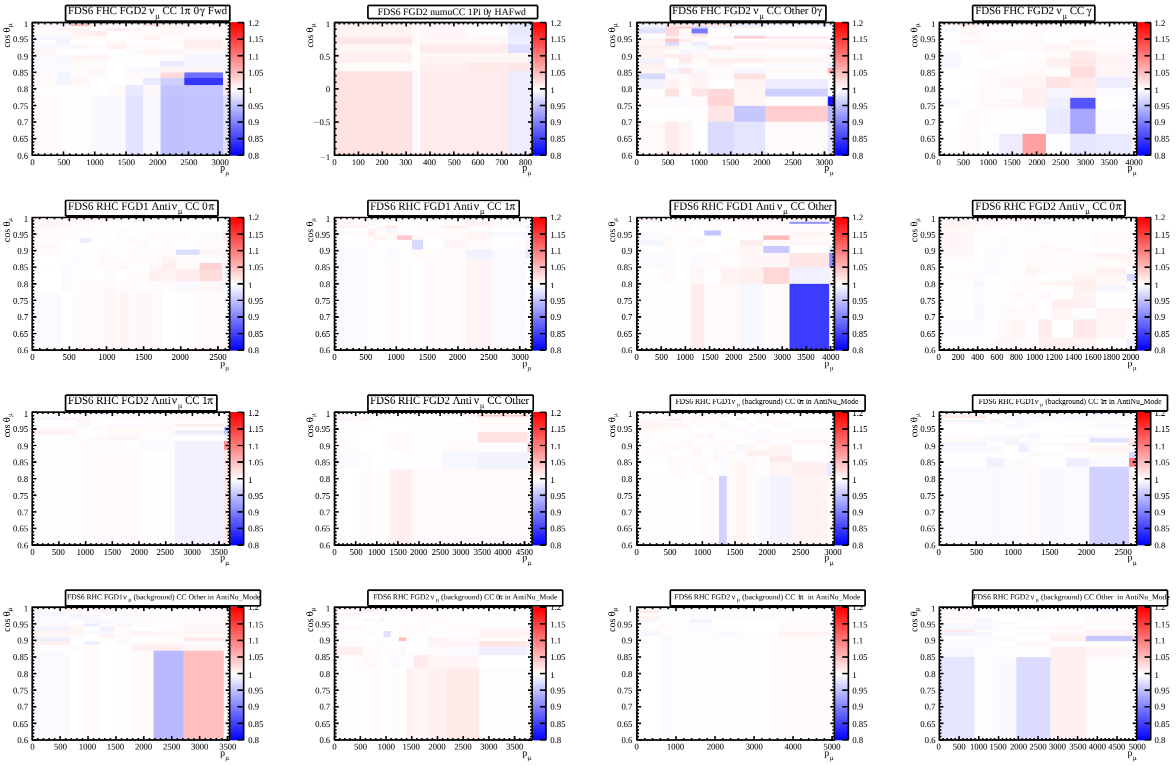

Figure B.14: Prefit (top 16) and postfit (lower 16) results for the AXFF ZExp Nom fake data set, showing the ratio of the angular and momentum distributions between the fitted MC and the nominal fake data across 4π selection samples.

Prefit:

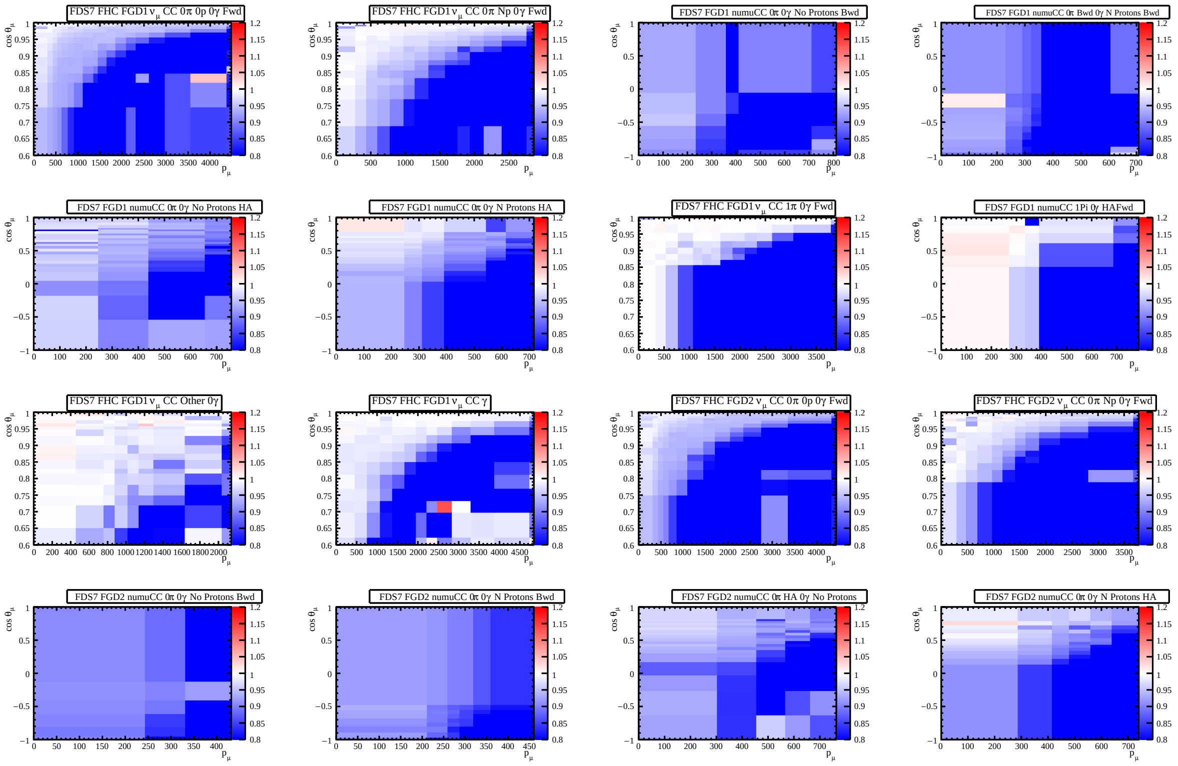

Postfit:

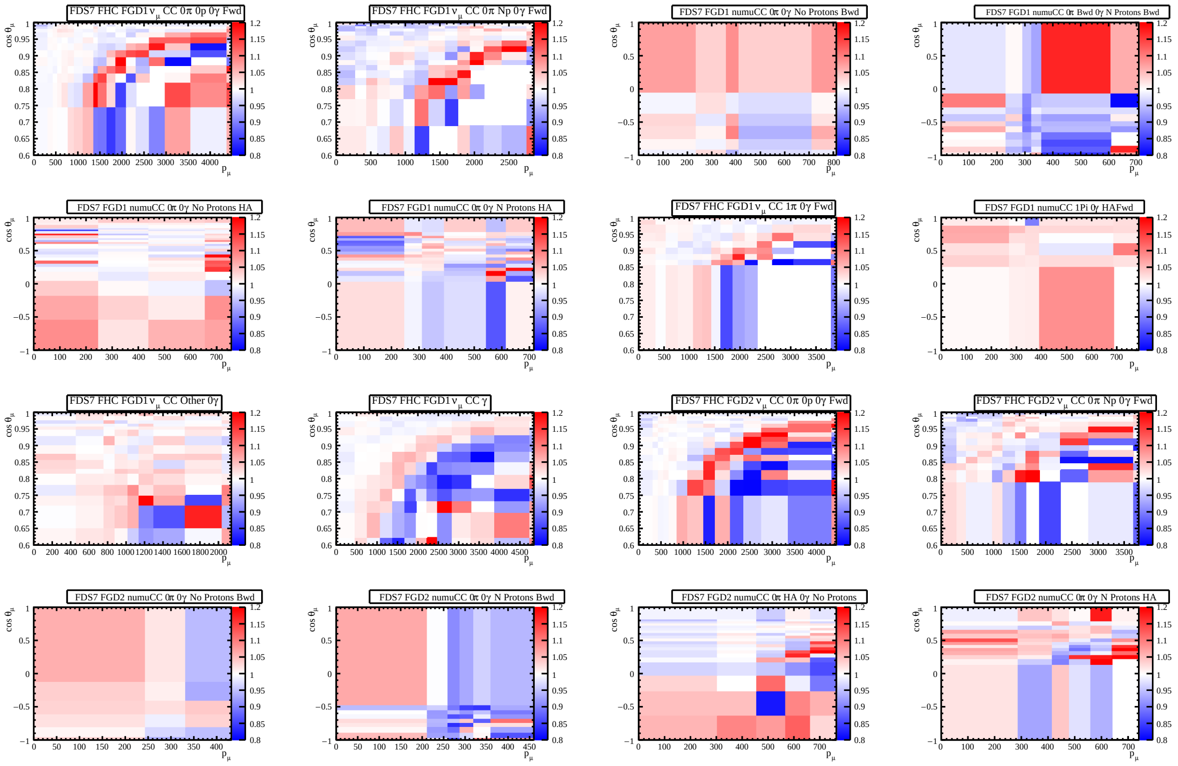

Figure B.15: Prefit (top 16) and postfit (lower 16) results for the AXFF ZExp P1sig fake data set, showing the ratio of the angular and momentum distributions between the fitted MC and the nominal fake data across 4π selection samples.

Prefit:

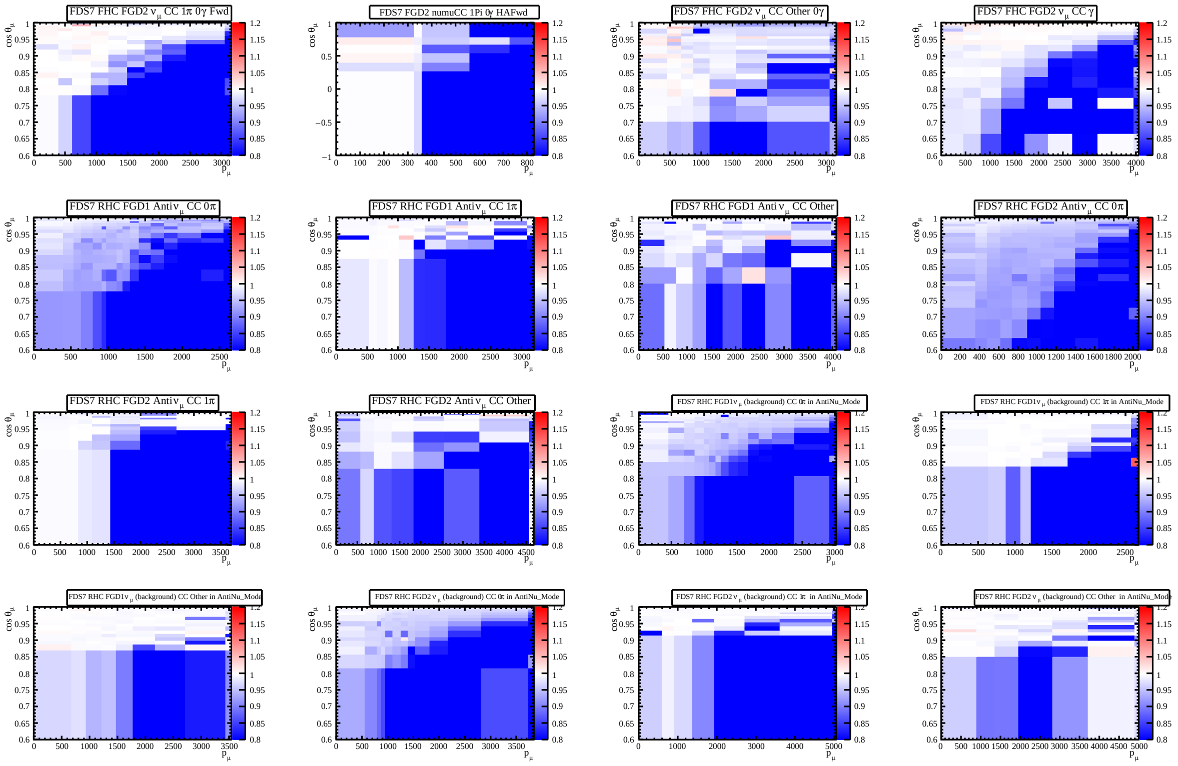

Postfit:

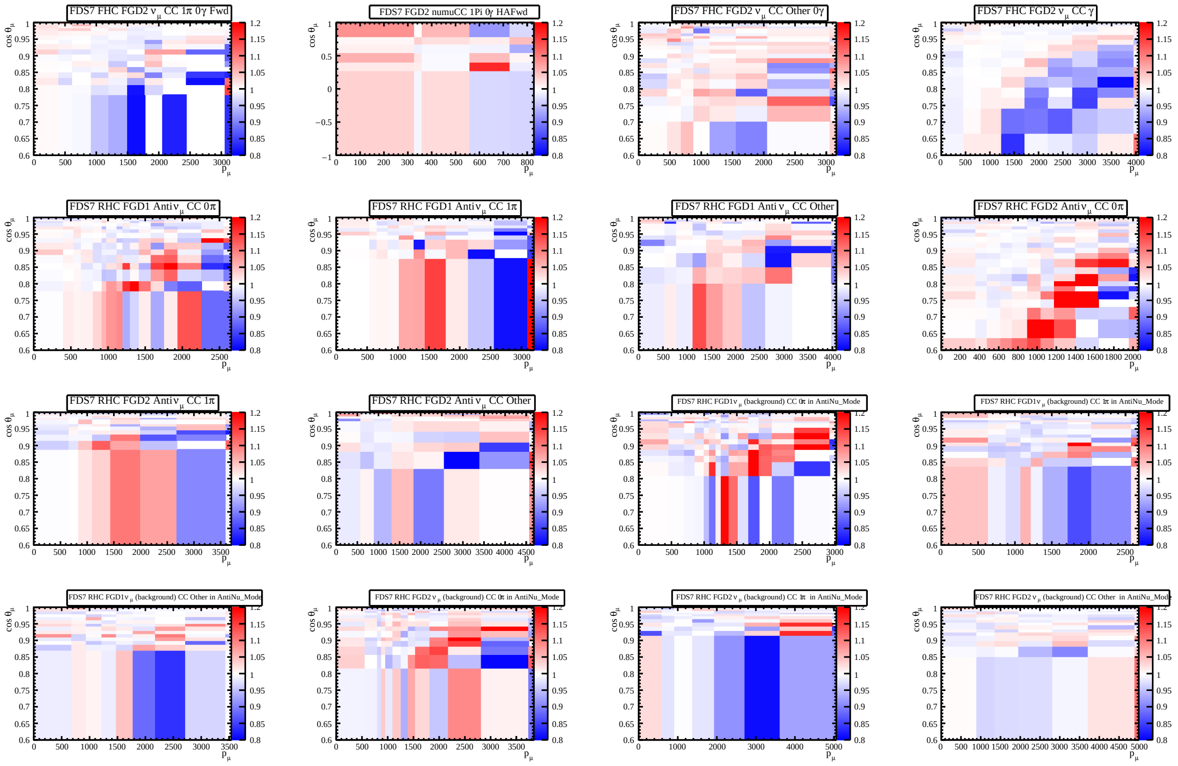

Figure B.16: Prefit (top 16) and postfit (lower 16) results for the AXFF ZExp P1sig fake data set, showing the ratio of the angular and momentum distributions between the fitted MC and the nominal fake data across 4π selection samples.

Prefit:

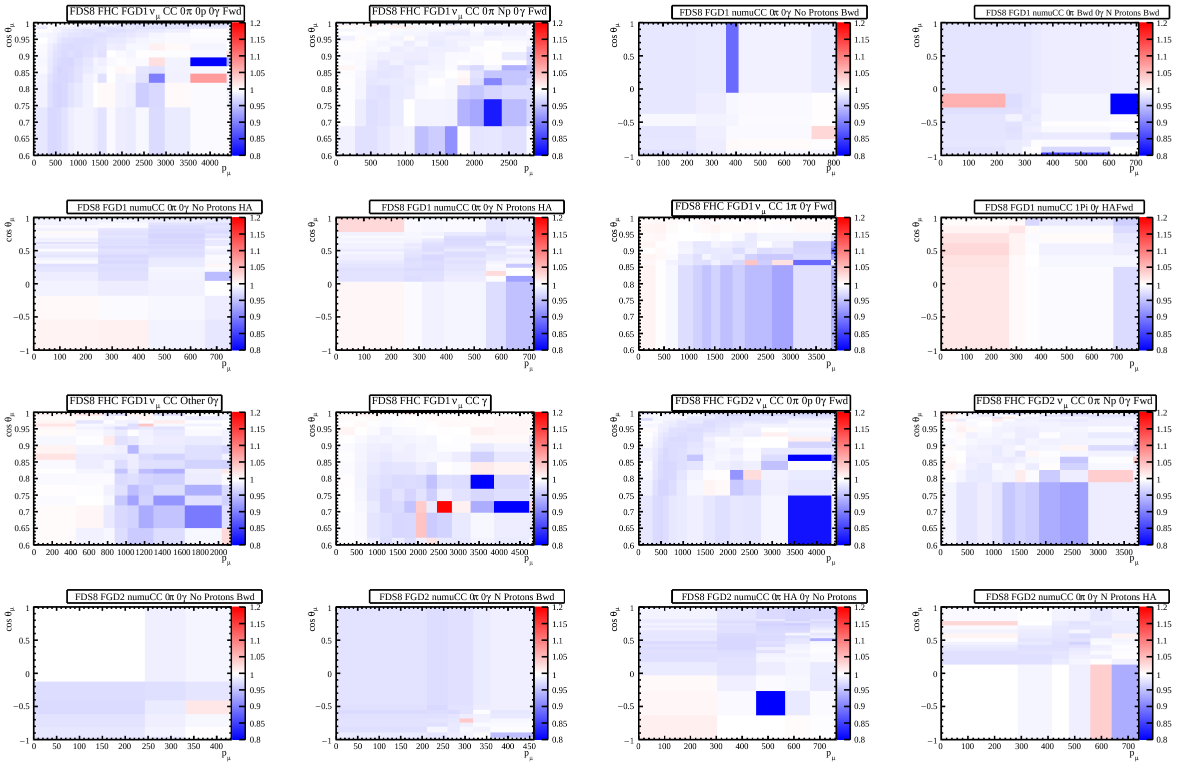

Postfit:

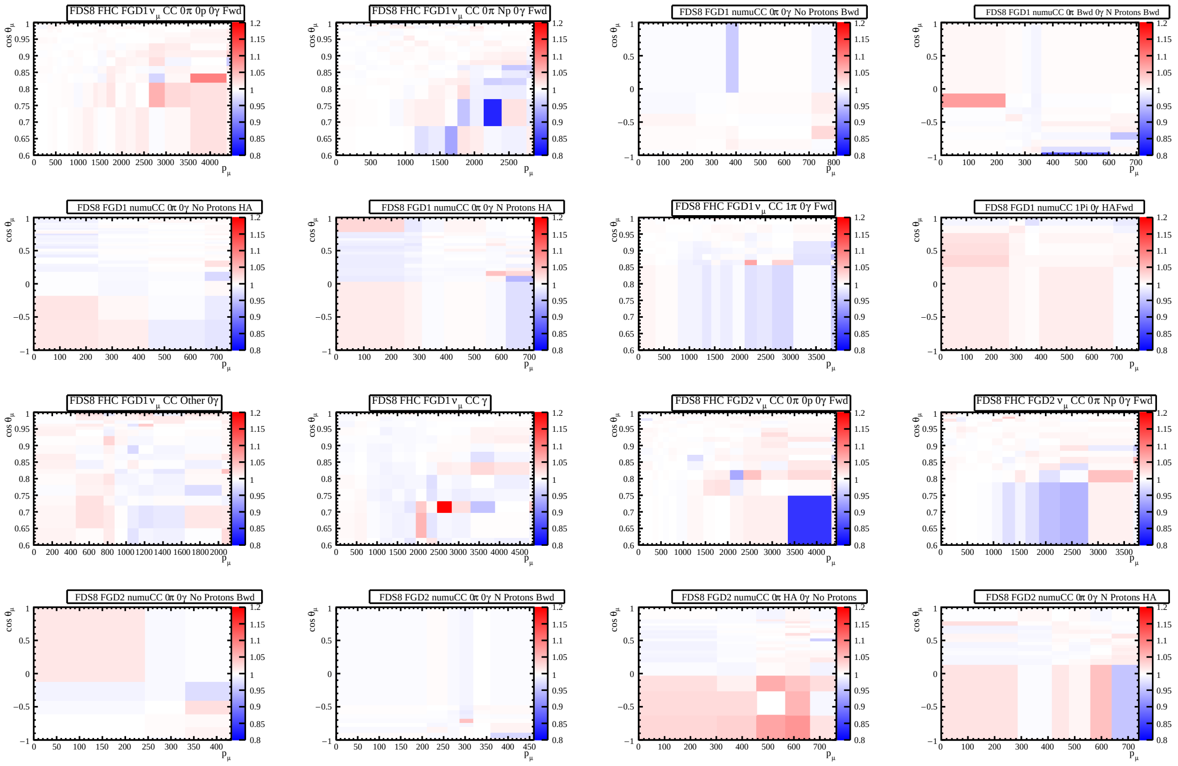

Figure B.17: Prefit (top 16) and postfit (lower 16) results for the LQCD Nom fake data set, showing the ratio of the angular and momentum distributions between the fitted MC and the nominal fake data across 4π selection samples.

Prefit:

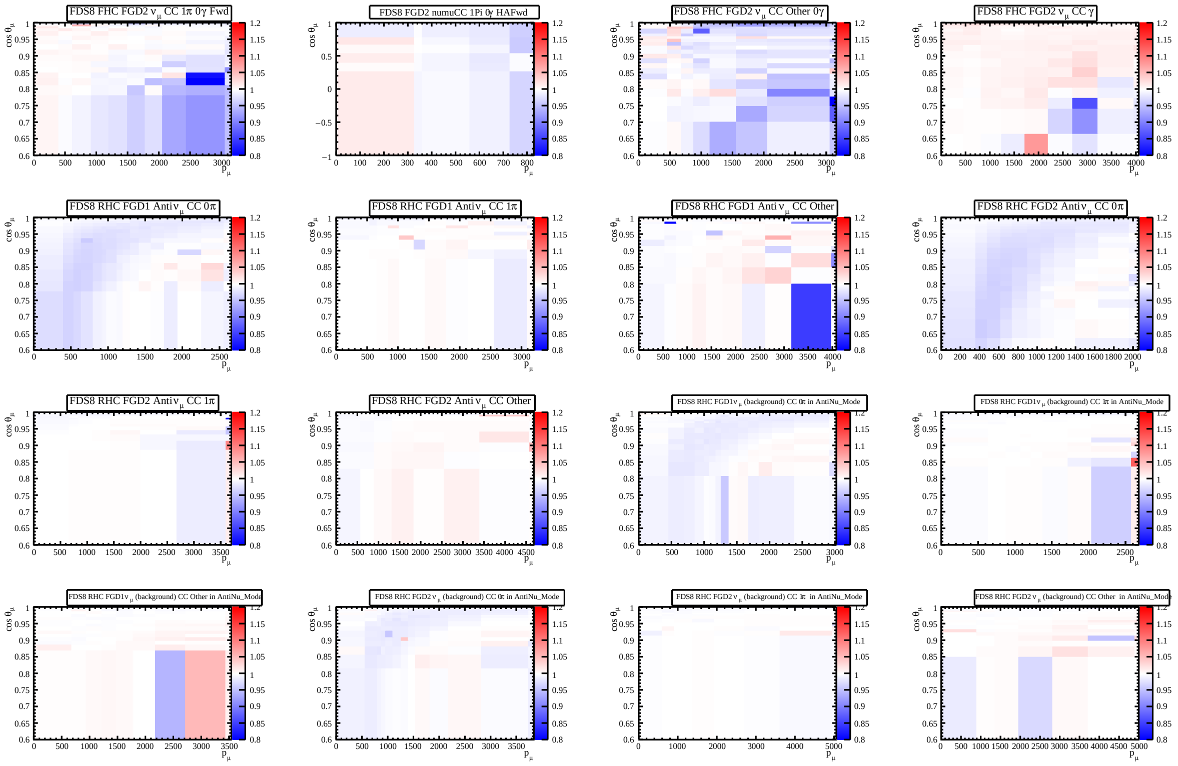

Postfit:

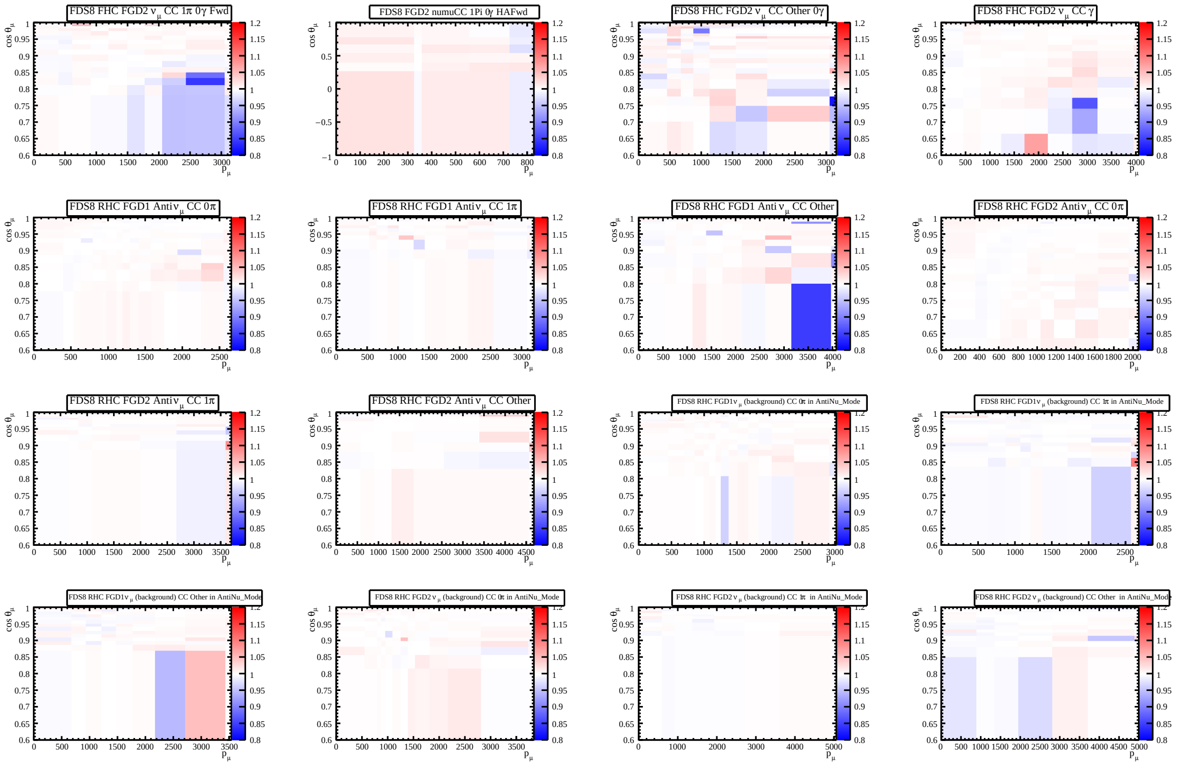

Figure B.18: Prefit (top 16) and postfit (lower 16) results for the LQCD Nom fake data set, showing the ratio of the angular and momentum distributions between the fitted MC and the nominal fake data across 4π selection samples.

Prefit:

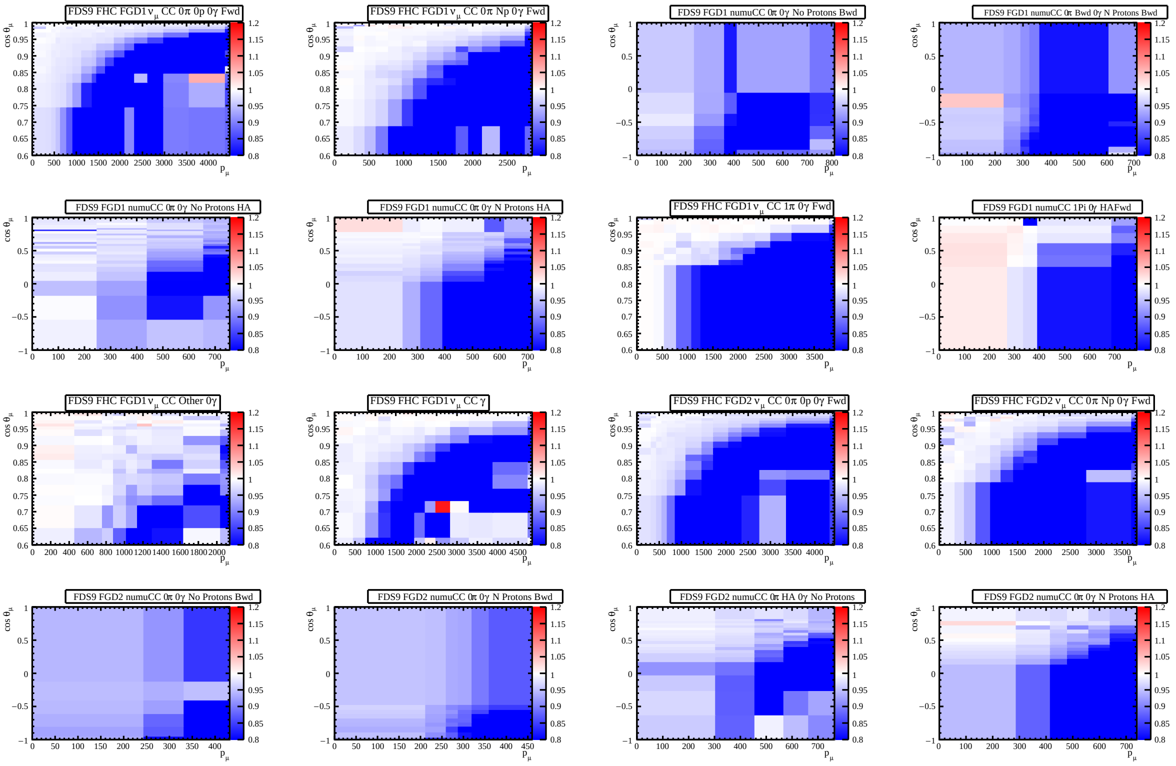

Postfit:

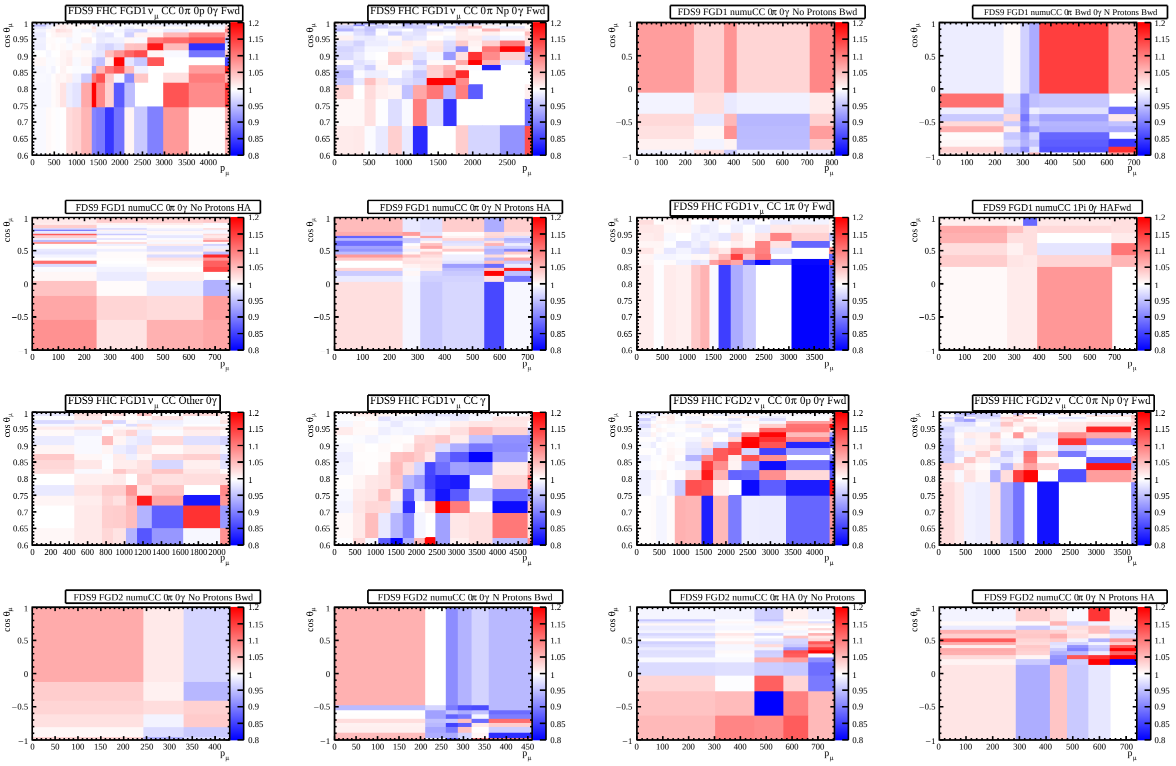

Figure B.19: Prefit (top 16) and postfit (lower 16) results for the LQCD P1sig fake data set, showing the ratio of the angular and momentum distributions between the fitted MC and the nominal fake data across 4π selection samples.

Prefit:

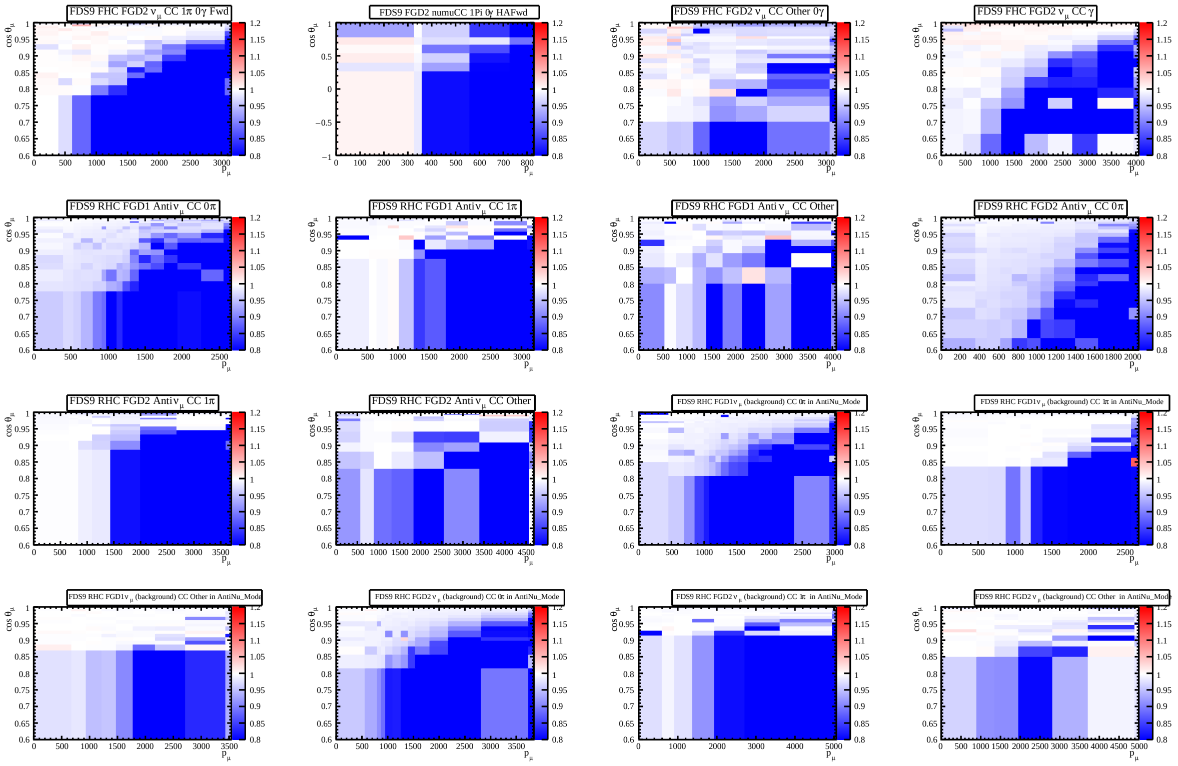

Postfit:

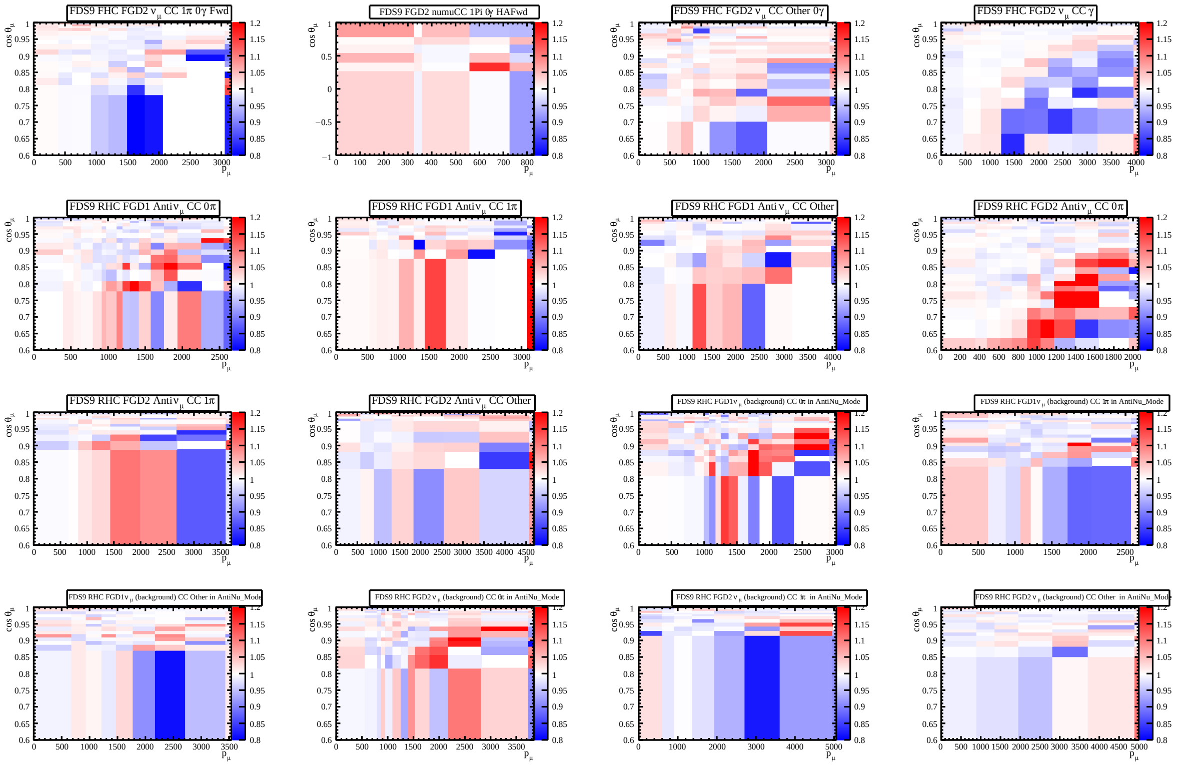

Figure B.20: Prefit (top 16) and postfit (lower 16) results for the LQCD P1sig fake data set, showing the ratio of the angular and momentum distributions between the fitted MC and the nominal fake data across 4π selection samples.

Prefit:

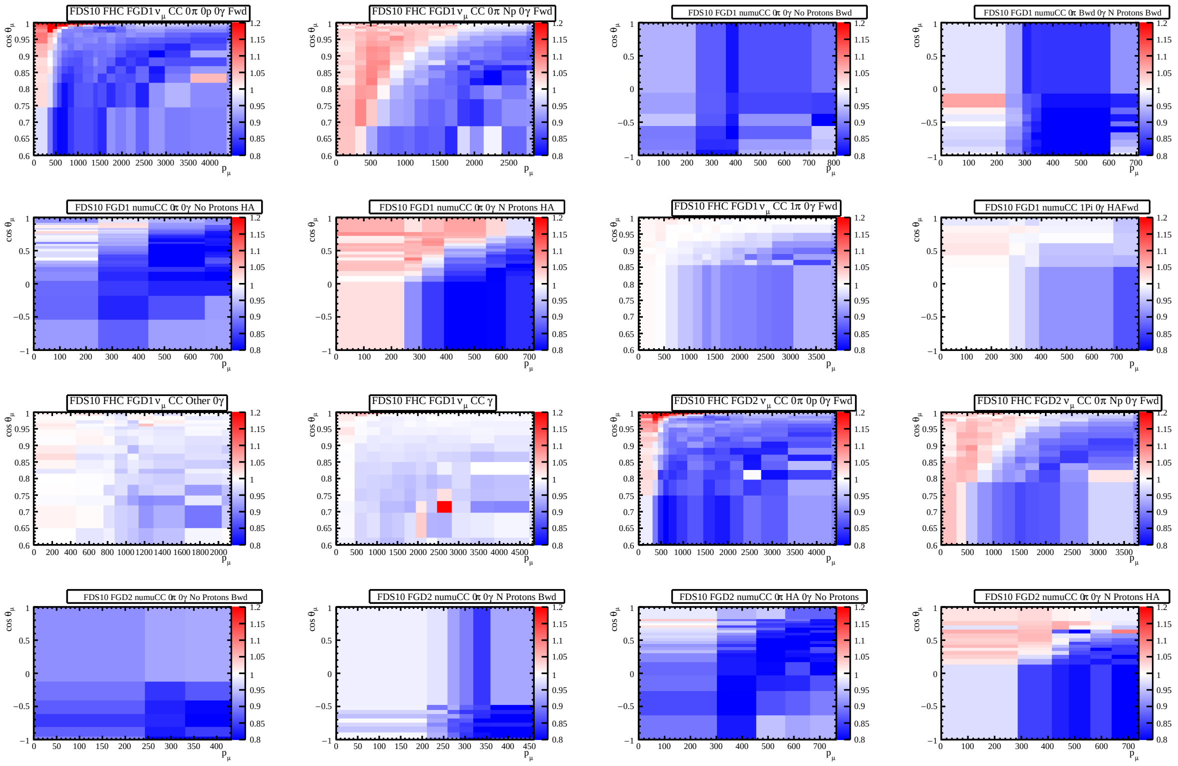

Postfit:

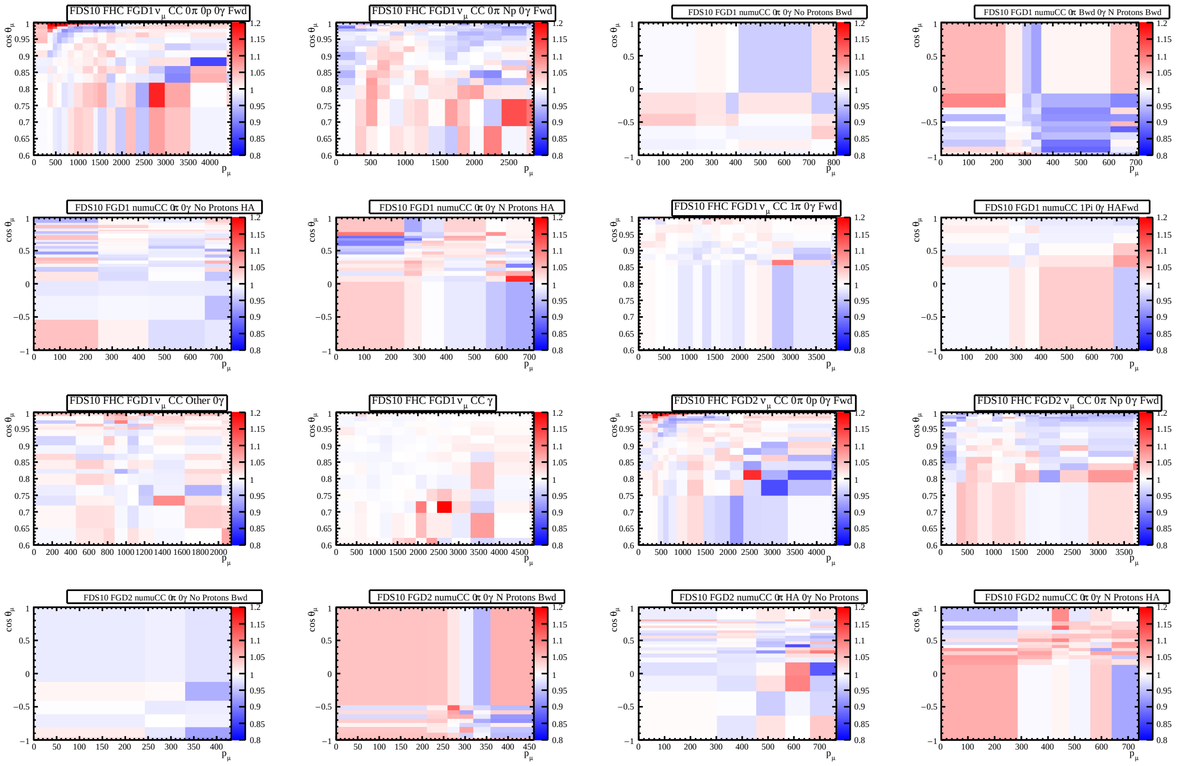

Figure B.21: Prefit (top 16) and postfit (lower 16) results for the SF to SuSAv2 fake data set, showing the ratio of the angular and momentum distributions between the fitted MC and the nominal fake data across 4π selection samples.

Prefit:

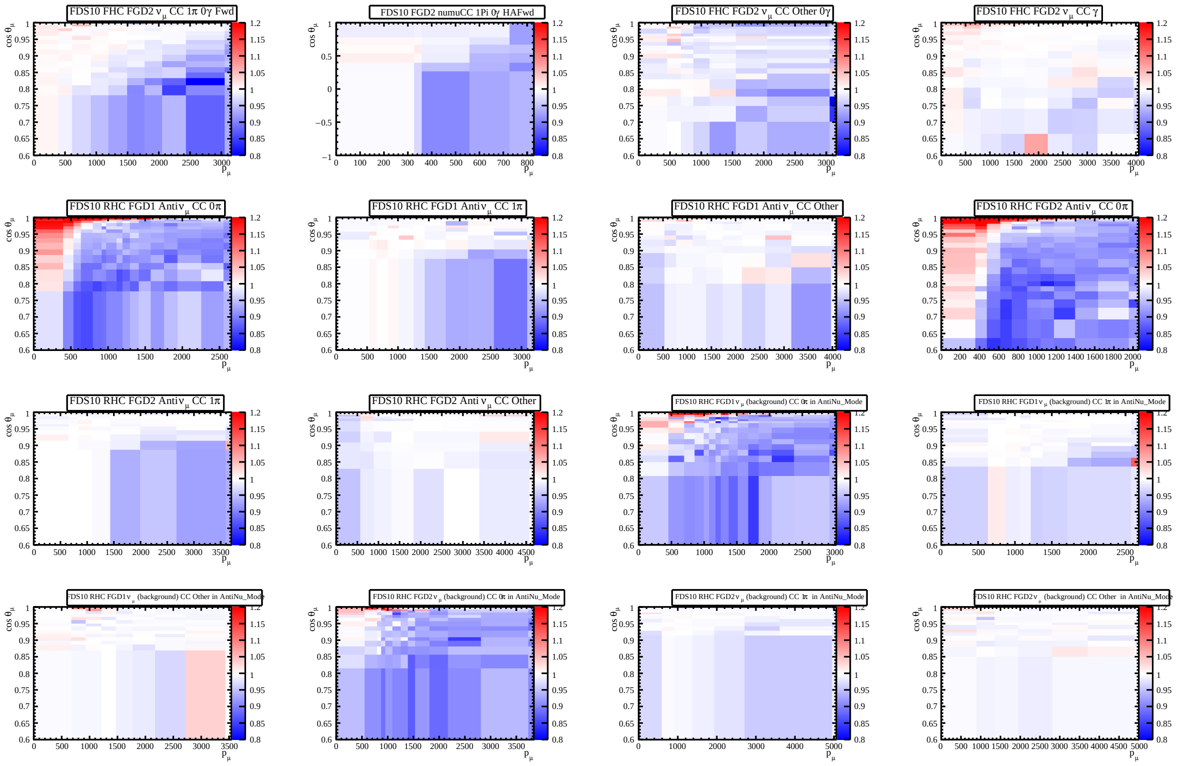

Postfit:

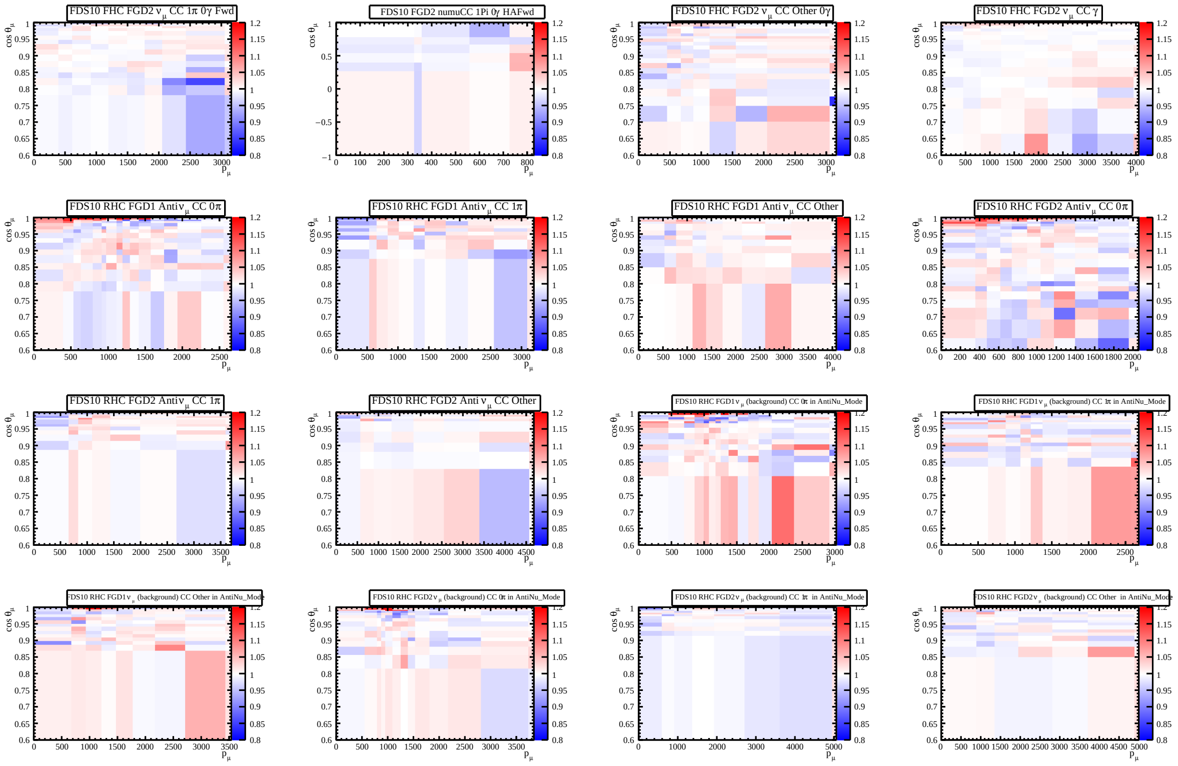

Figure B.22: Prefit (top 16) and postfit (lower 16) results for the SF to SuSAv2 fake data set, showing the ratio of the angular and momentum distributions between the fitted MC and the nominal fake data across 4π selection samples.

Prefit:

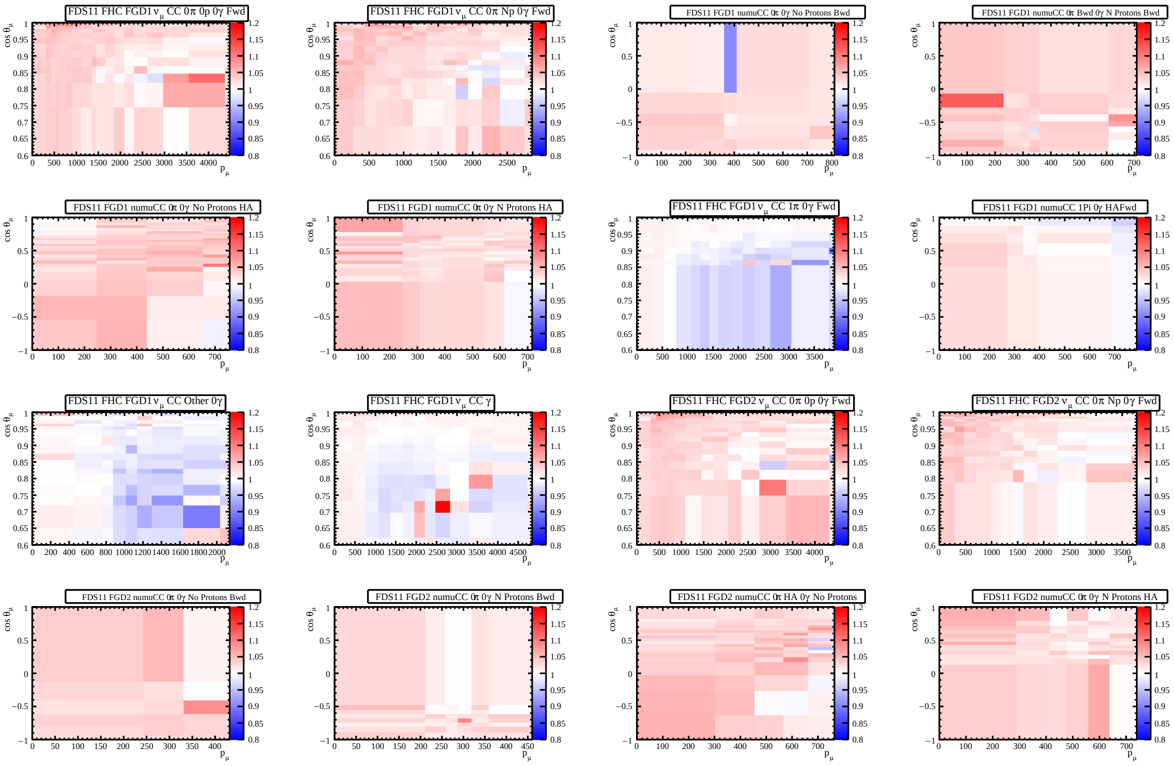

Postfit:

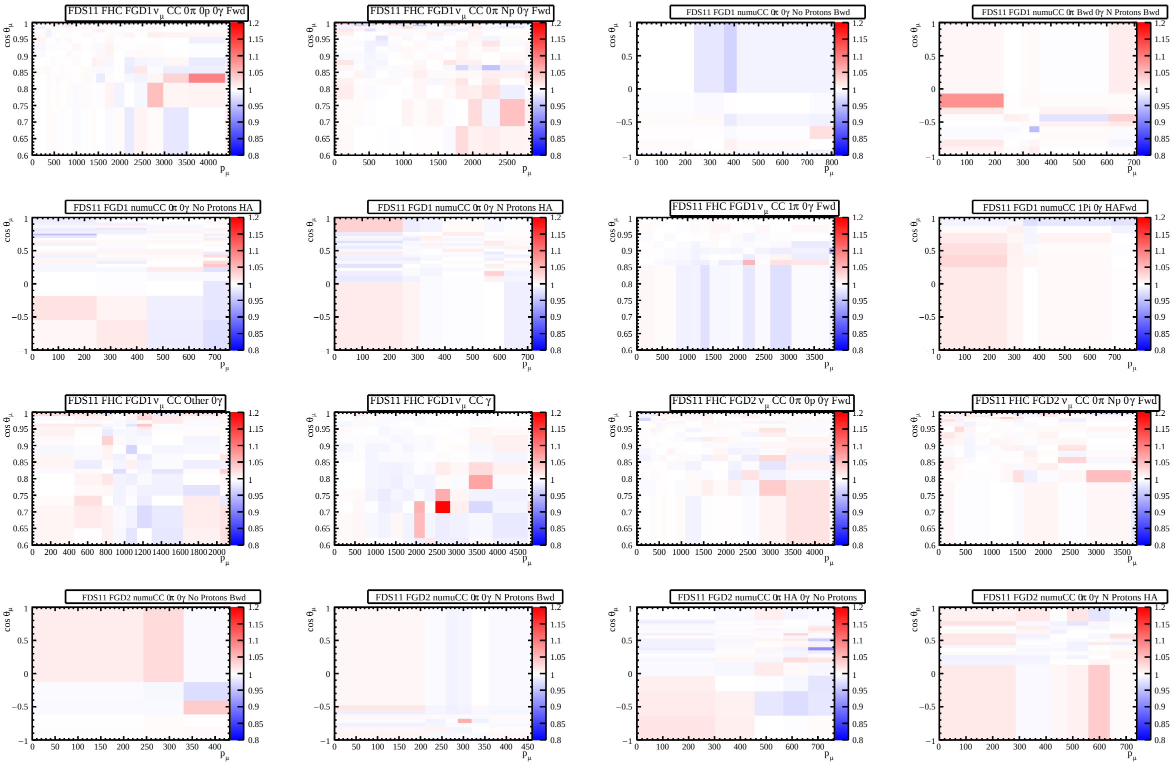

Figure B.23: Prefit (top 16) and postfit (lower 16) results for the 2p2h Eb Correction fake data set, showing the ratio of the angular and momentum distributions between the fitted MC and the nominal fake data across 4π selection samples.

Prefit:

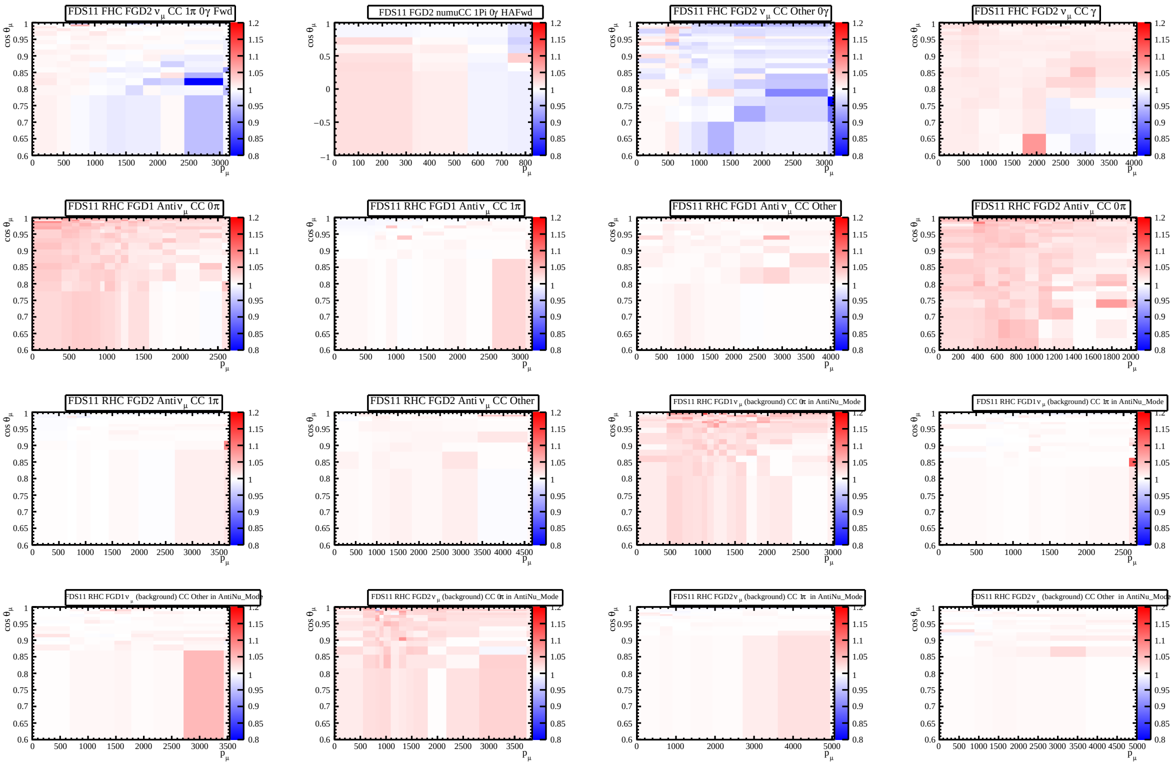

Postfit:

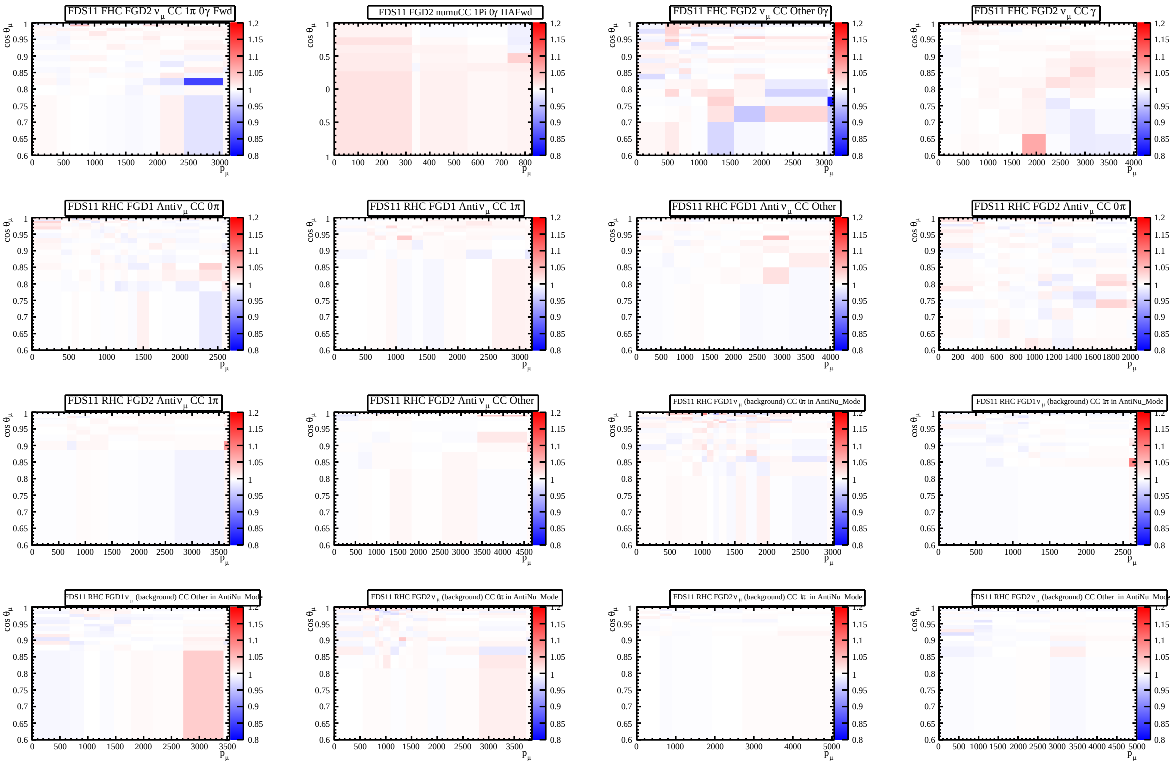

Figure B.24: Prefit (top 16) and postfit (lower 16) results for the 2p2h Eb Correction fake data set, showing the ratio of the angular and momentum distributions between the fitted MC and the nominal fake data across 4π selection samples.

Prefit:

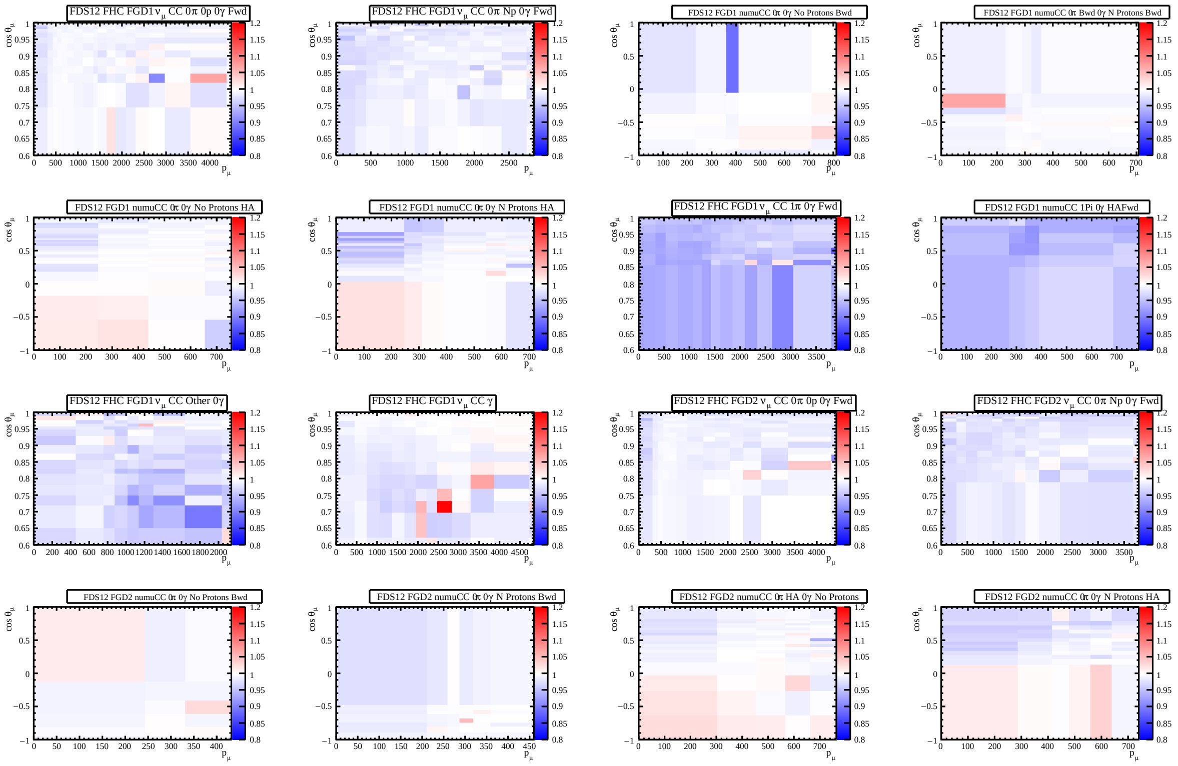

Postfit:

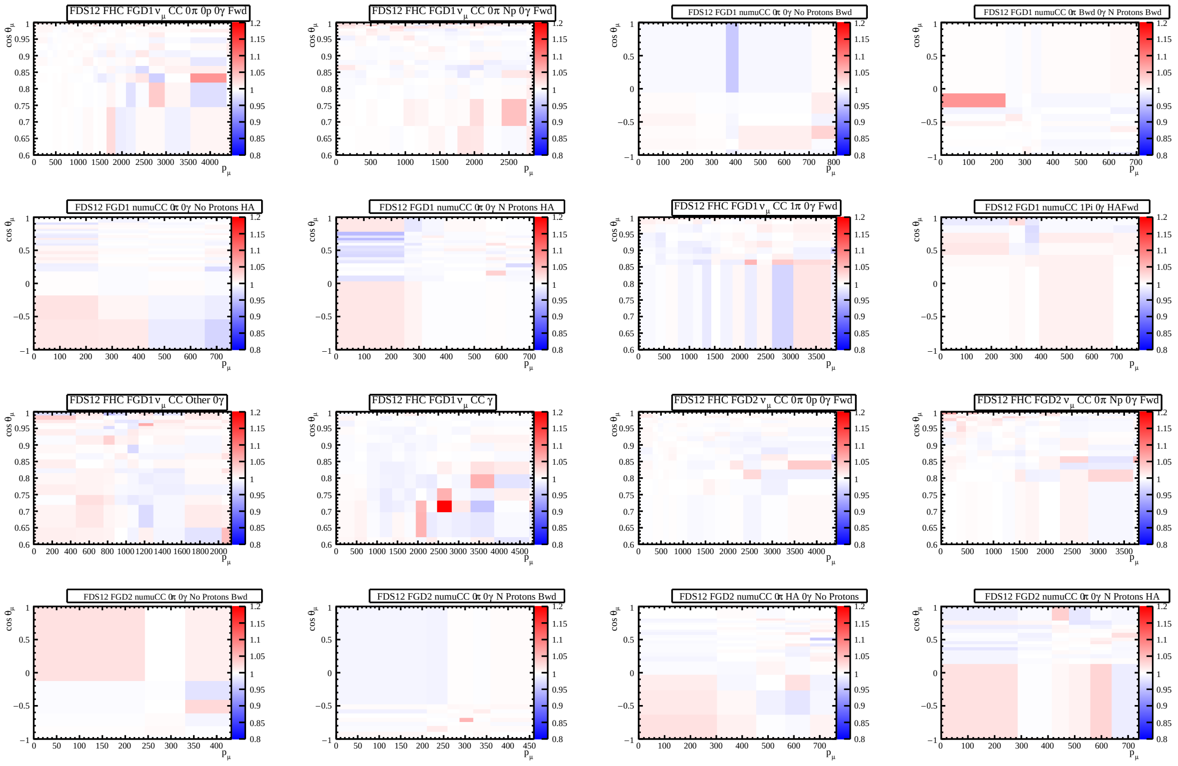

Figure B.25: Prefit (top 16) and postfit (lower 16) results for the SPP Adverserial fake data set, showing the ratio of the angular and momentum distributions between the fitted MC and the nominal fake data across 4π selection samples.

Prefit:

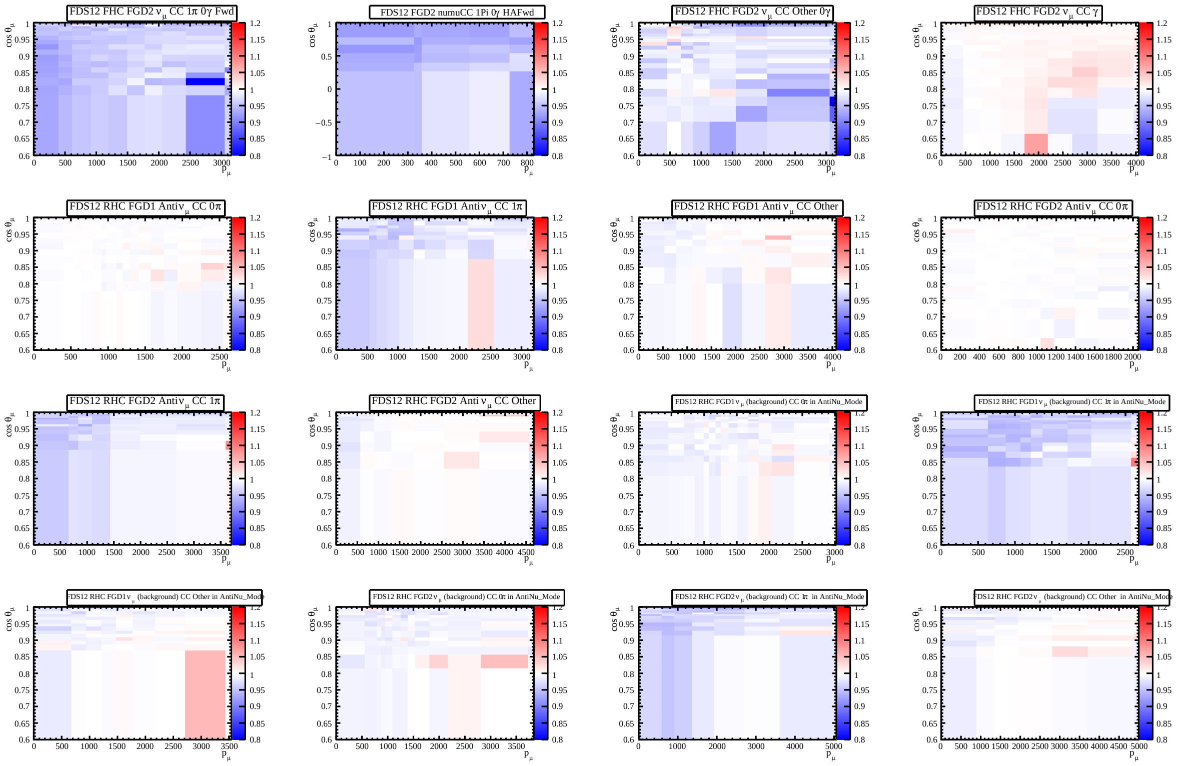

Postfit:

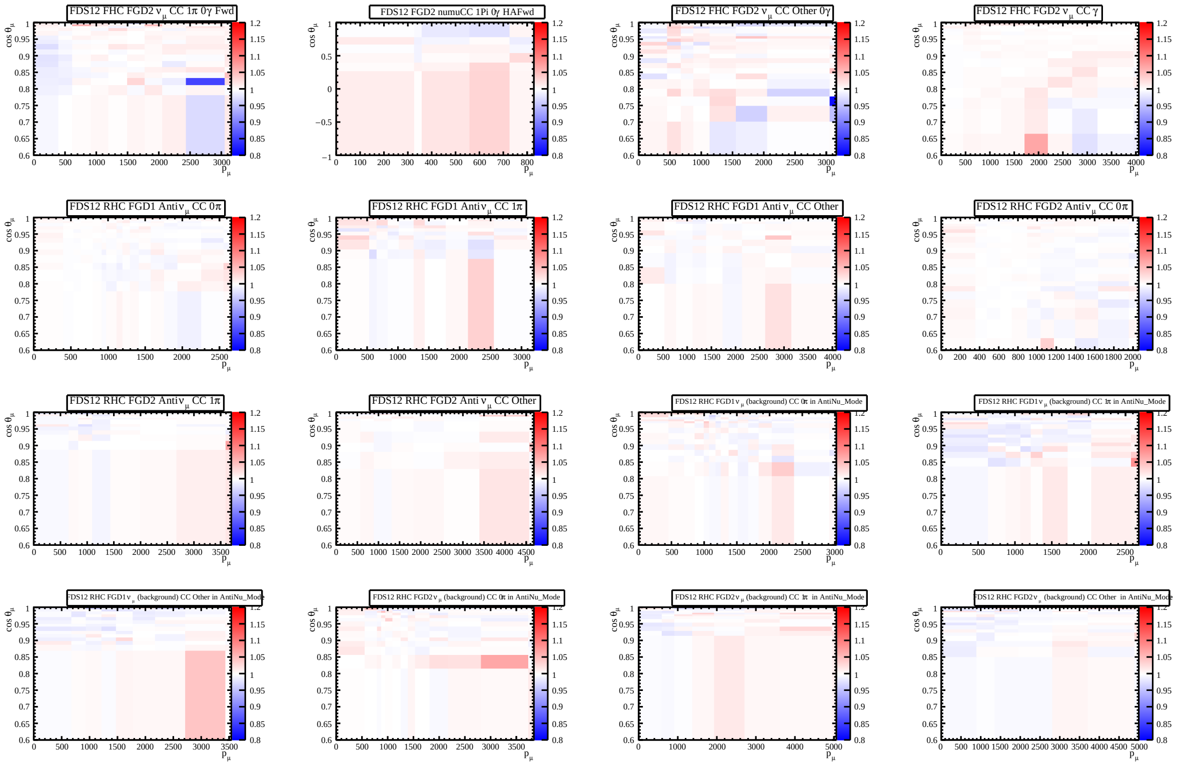

Figure B.26: Prefit (top 16) and postfit (lower 16) results for the SPP Adverserial fake data set, showing the ratio of the angular and momentum distributions between the fitted MC and the nominal fake data across 4π selection samples.

Prefit:

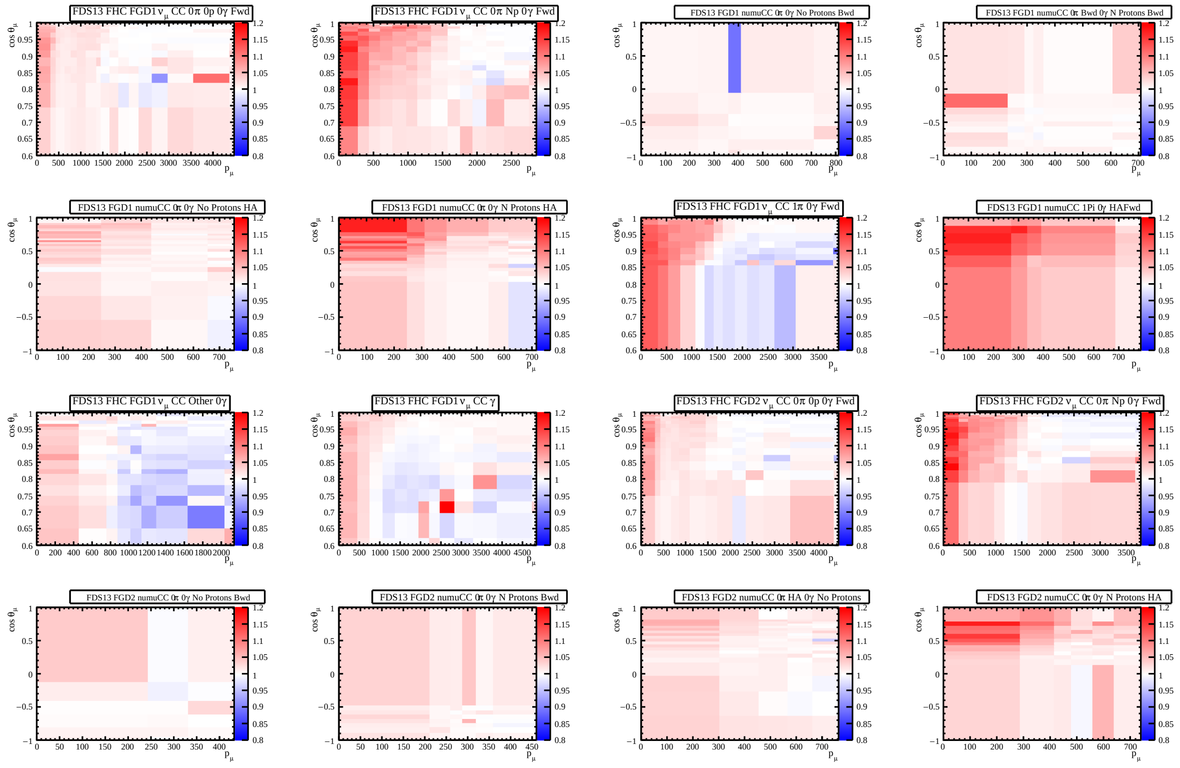

Postfit:

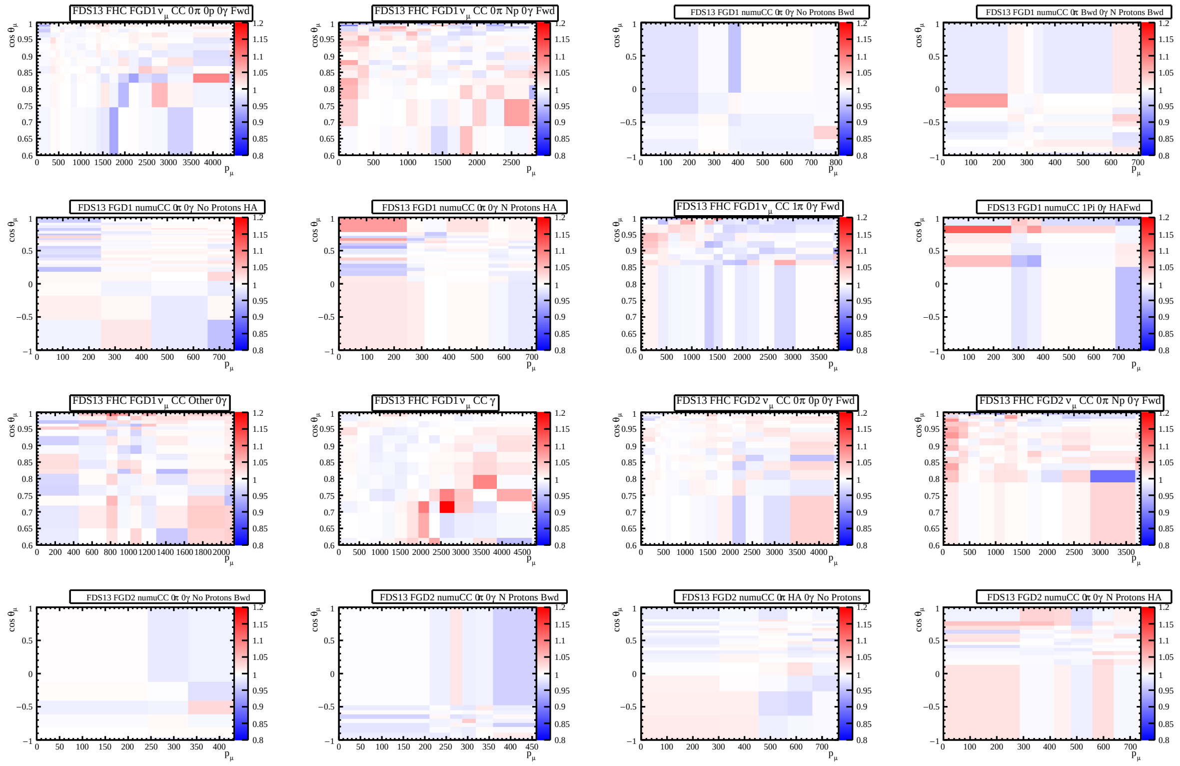

Figure B.27: Prefit (top 16) and postfit (lower 16) results for the RS to Martini fake data set, showing the ratio of the angular and momentum distributions between the fitted MC and the nominal fake data across 4π selection samples.

Prefit:

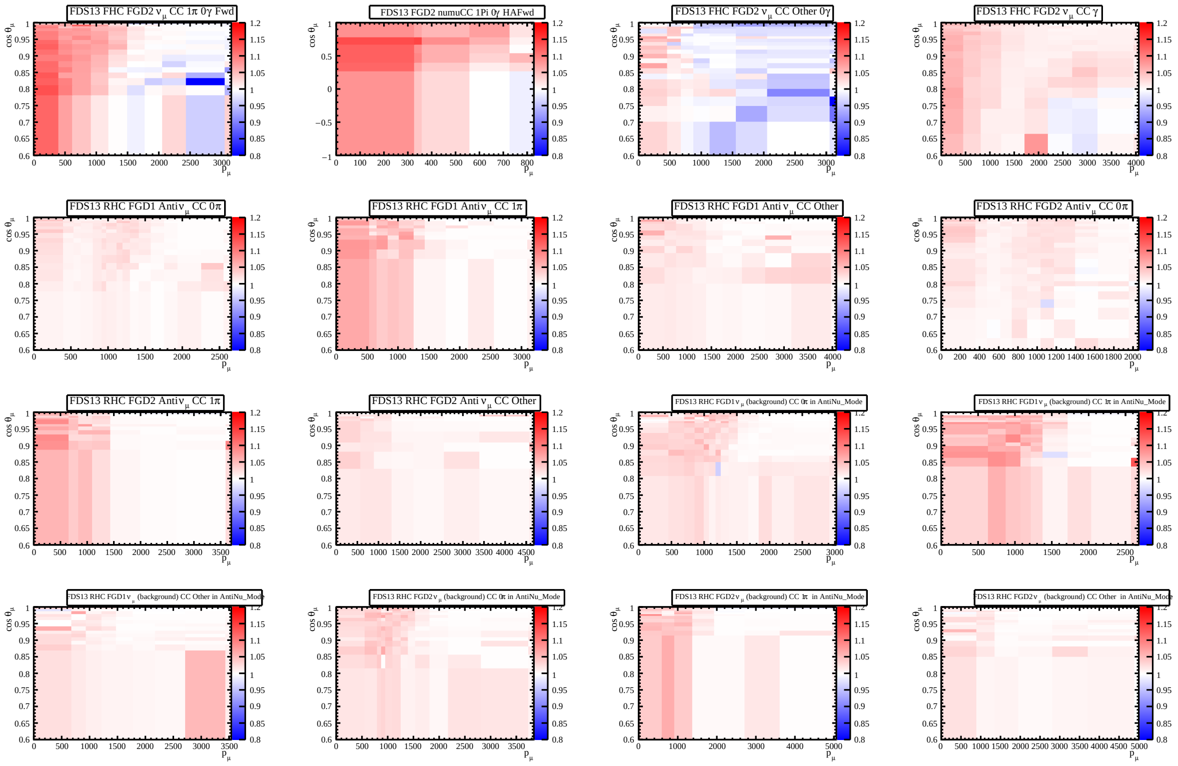

Postfit:

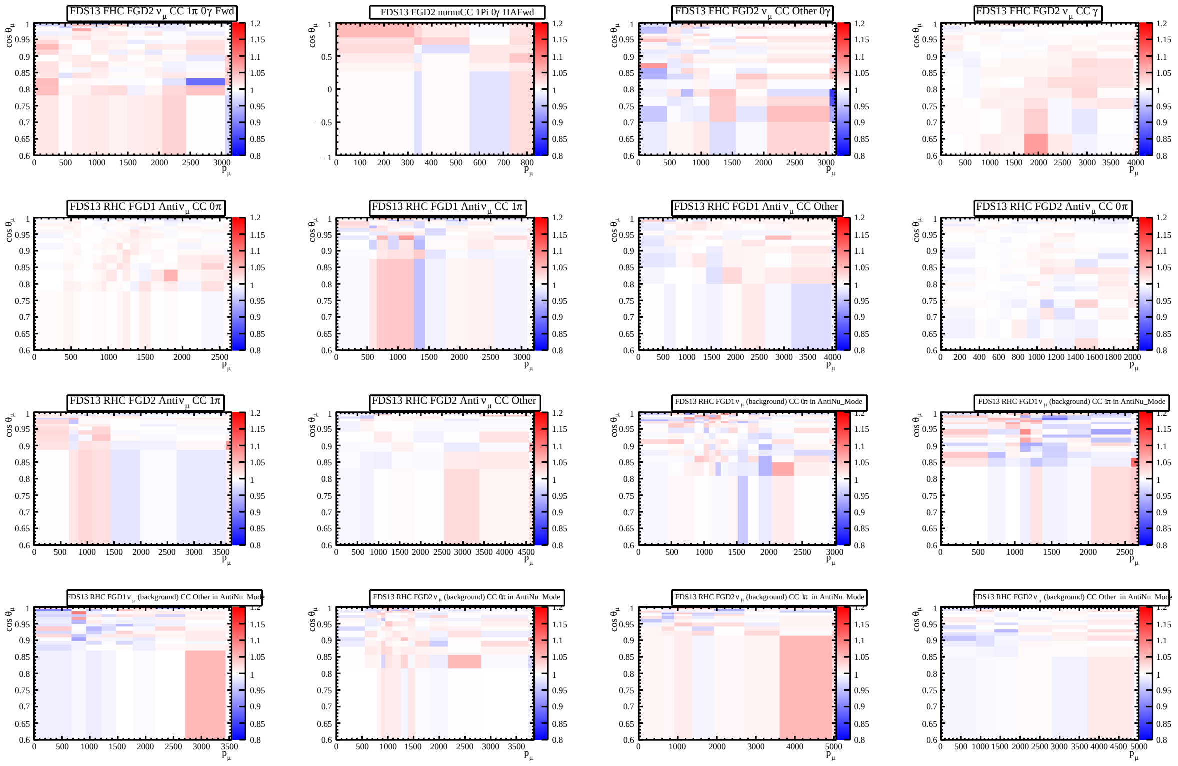

Figure B.28: Prefit (top 16) and postfit (lower 16) results for the RS to Martini fake data set, showing the ratio of the angular and momentum distributions between the fitted MC and the nominal fake data across 4π selection samples.

Prefit:

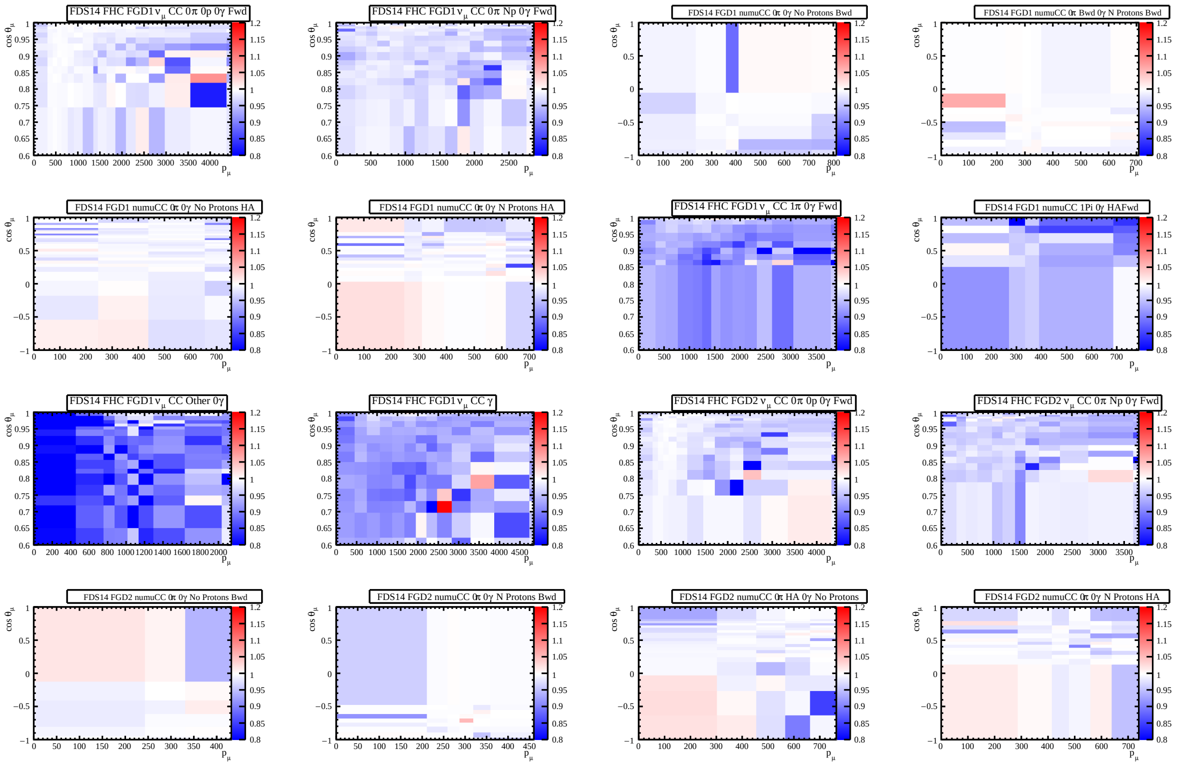

Postfit:

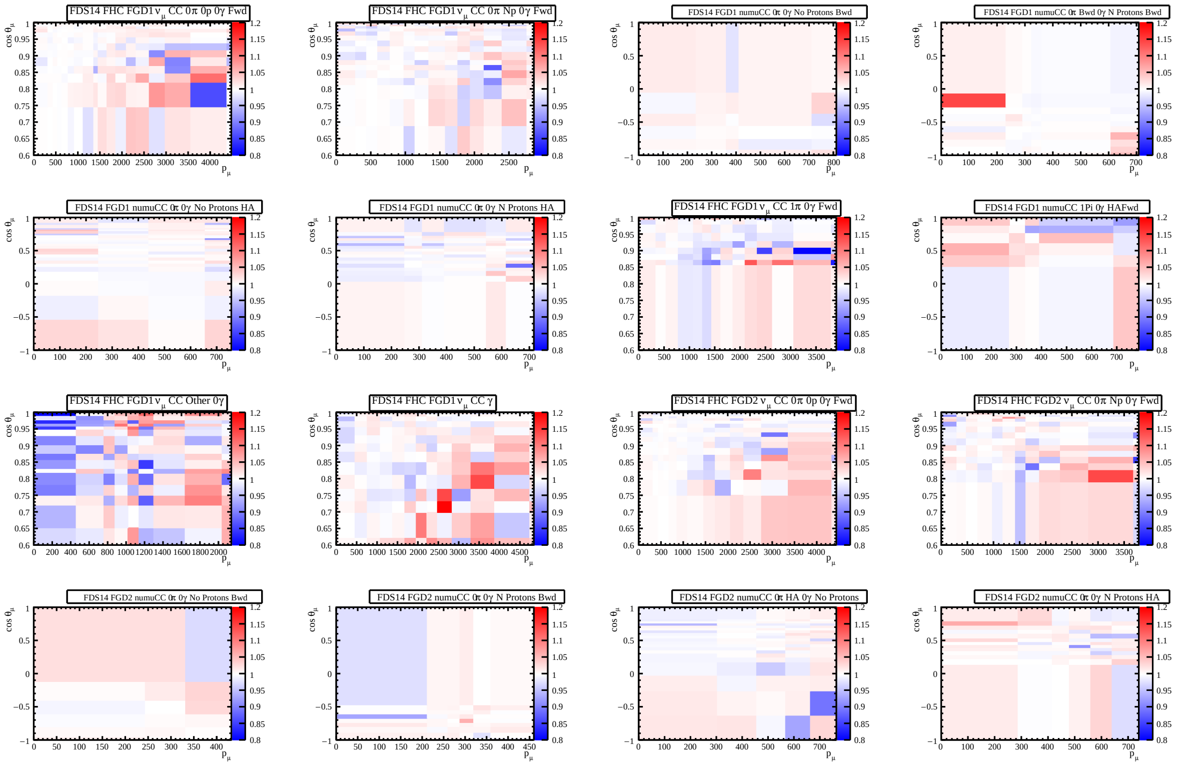

Figure B.29: Prefit (top 16) and postfit (lower 16) results for the MultiPi Multiplicity fake data set, showing the ratio of the angular and momentum distributions between the fitted MC and the nominal fake data across 4π selection samples.

Prefit:

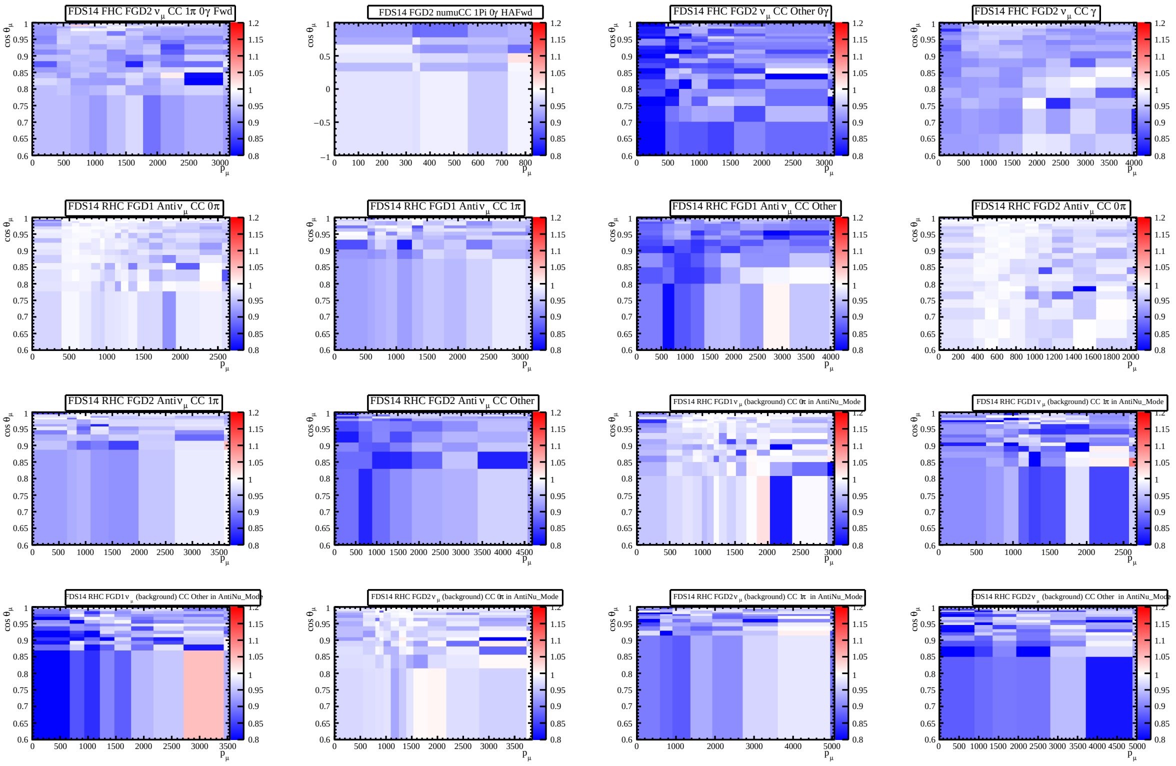

Postfit:

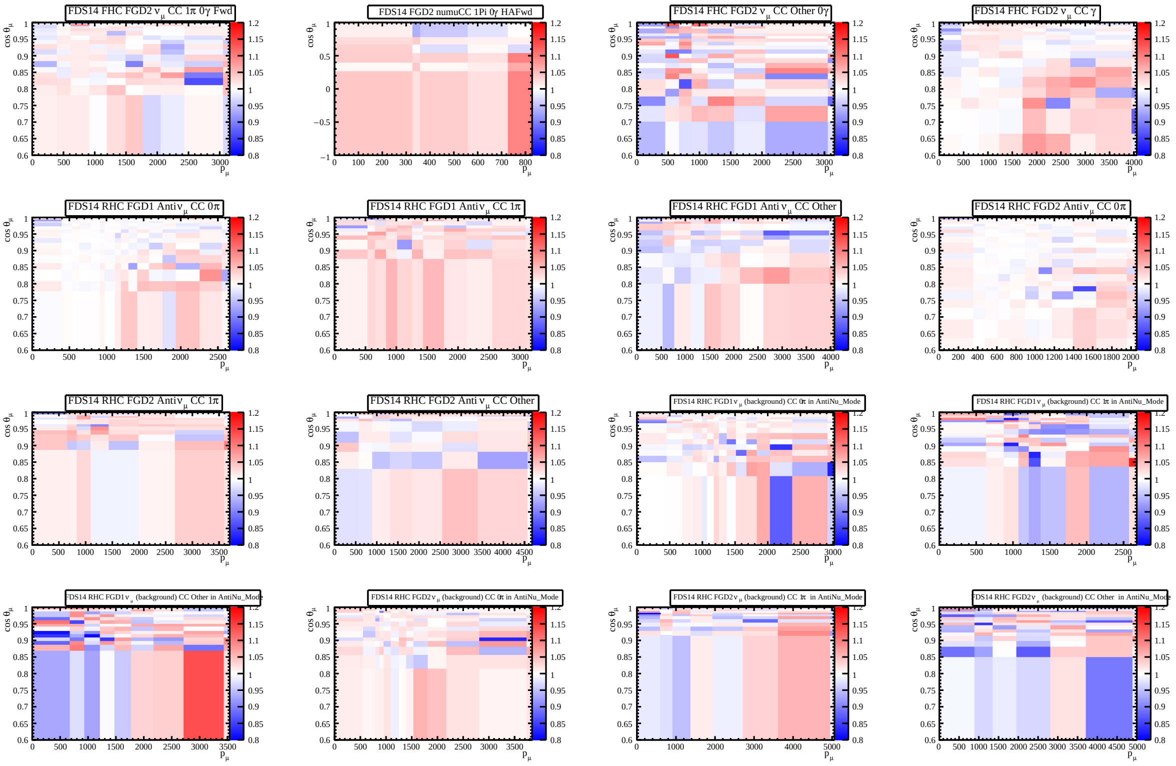

Figure B.30: Prefit (top 16) and postfit (lower 16) results for the MultiPi Multiplicity fake data set, showing the ratio of the angular and momentum distributions between the fitted MC and the nominal fake data across 4π selection samples.

Prefit:

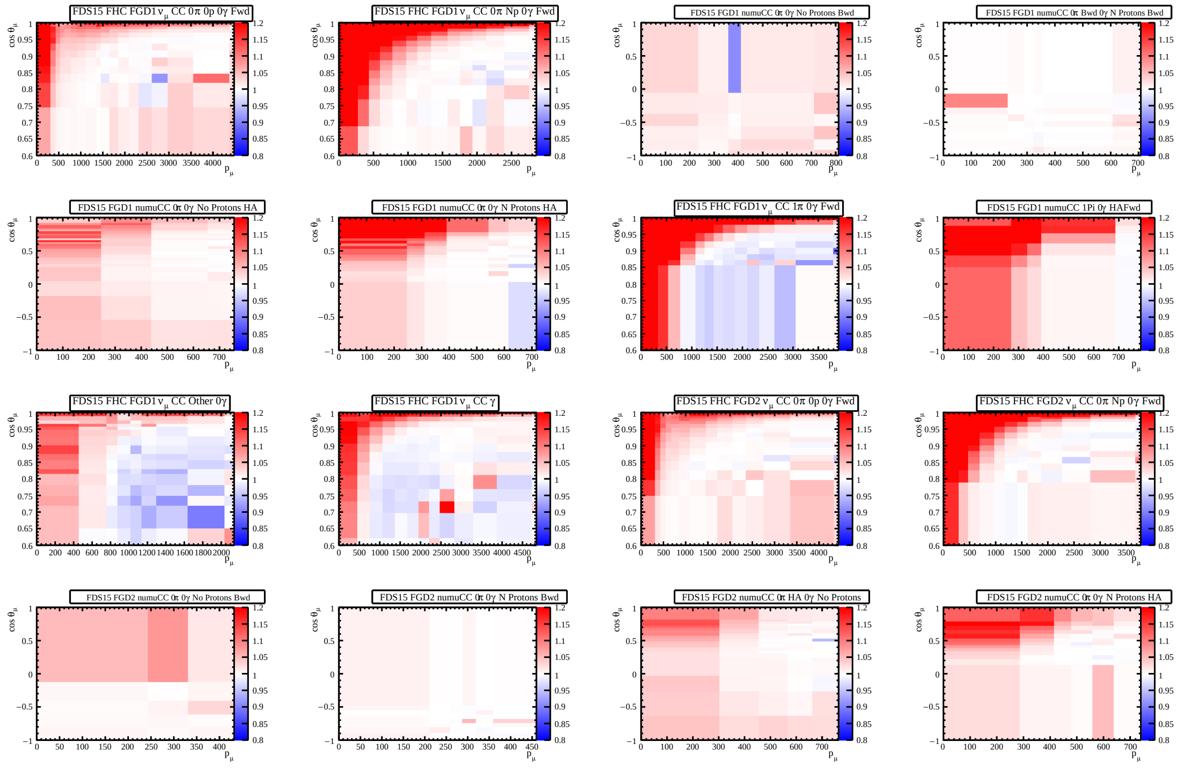

Postfit:

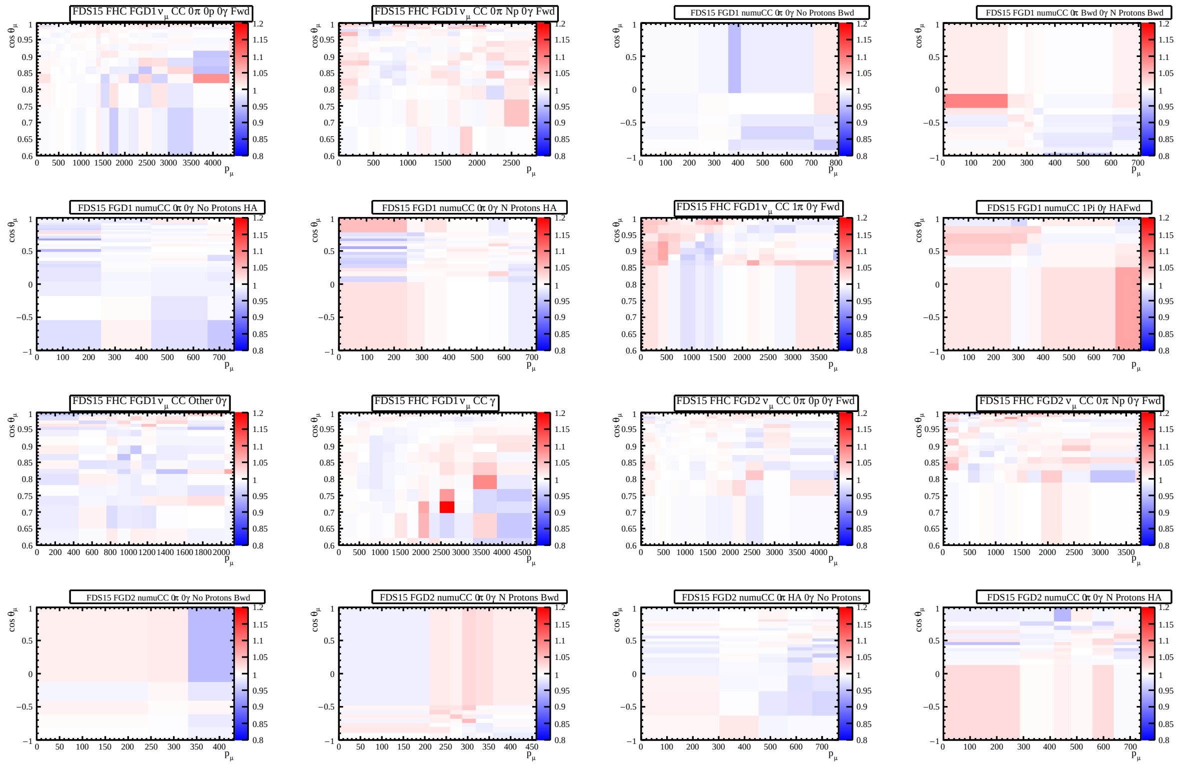

Figure B.31: Prefit (top 16) and postfit (lower 16) results for the Low Q2 SPP fake data set, showing the ratio of the angular and momentum distributions between the fitted MC and the nominal fake data across 4π selection samples.

Prefit:

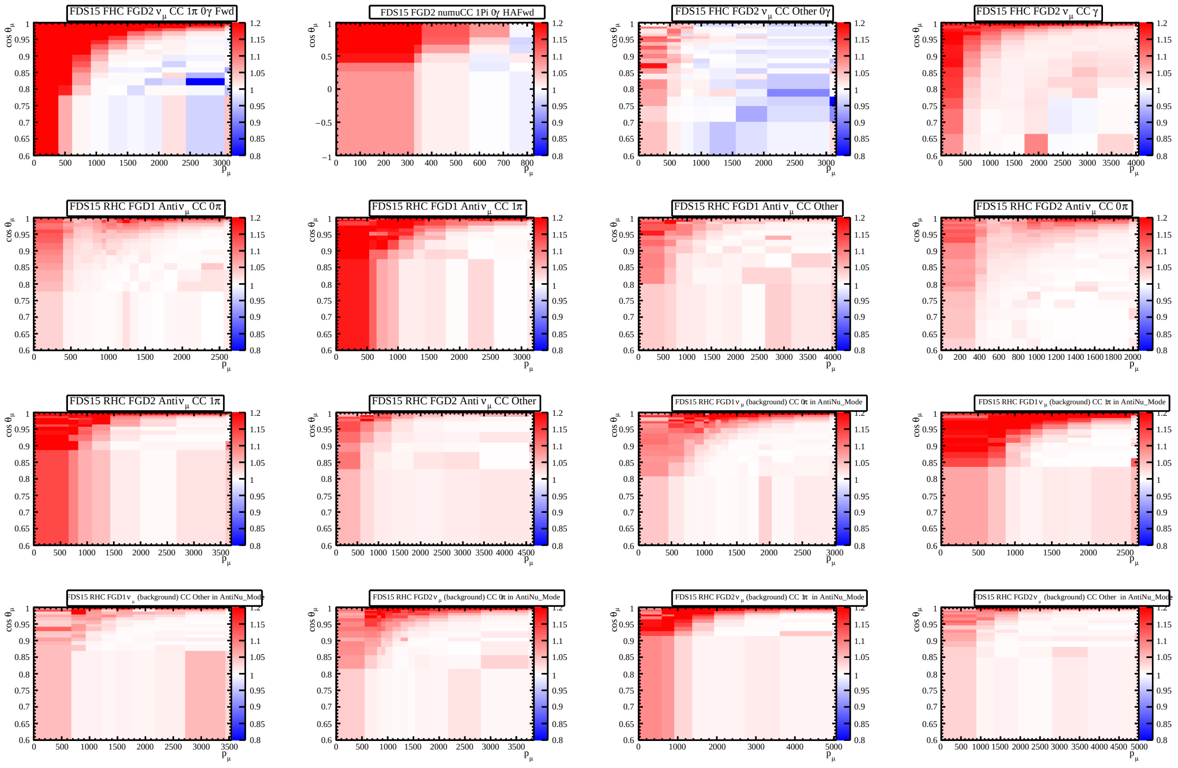

Postfit:

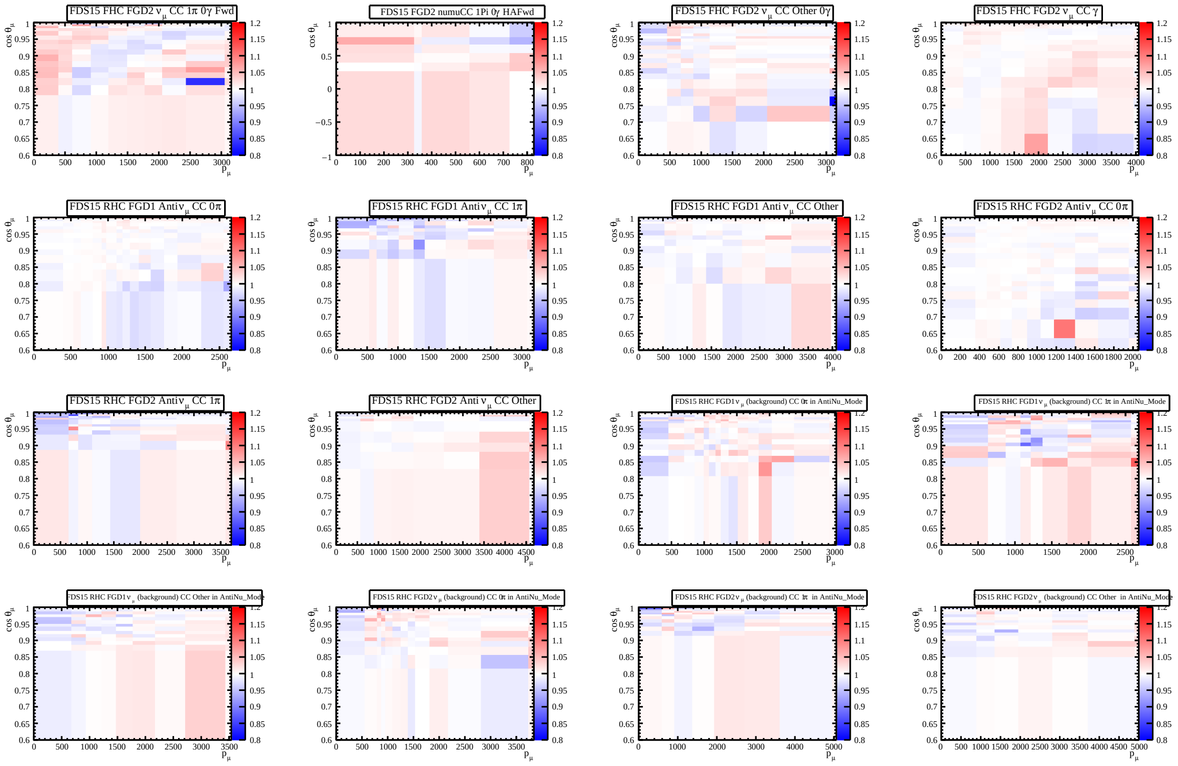

Figure B.32: Prefit (top 16) and postfit (lower 16) results for the Low Q2 SPP fake data set, showing the ratio of the angular and momentum distributions between the fitted MC and the nominal fake data across 4π selection samples.

Prefit:

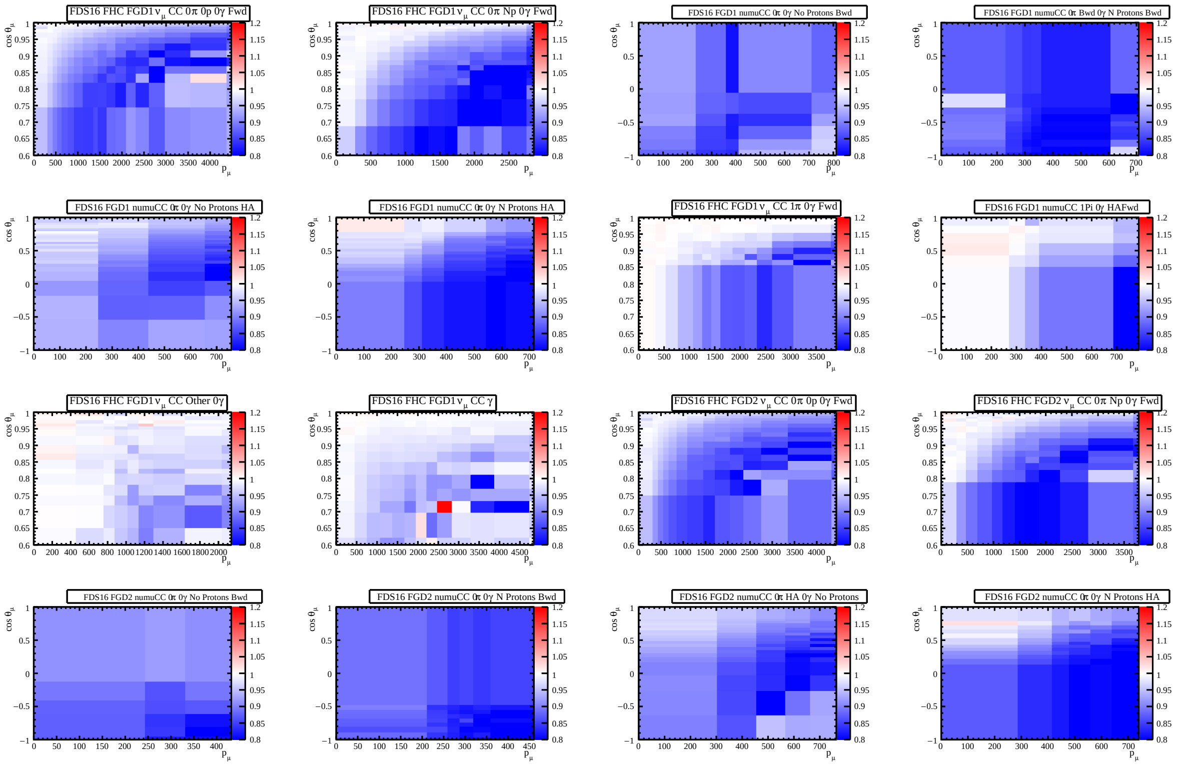

Postfit:

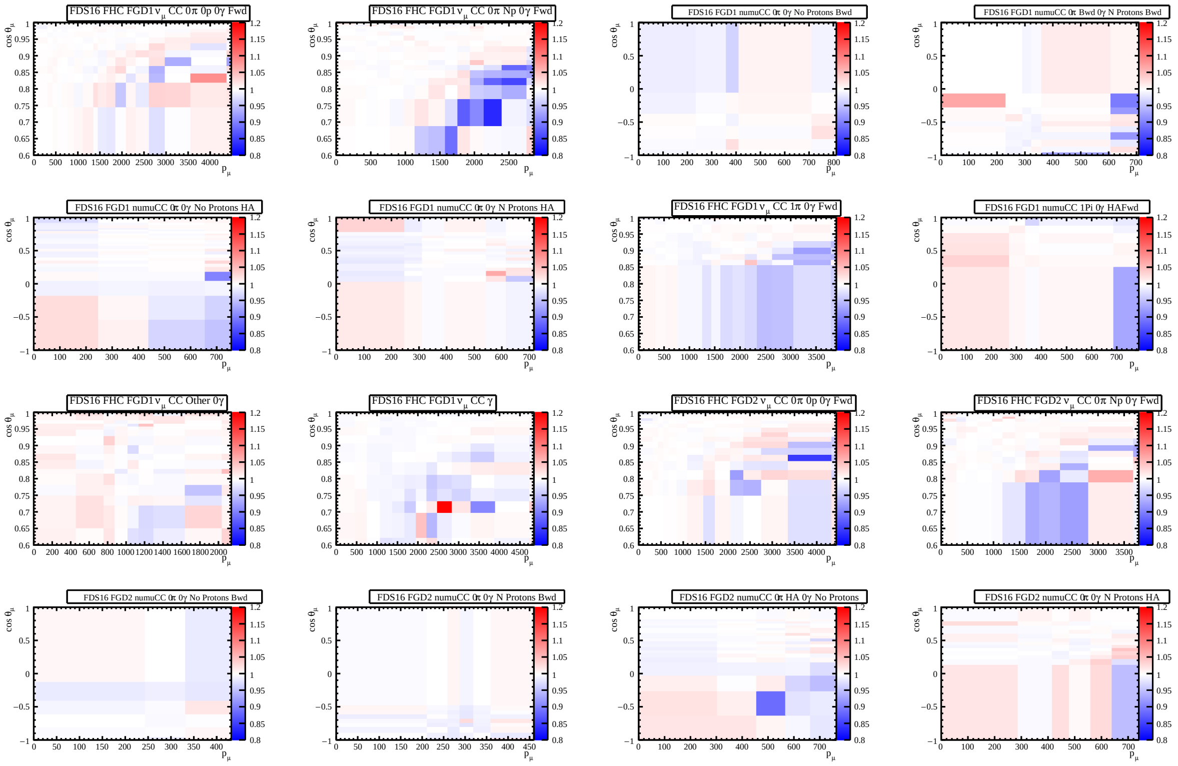

Figure B.33: Prefit (top 16) and postfit (lower 16) results for the AXFF 3comp M1sig fake data set, showing the ratio of the angular and momentum distributions between the fitted MC and the nominal fake data across 4π selection samples.

Prefit:

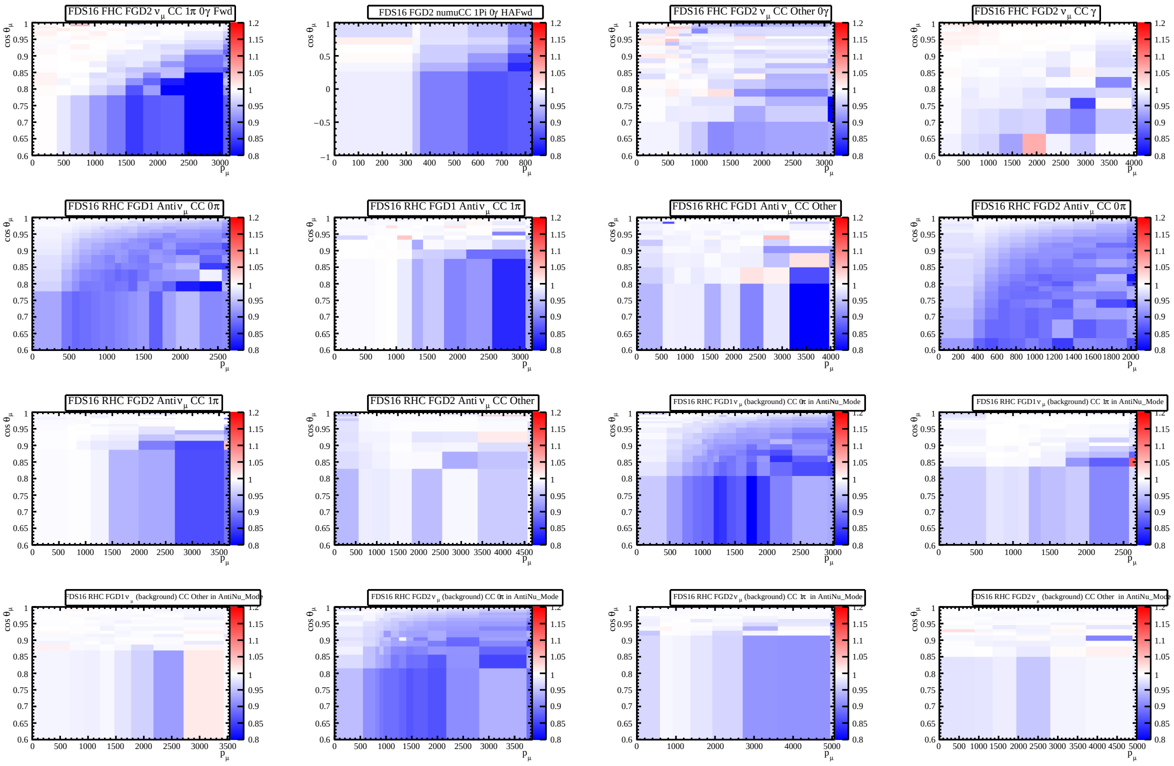

Postfit:

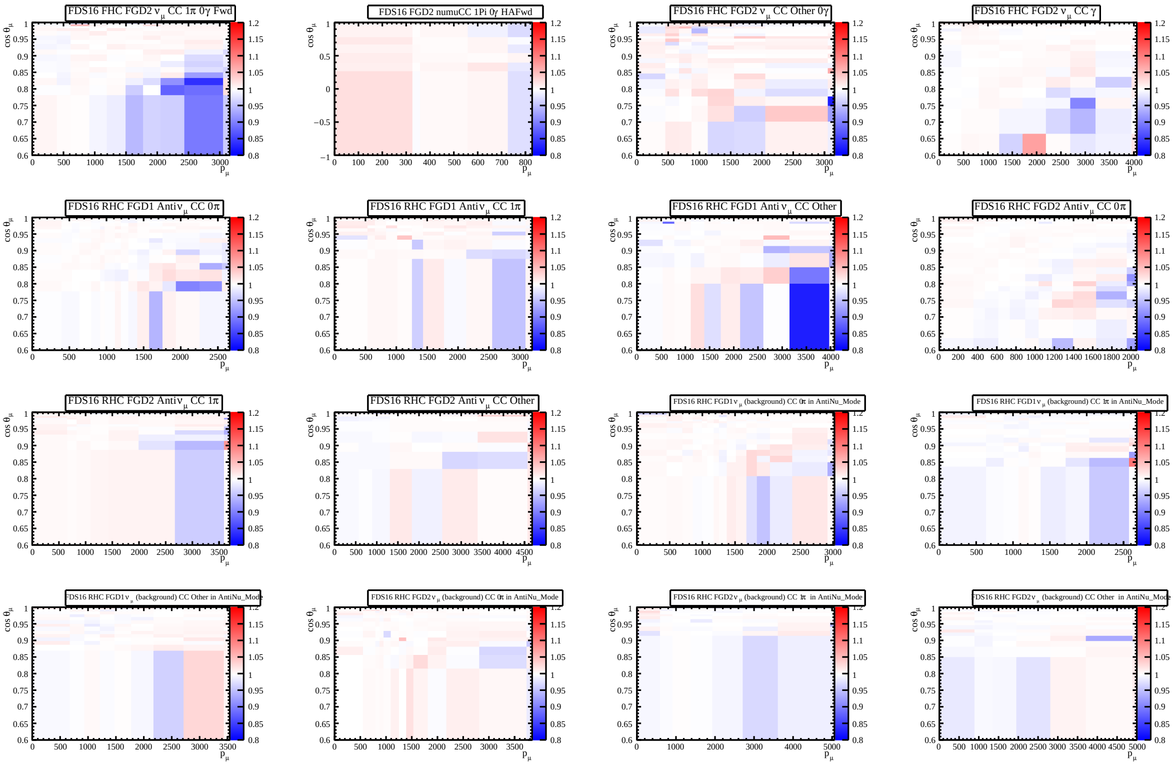

Figure B.34: Prefit (top 16) and postfit (lower 16) results for the AXFF 3comp M1sig fake data set, showing the ratio of the angular and momentum distributions between the fitted MC and the nominal fake data across 4π selection samples.

Prefit:

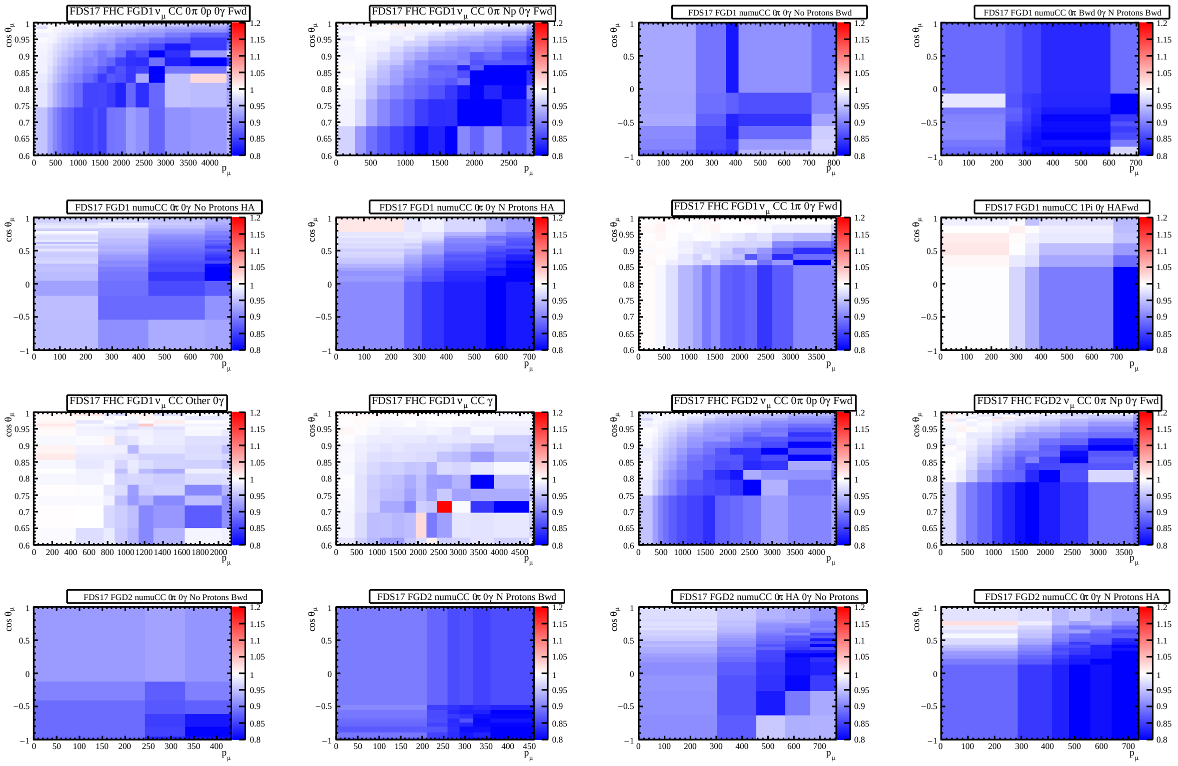

Postfit:

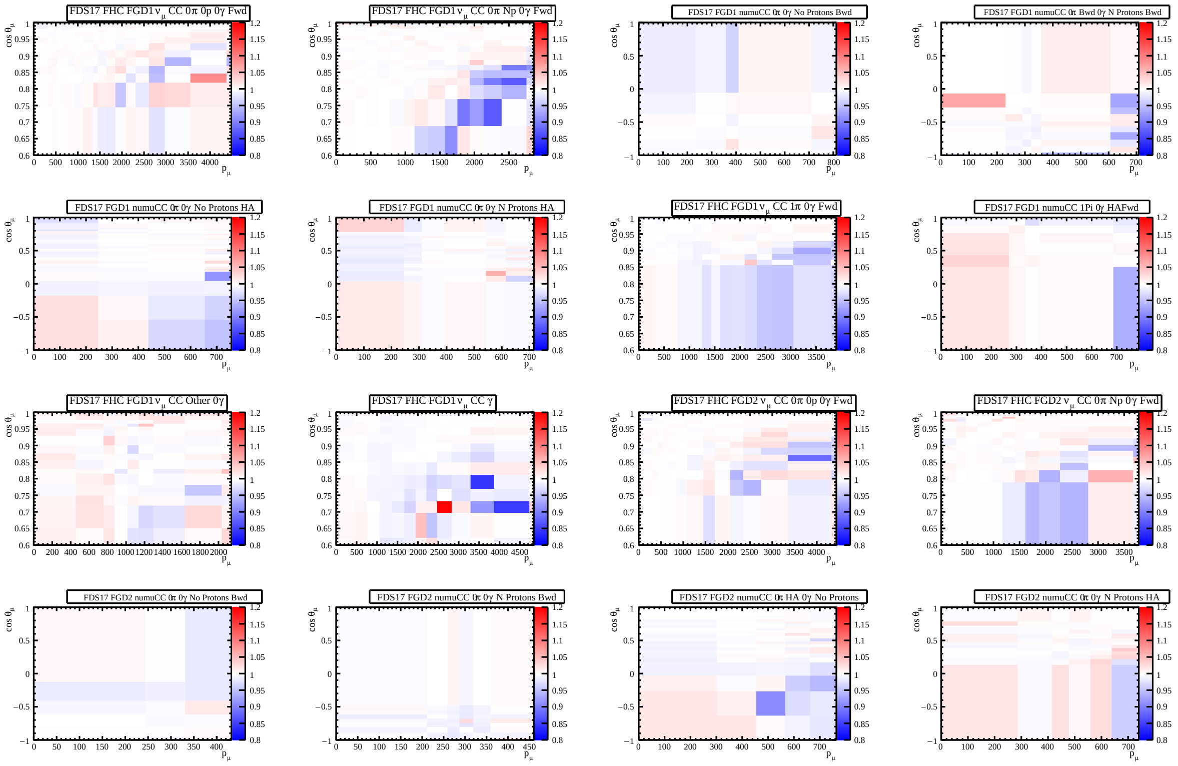

Figure B.35: Prefit (top 16) and postfit (lower 16) results for the AXFF 3comp Nom fake data set, showing the ratio of the angular and momentum distributions between the fitted MC and the nominal fake data across 4π selection samples.

Prefit:

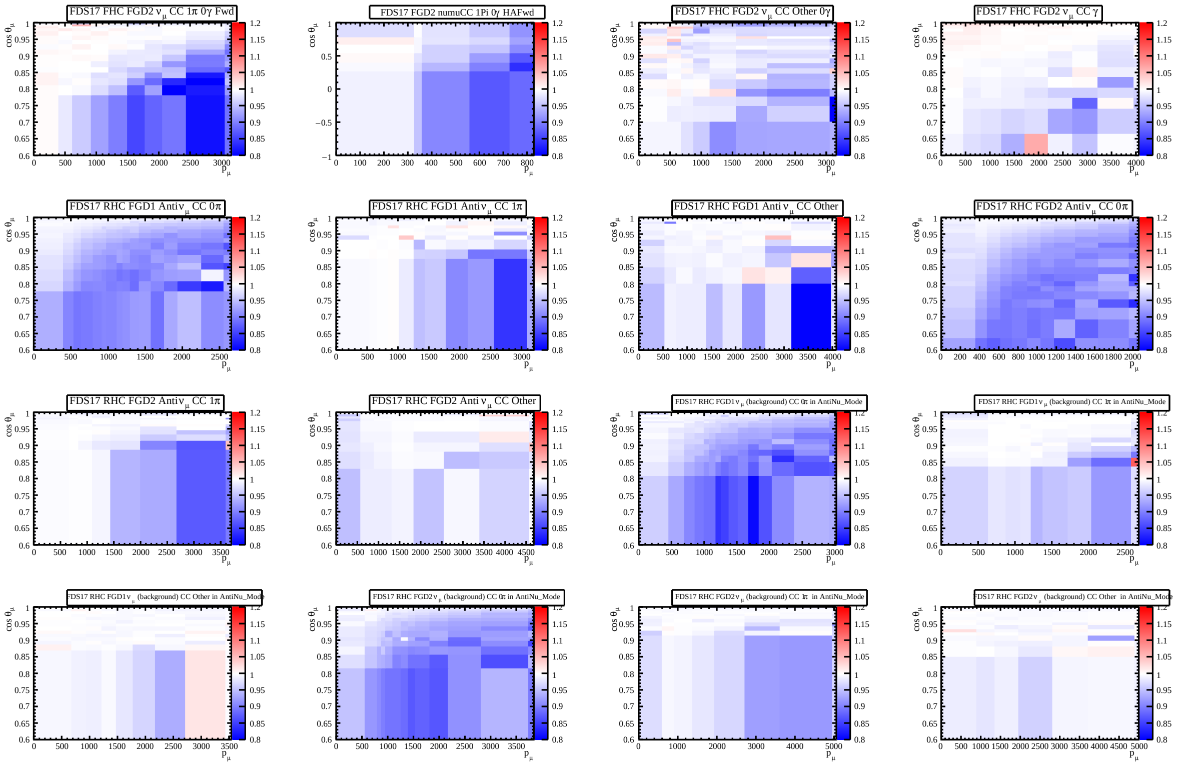

Postfit:

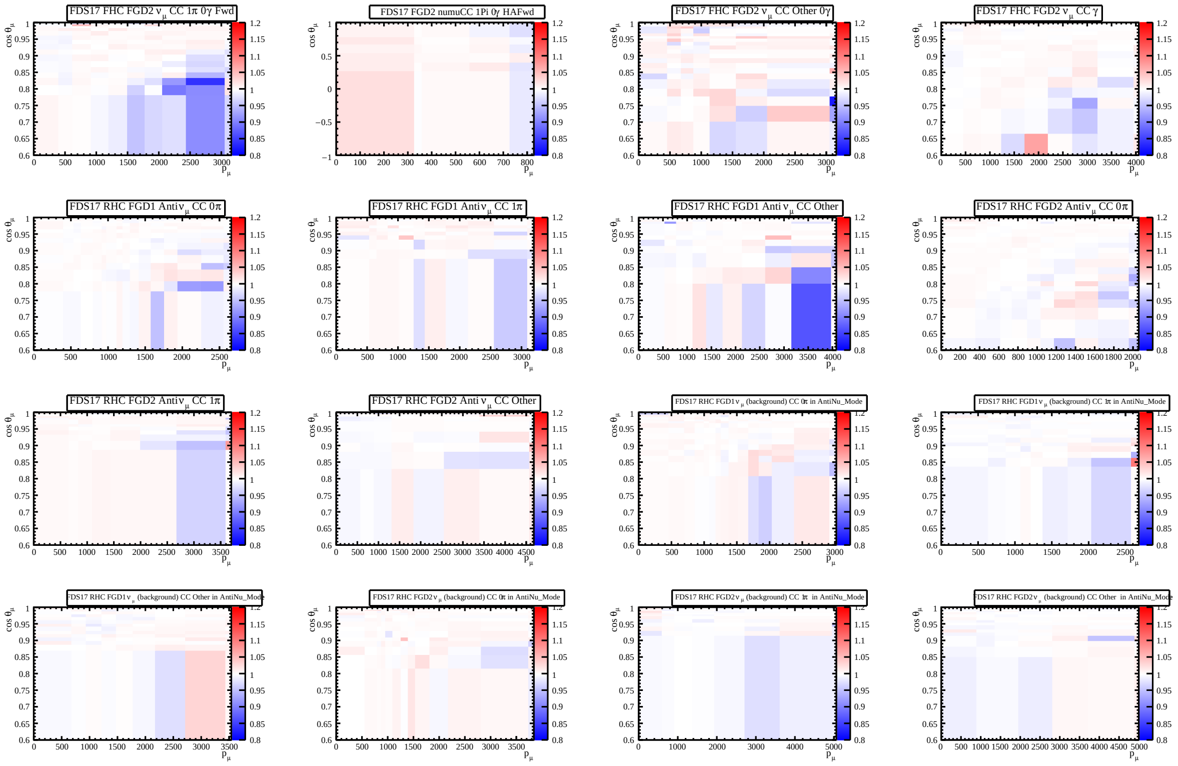

Figure B.36: Prefit (top 16) and postfit (lower 16) results for the AXFF 3comp Nom fake data set, showing the ratio of the angular and momentum distributions between the fitted MC and the nominal fake data across 4π selection samples.

Prefit:

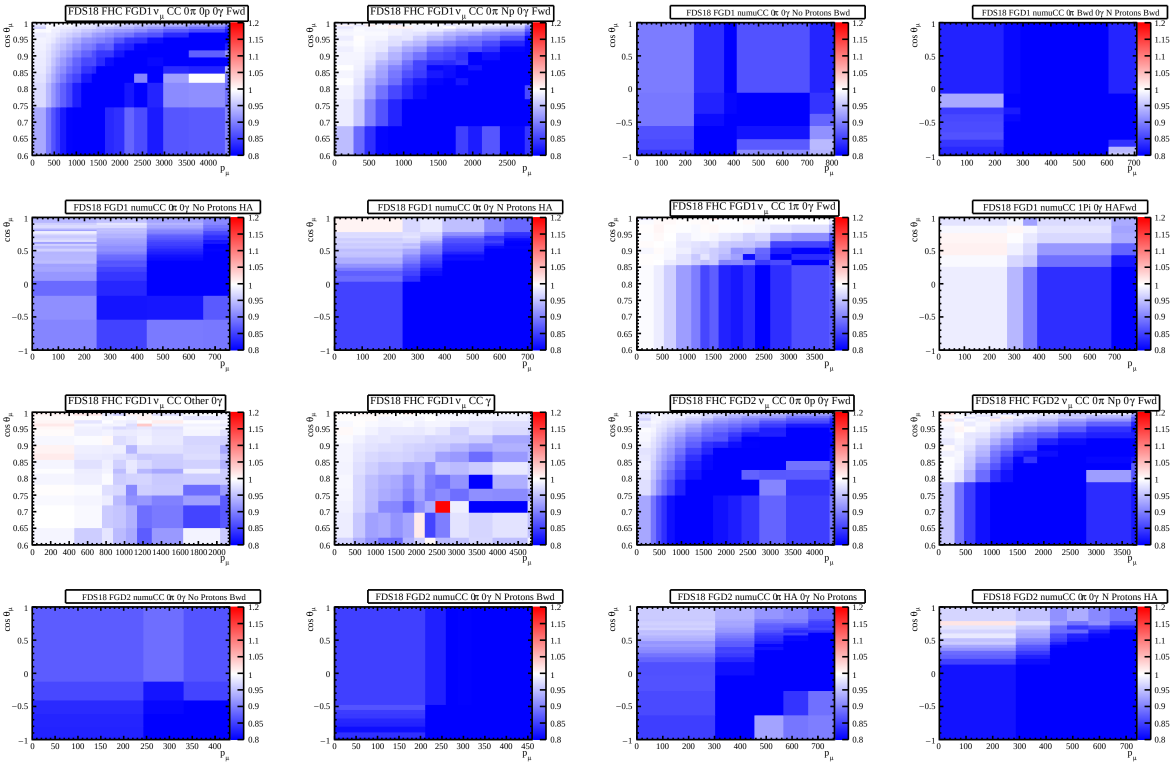

Postfit:

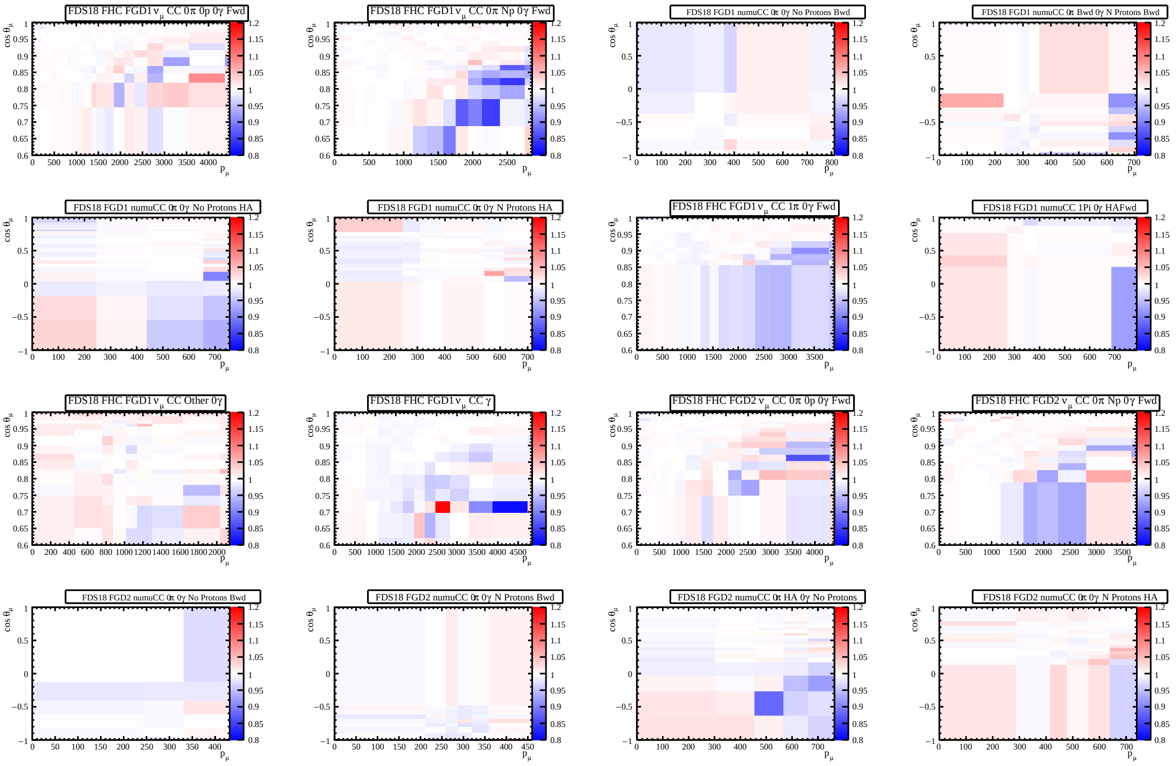

Figure B.37: Prefit (top 16) and postfit (lower 16) results for the AXFF 3comp P1sig fake data set, showing the ratio of the angular and momentum distributions between the fitted MC and the nominal fake data across 4π selection samples.

Prefit:

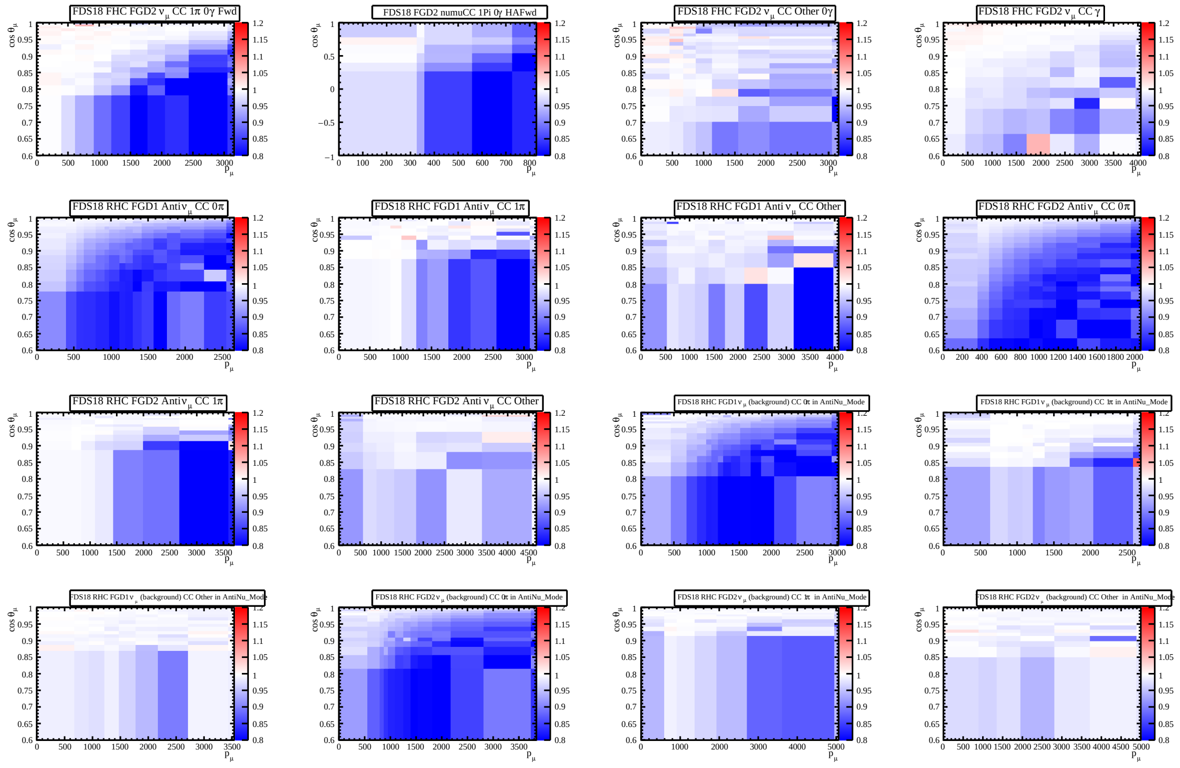

Postfit:

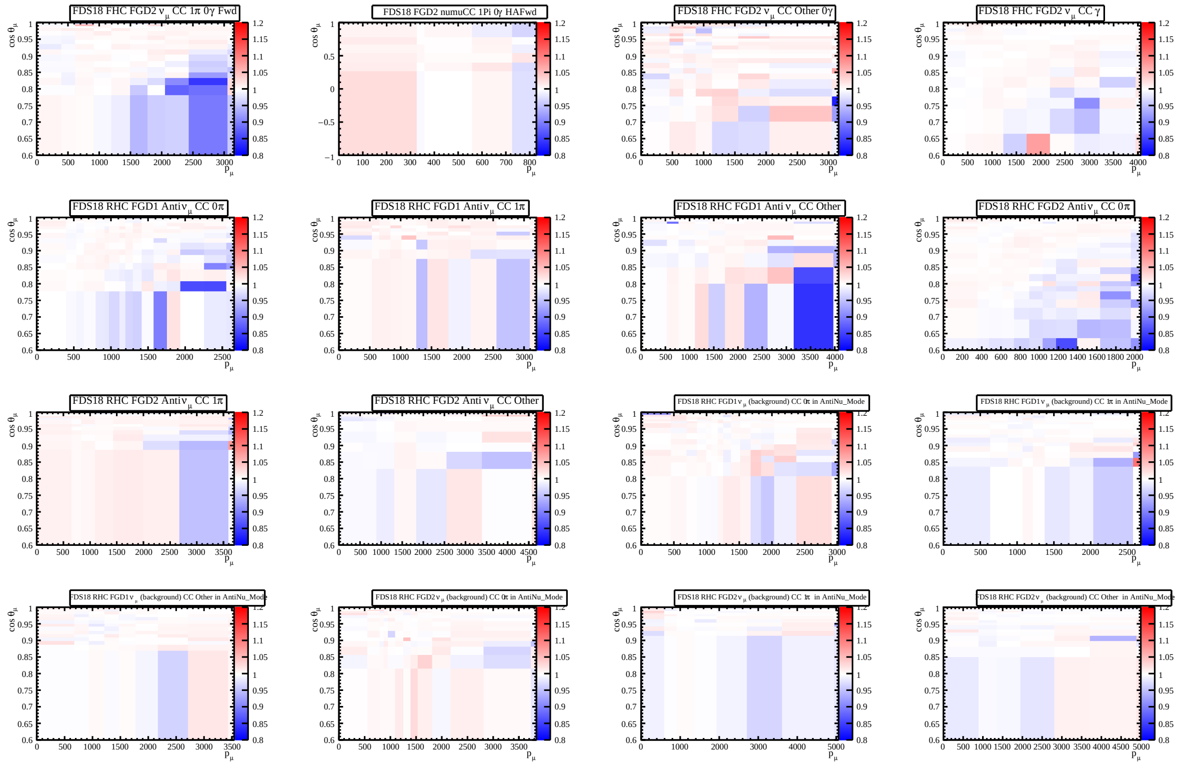

Figure B.38: Prefit (top 16) and postfit (lower 16) results for the AXFF 3comp P1sig fake data set, showing the ratio of the angular and momentum distributions between the fitted MC and the nominal fake data across 4π selection samples.